Tensor Virial Analysis and Magnetic Field Perturbations of Magnetized Molecular Cloud Cores

By
Erica Franzmann

A Thesis Submitted to the Faculty of Graduate Studies of
The University of Manitoba
In partial fulfillment of the requirements of the degree of

Doctor of Philosophy

Department of Physics and Astronomy
University of Manitoba
Winnipeg

Copyright © 2022 by Erica Franzmann

Abstract

We present a detailed analysis of the three-axis stability of molecular cloud core model geometries and the effects of three-dimensional magnetic field perturbations on simulated polarization maps. We have previously developed a molecular cloud core modelling package called "PolCat", which generates three-dimensional models of density and magnetic field structures constrained by reduced χ^2 fits to submillimetre polarization and continuum intensity data. PolCat fits provide insight into the underlying structures of cores, and by extension, the initial conditions from which stars form.

The most commonly applied form of the virial theorem in an astrophysical context is the scalar form, with relatively few applications of the full tensor form. We have found through examination of the three-axis virial equilibria not only the expected families of spheroidal geometries, but also families of triaxial ellipsoid geometries. In application as a PolCat stability check, we allowed our models to be slightly out of tensor equilibrium. We performed tests with both synthetic data and data of the OMC-1 BN/KL region from the SCUPOL Legacy Catalogue and BISTRO survey. We found that the virial criterion eliminated models with unrealistic geometries. Additionally, magnetic field strength estimates from the virial fits were in good agreement with independent measurements of the region.

A common method to estimate magnetic field strengths from polarization is the Chandrasekhar-Fermi method, where deflections of B-field polarization vectors from an assumed large-scale structure are assumed to directly equate to Alfvénic perturbations in the underlying magnetic field. However, a limitation of this method is that polarization maps are two-dimensional projections of three-dimensional structures, and the traced large-scale field may not be truly representative of the underlying structure. To examine the how three-dimensional perturbations would affect the polarization maps, we developed a method to propagate Alfvén waves along PolCat models' curved magnetic field lines and compared the perturbed and unperturbed maps. After perturbing our models with both individual and cumulative single-mode Alfvén waves, we find that patterns of deflection are highly dependent on the inclination of the magnetic field to the line of sight, and each model geometry has a characteristic pattern of deflection.

Acknowledgements

First, thanks to my supervisor, Dr. Jason Fiege for his help and guidance. Also for his willingness to drop everything to sort out several frustrating computational issues, and give pep-talks when I was discouraged. I also need to thank him for being a good sport about helping to edit my sometimes convoluted turns of phrase (sorry). I would also like to thank my committee for their understanding and advocacy over the course of this project. I am incredibly grateful for their support.

Thank you to the Department of Physics & Astronomy office staff for all their help, and notably Susan Beshta for her guidance and advocacy, and also her patience when dealing with high-strung graduate students.

A big thank you goes to Danielle Pahud for her enthusiasm and support in teaching, and her willingness to share her expertise and contribute her time to writing sprints. Thanks also to Suraj Srinivasan for his work in testing an early prototype of the tensor virial computation, and to Kelvin Au for his help with proofreading some of the material that makes up this thesis.

Thank you to the BISTRO collaboration, in particular Pierre Bastien, Derek Ward-Thompson, and Kate Pattle for providing access to the OMC-1 dataset, as well as giving their approval to publish my results in this document. Thank you also to Brenda Matthews and the SCUPOL Legacy Catalogue team for providing their data.

Thanks also to my office buddies (present and former) Benson Guest, Chelsea Braun, and Kelvin Au for your contributions to keeping me sane. On that note, thanks also to my cousin Nancy Young for agreeing to be my virtual office buddy during my intensive writing phase and whose presence greatly helped my productivity during these times of plague, when it was easy to get discouraged.

Thanks to my parents Alice Crawford and Michael Franzmann for their support and patience, and my brother Neale Franzmann for typical sibling shenanigans and occasional food delivery. Thank you for rearranging things to get me some home-office space and not letting me starve.

This research was funded by a NSERC Alexander Graham Bell Scholarship and the Sir Gordon Wu Graduate Scholarship, as well as my supervisor's NSERC Discovery Grant.

Preface

This thesis contains two chapters comprised of the following accepted manuscript versions of previously published works:

Chapter 3: Franzmann, E. L. and J. D. Fiege (2017). PolCat: Modelling sub millimetre polarization of molecular cloud cores using successive parameterized coordinate transformations. *Monthly Notices of the Royal Astronomical Society 466*, 4592-4613.

Chapter 4: Franzmann, E. L. and J. D. Fiege (2020). An Exploration of Tensor Virial Equilibrium in Magnetized Molecular Cloud Cores. *The Astrophysical Journal 899(2)*, 101.

The introductory sections of both these papers have been reworked in order to better incorporate into the thesis as a whole, and there have been additions in certain sections to address comments from my committee. Additionally, the results figures from the appendices of the first paper (Chapter 3) have been integrated into the text, and the data figures have been moved to Appendix B.

Contributions of Authors

I wrote both of the above papers included in this thesis, with my co-author and supervisor Jason Fiege providing input, editing, and direction. The work summarized within was likewise conducted by myself. Similarly, the rest of the thesis consists of my own original work, excepting Chapter 7, Sections 7.2-7.2.4.3 (and derivations in Appendices D-F), which adapted and generalized the framework developed by Scheurwater (1990) for propagating MHD waves in curvilinear bases. However, I note that while I did rely heavily on Scheurwater's framework, I also rederived it in detail to use for my more complex model geometries.

Table of Contents

Abstract ii
Acknowledgements iii
Preface iv
List of Tables viii
List of Figures ix

1 Introduction **1**
1.1 Motivation for New Techniques to Model Molecular Cloud Cores 3
1.2 Summary of Thesis Sections 4

2 Molecular Clouds **6**
2.1 Virial Theorem 7
2.2 Magnetic Field Structure and Strength 9
2.2.1 Dust Polarization 9
2.2.2 Alfvén Waves 11
2.2.3 The Chandrasekhar-Fermi Method 12
2.2.4 Zeeman Splitting 15
2.3 MHD Turbulence Diagnostics 16
2.3.1 Statistical Tools 17
2.4 Models of Molecular Cloud Cores 18

3 PolCat Summary and Methods **21**
3.1 Introduction 21
3.2 PolCat Fundamentals 22
3.2.1 Modelling Technique 23
3.2.2 Semi-Analytic Coordinate Transformation 24
3.2.3 Polarization Map Simulation 26
3.2.4 Fitness Functions 28
3.3 Ferret 31

3.4 Dimensional Scaling . . . 33
3.5 Coordinate Transform Primitives . . . 34
3.5.1 Polytropic Sphere Transformation (POLY) . . . 34
3.5.2 Asymmetric Linear Twist (LinearTwistA) . . . 35
3.5.3 Symmetric Linear Twist (LinearTwistS) . . . 35
3.5.4 Triaxial Scale (scale) . . . 36
3.5.5 Spheroidal Scale (scaleCyl) . . . 36
3.5.6 Solid Body Rotation (RotateA) . . . 36
3.5.7 Shift . . . 37
3.5.8 Other Transformations . . . 37
3.6 Model Tests . . . 37
3.6.1 Definitions . . . 38
3.6.2 Methodology . . . 38
3.6.3 Bonnor-Ebert Test Cores . . . 41
3.6.4 Non-Isothermal Test Cores . . . 56
3.7 Summary . . . 57

4 Exploration of Tensor Virial Equilibrium in Molecular Cloud Cores 59
4.1 Introduction . . . 59
4.2 PolCat . . . 60
4.2.1 Scaling . . . 61
4.2.2 The Bonnor-Ebert Sphere Transformation (BES) . . . 61
4.2.3 The Squeeze Transformation . . . 63
4.2.4 The Linear Twist Transformations . . . 65
4.3 Tensor Virial Theorem . . . 65
4.4 Implementation . . . 68
4.4.1 Non-magnetic tensor tables . . . 69
4.4.2 Magnetic Tensor Tables . . . 70
4.4.3 Virial Equilibrium Computation . . . 71
4.5 Analysis of Solutions in Tensor Virial Equilibrium . . . 72
4.5.1 Hourglass Field Models . . . 72
4.5.2 Twisted Hourglass Field Models . . . 76
4.6 Monte Carlo Sampling . . . 80
4.6.1 Method . . . 80
4.6.2 Results . . . 81
4.7 Discussion and Conclusions . . . 83

5 Exploration of Non-Equilibrium Molecular Cloud Cores Under Tensor Virial Constraint 86
5.1 Some Notes on Core Shape . . . 87
5.2 Hourglass Models . . . 88
5.3 Twisted Hourglass Models . . . 91
5.4 Discussion . . . 93

6 Virial Balance as a PolCat Fitness Penalty 95
6.1 Fits To Test data . . . 96
6.1.1 Composite Bonnor-Ebert Sphere Transformation (CBES) . . . 96
6.1.2 Test Data Generation . . . 97
6.1.3 Tweaks to PolCat . . . 99
6.1.4 Results . . . 99
6.1.5 Discussion . . . 108
6.2 Fits to Data: OMC-1 BN/KL . . . 109
6.2.1 Model Approach . . . 111
6.2.2 Fitness And Residuals . . . 112
6.2.3 Virial Quantities . . . 116
6.2.4 Model Geometries . . . 117
6.2.5 Density Profiles . . . 121
6.2.6 Discussion . . . 122

7 Alfvén Wave Propagation 125
7.1 Alfvén Wave Propagation in Uniform Media . . . 125
7.2 Alfvén Wave Propagation in Non-Isotropic Media . . . 127
7.2.1 PolCat Jacobians . . . 129
7.2.2 Curvilinear Basis and Metric Tensor Definitions . . . 130
7.2.3 MHD Equations in Curvilinear Coordinates . . . 132
7.2.4 The Eikonal Approximation . . . 133

8 Propagation Code 141
8.1 Computation Setup . . . 141
8.2 Propagating the Perturbation . . . 142
8.3 Characterizing the magnetic field perturbation . . . 143
8.4 Single-Mode Alfvén Perturbations . . . 145
8.4.1 Single wave perturbations . . . 145
8.4.2 Additive Perturbations . . . 151

8.5 Discussion and Conclusions 153

9 Summary of Conclusions 154
9.1 Tensor Virial Theorem 154
9.2 Application of the Virial Criterion to PolCat Fits 156
9.3 Alfvén Wave Propagation 157
9.4 Future Work 158

A Acronyms 172

B Test Data Figures from Chapter 3 174

C Volume and Surface Area Estimation 177

D Derivation of MHD Equations in Curvilinear Coordinates 180
D.1 Mass Conservation Equation 180
D.2 Lorenz Equation 180
D.3 Momentum Equation 181
D.3.1 Term $\boldsymbol{\mathcal{A}}$ 182
D.3.2 Term $\boldsymbol{\mathcal{B}}$ 182
D.3.3 Term $\boldsymbol{\mathcal{C}}$ 183
D.3.4 Bringing It Back Together 184

E Derivation of the 0^{th} Order MHD Wave Equation Under the Eikonal Approximation 185
E.1 Change of Variable 185
E.1.1 Term $\boldsymbol{\mathcal{A}}$ 186
E.1.2 Term $\boldsymbol{\mathcal{B}}$ 187
E.1.3 Term $\boldsymbol{\mathcal{C}}$ 189
E.1.4 Complete 0th order wave equation 189

F Derivation of the Alfvén Ray equations 191

List of Tables

3.1 Summary of Seed Model Parameters 40

4.1 Scaling Constants 69

6.1 Summary of Virial Seed Model Parameters 100
6.2 Summary of Parameters from OMC1 Fits 114

7.1 Vector Identities in Curvilinear Coordinates 132

List of Figures

2.1 Elliptical Polarization 10
2.2 Chandrasekhar-Fermi Method Geometry 13

3.1 PolCat Model Building Process 25
3.2 Model to polarization map projection 26
3.3 PolCat-Ferret Interface Flowchart 33
3.4 Test Case 1 Seed Model 41
3.5 Sample PolCat Solutions for Test Case 1 42
3.6 Sample PolCat Solutions for Test Case 2 43
3.7 Sample PolCat Solutions for Test Case 3 44
3.8 Pointing direction vs Twist Parameter 45
3.9 Sample PolCat Solutions for Test Case 4 46
3.10 Sample PolCat Solutions for Test Case 5 47
3.11 Equivalent Angles Due to Projection 48
3.12 Equivalent Angle Permutation Examples 49
3.13 Shape Maps for Seed Model Geometry 51
3.14 Shape Maps, Non-Seed Model Geometry 52
3.15 Example Density Profile Results 54
3.16 Density and Pressure vs. LOS Compression 55

4.1 Normalized pressure profile of the Bonnor-Ebert sphere 62
4.2 Core Shapes Defined by the Squeeze Transformation 64
4.3 Cartesian vs. Ellipsoidal Computation of the Gravitational Tensor 66
4.4 How to Find Tensor Equilibria 72
4.5 Shapes of Tensor Virial Equilibria with Hourglass Field Geometry 73
4.6 Gravitational Tensor Value Relative to Shape 74
4.7 Aggregate Magnetic Field Terms Relative to Shape 75
4.8 Kinetic Pressure Contribution To the Virial Balance 76

4.9 Compression vs ξ/ζ at Select Pressure Steps for Twisted Field Geometries . 77
4.10 Compression vs ζ for Spheroidal Solutions at Select Pressure Steps (Twisted Field Geometry) 78
4.11 Dimensionless Field Strength vs ζ 78
4.12 Aggregate Magnetic Tensor Terms as a Function of Shape 79
4.13 Sample of Monte Carlo Results 82
4.14 Vertical Slices from the Discrete Probability Distributions of Figure 4.13 . . 83
4.15 Most Probable values of ζ as a Function of Projected Axis Ratio 84

5.1 How to Interpret Shape Parameters 87
5.2 Shapes permitted by selecting normalized $R_{ii} \leq 0.2$ at select pressure steps . 89
5.3 Dimensionless Field Strengths Permitted by $VE_{ii} \leq 0.2$ 90
5.4 Shapes permitted by $VE_{ii} \leq 0.2$ at multiple C_t^* values for select pressure steps 92

6.1 Seed Model Geometries 98
6.2 All Case Shape Maps 102
6.3 All Cases, Compression vs Area-Equivalent Spheroidal Axis Ratio 104
6.4 Density 106
6.5 Twist Comparison 108
6.6 OMC-1 Data 109
6.7 BISTRO Data of the OMC-1 Region 111
6.8 Select Solutions for Each OMC-1 Dataset 113
6.9 Virial Magnetic Field Strength Scale vs Central Density Scale 117
6.10 OMC-1 Shape & Compression Maps 118
6.11 3D geometries of non-virial fits 119
6.12 3D Geometries of Virial Fits 120
6.13 OMC-1 Density Characteristics 122

8.1 Field line integration 142
8.2 Combined Single-Wave Perturbations 146
8.3 Effects of Model Orientation on Deflection Maps 147
8.4 χ_{pol} Deflection for three different energy ratios 149
8.5 χ_{pol} Deflection Scale and Twisted Geometries 150
8.6 Additive Perturbation RMS and Combined Histograms of $\Delta\chi_{pol}$ Deflections . 152

B.1 Test Case 2 Seed Model 174
B.2 Test Case 3 Seed Model 175
B.3 Test Case 4 Seed Model 175

B.4 Test Case 5 Seed Model 176

C.1 An Edge Voxel Intersection with a Surface Segment 178

Chapter 1

Introduction

Molecular clouds are complex, clumpy, turbulent collections of gas and dust in the interstellar medium. They range in size from the smallest 0.1 pc Bok globules to the most extreme 500 pc giant molecular cloud complexes (Bally, 1989) and are the sites of all known star formation (Elmegreen and Scalo, 2004; Hennebelle and Falgarone, 2012; Burkhart et al., 2015). Therefore, understanding the dynamics in these regions is essential for studying the conditions from which stars form. The conditions in the clouds and the denser star-forming cores are such that the magnetic field is effectively "frozen in" to the gas, meaning that as the gas and dust of the cloud moves, the field moves with it. This exerts an opposing force that resists gravitational contraction, and, as a result, influences the evolution of these clouds and affects the initial conditions of the stars that form within them.

Polarized submillimetre emission from spinning dust grains embedded in the clouds provides information on the integrated magnetic field direction. It can also be used to indirectly estimate the field strength. However, a notable limitation with deriving magnetic field parameters from polarization maps lies in their inherent degeneracy. Maps of integrated polarized emission naturally encompass contributions from all magnetic field directions along the line-of-sight, which can mask some aspects of three-dimensional structure (Fiege and Pudritz, 2000a; Crutcher, 2012). As a result, information along the line-of-sight is lost, and there are a wide range of physical density and magnetic field structures that produce polarization maps that would be almost indistinguishable observationally.

Franzmann (2014) was focused on developing the polarization modelling package PolCat, which is designed to model three-dimensional density and magnetic field geometries of molecular cloud cores from their submillimetre polarization data. PolCat uses the Ferret evolutionary optimization platform (Fiege, 2010) to explore a large parameter space of potential models and fit their intensity and polarization maps to input data sets. The use of Ferret allows for simultaneous fitting of intensity and polarization parameters, making

PolCat a powerful tool for providing insight into potential structure and conditions of the underlying cloud and – by extension – help shed light onto the environments from which stars form.

While PolCat makes excellent progress finding families of models that fit the input data sets, it is essentially fitting a full three-dimensional structure to a two-dimensional projection. The inherent degeneracy of the polarization maps leads to a wide array of core shapes and three-dimensional magnetic field geometries that can produce excellent fits to the data when projected. As a result, PolCat is chiefly designed as a tool to explore the range of core geometries that can describe observational data. However, the large sample of geometries that PolCat produces can include models that are unphysical, such as those that are unnaturally flat or fields that are twisted to an extent that is unrealistic, and an on-the-fly method to discourage selection of these very unstable models is desired.

A common method to study molecular core stability is to apply the scalar virial theorem, which in its simplest form states that in virial equilibrium the total potential energy of a system is equal to twice its kinetic energy. While we do not necessarily expect the cores be in perfect virial equilibrium, they are not expected to be very far from it (Dib et al., 2007). There is also a less commonly-used tensor form of the virial theorem, which describes stability on each individual axis. The scalar form of the virial theorem can be recovered by taking the trace of the tensor. By applying a "virial constraint" to the models such that the result of the virial equation is within some percentage of the gravitational energy for each of the diagonal tensor components eliminates some of the more unrealistic geometries and therefore reduces the model degeneracy in a manner that does not artificially limit the parameter space. In addition, this method also places tighter constraints on the density and velocity dispersion parameters and provides a method to approximate magnetic field strengths, which we cannot measure directly from polarization data alone.

An indirect method to estimate the plane-of-sky magnetic field strengths from polarization data is to use a variant of the Chandrasekhar-Fermi (CF) method (Chandrasekhar and Fermi, 1953) with some correction for magnetohydrodynamic (MHD) turbulence (e.g. Falceta-Gonçalves et al., 2008). The CF method assumes that the magnetic field consists of two components: 1) a large-scale ordered component $\mathbf{B}_0$, and 2) a random component $\mathbf{B}_t$ caused by turbulence, such that the total field is $\mathbf{B} = \mathbf{B}_0 + \mathbf{B}_t$. Turbulence perturbs the magnetic field away from the ordered structure, which causes disorder in the measured polarization angles. This effect decreases as the magnetic field strength increases due to the magnetic field lines resisting perpendicular motion. The CF method uses this property to derive the magnetic field strength from the polarization angle dispersion by assuming that all deflection from the ordered component is due to the turbulent field component.

Limitation of the CF technique is that the two-dimensional projection of the large-scale ordered field structure is typically inferred by rotating the polarization vectors 90° and fitting with an ordered two-dimensional field (e.g. Schleuning, 1998; Lai et al., 2002). These vectors are integrated quantities along the line of sight, and the final direction may not be representative of actual the plane-of-sky field direction (e.g. Fiege and Pudritz, 2000a).

In order to explore the effects of MHD perturbations on polarization maps, I have developed a method that propagates MHD waves through PolCat models in three-dimensions. By generating polarization maps of the perturbed model, I can explore the effect the perturbations have on the final polarization maps.

1.1 Motivation for New Techniques to Model Molecular Cloud Cores

Current models of molecular cloud cores do not easily lend themselves to directly fitting observational data. Spherical equilibrium models are not difficult to compute. However, magnetic fields result in anisotropic stresses, and therefore spherical models cannot include a magnetic field. Spherical models are therefore too simplistic for the complex geometries found in data. Self-Consistent field methods provide more complex spheroidal equilibrium models threaded by magnetic fields (e.g. Mouschovias (1976a); Tomisaka et al. (1988a); Fiege and Pudritz (2000b)). However, there is no practical method to perform thorough parameter searches of such models due to computational time and uncertainty of convergence, since not all initial conditions converge in general (Fiege and Pudritz, 2000b). Similarly, simulations are designed to evolve dynamically, which takes a large amount of time and computational resources, and the structures they create are structurally random and sometimes transient (Vázquez-Semadeni et al., 2005; Dib et al., 2007). Generating polarization maps from these models provides insight into the polarization patterns observed in turbulent flows. However, they cannot be used to fit detailed models of individual observed structures because of their random nature.

With PolCat, we have a highly controllable laboratory to generate computationally inexpensive theoretical models of magnetized cores on demand, which we can use to model data via parameter search and χ^2 minimization. The flexibility of our method also allows us to use our models as a framework to explore how magnetic fields impact the shapes of cores and the propagation of Alfvén waves through them. In this work, we take advantage of PolCat's flexibility to study the three-axis stability of our model geometries – both in general and those that fit observational data – and also study the effects that perturbations

to the cores' magnetic fields have on their polarization maps.

Our approach to estimate the three-axis stability of cores is to apply the tensor form of the virial theorem, which is less commonly used than the more familiar scalar form. Polarization maps do not directly infer the strength of the magnetic field. However, by assuming that our models are in scalar virial equilibrium, we can scale the strength of the magnetic field so that the model is in equilibrium. We then use this scaled magnetic field structure to calculate the diagonal components of the tensor virial theorem, to estimate the tensor virial equilibrium separately along all three major axes. This method is can be used to provide a constraint on PolCat models to ensure that the results are close to virial equilibrium on all three axes, to filter out extreme geometries such as long, spindle-like structures and extremely flattened disks. Due to the inherent degeneracy of polarization data, such models can often reproduce the structures seen in polarization data when viewed from finely tuned and opportunistic angles. Tensor virial theorem therefore provides a mechanism to select less extreme models that explain the polarization data equally well.

The perturbation of magnetic field lines by Alfvén waves forms the basis of the Chandrasekhar-Fermi method for estimating magnetic field strengths. This method is employed by analyzing the two-dimensional polarization vectors and measuring the dispersion in angles, which is attributed to Alfvénic perturbations of a large-scale ordered magnetic field structure. By visualizing three-dimensional randomized Alfvénic perturbations propagating through our models and measuring the effects on their polarization maps, we can map the predicted polarization angle dispersion and potentially provide an additional observable constraint on the results.

1.2 Summary of Thesis Sections

The remainder of this thesis is summarized as follows. Chapter 2 presents an overview of the virial theorem and observational techniques for determining magnetic field structure and strength, as well as a brief overview of theoretical models. Chapter 3 presents an in-depth summary of PolCat with results of fitting to test data (previously published as Franzmann and Fiege (2017)). Chapter 4 describes the methods by which we compute the virial balance for the core models, as well as an in-depth exploration of model geometries in three-axis equilibrium (previously published as Franzmann and Fiege (2020)). Directly following, Chapter 5 explores the range of allowed geometries under our proposed PolCat virial restriction, and Chapter 6 analyzes the results of applying the virial criterion to PolCat fits, both to test data and data from the SCUPOL Legacy Catalog (Matthews et al., 2009) and the BISTRO survey (Ward-Thompson et al., 2017). Chapter 7 derives the method I use to propagate

MHD waves through PolCat models, and Chapter 8 describes how the definitions of the previous chapter were applied, and discusses the results of MHD perturbations on PolCat model polarization maps. Finally, I summarize my results in Chapter 9.

Chapter 2

Molecular Clouds

Gravitational contraction is the main force that drives clouds to condense to form stars. However, without the presence of other forces to resist that contraction, star formation would occur at a much higher rate and shorter timescale (Crutcher, 2012). Observational evidence from polarized dust emission and Zeeman splitting of molecular lines shows that these clouds are magnetized, and the internal conditions are such that the magnetic fields are effectively "frozen-in" to the gas (Hennebelle and Falgarone, 2012). Charged particles in the cloud cannot move transverse to the field direction without experiencing the Lorenz force, and the neutral matter is collisionally coupled (albeit imperfectly) to the ions. This implies that the magnetic field introduces a preferential direction of gas motion, and resists being deformed. Therefore, the magnetic field has an effect on the turbulence, and it is magneto-hydrodynamic in nature (Lazarian, 2004). Because magnetic fields resist transverse motion, they introduce a preferred direction to movement with statistical signatures distinct from regular hydrodynamic turbulence (Elmegreen and Scalo, 2004; Hennebelle and Falgarone, 2012). However, while the collisional coupling effectively causes the field lines to be "frozen in, this coupling is not perfect. Eventually, the ions gradually leak away through ambipolar diffusion, which causes the field to weaken (Hennebelle and Falgarone, 2012) However, magnetic resistance and gravity are not the only important forces at play when it comes to the dynamics of molecular clouds.

Despite the large disparity in cloud structures and sizes, scaling laws have been found that relate mass, density, size, and velocity dispersion. The pioneering study by Larson (1981) used data from a collection of molecular clouds and smaller cores ranging in size from $\sim 0.1 - 130$ pc. He found several power-law relationships, including a relation between the three-dimensional velocity dispersion σ_{3D} and object size L of $\sigma_{3D} \propto L^{0.38}$, similar to the 1/3 power index expected from subsonic, non-magnetized, incompressible Kolmogorov turbulence (Hennebelle and Falgarone, 2012). However, the dataset used in Larson (1981)

was very heterogeneous, encompassing data from multiple different instruments, line tracers, and sensitivities, and results from more homogenous study from a single instrument by (Solomon et al., 1987) found a steeper index of 0.5. General power-law scaling is expected from structures that are part of a hierarchy of turbulent motions (Elmegreen and Scalo, 2004; Hennebelle and Falgarone, 2012). A point of interest is that results consistent with the Kolmogorov spectrum continue to be found, despite the presence of magnetic fields and supersonic motions.

Turbulence describes how energy injected at the largest scales cascades down to the smallest scales, where it is dissipated as heat (Elmegreen and Scalo, 2004; Hennebelle and Falgarone, 2012). In addition to influencing the clouds' structure, interstellar turbulence plays a large role in determining the clouds' dynamics, drives chemical mixing and transport, and is one of the main factors supporting clouds against gravitational collapse (Hennebelle and Falgarone, 2012).

2.1 Virial Theorem

Molecular clouds are clumpy, turbulent structures. Gravity tends to cause clumps to coalesce and contract, while turbulence has the effect of supporting the gas against gravity. A useful criterion to describe the balance of the various energies present in the system is to use the virial theorem. The most basic form of the virial theorem, which only considers gravitational potential, states that, in equilibrium, the magnitude of the gravitational binding energy is equal to twice the kinetic energy: $|\mathcal{W}| = 2\mathcal{T}$. This simplified analysis is commonly used in observational studies (e.g. Schleuning, 1998; Crutcher, 1999). A fairly common analysis is to compute a "virial parameter" $\alpha_{\rm vir}$ by taking the ratio which leads to

$$\alpha_{\rm vir} = \frac{2\mathcal{T}}{|\mathcal{W}|} = \frac{5\sigma^2 R_c}{GM_c} \tag{2.1}$$

(McKee and Ostriker, 2007) , where σ^2 is the one-dimensional velocity dispersion, R_c is the radial size of the object, and M_c is the object mass. For a virial-balanced, self-gravitating, unmagnetized, uniform sphere with no external pressure, $\alpha_{\rm vir} = 1$. Deviations from $\alpha_{\rm vir} = 1$ are used as an assessment of the balance between the kinetic and gravitational energies in objects (Dib et al., 2007).

The presence of magnetic fields creates a more complicated scenario. Conditions in molecular clouds are such that magnetic field lines are "frozen" into the gas and are dragged along as the gas moves (neutral and charged material are collisionally coupled). However, the magnetic field resists transverse movement, and therefore gravitational contraction perpen-

dicular to the field direction. The magnetic field also contributes to net (albeit anisotropic) cloud support. A more complete form of the virial theorem incorporates magnetic volume and surface energy terms and external surface pressure:

$$\frac{1}{2}\ddot{I} = 2\mathcal{T} + \mathcal{W} + 3(\gamma - 1)U + \mathcal{M} + \mathcal{M}s - \mathcal{T}s, \tag{2.2}$$

where $\mathcal{W}$, $\mathcal{T}$, U and $\mathcal{M}$ are, respectively, the volume-integrated gravitational, kinetic, internal heat, and magnetic energies, and $\mathcal{M}s$ and $\mathcal{T}s$ the surface magnetic and kinetic terms. The term $\ddot{I}$ represents the second time derivative of the moment of inertia of the system, and is equal to zero under commonly assumed equilibrium conditions.

Another useful parameter is the magnetic critical mass M_Φ, defined under conditions where $|\mathcal{W}| = \mathcal{M}$. For a uniform field, under the condition that magnetic flux Φ is conserved under contraction: $\mathcal{M} \propto B^2R^3 \approx \pi^2\Phi^2/R$. It then follows that the magnetic critical mass is

$$M_\Phi \equiv c_\Phi \frac{\Phi}{G^{1/2}} \tag{2.3}$$

(McKee and Ostriker, 2007) where c_Φ is a constant dependent on the density and magnetic field structure. Cores with $M_c < M_\Phi$ are magnetically dominated (magnetically subcritical) and the magnetic field alone is sufficient to support the cloud against gravity. Such an object cannot collapse gravitationally without first removing some magnetic flux to reduce M_Φ. For the case $M_c > M_\Phi$ (magnetically supercritical) the magnetic field is not sufficient to support the cloud against gravitational collapse, requiring additional contributions from internal heat and turbulence to maintain support and prevent collapse.

The scalar form of the virial theorem is used most widely. However, because this form has no directionality, considerable detail is lost. For a more in-depth analysis, we must examine the stability along each principal axis. As such, we apply the tensor form of the magnetic virial equation:

$$\frac{1}{2}\ddot{I}_{jk} = 2\mathcal{T}_{jk} + \mathcal{W}_{jk} + \delta_{jk}\{(\gamma - 1)U + \mathcal{M}\} - 2\mathcal{M}_{jk} + \mathcal{M}s_{jk} - \mathcal{T}s_{jk}, \tag{2.4}$$

which was derived by Chandrasekhar (1960). Taking the trace of equation (2.4) recovers the scalar form (equation (2.2)). The tensor virial theorem analyzes all three axes separately, which is valuable for anisotropic magnetic forces.

The tensor form of the virial theorem is not often used due to the complexity of computing the tensor components. However, there have been some theoretical studies that utilize it. Zweibel (1990) used the tensor virial theorem to explore the effect of field strength on core stability using an analytic approximation under very simple conditions. She found that the

presence of a magnetic field reduces the size of gravitationally bound clumps and can support the cloud at higher external pressures. Later work by Dib et al. (2007) using the Eulerian form of tensor virial theorem used simulations to assess whether cloud cores that formed out of model molecular clouds were "virialized" and the relative importance of the virial terms to the whole. Their simulated cores ranged from non-magnetic to magnetically subcritical. They found that the surface terms were as important as the volume energy terms, and that only the inner, high-density clumps were virialized (Dib et al., 2007).

2.2 Magnetic Field Structure and Strength

While we cannot directly measure magnetic fields in molecular clouds, astronomers have developed multiple techniques to indirectly infer strength and directional information from observable tracers. Every method has limitations, and so there is strong motivation to develop new techniques that fill in the gaps of what we can infer about magnetic fields (González-Casanova and Lazarian, 2017). Here we summarize the most common techniques relevant to the content of this thesis.

2.2.1 Dust Polarization

Molecular clouds contain a population of elongated dust grains. Even though these grains comprise a small fraction of the total mass of the molecular cloud, they are large enough in size that they preferentially absorb wavelengths of light into the blue part of the optical spectrum, effectively robbing the background starlight of its shorter wavelengths. These grains tend to spin around their short axis due differential scattering of anisotropic radiation, and the spin axes tend to align with the magnetic field on average (Lazarian, 2007; Crutcher, 2012; Hoang and Lazarian, 2016). As a result, these aligned grains have a larger emission and extinction cross-section perpendicular to the magnetic field (Lazarian, 2007). This causes them to 1) act as a polarizing filter on background starlight, and 2) emit polarized thermal emission (Lazarian, 2007; Crutcher, 2012). The polarization of both of these effects is perpendicular to the integrated POS magnetic field, allowing the POS field structure to be mapped (Crutcher, 2012). However, while useful magnetic field vectors can be obtained from the polarization of background starlight, this technique only provides information in the outer regions of molecular clouds where the extinction is low (optical depth $\tau \lesssim 1$) (Crutcher, 2012).

The thermal emission from the grains is linearly polarized and falls in the range from submillimetre to far infrared (Lee and Draine, 1985; Lazarian et al., 1997; Weintraub et al.,

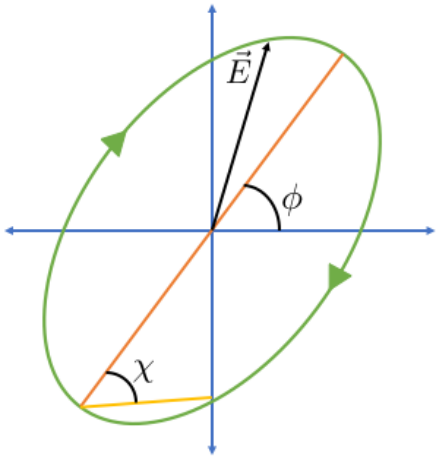


Figure 2.1: The planar representation of elliptical polarization (both linear and circular).

2000). Information on the polarization angle of the electric field vector is obtained from the Stokes vector. The Stokes vector has four parameters: I is the total intensity, Stokes $Q = I_p \cos 2\phi \cos 2\chi$ and $U = I_p \sin 2\phi \cos 2\chi$ represent the linear polarization, and $V = I_p \sin 2\chi$ represents the circular polarization, with I_p the intensity of the polarized light. Figure 2.1 shows how the angles ϕ and χ parameterize the polarization ellipsoid. The factor of 2 before ϕ in Q, U, and V originates from 180° rotation degeneracy in the ellipse, and the factor of 2 before χ results from degeneracy between two ellipsoids rotated 90° with axis ratios swapped. For pure linear polarization $\chi = 0$, and the polarization angle can be derived from

$$\phi = \frac{1}{2} \tan^{-1} \left(\frac{U}{Q} \right) \tag{2.5}$$

This method only obtains the angular orientation of the electric field vectors with 180° degeneracy. Mathematically, polarization vectors are not true vectors; rather, they behave like vectors where the head and tail are indistinguishable.

While polarization maps provide some information on the overall direction of the underlying magnetic field, they provide no direct measurement of its strength. Additionally, the physical characteristics of the dust, including geometry, composition, and degree of alignment with the magnetic field, also have an effect on the degree of polarization (e.g. Goodman et al. 1995; Lazarian et al. 1997; Weintraub et al. 2000; Draine 2003). However, by using "relative" stokes vectors it is possible to simulate the direction and fractional polarization of the emission without depending on the exact grain properties, as in the approach of Wardle and Konigl (1990).

It is common for observers to trace the magnetic field in the plane of the sky from the polarized emission by rotating the electric field vectors 90°. However, this technique is flawed,

because the observed Stokes vectors result from integrating all field directions along the line of sight. This takes a three-dimensional structure and projects it into two dimensions. The effective integration along the line of sight may mask structural features such as helical twists, or tangling of the field along the line of sight in the observed polarization vectors (Fiege and Pudritz, 2000a; Crutcher, 2012). As a result, there are multiple potential field structures (and core geometries) that produce very similar polarization maps. This degeneracy was a major influence for the approach we developed for our PolCat modelling software, which we discuss in Chapter 3.

2.2.2 Alfvén Waves

Alfvén waves are non-compressible magnetohydrodynamic waves that propagate along magnetic field lines. Their existence was first demonstrated by Alfvén (1942), as a natural consequence of motions of conducting fluid in the presence of magnetic fields. Starting with Maxwell's equations and Ohm's law, the electric charge density ($\mathbf{J}$), electric field ($\mathbf{E}$), and magnetic field ($\mathbf{B}$) obey

$$\boldsymbol{\nabla} \times \mathbf{E} = -\frac{1}{c}\frac{\partial \mathbf{B}}{\partial t}, \tag{2.6}$$

$$\boldsymbol{\nabla} \times \mathbf{B} = \frac{4\pi}{c}\mathbf{J}, \text{ and} \tag{2.7}$$

$$\mathbf{J} = \sigma_C \left(\mathbf{E} + \frac{1}{c}\mathbf{v} \times \mathbf{B} \right) \tag{2.8}$$

(Alfvén, 1942; Jackson, 1975), where σ_C is the conductivity of the medium. Under conditions of infinite conductivity (similar to the conditions in molecular clouds), equation (2.8) leads to

$$\mathbf{E} + \frac{1}{c}\mathbf{v} \times \mathbf{B} = 0. \tag{2.9}$$

In addition, the fluid is also susceptible to the hydrodynamic equations. For this analysis, the important contributor is the force equation

$$\rho \frac{d\mathbf{v}}{dt} = -\boldsymbol{\nabla} P + \frac{1}{c}\left(\mathbf{J} \times \mathbf{B}\right), \tag{2.10}$$

where P is the mechanical pressure of the system and the total time derivative on the left hand side is the convective derivative with respect to $\mathbf{v}$. For Alfvén's derivation, the imposed magnetic field $\mathbf{B_0}$ is constant and lies along the z-axis, the velocity points along the x-direction, and all variables are assumed to be dependent only on z and t. For this construction, it can easily be shown that $\boldsymbol{\nabla} \cdot \mathbf{v} = 0$, and therefore the flow is incompressible,

eliminating the $\boldsymbol{\nabla} P$ term in equation (2.10). Under these conditions, equation (2.9) produces an electric field (and corresponding $\mathbf{J}$) along the y-axis and an induced magnetic field $\mathbf{b}$ along the x-axis. Additionally, the z-dependence eliminates the $(\mathbf{v} \cdot \boldsymbol{\nabla})\mathbf{v}$ term from the convective derivative, leaving

$$\rho \frac{\partial \mathbf{v}}{\partial t} = -\frac{1}{4\pi}(\mathbf{B} \times (\boldsymbol{\nabla} \times \mathbf{b}), \text{ and} \tag{2.11}$$

$$\frac{\partial \mathbf{b}}{\partial t} = B_0 \frac{\partial v}{\partial z}\hat{\mathbf{x}}. \tag{2.12}$$

Equating the x-components of equation (2.11) gives

$$\frac{\partial \mathbf{v}}{\partial t} = \frac{B_0}{4\pi\rho}\frac{\partial b}{\partial z}. \tag{2.13}$$

After taking the partial derivative of equation (2.12) with respect to t, and equation (2.13) with respect to z, we can combine the equations to produce

$$\frac{\partial^2 b}{\partial t^2} = \frac{B_0^2}{4\pi\rho}\frac{\partial^2 b}{\partial z^2} \tag{2.14}$$

which describes the perturbed field as a wave propagating along the z-axis at the Alfvén speed

$$c_{A0} = \frac{B_0}{\sqrt{4\pi\rho}}. \tag{2.15}$$

This defines what is now also referred to as the "shear" or "torsional" magnetohydrodynamic wave. More detailed analysis of the magnetohydrodynamic equations also yields two magneto-acoustic wave modes, referred to as the "fast" and "slow" modes, which are coupled with the sound speed of the medium (Goedbloed et al., 2019; Carraro, 2021).

MHD waves are of particular importance in solar physics, where they are hypothesized to be an important factor in the coronal heating problem, and a driving force of the solar wind (Guo et al., 2016). In molecular clouds, Alfvén waves arising from MHD turbulence are expected to contribute to turbulent support against gravitational contraction (Curry and McKee, 2000; Carraro, 2021). Additionally, Alfvén waves form the basis of the Chandrasekhar-Fermi method (Chandrasekhar and Fermi, 1953), which is used to estimate magnetic field strengths from polarization maps.

2.2.3 The Chandrasekhar-Fermi Method

The Chandrasekhar-Fermi (CF) method (or sometimes Davis-Chandrasekhar-Fermi method (Davis, 1951; Chandrasekhar and Fermi, 1953) is a technique used to determine the strength

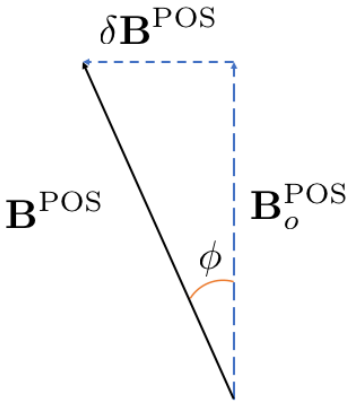


Figure 2.2: The geometrical construction for the Chandrasekhar-Fermi method.

of the plane-of-sky magnetic field based on turbulent perturbations from an assumed ordered distribution. The principle is based on estimating the effect that turbulence has on the field structure. The stronger the magnetic field strength, the more it resists being perturbed by turbulent motions. The total magnetic field in the plane of the sky is treated as a vector sum of two components: an ordered component $\mathbf{B}_o^{\mathrm{POS}}$, and a turbulent component $\delta\mathbf{B}^{\mathrm{POS}}$, as shown in Figure 2.2. Under conditions of flux-freezing, transverse perturbations to the field propagate at the Alfvén speed

$$c_{A0} = \frac{B}{\sqrt{4\pi\rho}}. \tag{2.16}$$

For a general plane wave perturbation $y = Ae^{ik(x-v_A t)}$, it follows that

$$(\partial_t y)^2 = c_{A0}^2 (\partial_x y)^2. \tag{2.17}$$

The displacement speed $\partial_t y$ is equal to the one-dimensional velocity dispersion σ, and $\partial_x y$ represents the deviation from the assumed ordered field:

$$\partial_x y \approx \frac{\Delta y}{\Delta x} = \frac{\delta B^{\mathrm{POS}}}{B_o^{\mathrm{POS}}} = \tan\phi \approx \delta\phi \tag{2.18}$$

where $\delta\phi$ is the dispersion in polarization angle. Substituting back into equation (2.17) and rearranging we obtain

$$B^{\mathrm{POS}} = \sqrt{4\pi\rho}\frac{\sigma}{\delta\phi}. \tag{2.19}$$

In the original method outlined in Chandrasekhar and Fermi (1953), the ordered contribution was assumed to be uniform and all deflection from this average uniform field was

attributed to the turbulent component. However, if the underlying ordered field is not uniform – such as, for example, the expected hourglass magnetic field configuration expected from gravitational contraction – the turbulent contribution would be overestimated, leading to an underestimate of the magnetic field strength (Crutcher, 2012). A common modification to minimize this effect is to replace the uniform (zeroth order) average field with one obtained by fitting the rotated polarization E-vectors to an assumed, smooth two-dimensional field (e.g. (Lai et al., 2002; Girart et al., 2006)). However, since the polarization observations are integrated along the line of sight, any tangling of the magnetic field in the line of sight direction leads to a reduction in the measured polarization angle dispersion (Crutcher, 2012). We also note that this method is very sensitive to the amount of smoothing used to determine the curved zeroth order field pattern. Greater/lesser smoothing results in greater/lesser measured σ, which in turn results in a lower/greater field estimate. Therefore, this method is sensitive to the user's bias when selecting a smoothing kernel. As a result, there have been a number of theoretical studies exploring the technique to try to calibrate and obtain finer modifications to the technique for more accurate results.

A correction factor commonly used by observers (Crutcher, 2012) originates from Ostriker et al. (2001), who performed a number of simulations to access the effects of this line-of-sight smoothing on various magnetic field measurement techniques. They found that, for $\delta\phi < 25°$, a correction factor of ≈ 0.5 to the right-hand-side of equation (2.19) produced good results. Heitsch et al. (2001) extended this analysis to the effects of map resolution, finding that as the telescope beam width increased, the magnetic field strength was increasingly overestimated. They also proposed a correction to attempt to get around the small angle restriction by measuring the dispersion in local $\tan\phi$, which also necessitated a correction to avoid underestimation when $|\phi| \mapsto \pi/2$. However, a more desirable approach would be to determine how turbulence contributes to $\delta\phi$ without the need to assume a particular ordered geometry.

Falceta-Gonçalves et al. (2008) executed a number of tests on numerical simulations to develop a different method. They expressed the total plane-of-sky magnetic field strength $B^{\rm POS} = B_o^{\rm POS} + \delta B$, and made a similar but simpler modification to the CF formula than Heitsch et al. (2001) to obtain

$$B_o^{\rm POS} + \delta B^{\rm POS} \simeq \sqrt{4\pi\rho}\frac{\sigma}{\tan(\delta\phi)}, \tag{2.20}$$

with $\delta\phi$ measured from the mean field. They also studied the effects of resolution on accuracy

and found that the degradation of accuracy with decreasing resolution followed

$$B^{\mathrm{POS}} = B_0^{\mathrm{POS}} \left(1 + \frac{C}{R^{0.5}}\right), \tag{2.21}$$

with R representing the observational resolution in pixels, and B_0^{POS} (the best possible CF estimation) and C are constants obtained from the fit. They found that this method produced magnetic field strength values within 20% or less of the known value of the simulations.

Another technique that does not assume a specific ordered geometry was proposed by Hildebrand et al. (2009), which uses the second-order structure function of polarization angles (see §2.3.1). When the separation is small, the contribution from the ordered field is linear, and when the separations are larger than the correlation length the turbulent contribution is constant (Hildebrand et al., 2009; Crutcher, 2012). This allows for both the polarization angle dispersion and the ratio of the turbulent to ordered magnetic fields to be determined. Application of the technique to M17 and OMC-1 yielded results that were an order of magnitude higher compared to Zeeman measurements, but this was attributed to not correcting for integration over the telescope beam and along the line of sight. A follow-up paper (Houde et al., 2009) applied this correction and reduced the discrepancy to a factor of a few.

2.2.4 Zeeman Splitting

The Zeeman effect refers to the behaviour of certain spectral lines in the presence of a magnetic field. A strong external magnetic field causes the magnetic moments of atoms and molecules to be coupled to the field, which in turn causes lines from degenerate energy states with nonzero total angular momentum to be "split" into multiple non-degenerate energy substates (Heiles et al., 1993). For the normal Zeeman effect in an arbitrarily oriented magnetic field, this produces three elliptically polarized components: an unshifted component (π), and two components ($\sigma_\pm$) with frequencies $\nu = \nu_0 \pm \Delta\nu_z$ (Heiles et al., 1993; Crutcher et al., 2003; Heiles and Crutcher, 2005). Thus far, Zeeman observations are the only method available to directly measure the magnetic field strength of molecular clouds (Crutcher, 2012; Crutcher and Kemball, 2019).

Theoretically, Zeeman measurements should provide all of the information required to directly measure the full three-dimensional magnetic field strength between the three components (Heiles et al., 1993; Crutcher et al., 2003; Heiles and Crutcher, 2005; Crutcher, 2012; Crutcher and Kemball, 2019). The linear polarization of the π component is proportional to the plane-of-sky magnetic field strength, the circular polarization (Stokes V) of the σ com-

ponents is proportional to the line-of-sight magnetic field strength $B_{\rm LOS}$, and the frequency offset is proportional to the total magnetic field strength via $\Delta\nu_z = Z|\mathbf{B}|$, where Z is the transition-specific Zeeman sensitivity

$$Z = \frac{g\mu}{h} \tag{2.22}$$

where h is the Planck constant, g is the appropriate Landé g-factor, and μ is either the Bohr magneton or the nuclear magneton depending on the properties of the species under observation (Heiles et al., 1993; Crutcher et al., 2003; Crutcher, 2012).

However, there are some practical factors that make detection of the Zeeman effect difficult. One such limitation is that in order to have a detectable $\Delta\nu_z$ either the magnetic field in the region must be strong, or the species must have a large Z(Heiles et al., 1993; Crutcher et al., 2003; Heiles and Crutcher, 2005). The strongest Z factors belong to paramagnetic species, which have Z comparable to the Bohr magneton (Crutcher et al., 2003; Heiles and Crutcher, 2005; Crutcher, 2012). Most of the important astrophysical tracer molecules are diamagnetic (Crutcher, 2012), and so have Z comparable to the nuclear magneton, which is smaller by a factor of 1840 (Heiles et al., 1993; Crutcher et al., 2003). As a result, the Zeeman effect has so far only been detected for OH, CH_3OH, SiO and H_2O masers and select lines in HI, OH, and CN for non-mased gas (Crutcher, 2012).

With the exception of OH maser detections, the frequency offset $\Delta\nu_z$ for all species is much smaller than the line width $\delta\nu$, meaning that the frequency of the $\sigma_\pm$ components generally cannot be resolved (Heiles et al., 1993; Crutcher, 2012). This prevents the direct measurement of the total magnetic field strength from the offset frequency. In addition, the linear polarization of the Zeeman components is much smaller than the circular polarization by a factor of approximately $\Delta\nu_z/\delta\nu$ (Crutcher et al., 2003; Heiles and Crutcher, 2005), preventing measurement of the plane-of-sky magnetic field. As a result, only information on the line-of-sight magnetic field component via circular polarization can practically obtained (Crutcher, 2012). However, statistical analysis indicates that for a large sample of randomly oriented magnetic fields, the average full magnetic field strength is $2B_{\rm LOS}$ (Crutcher et al., 2003; Crutcher, 2004).

2.3 MHD Turbulence Diagnostics

Interstellar turbulence is characterized by fluctuations in density and velocity that appear random. However, analysis via a number of statistical quantities shows that there is underlying structure in the statistics of the gas motions and density fluctuations (Lazarian, 2004). Because turbulence is a main factor in supporting clouds against gravitational collapse, it is

important to study how it dissipates to allow for stars to form (Hennebelle and Falgarone, 2012).

To fully explore turbulent statistics, observers must obtain measurements of velocity, density, and size. Unfortunately, we can only directly measure velocity in the line of sight (LOS) direction via Doppler shifts, and infer density from the two-dimensional spatial distribution of emission in the POS. It is most important to measure the velocity fluctuation statistics, as they describe the nature of the type of motions involved (Lazarian, 2009).

2.3.1 Statistical Tools

There are multiple statistical tools that can be used to obtain the structure of chaotic fluctuations in velocity and density. Here I summarize the general forms of the most common statistical tools used for this purpose. Definitions for this section are from Elmegreen and Scalo (2004) unless otherwise stated. The one-dimensional energy spectrum $E(k)$ is related to the power spectrum via $E(k)dk = P(\mathbf{k})d\mathbf{k} = P(\mathbf{k})dk^D$ where D is the dimensionality of $P(\mathbf{k})$ (Elmegreen and Scalo, 2004). If $P(\mathbf{k})$ is the full three-dimensional power spectrum then $E(k) \sim k^2 P(\mathbf{k})$.

For any observational analysis of turbulence, the two most fundamental observables are velocity and density. For the velocity field, the power spectrum represents how energy is distributed in the system with spatial scale (Brunt and Heyer, 2002b; Elmegreen and Scalo, 2004) and $E(k)$ has an expected single power-law distribution

$$E(k) \sim |k|^{-\beta} \tag{2.23}$$

with power spectrum

$$P(k) \sim |k|^{-\beta+(D-1)} \tag{2.24}$$

(Brunt and Heyer, 2002a,b). The power law index β of these spectra helps to characterize the underlying physics of the turbulence.

The Kolmogorov turbulence theory describes the expected statistics for isotropic, incompressible turbulence where energy is injected at the largest scales and cascades down to smaller scales without dissipation (Elmegreen and Scalo, 2004). For size scale r, the kinetic energy transfer rate follows $\epsilon \sim v(r)^2/t(r)$ =constant, with scale-dependent turnover time $t(r) = r/v(r)$. It therefore follows that $v(r) \propto l^{1/3}$, and leads to an energy spectrum with an expected β of 5/3 (Elmegreen and Scalo, 2004; Hennebelle and Falgarone, 2012).

When the medium is magnetized, the preferred direction of motion along the field lines leads to turbulent anisotropy, with evidence from simulation and observation that most of

the energy transfer happens perpendicular to the field direction (Hennebelle and Falgarone, 2012). Goldreich and Sridhar (1995) derived the energy spectrum while accounting for this anisotropy, and found that $k_\parallel \propto k_\perp^2/3$, which leads to Kolmogorov scaling for the energy spectrum perpendicular to the field: $E(k_\perp) \propto k_\perp^{-5/3}$. However, most numerical studies produce a power law of $E(k_\perp) \propto k_\perp^{-3/2}$ and the origin of the discrepancy and the correct index are still a subject of debate (Hennebelle and Falgarone, 2012; Alexakis and Biferale, 2018). While these turbulent formulations were computed analytically, modern turbulence theory and its connection to observation is derived from numerical turbulence simulations.

Because the observables only provide information in projection on the plane of the sky, multiple techniques have been developed to try to reconstruct the underlying three-dimensional spatial statistics from the limited observational information. This is complicated, because the observed emission is affected not only by the density, but also by fluctuations in velocity, and so the contributions of each cannot be easily separated (Esquivel et al., 2007; Swift and Welch, 2008; Lazarian, 2009).

2.4 Models of Molecular Cloud Cores

Models of molecular cloud structures fall into two broad categories:

1. analytical or numerical models that assume detailed equilibrium, and
2. turbulent simulations of cloud formation, fragmentation and evolution, where condensations emerge via stochastic magnetohydrodynamic perturbations.

The first category of models involves methods of varying complexity. For spherical core models lacking a magnetic field, solutions can be found by solving linked ordinary differential equations (ODEs) describing the system. The simplest case uses Poisson's equation for self-gravitation and the equation for hydrostatic equilibrium, assuming radial symmetry. A foundational example of this category of models is the self-gravitating pressure-bounded isothermal core model described by Ebert (1955) and Bonnor (1956). Other authors have assumed a polytropic equation of state $P = K\rho^\gamma = K\rho^{1+1/n}$, for example Curry and McKee (2000). There are assorted variations on the same theme, such as the "TNT" model of Myers and Fuller (1992), the multipressure polytropes of McKee and Holliman II (1999), and the composite polytropes of Curry and McKee (2000). Each of these models attempts to incorporate both thermal and non-thermal support via the equation of state. The "TNT" model uses a composite equation of state that smoothly joins a primarily thermal interior, representing the core, to a primarily non-thermal envelope structure. McKee and Holliman II (1999) use a similar construction that treats the total pressure as a sum of individual

polytropes which represent the important non-thermal contributions, such as turbulent support. Curry and McKee (2000) use a Bonnor-Ebert-like construction of a core embedded in a pressure-bounded medium, but split the core region into an interior and warmer envelope, with specific jump conditions at a sharp interface.

The spherical equilibrium models have the benefit of being inexpensive to compute using numerical ODE solvers. However, these models are also over-simplified, as they rely strongly on spherical symmetry, do not explicitly incorporate turbulence (though they attempt to include it as a simplified isotropic pressure term), and neglect contributions from the magnetic field.

Another common equilibrium modelling technique is the "self-consistent field method," which was first applied to this problem by Mouschovias (1974), and greatly elaborated upon by Tomisaka et al. (1988a); 1988b; 1989; 1990; and Tomisaka (1991), which henceforth we shall collectively refer to as the "TIN" papers. These techniques begin with a uniform density and magnetic field in a spherical or spheroidal region, and then relax the structure to equilibrium by self-consistently solving the equations of self-gravitating MHD using an iterative algorithm. This method has an advantage over the spherical models mentioned above, since it can produce magnetized, non-spherical cores that are in equilibrium, and sometimes threaded by so-called hourglass magnetic fields, which have been observed in nature (e.g. Girart et al. (2006); Doi et al. (2021)).

The initial work of Mouschovias (1974) (and 1976a; 1976b) only considered gravity and poloidal magnetic fields, which resulted in flattened core structures. The work of TIN extended this analysis to include the effects of rotation and toroidal magnetic fields (Tomisaka, 1991). Fiege and Pudritz (2000b) explored the application of cores containing both poloidal and toroidal field components starting from a spheroidal region within a filament, often finding substantially elongated structures dominated by the toroidal field.

Self-consistent field models are more computationally expensive than their spherical counterparts in terms of both computational requirements and convergence time, and they are complex to implement. They typically also assume azimuthal symmetry, although some application to lateral slices of infinite cylinders with magnetic fields perpendicular to their long axes have been explored by Tomisaka (2014).

Three-dimensional computational simulations can be used to explore the structures of magnetized cores from an entirely different perspective. Unlike the models above, the cores that form are usually not in equilibrium, and can potentially disperse under certain conditions (Vázquez-Semadeni et al., 2005; Dib et al., 2007). Simulations begin with relatively simple and often uniform initial conditions, but quickly evolve to generate structures such as clumps, filaments and cores (e.g. Tilley and Pudritz (2007); Kudoh and Basu (2008);

Ballesteros-Paredes et al. (2018)). The resulting structures are dynamic, and can be studied to connect their simulated properties to those measured from data. One important application is using polarization maps derived from these simulations to provide a correction to the Chandrasekhar-Fermi method (e.g. Ostriker et al. (2001); Heitsch et al. (2001); Falceta-Gonçalves et al. (2008); Chen et al. (2022)). However, while these simulations are powerful, they cannot be used to fit individual observed objects due to the inherent randomness of the individual condensations that naturally emerge from turbulence.

Chapter 3

PolCat Summary and Methods

This chapter is a pre-copyedited, author-produced PDF of an article accepted for publication in Monthly Notices of the Royal Astronomical Society, following peer review. The version of record Franzmann, E. L. and J. D. Fiege (2017). PolCat: Modelling sub millimetre polarization of molecular cloud cores using successive parameterized coordinate transformations. *Monthly Notices of the Royal Astronomical Society 466, 4592-4613.* is available online at: `http://dx.doi.org/10.1093/mnras/stw3380`.

The structure of the paper has been reformatted slightly, and the introduction has been reworked to better integrate with the thesis as a whole.

3.1 Introduction

In this chapter, we introduce our PolCat software for modelling submillimetre polarization and continuum maps. As discussed in Section 2.2.1, polarization maps provide information on the direction of the underlying magnetic field, but are highly degenerate, in that multiple field geometries can produce very similar polarization patterns. To accommodate the range of geometries possible in this degeneracy, PolCat's model-building framework was designed to efficiently generate three-dimensional magnetized cloud core models with corresponding polarization maps that can be fit for both continuum intensity and polarization angle simultaneously.

PolCat's basic operating principle is to use an advanced multi-objective optimization platform called "Ferret'' (Fiege, 2010) to search a space of parameterized coordinate transformations, corresponding to a reasonable history of gas motions. The name "PolCat" is a playful reference to its purpose both as a polarization modelling code, and the fact that polecats are wild relatives of ferrets. The Ferret optimization software is discussed in Section 3.3.

PolCat's transformations use the principle of flux-freezing in MHD to link a simple initial cloud, uniform in both gas density and field, with a final core containing a realistic density profile, which is obtained from a triaxially squashed/elongated Bonnor-Ebert (Bonnor, 1956) or polytropic sphere. Our library of transformations is designed to be representative of the kinds of motions that a core might experience as it condenses from a more diffuse configuration, and the library itself is extensible by the user. Our overall strategy is to limit degeneracy by restricting the space of models to those that can be produced from physically reasonable transformations, corresponding to previous motions of the gas.

While our current density models set up what is, in effect, a contraction from a uniform density into a centrally-condensed profile, PolCat is not limited to the assumption of an initial uniform distribution. PolCat's transformation library is extensible, and, theoretically, we may apply any initial conditions to the cloud that we wish, such as magnetic field topologies with closed loops. The extension of PolCat's modelling framework to other geometries, such as filaments, is an eventual goal of development.

In its present form, PolCat does not completely eliminate the degeneracy that is inherent to polarization modelling, although we are developing new methods to impose further limitations. We are not able to confirm any specific model geometry as the "true" model representing the actual field structure threading the core. However, we are are able to eliminate non-physical candidate geometries. Each run of the code provides a database of three-dimensional models that may explain the data, while eliminating large swaths of parameter space that can be ruled out. Thus, PolCat provides an in-depth exploration of models, providing insights into both what can and cannot be determined from the data. Our modelling strategy is data-driven in the sense that we focus on internally consistent, empirical models with a great deal of flexibility and minimal physical assumptions, allowing the data to guide the exploration.

3.2 PolCat Fundamentals

Polarized emission from molecular cloud cores gives us information on the plane-of-sky magnetic field component averaged over the line-of-sight. Total intensity I provides information on the shape and density structure of the core, and the linear polarization parameters Q and U provide information on the core's magnetic field structure and dust properties via the strength and direction of the polarized electric field of the dust emission. It is common practice to simply rotate the electric field polarization vectors by 90° to deduce the structure of the plane-of-sky magnetic field component of the object. However, observed polarized emission is the integrated result along the line of sight, meaning that the field inferred from

a rotated polarization map may not bear much resemblance to the actual three-dimensional magnetic field structure.

We created PolCat to explore the range of possible three-dimensional core and field geometries that produce observed polarization patterns. PolCat generates three-dimensional parametrized models of magnetized molecular cloud cores and simulates telescope observations to produce simulated Stokes I, Q, and U maps, which are converted to I, polarization position angle χ_{pol}, and polarization fraction P_{frac}. PolCat uses the Ferret multi-objective optimizer to search the configuration space of density and magnetic field structures, to find models that best agree with observational maps (usually using only I and χ_{pol}). The details of our modelling method are described in Section 3.2.1, and our parameter search method is described in Section 3.3.

3.2.1 Modelling Technique

PolCat's approach to building three-dimensional models uses successive parametrized coordinate transformations to transform a uniform field and density distribution into the final configuration. To simplify ray-tracing of the three-dimensional model for polarization map simulation, we require the final grid to be rectangular, with the x-z plane of the grid defined with the same dimensions as the input polarization map. We begin with this uniform, rectangular grid, which we define as the "final" or "most-primed" system of coordinates ($\mathbf{r}^{(n)}$ for n transformations). We apply the inverse of each coordinate transformation in reverse order to the grid to take it into the "initial" or "unprimed" system of coordinates ($\mathbf{r}^{(0)}$), on which the initial density $\rho^{(0)}$ and field configuration $\mathbf{B}^{(0)}$ are defined. The density and magnetic field of the core are then transformed forward according to

$$\mathbf{B}^{(n)} = \frac{\boldsymbol{\mathcal{J}}^{(n)}\boldsymbol{\mathcal{J}}^{(n-1)}\cdots\boldsymbol{\mathcal{J}}^{(1)}}{\det\boldsymbol{\mathcal{J}}^{(n)}\det\boldsymbol{\mathcal{J}}^{(n-1)}\cdots\det\boldsymbol{\mathcal{J}}^{(1)}}\cdot\mathbf{B}^{(0)} \tag{3.1}$$

and

$$\rho^{(n)} = \frac{\rho^{(0)}}{\det\boldsymbol{\mathcal{J}}^{(n)}\det\boldsymbol{\mathcal{J}}^{(n-1)}\cdots\det\boldsymbol{\mathcal{J}}^{(1)}}, \tag{3.2}$$

where each $\boldsymbol{\mathcal{J}}^{(k)}$ is the 3×3 Jacobian matrix of the kth coordinate transformation with elements

$$\mathcal{J}_{ij}^{(k)} = \frac{\partial x_i^{(k)}}{\partial x_j^{(k-1)}}. \tag{3.3}$$

Figure 3.1 shows this process for a simple model with three transformations. PolCat models are defined by the list of applied transformation components and their corresponding parameters, which it uses to generate three-dimensional core models. We then project this

three-dimensional core model to create a simulated polarization map using a modified form of the technique of Fiege and Pudritz (2000a), which we outline in §3.2.3. We outline the main transformations in the PolCat transformation library in Section 3.5.

3.2.2 Semi-Analytic Coordinate Transformation

In this section we show how to derive the Jacobian (equation (3.3)) to transform an initially uniform region into a numerically defined, radially symmetric density profile. We discuss specific transformations in the PolCat library in Section 3.5.

For radial symmetry, a transformation from an initially uniform density profile to a centrally concentrated core-like configuration behaves like a radial "stretch". Assuming co-linear axes, the coordinate transformation equation is therefore

$$x'_i = \frac{r'}{r} x_i. \tag{3.4}$$

We can link r' and r by mass conservation. We require a sphere of radius r in the less-primed (uniform density) coordinate system to enclose the same amount of mass as the corresponding sphere of radius r' in the more-primed (centrally concentrated density) system. In differential form, this condition of mass conservation becomes

$$dM = 4\pi\rho r^2 dr = 4\pi\rho' r'^2 dr', \tag{3.5}$$

which we can integrate, accounting for ρ being uniform in the less-primed medium, obtaining

$$r = \left(3 \int r'^2 \frac{\rho'(r')}{\rho(r(r'))} dr'\right)^{1/3}. \tag{3.6}$$

However, realistic density distributions often do not have a closed, analytical form, which requires them to be expressed numerically. Analytic approximations of core density profiles exist, but often the result of equation (3.6) is so complicated that they are impractical to use. To eliminate the need to take numerical derivatives to compute the elements of the Jacobian matrix, we can use equation (3.5) and apply product rule and chain rule to expand equation (3.3) into the form

$$\mathcal{J}_{ij} = \frac{\partial x'_i}{\partial x_j} = \frac{\rho r^2}{\rho' r'^2} \frac{x_i x_j}{r^2} - \frac{r'}{r}\left(\frac{x_i x_j}{r^2}\right) + \frac{r'}{r}\delta_{ij}, \tag{3.7}$$

where δ_{ij} is the Kronecker delta. Currently, PolCat's main density profile is that of a general truncated polytropic sphere in hydrostatic equilibrium, with equation of state $P \propto \rho^\gamma$

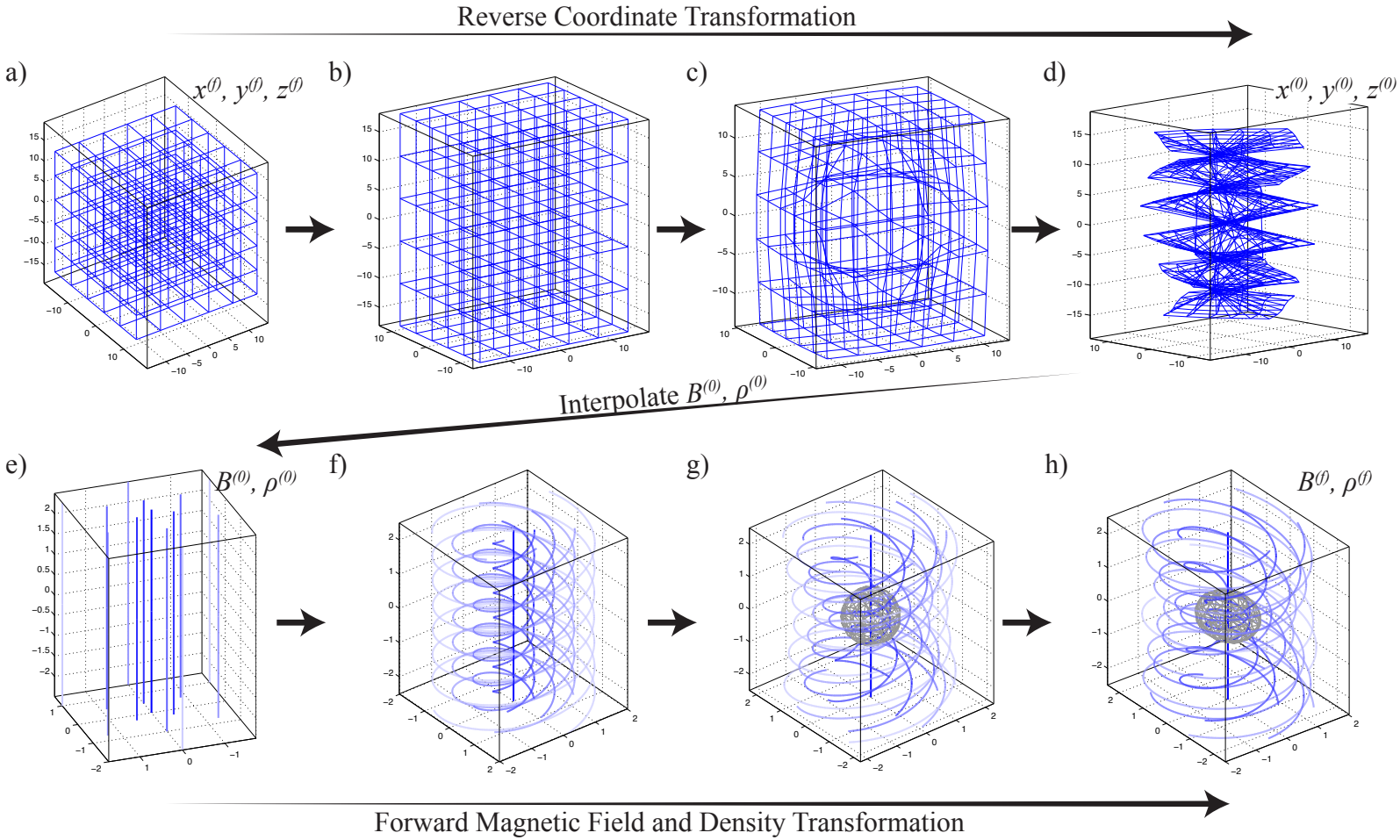


Figure 3.1: PolCat model process for a 3-component model consisting of the transformations LinearTwistA (§3.5.2), POLY (§3.5.1), and Scale (§3.5.4), in order of operation. a)-d) show the reverse coordinate transformation, starting with (a) the most-primed rectangular grid, through (b) Scale, (c) POLY, and (d) LinearTwistA. In the bottom row, (e) starts with a uniform field and density defined on the transformed coordinates, then applies the forward transformations for the (f) LinearTwistA, (g) POLY, and (h) Scale. Figure adapted from Franzmann (2014).

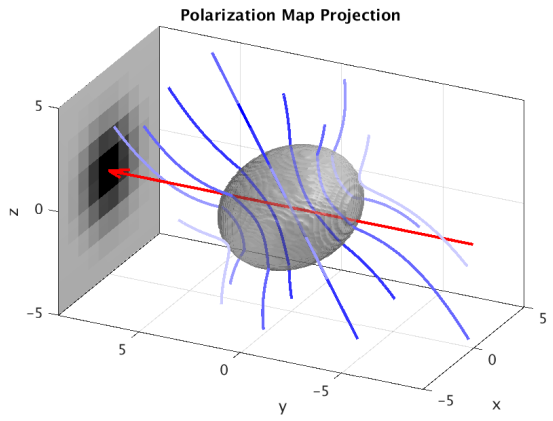


Figure 3.2: Internal model geometry demonstrating the direction of polarization map projection

and with density outside the truncation radius set to a constant value (see Section 3.5.1). The commonly used Bonnor-Ebert sphere (Bonnor, 1956) is a special case of our polytropic model with $\gamma = 1$.

3.2.3 Polarization Map Simulation

Here, we present our technique for simulating polarization maps, which is slightly modified from the technique of Fiege and Pudritz (2000a).

To compute the simulated I, Q, and U maps for our models, we first integrate the following quantities along the line of sight (y-direction, see Figure 3.2):

$$\Sigma = \int \rho \; dy, \tag{3.8}$$

$$\Sigma_2 = \int \rho \; g(\rho) \left(\frac{\cos^2 \gamma_{sky}}{2} - \frac{1}{3} \right) dy, \tag{3.9}$$

$$q = \int \rho \; g(\rho) \cos 2\psi \cos^2 \gamma_{sky} \; dy, \tag{3.10}$$

$$u = \int \rho \; g(\rho) \sin 2\psi \cos^2 \gamma_{sky} \; dy, \tag{3.11}$$

with γ_{sky} representing the angle between the field and the plane of the sky (x-z plane by our convention). Angle ψ is defined such that $\psi - 90°$ is the angle of the plane-of-sky magnetic field component counter-clockwise from the z-axis (North). Evaluation of these integrals is computationally trivial due PolCat's final grid being uniform, with the y-axis parallel to the line of sight by construction. The function $g(\rho)$ represents our attempt to empirically model variations in grain alignment efficiency and their ability to emit polarized light, which

we assume to be a function of the local gas density. We parametrize $g(\rho)$ as

$$g(\rho) = \left(1 - \Gamma \frac{\rho}{\rho_{max}}\right)^{\beta}, \tag{3.12}$$

where Γ and β are model parameters. This function allows the effect of grain alignment in denser regions of the core to be reduced, thus simulating the "polarization hole" effect (Weintraub et al., 2000). The effect of this function on the maps can be eliminated entirely by setting either β or Γ to a value of 0. *We note that the analysis in this paper assumes that* $\beta = \Gamma = 0$. *However,* PolCat *contains this functionality as an option to explore grain properties and alignment.*

The Stokes vector components are then calculated by

$$I = C_{flux} \left(\Sigma - \alpha \Sigma_2\right), \tag{3.13}$$

$$Q = C_{flux} \alpha q, \tag{3.14}$$

and

$$U = C_{flux} \alpha u, \tag{3.15}$$

where C_{flux} and α are constants that estimate the dust grain emission properties (see Fiege and Pudritz 2000a). The flux constant C_{flux} is in units of Jy beam^{-1} g^{-1} cm^2, and is dependent on cloud temperature and dust extinction (Johnstone et al., 2003). We may treat C_{flux} as a free parameter, but we obtain better results if we fix this value to a reasonable estimate. We choose an estimate of 5.18 Jy beam^{-1} g^{-1} cm^2 using the method of Johnstone et al. (2003), adjusted for the 20″ effective beam size of the maps in the SCUPOL Legacy Catalog (Matthews et al., 2009), which is our primary data source. Once the Stokes vector components have been computed, we convolve each map with a Gaussian with FWHM equivalent to the beam size of the instrument that produced the data. For our simulated data, we set this to 20" to match the SCUPOL Legacy Catalog.

Position angle χ_{pol}, intensity of polarized emission P_{flux}, and the corresponding fractional intensity P_{frac} are then determined by the equations

$$\chi_{pol} = \frac{1}{2} \tan^{-1}\left(\frac{U}{Q}\right), \tag{3.16}$$

$$P_{flux} = \sqrt{Q^2 + U^2}, \tag{3.17}$$

and

$$P_{frac} = \frac{P_{flux}}{I}. \tag{3.18}$$

3.2.4 Fitness Functions

Our approach clearly divides the tasks of model generation, performed by PolCat, from the parameter search, which is controlled by Ferret. A setup file specifies the range of all parameters that are to be searched, plus other control parameters required by Ferret to control the search. PolCat generates three-dimensional core models from the parameters received from Ferret, simulates an observation to produce model polarization maps, and evaluates their goodness of fit. These goodness of fit objectives are then sent back to Ferret, which chooses the next set of parameter sets to evaluate.

Linear polarization data are typically split into maps of the Stokes vector components I, Q, and U, from which maps of polarized intensity P_{flux}, fractional polarization P_{frac}, and position angle of the polarized electric field vectors χ_{pol} are computed. Fitting to I alone only yields information on the core shape and density structure, and the polarization parameters only yield information on the magnetic field. Ideally we must fit for the intensity and polarization simultaneously. However, the approach of combining these quantities into a single fitness objective is problematic, as the uncertainty in I is typically far smaller than that on Q and U. When combined into a single objective, the fit to intensity completely dominates and produces polarization maps that are a very poor match to the input dataset. Therefore, we take a multi-objective approach that does not combine the objectives.

In multi-objective optimization, the optimal solutions exist on a Pareto front, or tradeoff surface, which has the property that for any Pareto-optimal solution, no objective function can be further improved without degrading at least one other. In practice, the true Pareto front may be difficult to find. Ferret is designed to seek a set of non-dominated solutions, defined by the property that no solution in the set is equal to or superior to any other in all objectives. With a sufficiently large population evolved over many generations, Ferret's final non-dominated set of optimal solutions should ideally approximate the Pareto surface, although this is difficult to prove in practice, especially for non-linear problems like this one. A dual-objective Pareto surface generally has a bend or "knee" where solutions that are the most balanced between the two objectives reside. The benefits of a multi-objective approach when attempting to fit to polarization data is that it allows for consideration of both continuum intensity and polarization separately but simultaneously, potentially producing models that can describe both the intensity and polarization characteristics. However, it is

not straightforward to apply some statistical analysis techniques such as confidence maps to multi-objective problems, due to the solutions representing the tradeoff between two different fitness criteria. One potential approach for future consideration could be to use the tradeoff curve to determine the equivalent weights of the two reduced χ^2 values, to combine them into a single factor (i.e. $\chi^2 = w\chi^2_I + (1-w)\chi^2_{pol}$). This value could then be used to calculate confidence intervals, bridging the multi-objective approach and the standard confidence interval approach.

The objective functions F_X that we minimize are given by the reduced chi-squared function χ^2_ν:

$$F_X = \chi^2_\nu = \frac{1}{N-\nu-1}\sum_{i=1}^{N}\frac{\left[(X_i)_M - (X_i)_D\right]^2}{\sigma^2_{X_i}} \tag{3.19}$$

for N real-valued data map pixels $(X_i)_D$ (with corresponding model map pixels $(X_i)_M$), and ν model parameters. Here X is a placeholder for I, χ_{pol}, and possibly P_{frac}.

Computing the $F_{\chi_{pol}}$ objective is complicated by the 180° cyclical nature of polarization vectors. To ensure that we are truly computing the smallest possible distance between the data and the model angles, the difference between the data and model values must be less than 90°. We first take the remainder of dividing the angle values by 180°, which reduces the angles to their smallest equivalent between 0 and 180°, and take the absolute value of the difference. Differences of greater than 90° are set to their equivalent value in the $0-90°$ range by subtracting them from 180°, from which we compute the fitness value.

We obtain poor results when we use the Stokes vector components I, Q, and U directly in equation (3.19). In particular, we find poor results in the pattern of the polarization vectors immediately outside the bend of the trade-off surface. Small changes in Q and U have a large effect on the polarization position angle χ_{pol}. Thus, while the simulated Q and U maps are often reasonable fits to the Q and U observational maps, they tend to poorly reproduce the observed polarization angles. We instead replace I, Q and U equivalently with I, χ_{pol}, and P_{frac}. This reparameterization produces better results.

We find the best results from a two-objective fit using I and χ_{pol} only. Adding P_{frac} as a third objective tends to prioritize fits to the polarization objectives over intensity, as two of the three objectives are dependent Q and U. The results may become degraded to the point where none of the optimal solutions match the input dataset, due to dilution of the models over parts of the Pareto front far from the region of best fit in I and χ_{pol}. We argue that for a selected model, the fit to the intensity map is more important due to the polarization patterns being highly degenerate in general. While we may obtain a model with a polarization pattern that fits the dataset, if the model geometry produces an intensity map completely inconsistent with the data the model geometry can be ruled out.

3.2.4.1 Fitness Penalty Functions

We apply a series of penalty functions to the fitness values to discourage the code from selecting models in undesirable areas of the parameter space, such as locating the model core at the edges of the map where the intensity is low. Note that this situation can occur in a multi-objective approach without constraints on the fitness values, since a very poor fit to I would not be disallowed if it were an exceptional fit in χ_{pol}.

Each penalty function P operates in the same way. When the penalty function is triggered, it starts at a large discontinuous value that gets larger as the penalized violation gets worse. If the penalty is not triggered, then the value reduces to zero. A P value is calculated for every solution in the set and added to every objective in the fit. The magnitude of P does not matter as long as it is much larger than typical values of the objective functions and reduces to zero inside the allowed region. The three penalty functions that we use are outlined below.

To prepare a dataset for use with PolCat, the first step is to use an intensity contour to "clip" the core out of a larger map while leaving enough of the background for context. However, this technique typically leaves empty pixels (NaN) at the corners of the map due to the generally ovular core shape. Earlier versions of PolCat showed an occasional tendency to centre the model in these areas as it could occasionally gain excellent fits to the position angle map despite the poor fit to the intensity map. The first penalty function, P_{cen}, discourages selection of models centred on masked (removed) pixels, scaling with distance of the core center from the nearest non-masked pixel:

$$P_{cen} = \begin{cases} 0, \text{where } I(\Delta x, \Delta z) \text{ is defined} \\ 100 \times \left[1 + \min\left(\sqrt{(X-\Delta x)^2 + (Z-\Delta z)^2}\right)\right], \\ \qquad\qquad \text{where } I(\Delta x, \Delta z) \text{ is NaN} \end{cases} \tag{3.20}$$

where X and Z are arrays representing the x and z positions of all non-masked pixels in the map, and Δx and Δz are the coordinates of the model centre (offset from $(0, 0)$, see §3.5.7). This penalty goes to zero if I at the model centre is not NaN.

The second penalty function P_{int} discourages the code from selecting solutions with surfaces that intersect with the front and back of the model cube:

$$P_{int} = 5 \times (A + B) \tag{3.21}$$

for A voxels at $y = y_{\min}$ and B voxels at $y = y_{\max}$ with density greater than that at the core surface. The jump in fitness value is implicit because A and B are integers. A scaling

constant of 5 is enough for this penalty to be effective. Such models are undesirable because parts of the core that extend outside the computational grid are effectively missing, and not counted when we compute the polarization map. In addition, the code sometimes explores nearly cylindrical solutions oriented with their long axes parallel with the line of sight. Such models are not core-like and require a very precise and unlikely viewing angle. They generally intersect with the front and/or back of our computational domain, and are therefore excluded by equation (3.21).

The third penalty function restricts the acceptable range of fitness values to some specified upper threshold:

$$P_{fit} = \sum_i w_i \times \sqrt{(100 \times F_i)^2 + (F_i - F_i^{max})^2}, \tag{3.22}$$

where i counts over the number of objectives, and w_i is a logical constant with a value of 0 if F_i is under the threshold F_i^{max}, and 1 if it is over.

We include the second term, which scales with the difference between F_i and the threshold, to help "guide" Ferret toward more useful areas of the parameter space. This penalty function reduces to zero when all fitness values are within the threshold.

3.3 Ferret

The Ferret Genetic Algorithm is a powerful multi-objective evolutionary optimizer, which is a part of the QUBIST global optimization toolbox for MATLAB developed by co-author JDF. Ferret has been in development since 2002 and is distributed by nQube Data Science Inc. (`www.nqube.com`), which distributes the software and applies it to data modelling and optimization problems in industry. In astronomy, Ferret has been applied to the problem of modelling the density structure of a filamentary molecular cloud (Fiege et al., 2004), modelling strong gravitational lens systems (Rogers and Fiege, 2011b,a, 2012), kinematic modelling of warped rotating galaxy disks (English et al., 2010), and pulse profiles from pulsars (Stevens et al., 2016). Ferret is also the optimizer that drives PARETO (Pareto-Aware Radiotherapy Evolutionary Optimization), an experimental treatment planning and optimization system for cancer radiotherapy (Fiege et al., 2011).

Ferret began as a real-valued multi-objective genetic algorithm (GA) similar to that described by Fonseca and Fleming (1993, 1998a,b). Multi-objective optimization algorithms are designed for problems that require optimization of more than one objective function. Our problem is of this nature, since we wish to explore the trade-offs between fits to I, χ_{pol}, and possibly P_{frac}, as discussed in Section 3.2.4. A multi-objective code searches for the set of non-dominated solutions defined by the property that no solution can be found that

improves any one objective without degrading at least one other. This principle is known as Pareto-optimality, which represents an unbiased way to perform optimization of multiple objectives. A code that performs multi-objective optimization in the Pareto sense does not combine objective functions in any way, but rather attempts to sample a curve (for dual objectives) or a multi-dimensional surface containing these non-dominated solutions. The resulting solution set represents a database of models that are all optimal in the Pareto sense.

Several features have been added to Ferret since its inception, which are not typical of genetic algorithms. For example, Ferret includes an auto-adaptation algorithm that optimizes several of its own control parameters using a technique that is similar in spirit (but quite different in implementation) to Evolution Strategies. Ferret also includes a unique type of "linkage-learning" algorithm (Goldberg, 2002), which has the ability to break large parameter search and optimization problems into smaller sub-problems, thus greatly simplifying the search. With these features, Ferret is quite an unusual evolutionary code, which does not strictly conform to the definition of a GA. However, the name "Ferret Genetic Algorithm" is retained, partly for historical reasons, and partly because it remains closer to the GA paradigm than to other types of evolutionary optimizers.

Ferret contains numerous other features that make it well-suited for the computationally intensive polarization modelling problem at hand. For example, it contains built-in parallelization, which greatly decreases the overall run time by splitting the calculations over multiple processors. It is a multi-population code with an automated zooming feature, which allows each population to focus on its own particular region of the parameter space. This technique is especially useful for problems that contains separated "islands" of solutions in parameter space. Ferret also contains an integrated visualization system, which helps users to monitor progress and understand the structure of the parameter space and trade-off surface. The features of the software are discussed at length in a comprehensive user's manual (Fiege, 2010), which is included with the code, and also available on the nQube website.

It is important to note that PolCat and Ferret are packaged together, but function as separate programs that work together at arms length (Figure 3.3). PolCat is a self-contained model-building package that uses Ferret as an optimizer, but contains no optimization capabilities of its own. Similarly, Ferret is a general purpose optimization code, which embodies no understanding of molecular clouds, magnetic fields, or polarization on its own. PolCat defines the parameter bounds, builds models of the density and magnetic field, and judges the fitness of any given parameter set. Ferret's role is to intelligently select parameter sets where it wishes to search. PolCat's parameter space is moderately large (typically on the order of approximately 13 parameters, although this may vary depending on the transformation template chosen), and each evaluation is computationally expensive;

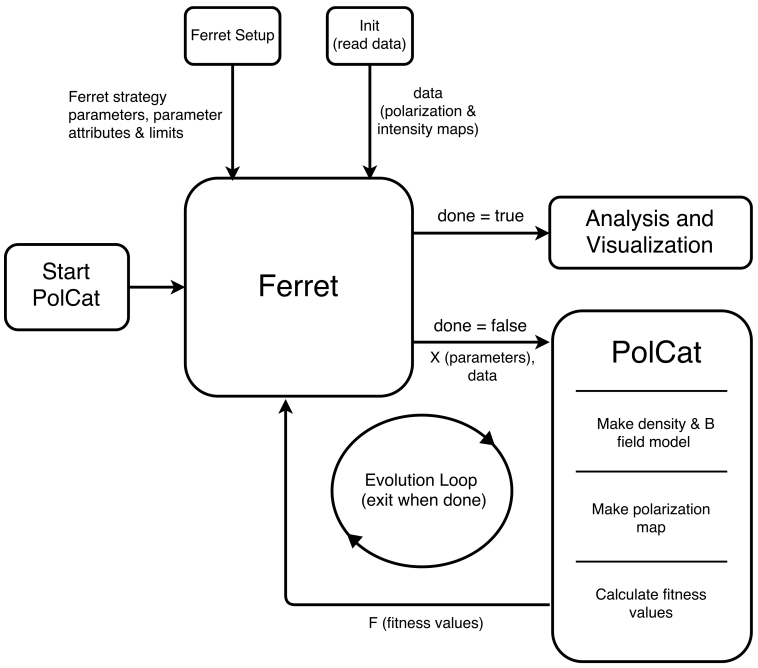


Figure 3.3: An illustration of how PolCat interfaces with Ferret

thus, Ferret's ability to efficiently navigate high dimensional spaces and map regions containing solutions is crucial.

3.4 Dimensional Scaling

The model is computed in dimensionless units so dimensional scales must be restored to compare with data. We define the dimensional units (r, ρ) as related to the dimensionless units ($\tilde{r}$, $\tilde{\rho}$) in the following way:

$$r = r_0 \tilde{r}, \tag{3.23}$$

$$\rho = \rho_0 \tilde{\rho}. \tag{3.24}$$

In general, the magnetic field does not need to be scaled, as its only influence on the polarization map calculation is in its direction and not its magnitude. The radial scale r_0 is defined as:

$$r_0 = \sqrt{\frac{\sigma_0^2}{4\pi G \rho_0}}, \tag{3.25}$$

with ρ_0 and σ_0 – defined for our model's purposes as the initial density and velocity dispersion of the cloud – as parameters in the model. Since the Jacobian is dimensionless, the model can be computed in dimensionless units and scaled back into physical units at the end of the

computation.

3.5 Coordinate Transform Primitives

This section introduces the reader to the library of coordinate transformations that are currently defined in the PolCat software. We note that 1) not all transformations need to be applied at once, 2) the sequence of transformations can be defined by the user, and 3) the library can easily be extended by the user. We first discuss a numerically defined polytrope transformation, followed by several simple analytic transformations. For a more thorough description of PolCat's complete transformation library, see Franzmann (2014).

In the discussion that follows, we define the "core axes" as the principal axes of the triaxial core, which remain attached to the core regardless of its final orientation. For an axisymmetric model, the core z-axis is the field symmetry axis.

3.5.1 Polytropic Sphere Transformation (POLY)

PolCat's current basic density model transforms a uniform density and magnetic field to that of a self-gravitating, equilibrium, pressure-truncated polytropic sphere, obeying a polytropic equation of state

$$P = K\rho^{\gamma}. \tag{3.26}$$

In addition to the dimensional scaling as defined by equations (3.23) and (3.24), we also define dimensionless pressure P, polytropic constant $\tilde{K}$, gravitational potential $\tilde{\Phi}$, and gravitational acceleration magnitude $\tilde{g}$:

$$P = \sigma_0^2 \rho_0 \tilde{P} \tag{3.27}$$

$$K = (\sigma_0^2/\rho_0^{\gamma-1})\tilde{K} \tag{3.28}$$

$$\Phi = \sigma_0^2 \tilde{\Phi} \tag{3.29}$$

$$g = (\sigma_0^2/r_0)\tilde{g}. \tag{3.30}$$

For convenience, we drop the tilde notation, but quantities will be assumed dimensionless for the remainder of the paper unless stated otherwise.

The density profile inside the truncation radius is obtained by rewriting Poisson's equation for gravitational potential $\nabla^2\Phi = \rho$, in conjunction with the equation for non-magnetic

hydrostatic equilibrium, $\rho\nabla\Phi + \nabla P = 0$:

$$\frac{d\Phi}{dr} = g, \tag{3.31}$$

$$\frac{dg}{dr} = \rho - \frac{2}{r}g, \tag{3.32}$$

$$\frac{d\rho}{dr} = -\frac{g}{\gamma K \rho^{\gamma-2}}. \tag{3.33}$$

This transformation has five (dimensionless) parameters: K, the constant in (3.26); γ, the polytropic index; ρ_c, the central density of the core relative to the initial density of the cloud; ρ_{ext}, the density outside the truncation radius; and P_{ext}, the external pressure. The truncation radius is determined at the point of pressure balance $P = P_{ext}$, and the density external to this radius is set to ρ_{ext}. The result is a sharp-edged, pressure-bounded core with an hourglass (centrally contracted) field geometry embedded within a uniform external isothermal medium that contributes to intensity and polarization. We note that cores produced with POLY are not precisely in equilibrium, which would require the inclusion of magnetic field terms. Such models are generally too slow to compute and do not produce a radially symmetric density profile, which is required for this method. We note that equilibrium models such as those calculated by Tomisaka et al. (1988a) are axisymmetric, in contrast to the non-equilibrium triaxial models computed by our method.

3.5.2 Asymmetric Linear Twist (LinearTwistA)

The asymmetric linear transformation twists the field parallel to the core z-axis by adding a displacement to the azimuthal angle that scales linearly with height. The forward coordinate transformation (in terms of cylindrical coordinates) is given by

$$\phi' = \phi + c_{twist} z;\ r' = r;\ z' = z, \tag{3.34}$$

with c_{twist} being the model parameter governing the amount of twist. The end result is a helical magnetic field with no change to the density distribution.

3.5.3 Symmetric Linear Twist (LinearTwistS)

This transformation behaves similarly to the asymmetric linear twist (§3.5.2), but with the twist being symmetric about the core x-y plane such that the twist switches direction at core

z=0. The forward transformation is

$$\phi' = \phi + c_{twist}|z|;\ r' = r;\ z' = z, \tag{3.35}$$

again with c_{twist} as the parameter governing the amount of twist. As with LinearTwistA, the amount of twist scales linearly with z and does not alter the density distribution.

3.5.4 Triaxial Scale (scale)

The scale transformation converts spherical surfaces into triaxial ellipsoidal surfaces while conserving volume. The amount of "stretch" on the $x-$ and $y-$axes are defined by parameters a and b, with the transformation itself given by

$$x' = ax;\ y' = by;\ z' = z/(ab). \tag{3.36}$$

The effect of this transformation on a spherical core is to transform it into a triaxial ellipsoid, without affecting the central density or volume of the core.

3.5.5 Spheroidal Scale (scaleCyl)

This transformation is identical to the triaxial scale transformation 3.5.4, but the stretch on the $x-$ and y-axes is defined by a single parameter, a, producing core shapes symmetrical about the z-axis. The transformation is given by

$$r' = ar;\ z' = z/a^2. \tag{3.37}$$

The Jacobian determinant of this transformation is unity, therefore this scale also conserves volume.

3.5.6 Solid Body Rotation (RotateA)

This transformation is a basic three-dimensional rotation that orients the core axes relative to our projection direction, or line of sight (the negative y-axis in our convention). This transformation is performed by: 1) A rotation about the positive z-axis by angle ϕ, 2) A rotation about the positive x-axis by angle i, and 3) A rotation about the positive y-axis by angle PA.

After this sequence of solid-body rotations, i represents the inclination of the core z-axis to the line of sight, and PA represents its position angle to the most-primed z-axis projected

onto the plane of the sky.

3.5.7 Shift

The shift transformation moves the core away from the origin in the x-z plane by adding a constant offset to the x- and z-coordinates.

$$x' = x + \Delta x;\ y' = \Delta y;\ z' = z + \Delta z. \tag{3.38}$$

The Jacobian for this transformation is the identity matrix. This transformation is required because a dataset created by clipping the core out of the background may not be perfectly centred in the map.

3.5.8 Other Transformations

The other transformations in the PolCat library include:

1. A transformation which produces a singular isothermal sphere density profile,

2. Symmetric and asymmetric twists which substitute the linear angular displacement in equations (3.34) and (3.35) with a factor that scales as z^m,

3. A transformation that bends the core such that segments between $z = z_0$ and $z = z_0 + \alpha r_0$ are mapped to circular arcs of angular size α, and

4. A bend that maps the z-axis of the core to a sinusoidal wave.

The analysis in this paper did not require the use of these transformations, and therefore they will not be discussed in further detail here. For a more complete discussion of these transformations, see Franzmann (2014).

We note that PolCat's library is extensible; any transformation can be added as long as the forward coordinate transformation, the reverse coordinate transformation, and the Jacobian matrix can be computed. Additionally, the methodology of Section 3.2.2 can be applied to any numerical radial density profile that can be computed by the user.

3.6 Model Tests

As a test of PolCat, we generated test datasets from three of PolCat's basic model templates: 1) a 4-component template consisting of (in order) POLY, Scale, RotateA, and

Shift (noTwistBE); 2) a 5-component template that consisted of the 4-component template with a LinearTwistA as the first transformation (basic5BE); and 3) a 5-component template identical to the previous, with a LinearTwistS transformation in place of LinearTwistA (basic5BES).

3.6.1 Definitions

We refer to the generating model for a particular artificial test dataset as the "seed model" of that dataset for the remainder of this paper. We note a difference in our terminology between the "seed model," which is the noise-free artificial dataset generated from the list of transformations, specified by the parameter values used to generate the dataset, and the "seed model *template*," which specifies the *class* of models defined by the list of transformations only (with appropriate parameter ranges). We define the "artificial dataset" as the seed model with added Gaussian noise, as discussed below.

3.6.2 Methodology

For an actual dataset, we normally run fits with multiple models to properly explore the range of possible geometries (model classes) that might describe the core. Our main objective with these tests is to not only evaluate PolCat's effectiveness at reproducing features of the seed model, but also to identify trends in the results to create a "litmus test" of sorts, which helps identify when the "wrong" model is applied to real data.

As the size of the cores from the SCUPOL Legacy Catalog (Matthews et al., 2009) are typically 10 pixels to a side, we have chosen simulated map dimensions of 10×10 for all of our tests. We have generated five categories of seed model:

Case 1: A 4-component spherical core with RotateA inclination angle set to 0°, 30°, 60°, and 90° (noTwistBE, four datasets),

Case 2: A 4-component oblate spheroid core oriented at 0°, 30°, 60°, and 90° inclination (noTwistBE, four datasets),

Case 3: A 4-component triaxial hourglass field core flattened along the core's z-symmetry axis, with ϕ of 30° and inclination angles of 0°, 30°, 60°, and 90° (noTwistBE, four datasets),

Case 4: A 5-component twistA triaxial core elongated along the core's z-symmetry axis, with a ϕ of 60° and inclination angles of 0°, 30°, 60°, and 90° (basic5BE, four datasets),

Case 5: A 5-component twistS triaxial core with the same shape as Case 3, oriented at the same inclination angles.(basic5BES, four datasets).

The input parameters for each seed model are shown in Table 3.1.

In addition to the Stokes I, Q, and U maps, PolCat also requires variance maps for each quantity so that it can compute the reduced χ^2 (equation (3.19)) between the solutions and the data. For our test data, we generated variance maps by

$$\sigma_I^2 = c_I I \tag{3.39}$$

$$\sigma_Q^2 = c_Q P_{flux} \tag{3.40}$$

$$\sigma_U^2 = c_U P_{flux}, \tag{3.41}$$

with each c_X computed by averaging the median values of σ_X^2/X (where $X = I, Q$ or U respectively) from a selection of SCUPOL Legacy catalogue datasets. After this step, we produced the final artificial data maps X_{dat} by adding scaled Gaussian noise via

$$X_{dat} = X + \sigma_X \times \text{randn}(\text{size}(X)), \tag{3.42}$$

where randn(size(X)) is a random array generated from a Gaussian distribution with the same dimensions as X, scaled by the uncertainty map σ_X calculated in equation (3.41). The three-dimensional structure of the Case 1 seed model with the four artificial datasets for each inclination are shown in Figure 3.4. For brevity, the corresponding figures for Cases 2-5 are shown in Figures B.1-B.4 in Appendix B.

We performed fits to each test dataset using both hourglass and twisted field geometries[1] (either with an asymmetric twist template, or both asymmetric and symmetric twist templates) with both spheroidal and triaxial geometries (between four and six different model templates).

In total, approximately 400 individual runs were performed. The final merged trade-off surfaces represent the cumulative results of at least three runs for each template geometry. There were 106 solution sets after merging.

Due to the small size of the images used, it is not feasible to fit for the polytropic index γ. As such, we have frozen γ to a value of 1 for all runs. To test the effect of fitting a non-Bonnor-Ebert polytropic model with a Bonnor-Ebert profile, we also generated several test cases with $\gamma = 0.8$ and $\gamma = 1.2$ and fit them with model templates where γ was fixed to a value of 1, as in the runs on the Bonnor-Ebert sets. To further help the parameter search,

[1]We note that the twisted fields do also show an "hourglass" shape, with the field lines wrapping around the hourglass due to the nature of the density transformation. However, we use the term "hourglass fields" to refer to the twist-less models for simplicity.

Case	Template		Parameter Values														
	Name	Sequence	ρ_0 (g cm^{-3})	σ_0 (km s^{-1})	c_{twist}	K	ρ_c	ρ_{out}	P_{out}	a_{scale}	b_{scale}	ϕ (°)	Δx (pix)	Δz (pix)	i (°)	F_I	$F_{\chi_{pol}}$
1	Spherical Hourglass	POLY→Scale→ RotateA→Shift (noTwistBE)	5×10^{-20}	1	–	0.8	150	0.2	0.1	1	1	0	0	0	0	1.04	1.25
															30	1.07	1.20
															60	1.20	1.25
															90	0.99	1.08
2	Oblate Hourglass	POLY→Scale→ RotateA→Shift (noTwistBE)	5×10^{-20}	1	–	0.8	150	0.2	0.1	1.2	1.2	0	0	0	0	0.75	1.19
															30	0.99	1.04
															60	1.22	1.39
															90	1.06	1.37
3	Triaxial Hourglass	POLY→Scale→ RotateA→Shift (noTwistBE)	5×10^{-20}	1	–	0.8	150	0.2	0.1	1	1.2	30	0	0	0	1.08	1.17
															30	1.21	1.15
															60	1.27	1.49
															90	1.15	1.35
4	Triaxial Asymmetric Twist	LinearTwistA→ POLY→Scale→ RotateA→Shift (basic5BE)	5×10^{-20}	1	5	0.8	150	0.2	0.1	1	0.8	60	0	0	0	0.96	1.28
															30	0.95	1.42
															60	1.01	1.37
															90	1.17	0.95
5	Triaxial Symmetric Twist	LinearTwistS→ POLY→Scale→ RotateA→Shift (basic5BE_S)	5×10^{-20}	1	5	0.8	150	0.2	0.1	1	1.2	30	0	0	0	1.37	1.18
															30	1.49	1.08
															60	1.07	0.98
															90	1.11	1.09

Table 3.1: Parameters and templates used to generate the seed models for the test data. RotateA position angle PA is set to zero in all cases.

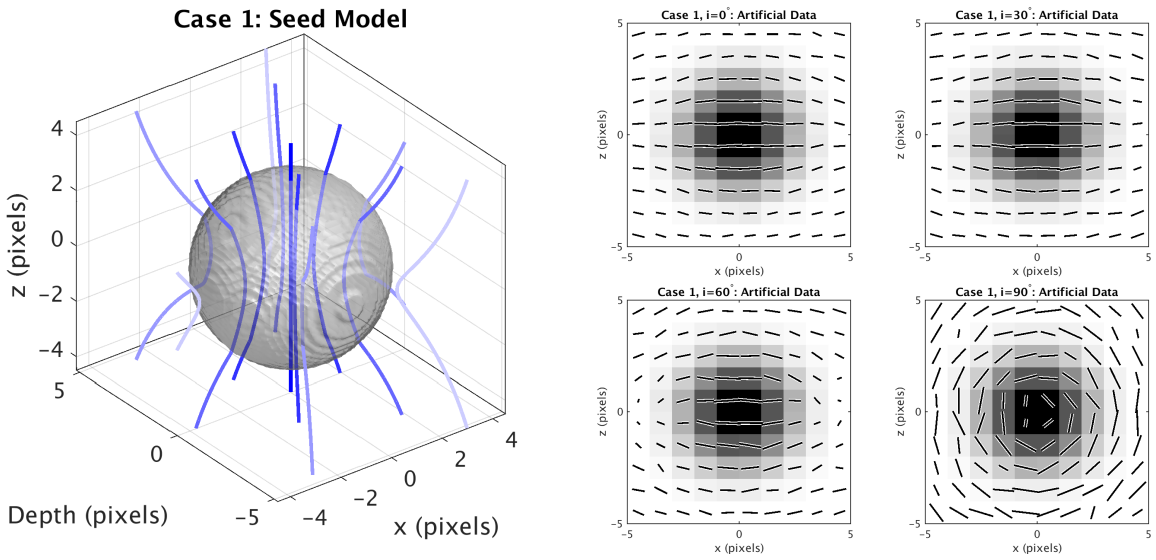


Figure 3.4: Seed model for the Case 1 dataset at 0° inclination (top), with all four of the Case 1 artificial datasets (0°, 30°, 60°, and 90°, bottom). Corresponding figures for Cases 2-5 are located in Appendix B.

we have also applied the threshold penalty (equation (3.22)) for solutions with $F_I > 25$ and $F_{\chi_{pol}} > 10$.

3.6.3 Bonnor-Ebert Test Cores

Here we present the results of fits to the artificial datasets specified in the previous section to model templates with Bonnor-Ebert density profiles. Figures 3.5, 3.6, 3.7, 3.9, and 3.10 show a selection of knee solutions from fits to each of the test cases, with the three-dimensional structure shown on the left of each subfigure, and the model polarization vectors and intensity contours plotted on top of the seed model and artificial data for comparison.

3.6.3.1 Fitness Values

In many cases, when a 4-component untwisted hourglass model was applied to datasets generated from cores with twisted magnetic fields (Cases 4 and 5), the results were above the fitness threshold penalties for both I and χ_{pol}. As an experiment, we relaxed the fitness thresholds for these models to test if the restriction was causing the code to converge too early, preventing it from finding a better region of the parameter space. However, this did not improve the non-penalized fitness values, nor did it change the families of solutions produced. *Therefore, acceptable untwisted models could not be found when the seed model*

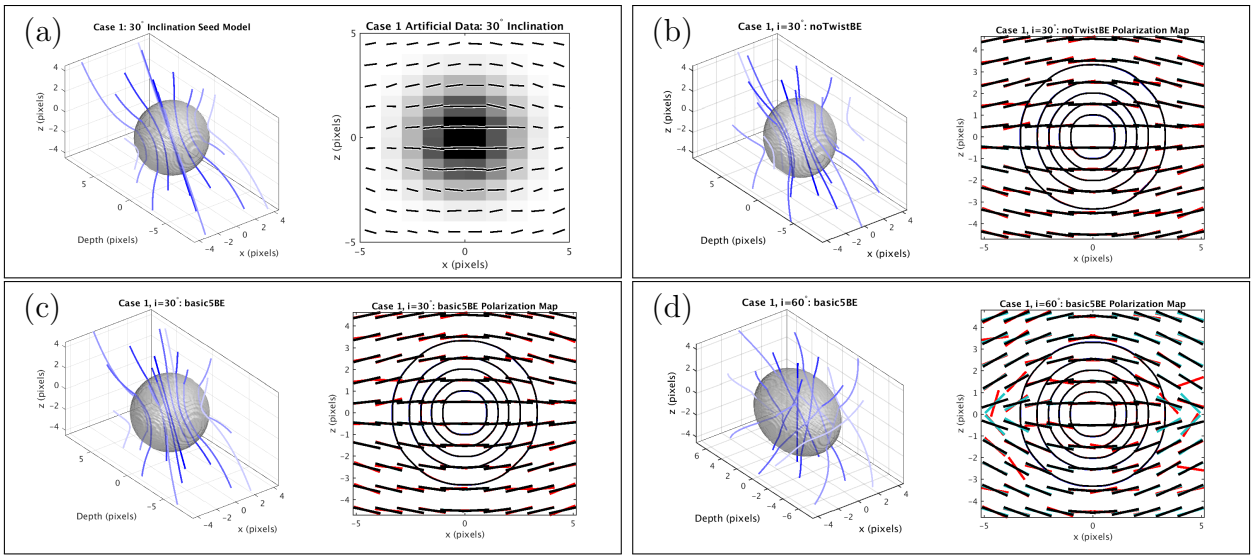


Figure 3.5: A selection of model solutions for Case 1, with (a) the 30° inclination seed model shown for comparison. Each model shown shows a selected knee solution corresponding to a fit with: (b) the seed template (noTwistBE) to the 30° set; and (c) the basic5BE template to the 30° and (d) 60° sets. Each pair of images shows the three-dimensional structure (left) and polarization maps with intensity contours (right), with the selected model shown in black, and the corresponding artificial dataset (red) and seed model (blue) shown for comparison. Corresponding figures for Cases 2-5 are located in Section **??**.

had a twisted field geometry.

For every test dataset that we generated, we calculated a fitness value for the parameters of the noise-free seed model and its corresponding noisy artificial dataset. This gave us a direct comparison between the models found within a solution set and the seed model. We found that, for the seed models with a high degree of symmetry (i.e. the spherical and oblate spheroid test sets), the majority of the applied models show fitness curves where the knee falls in a region that is an improvement over one or both the seed model fitness values. In all cases, if this behaviour was exhibited, it was from the seed template. This effect is explained by the added noise perturbing the best fitting solutions away from the seed model.

3.6.3.2 Field Twists

Models with a twisted field component reduce to simple hourglass magnetic field when the twist parameter c_{twist} is set to zero. Therefore, all four of the models with twisted magnetic field components that we applied to the data had the potential to recover an hourglass field geometry with their selected choice of c_{twist}. When a field twist was allowed, most of the fits to the Case 1 (spherical hourglass) and 2 (spheroidal hourglass) datasets tended to select

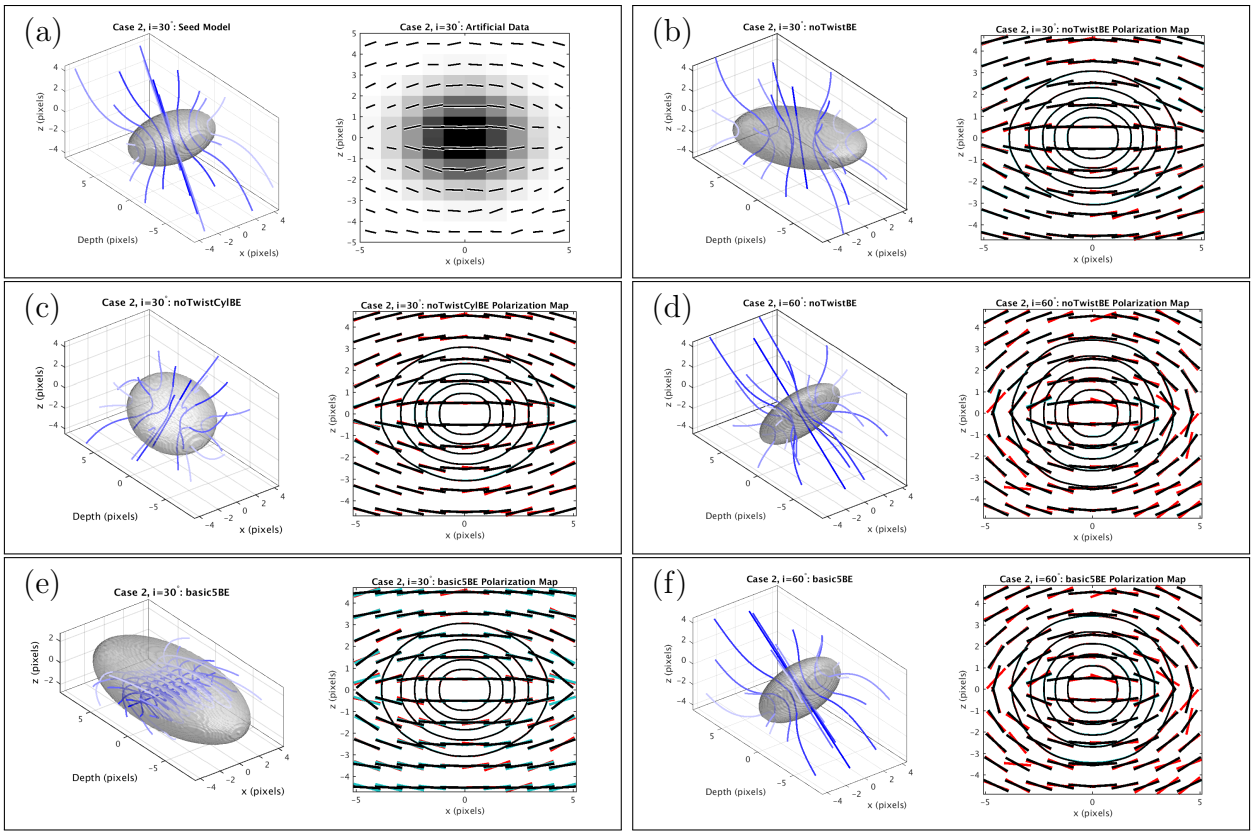


Figure 3.6: A selection of model solutions for Case 2, with (a) the 30° inclination seed model shown for comparison. Shown are selected knee solutions corresponding to fits with: (b) the seed template (noTwistBE) to the 30° set; (c) the noTwistCylBE template to the 30° set (seed geometry), (d) the seed template to the 60° set; and (e) the basic5BE template to the 30° and (f) 60° sets. Polarization maps are coloured identically to those in Figure 3.5.

small values of c_{twist} that did not produce significant twists. The exceptions were in the 60° inclination Case 1 set (Figure 3.5(d)), and the 30° inclination Case 2 set (Figure 3.6(e)). *Generally, spheroidal models did not produce twists when the seed model did not contain one.*

For the Case 3 (triaxial hourglass) tests, approximately half of the applied model templates that allowed twisted field geometries did not reproduce the seed model geometry. The solutions tended towards models with significant field twists, with the core z (field symmetry) direction aligned perpendicular to the line of sight along the x-axis of the image as in the example shown in Figure 3.7(f). This is illustrated in Figure 3.8, which shows the core z-direction (initial magnetic field direction) as a position on a unit sphere and the corresponding two-dimensional projection onto the x-y plane with the points sized by c_{twist}. For core models with PA of 0° – such as the seed models that we used – the solutions should be aligned with the line of sight in the x-y plane projection (xz, zz=0). Solutions with

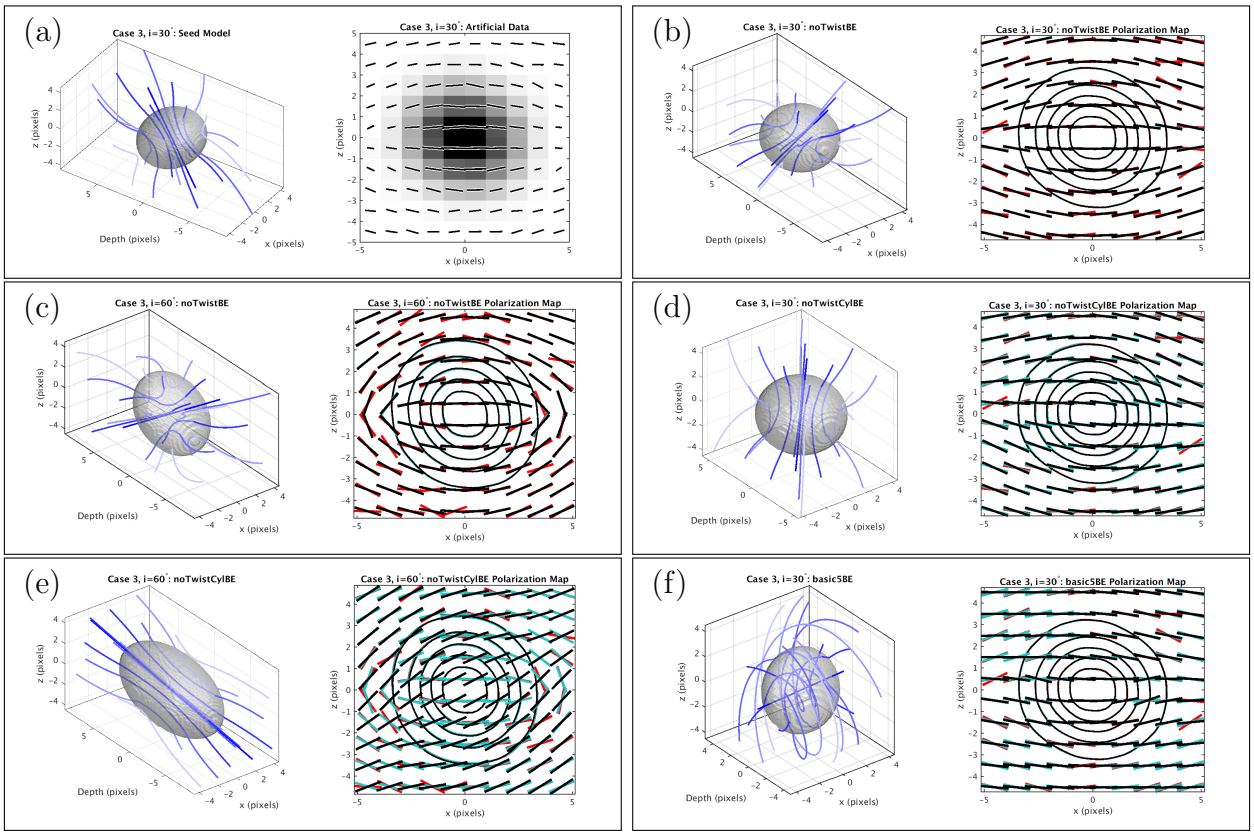


Figure 3.7: A selection of model solutions for Case 3, with (a) the 30° inclination seed model shown for comparison. Shown are selected knee solutions corresponding to fits with: (b) the seed template (noTwistBE) to the 30° set and (c) the 60° set; (d) the noTwistCylBE template to the 30° set and (e) the 60° set (seed field geometry); and (f) the basic5BE template to the 30° set. Polarization maps are coloured identically to those in Figure 3.5.

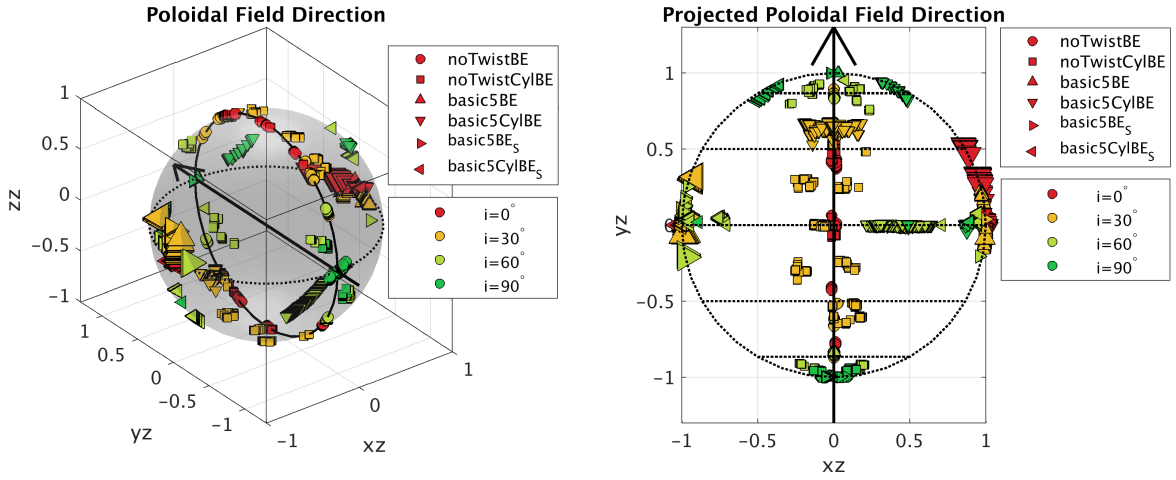


Figure 3.8: The core z-direction ("Pointing") vs. twist parameter c_{twist} for all Case 3 test runs, in three-dimensions (top) and projected down onto the x-y plane (bottom). The points are sized by c_{twist} value. The black arrow represents the line of sight/direction of polarization map integration. Each horizontal line on the bottom figure indicates all possible pointings for i of 0°, ±30°, and ±60°.

$c_{twist} \gtrsim 1$ mostly lie perpendicular to the line of sight ($yz = 0$), with the majority in the x-y plane. This effect tapered off as the inclination angle of the dataset increased. Despite the difference in geometry from the seed model, the polarization maps produced are nearly indistinguishable from the test data (Figure 3.7(f), right). *Thus a highly twisted model can reproduce the features of an untwisted hourglass model, with the core z-direction in the x-y plane, oriented 90° to the line of sight.*

In all cases, we found that untwisted hourglass field models applied to the Case 4 (triaxial asymmetric twist) and 5 (triaxial symmetric twist) datasets were unable to reproduce the seed model shape and observed polarization patterns (Figures 3.9(e)-(g), and 3.10(e)-(g)). Not only were the fitness values exceptionally poor (§3.6.3.1), but the triaxial cores were indisputably unphysical, and the maps were visually different from the dataset. Additionally, there was a significant spread in the orientation angles for the cores. Solutions from these datasets typically showed an approximately 90° difference between their z-axis and the z-axis of the seed model, which, in turn, had an effect on the core shapes of the models (to be discussed in the next section). *This implies that an hourglass model fit to a core with a twisted magnetic field cannot reproduce the observed polarization pattern.*

When we applied model templates with the opposite twist geometry to these cases (e.g. Case 4 fit with a symmetric twist), the resulting models exhibited tightly wrapped, unphysical magnetic fields (Figures 3.9(h) and 3.9(h)). This is in contrast to models using the correct twist symmetry, which accurately reproduced the twist parameter (Figures 3.9(b)-(d), and

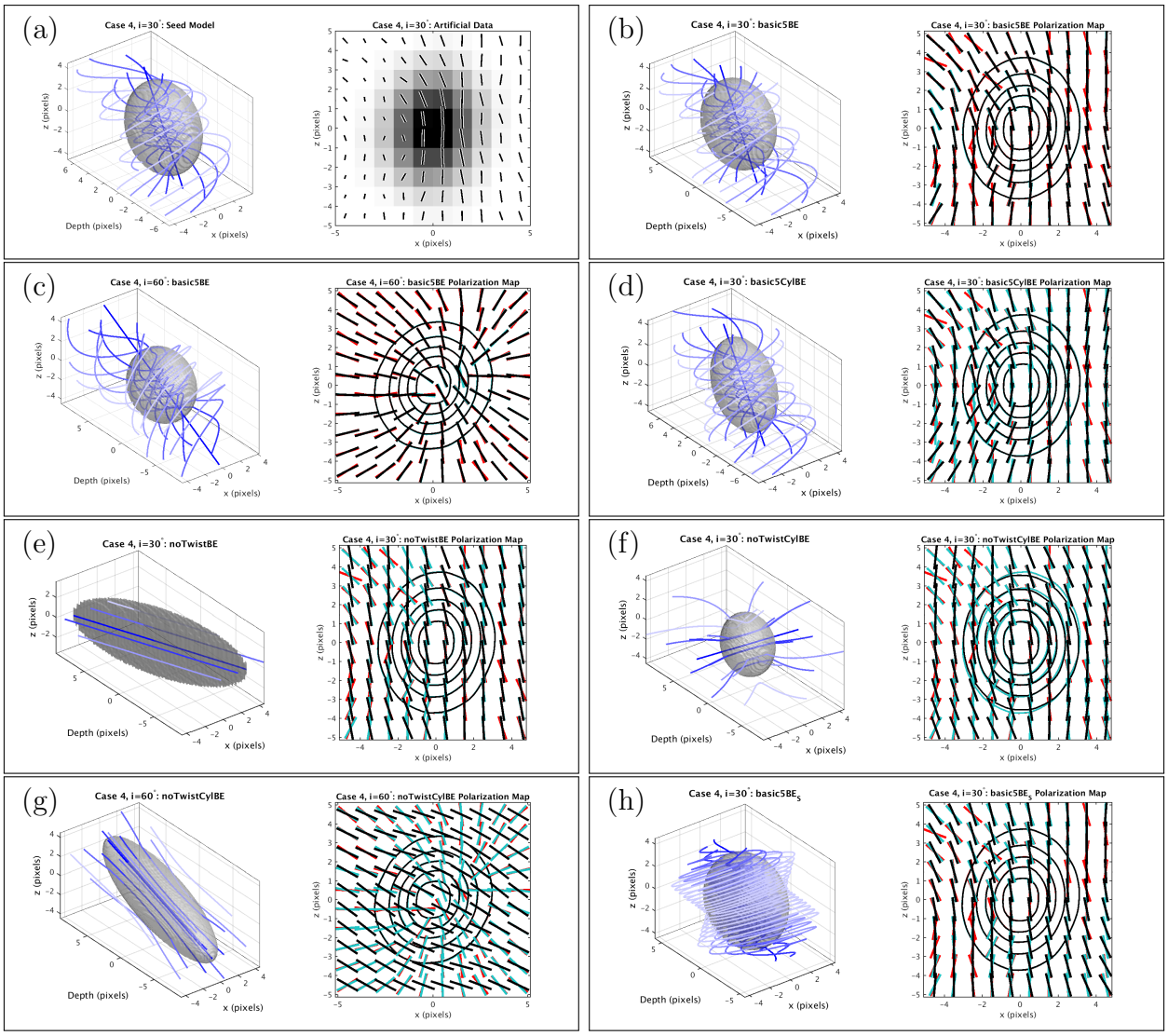


Figure 3.9: A selection of model solutions for Case 4, with (a) the 30° inclination seed model shown for comparison. Shown are selected knee solutions corresponding to fits with: (b) the seed template (basic5BE) to the 30° set and (c) the 60° set; (d) the basic5CylBE template to the 30° set; (e) the noTwistBE template to the 30° set; (f) the noTwistCylBE template to the 30° and (g) 60° sets; and h) the basic5BE_S template to the 30° set (opposite twist). Polarization maps are coloured identically to those in Figure 3.5.

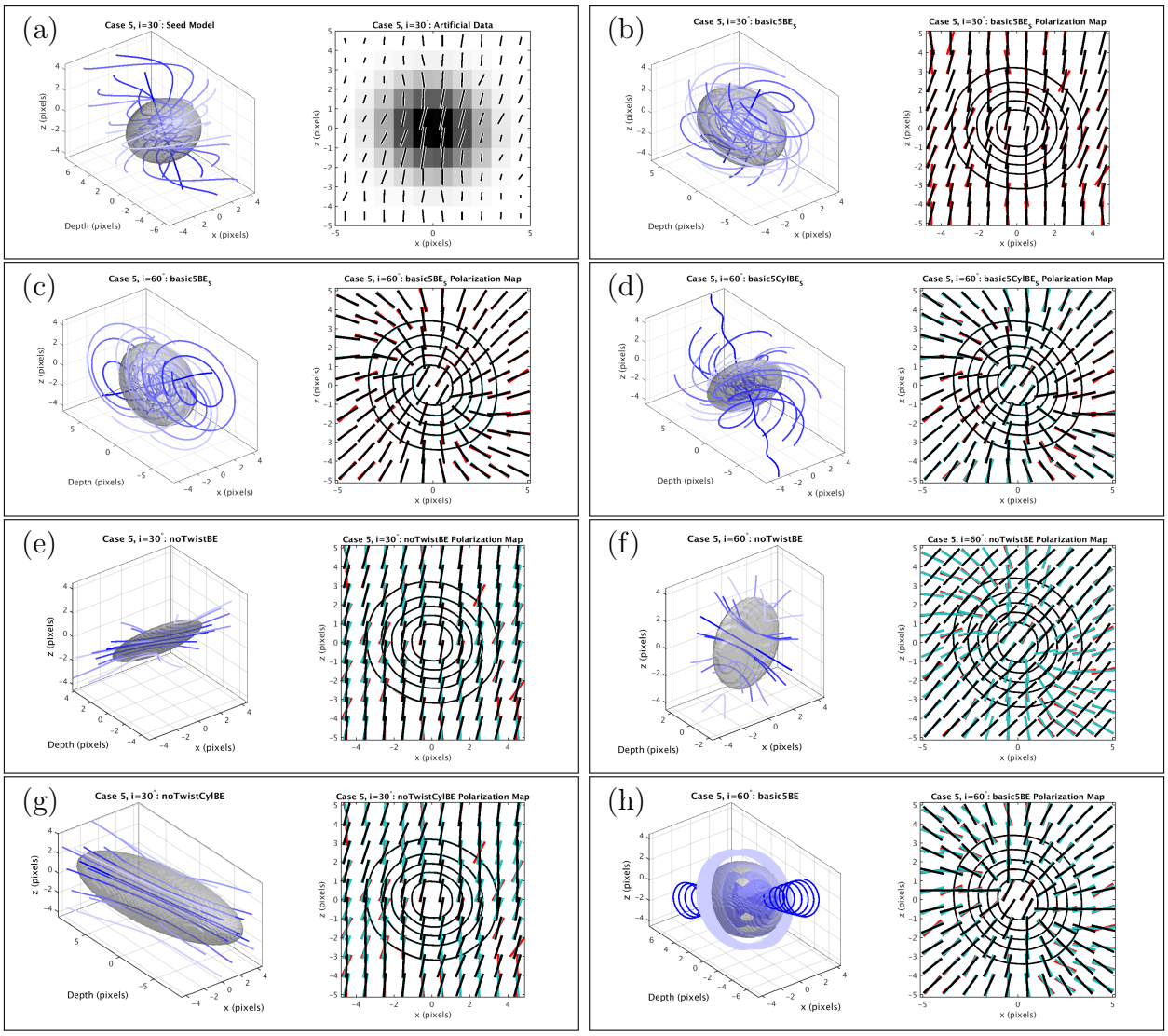


Figure 3.10: A selection of model solutions for Case 5, with (a) the 30° inclination seed model shown for comparison. Shown are selected knee solutions corresponding to fits with: (b) the seed template (basic5BE_S) to the 30° set and (c) the 60° set; (d) the noTwistBE template to the 30° set and (e) the 60° set; (f) the noTwistCylBE template to the 30° set; and (g) the basic5BE_S template to the 30° set (opposite twist). Polarization maps are coloured identically to those in Figure 3.5.

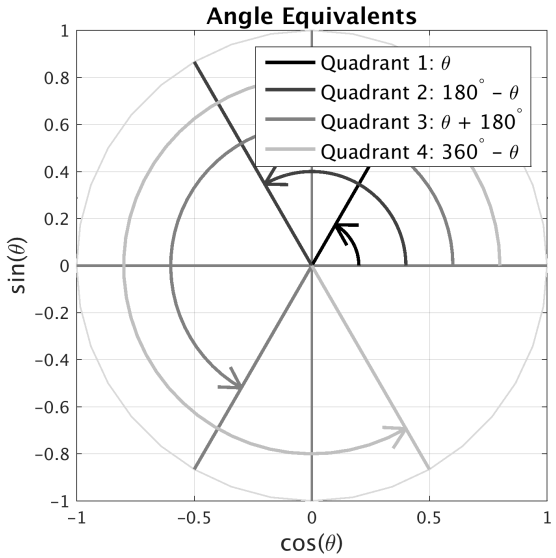


Figure 3.11: Equivalent angles of θ in each quadrant in the plane of rotation. Each angle ϕ, i, and PA can be characterized by the quadrant in which it falls and converted to equivalent angles in the other quadrants.

3.10(b)-(d)). *We conclude that we can distinguish cases where a core dataset containing a field twist is fit with the wrong symmetry.*

In all cases, the polarization produced by the magnetic field constrained the models' rotation angles, which had an effect on the model shapes selected. This constraint on orientation is expected, as the field symmetry direction is determined exclusively by the i and PA parameters independently of the shape parameters a and b. *Generally,* PolCat *had little difficulty obtaining the correct orientation angles when the model template had the correct field geometry (regardless of twist symmetry), and some difficulty when this was not the case.*

3.6.3.3 Core Orientations

The fit to χ_{pol} appears to have the largest weight in determining the orientation of the model core, whereas I seems to most strongly impart the model shape. If there is a significant discrepancy between the determined orientation angle and that of the model core, the shape is more likely to be radically different from the seed model.

When we set the limits on the orientation angles, we allowed them to vary such that the core z-direction (field symmetry direction) has the potential to be oriented in any spatial direction. However, the symmetry of the model introduces complex orientation degeneracy because the combined effect of the three angles ϕ, i, and PA can produce exactly the same density and magnetic field structure as another set. Additionally, the effect of computing the polarization maps further introduces projection degeneracy; there are orientations that

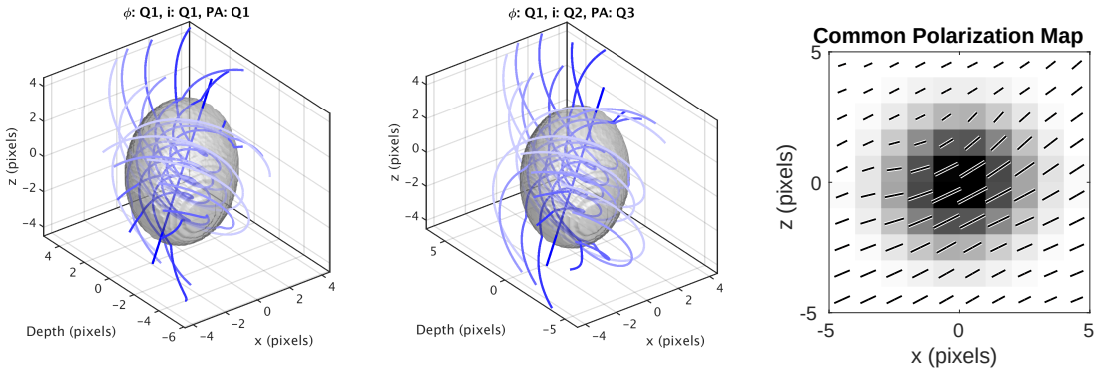


Figure 3.12: Two orientation angle quadrant permutations that produce identical polarization maps. The permutations that have this common map are $[\phi, i, PA]$: $[Q1, Q1, Q1]$, $[Q1, Q2, Q3]$, $[Q2, Q3, Q1]$, $[Q2, Q4, Q3]$, $[Q3, Q1, Q1]$, $[Q3, Q2, Q3]$, $[Q4, Q3, Q1]$, $[Q4, Q4, Q3]$

produce polarization maps with identical intensity and χ_{pol} while the three-dimensional core orientation is different from the original.

To explore the degeneracy of ϕ, i, and PA, we characterize each orientation angle by the Cartesian quadrant in which it falls (e.g. an angle greater than 90° and less than 180° is classified as quadrant 2), and define equivalent angles in the other three quadrants (see Figure 3.11). With this definition there are 64 possible permutations of equivalent angles. After some experimentation with our most asymmetric model (basic5BE), we find that these 64 permutations produce eight different polarization maps, and each permutation can be sorted into eight "groups" of eight based on the polarization maps produced (Figure 3.12). That is, for our models, any polarization map is at least eight-fold degenerate in orientation.

However, we note that the basic5BE model is the most asymmetric model that we apply. For spheroidal models, symmetry renders ϕ irrelevant and groups combine such that the number of separate groups reduce to four (16-fold degenerate polarization maps). Similar combinations occur with the hourglass and symmetric twist field geometries, as they produce polarization maps with 180° rotational symmetry. We can use this result to restrict the range of allowed angles in the fit, which simplifies the parameter space.

3.6.3.4 Core Shapes

Figures 3.13 and 3.14 plot the Scale parameters a and b (§3.5.4) adjusted for rotational symmetry for all the solution sets for all five cases. Figure 3.13 shows solution sets from templates with seed model magnetic field geometries, and Figure 3.14 shows solution sets with incorrect templates applied. The dotted lines in each figure represent the seed model values of a, b, and $c = 1/ab$. Spheroidal solutions exist on the diagonal line where $a = b$.

Overall, the datasets with 90° inclination to the line of sight showed the poorest agreement with the seed model shape in all cases, and for all applied model templates. While some solutions in a particular set may be close to the original shape, these solutions do not lie on the knee of the fitness curve for their respective runs (dark green points in Figures 3.13 and 3.14). This was also true to a lesser extent for the datasets with 0° inclination, with the exception of the Case 1 and Case 4 models. We now limit the discussion of core shapes to those of the 0-60° inclination datasets, as these results are consistent across all the 90° inclination runs.

While not all of the solutions obtained by fitting the triaxial hourglass model to the spherical test case (Case 1) selected spherical geometry, those that did were primarily located near the knee region of the fitness curve. There was one exception other than the 90° inclination set. In the 30° case, the solutions were all clustered around $a = 1.1$ and $b = 0.8$, where $a \simeq c$. When examined, these solutions are not particularly elongated and are a reasonable approximation to spherical geometry as in the example of Figure 3.5(b). *Therefore, fitting an untwisted triaxial model to an untwisted spherical model usually results in approximately the correct geometry for solutions near the knee of the tradeoff curve.*

When a field twist was added, all cases except the 60° inclination set showed some solutions with nearly spherical geometry. However, in the majority of cases these were the solutions with the best intensity fitness and were not close to the knee of the fitness curve. Overall, elongated solutions were favoured (e.g. Figure 3.5(d)). The results for the spheroidal core (Case 2) tests were similar, with the solutions reaching the seed model shape in only a few cases. In this case, adding a twisted field to the model did not improve the shape results. A large portion of solutions selected models elongated along the line of sight such as that in Figure 3.6(e). *However, twisted field models fit with a spheroidal constraint to the geometry selected the appropriate shape in all cases except the 90° inclination datasets.*

With Case 3, the majority of triaxial hourglass models fell into the correct area of the parameter space, with the best results for the 60° inclination case. The largest discrepancy fell in the 30° inclination case, where a significant portion of the solutions fell in the area of the parameter space where z-stretch parameter $c = 1/(ab)$ is greater than both a and b (prolate-like), including the primary knee region. Fits to spheroidal templates selected oblate solutions in the low inclination datasets (Figure 3.7(d)), and prolate in the high inclination datasets (Figure 3.7(e)). *Generally, reasonable fits were obtained when an untwisted triaxial hourglass model was fit to a seed model of the same type. Fits were improved as inclination angle increased.*

When an untwisted hourglass field model was applied to the two test datasets generated from twisted field seed models (Cases 4 and 5), they were unable to reproduce the original

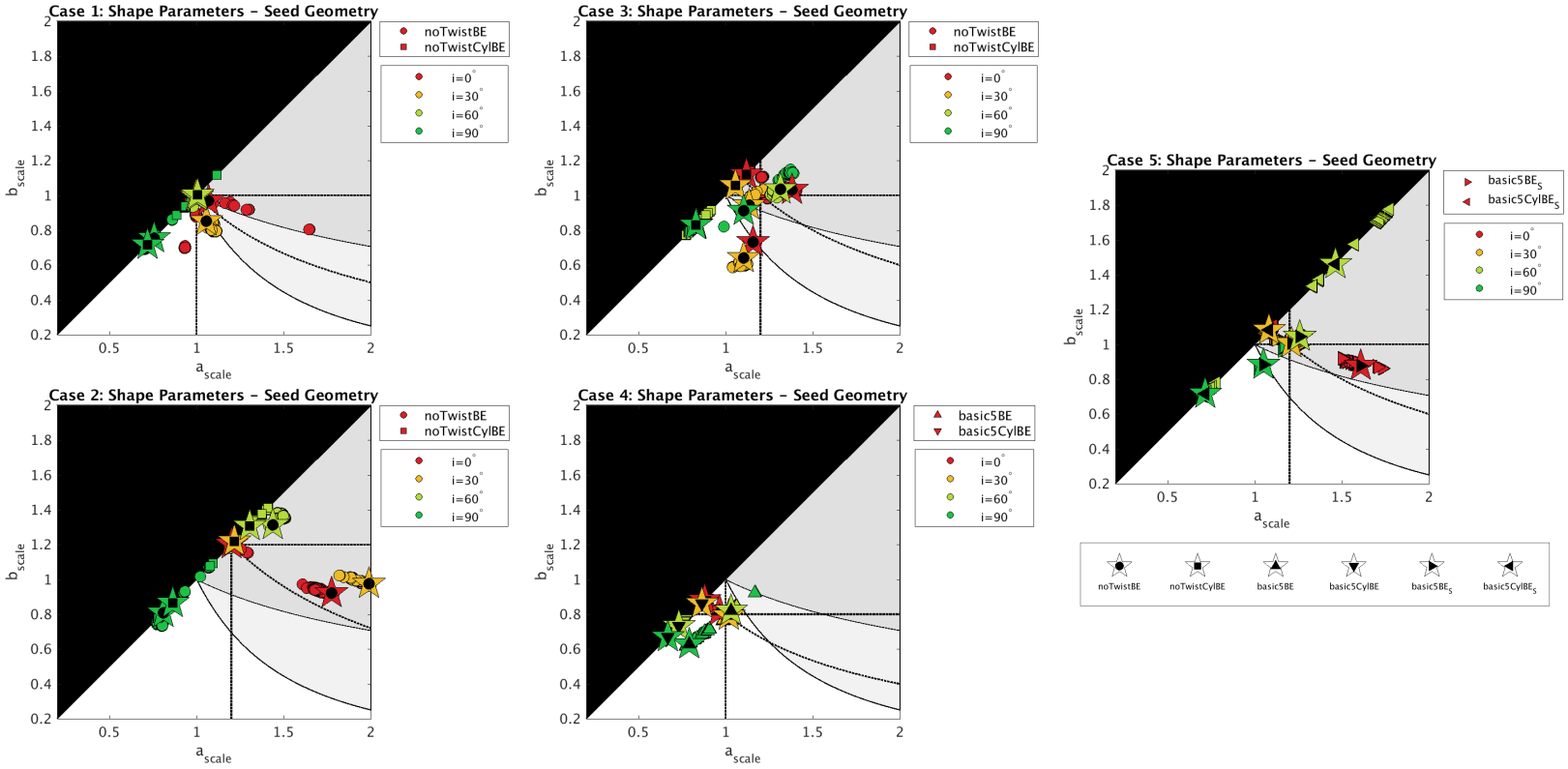


Figure 3.13: Maps of the shape parameters for all runs using seed model geometry, adjusted for symmetry, with background regions shaded by the amount of stretch on the z-axis. Dark grey indicates z is the shortest axis (more oblate), and white indicates that it is the longest (more prolate). Point shape represents applied model template, and colour indicates the inclination of the seed model. Knee solutions from each solution set are indicated by stars of the appropriate colour with the corresponding template shape marker. Seed model values are indicated with dotted lines for a and b, and $c = 1/ab$ (curve).

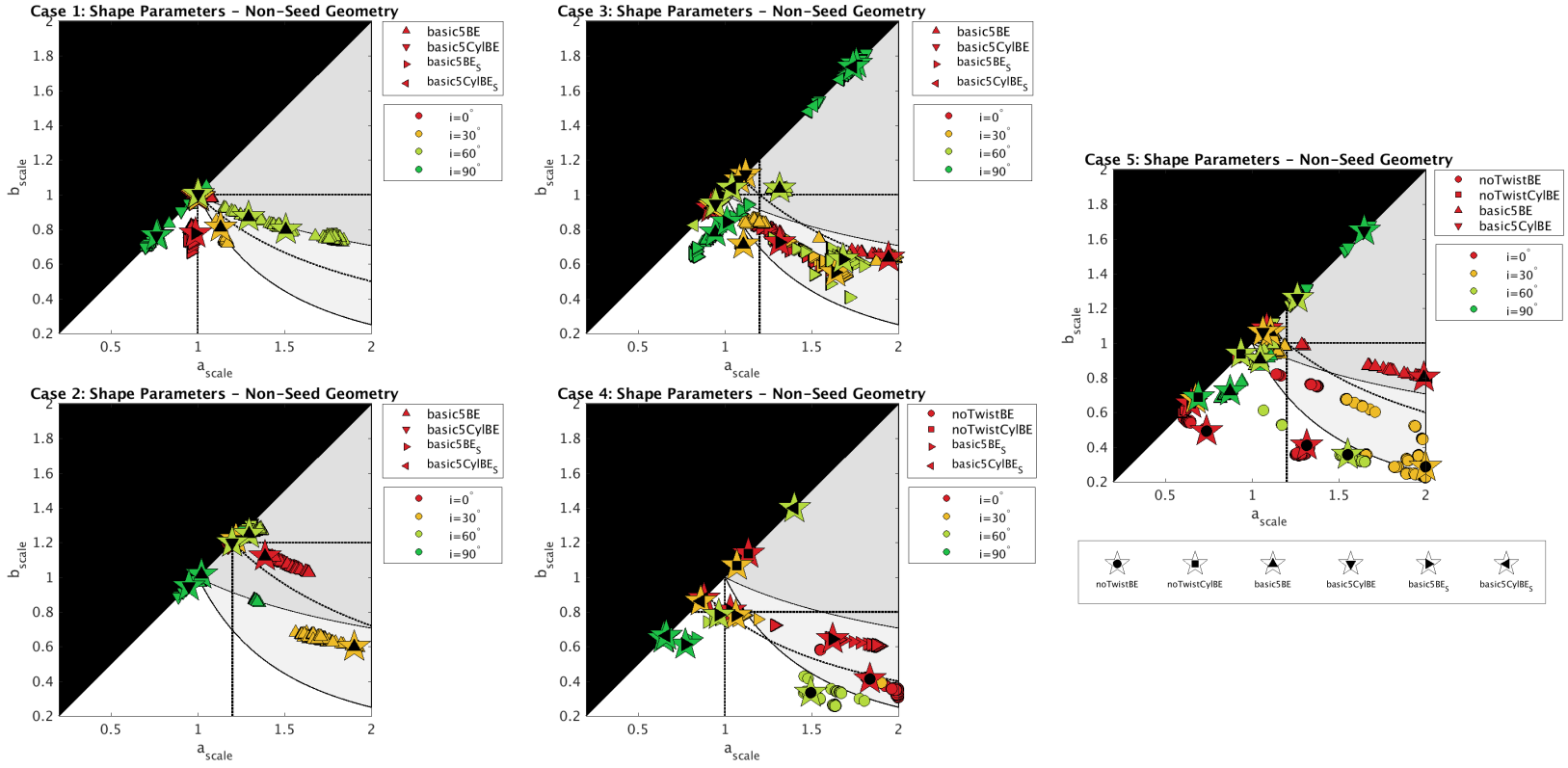


Figure 3.14: Maps of the shape parameters for all runs with "wrong" geometry. The background regions are shaded by the amount of stretch on the z-axis as in Figure 3.13. Dark grey indicates z is the shortest axis (more oblate), and white indicates that it is the longest (more prolate). Shape represents applied model template, and colour indicates the inclination of the seed model. Knee solutions from each solution set are indicated by stars of the appropriate colour with the corresponding template shape marker. Seed model values are marked as in Figure 3.13

core shape. The triaxial solutions showed a tendency to select shapes extremely flattened perpendicular to the magnetic field direction, while the spheroidal solutions generally chose the opposite geometry to what was expected, such as the flattened core of Case 5 showing solutions with prolate geometry (Figure 3.10(g)). However, in projection, the model core shapes actually fit within the test data shape reasonably well. The large discrepancy between the models found and the seed model is caused by PolCat struggling to fit the polarization vectors because this test deliberately used an untwisted model template. In all cases, the fit to the polarization map was poor. *Attempting to fit an untwisted template to a twisted seed model often results in very elongated or flattened cores and generally results in a poor fit to the polarization map.*

As expected, solutions using a spheroidal template (either twisted or untwisted) fitted to Cases 1 and 2 (e.g. Figure 3.6(c)) reasonably reproduced the seed model shape (except the 90° inclination cases). Applying these templates to the triaxial core of Case 3 produced results with varying degrees of success. In most cases, the solutions selected shapes that produced approximately the same z-axis stretch as the test data. Of those that did not, most were from twisted field templates where the solutions had significant field twists and selected orientations with the core z-direction approximately 90° to that of the seed model as in Figure 3.7(f). The single exception was the hourglass fit to Case 3 at 60° inclination. In this case, while approximately half the solutions deviated between 50-70° in core z-direction from the seed model, the other solutions in the set had deviations less than 20°. Upon examination, these solutions were more inclined than the seed model and more elongated along the line of sight. *Generally, fitting a spheroidal template to a spheroidal seed model produces reasonable results, as expected.*

When we compare the results between fitting Cases 4 and 5 with models exhibiting both the correct and opposite twist symmetry, we find that the magnetic field twist symmetry has a negligible affect on the core shapes exhibited by the solution sets. *Therefore, twisted templates reproduce the correct shape regardless of the symmetry of the field. However, we remind the reader that an incorrect twist symmetry often results in extremely wrapped, unphysical field structures (§3.6.3.2).*

When we look at the spheroidal models fit to Cases 4 and 5 (excluding the hourglass cases discussed above) we find that for low inclination angles, the solution sets again selected a to produce an identical stretch on the core z-axis to the original triaxial core. However, at higher inclinations this was not the case. The Case 4 solutions that locked onto prolate geometry selected a lower scale parameter (more elongated) and the Case 5 solutions that locked onto oblate geometry chose a higher scale parameter (more flat). This produced cores that were very different than the seed model cores, and therefore not a good match. However, solution

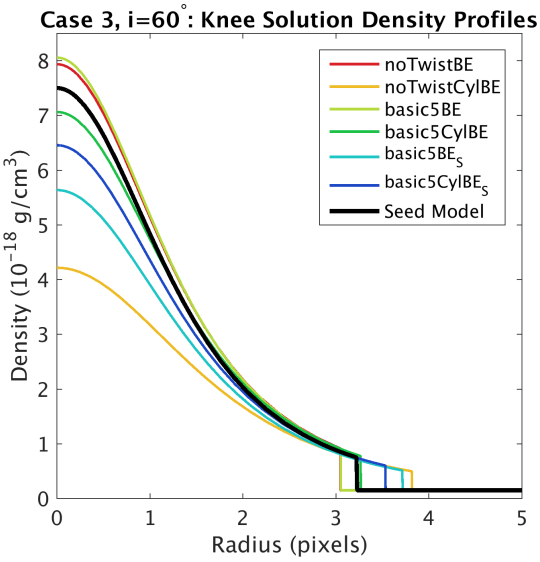


Figure 3.15: An example of knee solutions from the 60° inclination results for Case 3. The seed model profile is indicated in black.

sets fit with either field twist geometry tended to retrieve the correct inclination angle. *As expected,* PolCat *had difficulty fitting spheroidal model templates to triaxial seed models. Interestingly, the fits became more difficult as the seed model inclination angle increased.*

3.6.3.5 Density Profiles

Here we resume our convention of using tildes for dimensionless quantities for clarity. The central density $\rho_0\tilde{\rho}_c$ (g cm^{-3}) of the Bonnor-Ebert profile for the knee solutions was poorly constrained. As a result, there was a substantial variation in the central density of models near the knee of the curve. Additionally, while cores often selected the same truncation radius as the seed model, in cases where shallower profiles were selected, the cores sometimes truncated outside this radius. However, all knee profiles for a dataset tend to converge at the same density as that at the seed profile's truncation radius (Figure 3.15). This may be further complicated by the data resolution, as this convergence typically happened on the scale of approximately one pixel.

Despite the spread of central density values, we find that there is considerable degeneracy between the model's central density and pressure and the elongation of the core along the line of sight determined by the Scale transformation. In most cases, solutions with $\rho_0\tilde{\rho}_c$ higher than the seed model value corresponded to increased compression along the line of sight compared to the seed model. Likewise, cases where the profiles were lower corresponded to elongation along the line of sight (LOS). To quantify the amount of compression along the

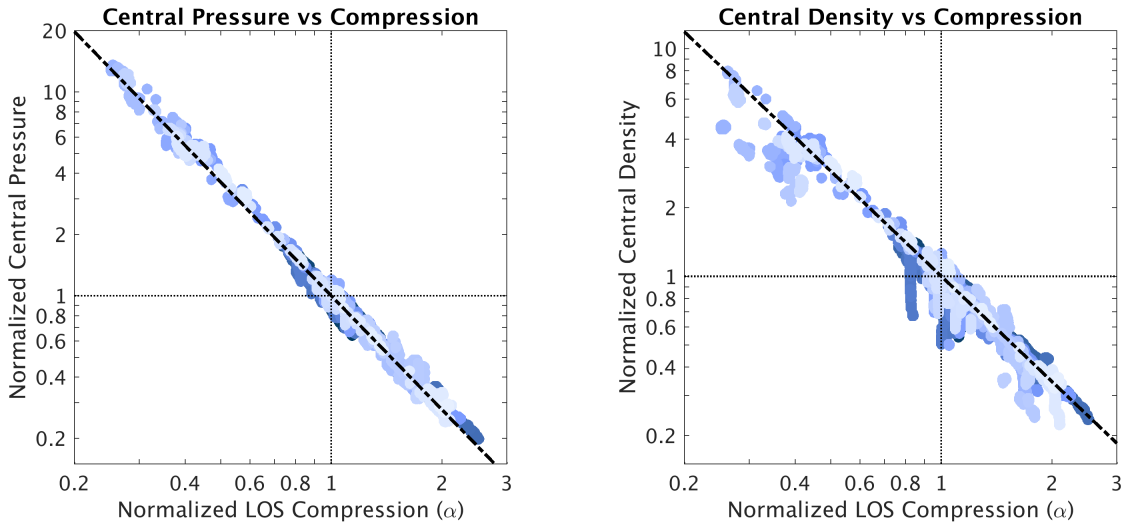


Figure 3.16: Log-log plots of central pressure (left) and density (right) vs line-of-sight compression for all Bonnor-Ebert test cases (106 solution sets). Each set is normalized by its respective seed model value on both plots. The dashed curves represent $P_{norm} = \alpha^{-1.85}$ and $\rho_{norm} = \alpha^{-1.54}$ respectively

line of sight direction relative to the seed model α, we must first determine the amount of stretch along the LOS ε introduced by the scale transformation. To calculate this quantity, we apply the reverse RotateA and Scale coordinate transformations to a unit vector along the LOS-direction, as per the modelling technique described in Section 3.2.1. The length of the transformed unit vector in this coordinate system, l, is $1/\varepsilon$. The amount of compression along the LOS-direction normalized relative to the seed model is therefore $\alpha = \varepsilon_{model}/\varepsilon_{seed}$. Computing central polytrope pressure P and density ρ:

$$P = \sigma_0^2 \rho_0 \tilde{K} \tilde{\rho}_c \tag{3.43}$$

$$\rho = \rho_0 \tilde{\rho}_c, \tag{3.44}$$

and normalizing by the corresponding seed model values ρ_{seed} and P_{seed} reveals a power-law relation for both to the LOS compression. Values from a logarithmic linear regression show a $P_{norm} = \alpha^{-1.85}$ relationship, with the density following an approximate $\rho_{norm} = \alpha^{-1.54}$ relation. This correspondence is exhibited on all of the Bonnor-Ebert test cores, as shown in Figure 3.16. At present we do not fully understand the nature of this relationship, but we are pursuing a plausible analytical explanation that may reproduce this intriguing scaling law. This relationship is symptomatic of the degeneracy in our model, and understanding it may result in an improved model parameterization.

3.6.4 Non-Isothermal Test Cores

Many tests revealed that we are unable to constrain γ at typical SCUPOL Legacy Catalogue pixel resolutions. We have therefore restricted the polytropic index to the isothermal case ($\gamma = 1$) in our tests. The width of the profile at half maximum is often two pixels wide at most, and much of the visible spread of the cores in the images are due to the point-spread-function of the telescope rather than the physical extent of the source itself.

We provide contrasting results of fitting a selection of artificial datasets generated from non-isothermal seed models with the same Bonnor-Ebert templates as in our previous analysis for completeness. We restricted our analysis to inclinations of 30° and 60° of the equivalent Cases 2-5 for both $\gamma = 0.8$ and $\gamma = 1.2$. This resulted in 42 merged solution sets.

While we used the same parameters as the Bonnor-Ebert (BE) sets to generate the artificial datasets for $\gamma = 0.8$, when we changed the γ value to 1.2 this "puffed-up" the cores enough that the oblate-like geometries (equivalent Cases 2, 3, and 5) were no longer completely contained within the grid in the x-direction. Therefore, we adjusted the ρ_0 and K values of the seed model to 7.5×10^{-20} g cm^{-3} and 0.7 respectively for these sets.

As in the main batch of tests, untwisted hourglass models could not produce acceptable results when fit to the artificial datasets from Cases 4 and 5, and when these datasets were fit with templates of the opposite twist symmetry the same high-twist results occurred.

The triaxial fits also had difficulty retrieving the shape parameters for the Case 2 (oblate spheroidal) geometry, however, the solutions were clustered over a similar range of values for the equivalent orientations in the BE fit.

When we plot the normalized central pressure vs the line of sight compression as in Section 3.6.3.5 for both $\gamma = 0.8$ and $\gamma = 1.2$, the results are not quite so well-defined as Figure 3.16. However, this larger scatter is only due to 3-4 of the 42 solution sets in each case. These models were all from fits to untwisted hourglass and symmetric twist templates to the Case 4 datasets, which we do not expect to reproduce the correct geometry. When these high-scatter sets were eliminated from the linear regression, we found power law values of -2.1 ($\gamma = 0.8$) and -1.9 ($\gamma = 1.2$), which are consistent with the Bonnor-Ebert results. When this scaling law is better understood, it may be possible to use it to constrain the ρ_0, ρ_c, σ_0, and K parameters.

These cumulative results show that fitting models with a Bonnor-Ebert density profile to a general polytrope is an acceptable approximation to datasets with the pixel resolution of the cores in the SCUPOL Legacy Catalogue. For more resolved data, we expect the overall shape of the density profile to have a larger effect on the results and allowing γ to vary with the fit may be more reasonable.

3.7 Summary

This paper presented our PolCat software for modelling submillimetre polarization and continuum intensity maps of molecular cloud cores. PolCat is based on a novel coordinate transformation method that appears to be unique in the astronomy literature. This paper summarized approximately 400 test runs, typically run on 9-10 AMD Opteron cores, requiring approximately 20 hours each. Our goal was to characterize the code in order to make some general statements about its performance and our ability to correctly characterize core shapes and magnetic field geometries. We briefly summarize our most important findings.

1. Triaxial model templates fit to spheroidal test data generally produces approximately the correct geometry for solutions near the knee of the tradeoff curve.

2. As expected, fitting spheroidal model templates to spheroidal seed model datasets produces reasonable fits that well-reproduce the data.

3. PolCat had difficulty fitting spheroidal templates to triaxial test data. The results tended to approximate the shapes acceptably well, but worsened with increasing seed model inclination.

4. As expected, untwisted hourglass models cannot reproduce polarization patterns produced from a core with a twisted field, and are likely to select geometries too unstable to exist in nature.

5. Models that allow a twisted field can reproduce the polarization map features of an untwisted hourglass model. The field lines in such models have little to no twist.

6. PolCat can usually distinguish between symmetric and asymmetric twist symmetries. Searching a model templates with the *wrong* symmetry often produced very tightly wrapped magnetic fields, which are not likely to be physical. These templates still produced cores with shapes very close to the seed model geometry. The fits to the polarization map were generally poor.

7. Core shape has a complex relationship to the central pressure and density, such that model cores with more compression along the line of sight often have a higher density and vice versa. This is indicative of model degeneracy, which we are presently exploring.

8. Low pixel resolution maps (such as those in the SCUPOL Legacy Catalogue) cannot be used to constrain the polytropic index γ. However, they can be adequately fit with Bonnor-Ebert density profiles. Higher resolution maps may constrain γ.

We can use these results to provide insight into PolCat fits to real data.

Our analysis included a detailed exploration of degeneracies due to the symmetry of our triaxial and spheroidal models. We discovered that the polarization maps are (at minimum) 8-fold degenerate due to the combined effect of the orientation angles and projection effects. Understanding these orientation degeneracies can greatly help to decrease the size of the parameter space. Note that the PolCat runs discussed in this paper did not take advantage of this information. Doing so in the future will almost certainly result in improved run times, and a better characterization of the Pareto curve.

We are currently developing a method based on tensor virial theorem to eliminate solutions that are very far from equilibrium (such as those in Figure 3.9(e)) from the PolCat results. While we do not generally expect our polytropes to be in equilibrium due to excluding the magnetic field terms from POLY, we do not expect them to be extremely far from equilibrium. We expect that the inclusion of a penalty function rejecting highly unstable models will filter out unreasonable solutions, decrease the size of our solution sets, and limit the degeneracy of our models.

Chapter 4

Exploration of Tensor Virial Equilibrium in Molecular Cloud Cores

In the previous chapter, we outlined our model-building software package, PolCat, and the types of models it produces when fit to data. One issue with the code as it stood at the time of the publishing of the original paper was the lack of a criterion for judging how "physical" the solutions produced were. This motivated the development of such a criterion, which we detail in the following chapter. The content of this chapter is the Accepted Manuscript version of the published article: E. L. and J. D. Fiege (2020). An Exploration of Tensor Virial Equilibrium in Magnetized Molecular Cloud Cores. *The Astrophysical Journal, 899, 101.* , available online at `https://dx.doi.org/10.3847/1538-4357/aba0b7`.

The introduction in the following section has been reworked for better flow, and to avoid repetition with the rest of the thesis.

4.1 Introduction

While PolCat is a robust modelling package, fitting a three-dimensional model to two-dimensional polarization and intensity data results in geometric degeneracy. Many models allowed by the data are very flattened or elongated, and very far from equilibrium. Therefore, to make PolCat a more useful tool for observers, we require a constraint to ensure the models it produces are physical. One method would be to use the tensor virial theorem (as discussed in Section 2.1) and apply a filtering threshold to reject models that are "too far" from three-axis equilibrium. Whether or not cores are indeed close to equilibrium or not is debatable. However, this technique may help to answer this important question by determining whether or not near-equilibrium models exist that adequately describe submillimetre polarization and continuum data.

This chapter establishes the theoretical foundation for a new triaxial virial constraint that decreases PolCat's model degeneracy, which helps to understand the three-dimensional fields that it infers from data. We present an in-depth analysis of the geometry of tensor virial equilibria and provide a metric by which observed axis ratios can be mapped to cores in virial equilibrium.

4.2 PolCat

PolCat is a molecular cloud core modelling package written in MATLAB. It constructs models of magnetized molecular cloud cores by applying a sequence of parameterized coordinate transformations to a cloud with an initially uniform density and magnetic field and "observes" the results to create simulated Stokes I, Q, and U polarization maps, which are then fit to observations using evolutionary optimization methods. An earlier version of PolCat is discussed in detail in FF1 (Chapter 3). Here we only briefly summarize PolCat's basic principles, as well as some modifications that were required to implement the virial criterion.

Each PolCat model is defined by N coordinate transformations that are applied to a uniform density ($\rho^{(0)}$) and magnetic field ($\boldsymbol{B}^{(0)}$). The density and magnetic field transform according to

$$\boldsymbol{B}^{(N)} = \frac{\boldsymbol{\mathcal{J}}^{(N)}\boldsymbol{\mathcal{J}}^{(N-1)}...\boldsymbol{\mathcal{J}}^{(1)}}{\det\boldsymbol{\mathcal{J}}^{(N)}\det\boldsymbol{\mathcal{J}}^{(N-1)}...\det\boldsymbol{\mathcal{J}}^{(1)}}\cdot\boldsymbol{B}^{(0)}, \tag{4.1}$$

and

$$\rho^{(N)} = \frac{\rho^{(0)}}{\det\boldsymbol{\mathcal{J}}^{(N)}\det\boldsymbol{\mathcal{J}}^{(N-1)}...\det\boldsymbol{\mathcal{J}}^{(1)}} \tag{4.2}$$

where $\boldsymbol{\mathcal{J}}$ is the 3×3 Jacobian matrix of the transformation.

To simplify the ray-tracing process, the "final" or "most-primed" rectangular coordinate grid, $\boldsymbol{r}^{(N)}$ is defined first, then the inverse of each coordinate transformation in the sequence is applied in reverse order to obtain the "initial" or "least-primed" system of coordinates $\boldsymbol{r}^{(0)}$. We then interpolate a uniform density and magnetic field onto the deformed coordinates, and apply equations (4.1) and (4.2) to obtain the final density and field. *When describing a single transformation in the sequence* $\boldsymbol{r}^{(n)} \mapsto \boldsymbol{r}^{(n+1)}$*, the transformation is denoted as* $\boldsymbol{r} \mapsto \boldsymbol{r}'$. PolCat transformations are a user-extensible library, but are required to be one-to-one invertible.

The virial technique that we employ in this paper was developed to apply to PolCat models, and therefore defines the virial balance in terms of PolCat's model parameters. Here we have a brief description of the parameters involved and their purpose in defining

the model.

4.2.1 Scaling

To simplify the number of parameters required in computation, models are computed in generic dimensionless coordinates, $\tilde{r} = r/r_0$, that can be rescaled back into physical units after the model is generated and before the polarization map is computed. The relevant physical scales are the initial density (ρ_0) and velocity dispersion (σ_0) of the uniform cloud, and the radial scale r_0 defined as

$$r_0 = \sqrt{\frac{\sigma_0^2}{4\pi G \rho_0}}. \tag{4.3}$$

To reduce complexity in notation, we drop the tildes from the notation and the quantities are assumed to be dimensionless for the remainder of this section.

4.2.2 The Bonnor-Ebert Sphere Transformation (BES)

This is a slightly altered version of the POLY transformation described in FF1 (§3.5.1), where the polytropic index of the density profile is set to a value of 1. This transformation converts a spherical region of uniform density $\rho(r) = 1$ to that of a pressure-truncated Bonnor-Ebert density profile $\rho'(r')$ with central density ρ_c. The Bonnor-Ebert profile can be computed by integrating the following linked equations in spherical coordinates with equation of state $P' = \rho'$:

$$\nabla'^2 \Phi' = \rho' \tag{4.4a}$$

$$\rho' \boldsymbol{\nabla}' \Phi' + \boldsymbol{\nabla}' P' = 0. \tag{4.4b}$$

Here P' is the pressure and Φ' is the gravitational potential in our primed coordinate system. Equations (4.4a) and (4.4b) are, respectively, Poisson's equation for gravitation and the hydrostatic equilibrium equation, solved under the boundary conditions $\rho(0) = \rho_c$ and $\Phi(0) = 0$. To obtain the relation between r' and r, we assume that a uniform sphere of radius r and $\rho = 1$ maps to a Bonnor-Ebert sphere of equivalent mass:

$$\frac{dM'}{dr'} = 4\pi r^2 \frac{dr}{dr'} = 4\pi \rho' r'^2. \tag{4.5}$$

The equivalent coordinate transform assuming mass moves along the radial direction is

$$x_i{}' = \frac{r'}{r} x_i. \tag{4.6}$$

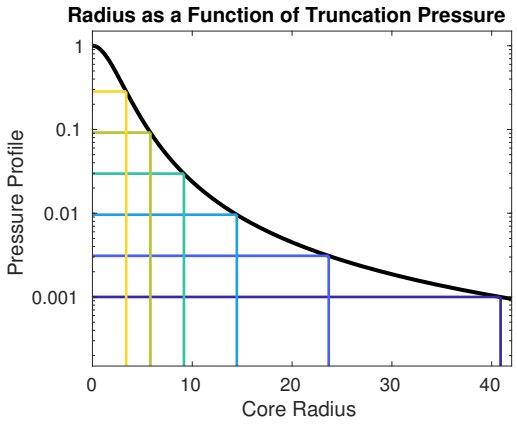


Figure 4.1: Normalized pressure profile of the Bonnor-Ebert sphere. The horizontal and vertical lines connect specific values P_{ext} to their corresponding radii.

When the result is scaled into dimensional units, the central density will have a value of $\rho_0\rho_c$. We note that the constant σ_0^2 in the equation of state and the factor $4\pi G$ in Poisson's equation have been cancelled by converting to dimensionless units.

Once we have the density profile and corresponding unprimed radii from equation (4.5), we truncate the profile at external pressure $P = P_{ext}$, which defines the radius of the surface (see Figure 4.1), and set the density of the medium external to this surface to ρ_{ext}. The truncation pressure P_{ext} is defined as a fraction of the central pressure in dimensionless units, and ρ_{ext} is defined as a fraction of the surface density ρ_s which is required for pressure equilibrium with the external medium. We then compute r external to this surface by integrating equation (4.5) under these conditions. The characteristics of the truncated Bonnor-Ebert profile are therefore defined by three parameters: P_{ext}, ρ_c, and ρ_{ext}.

To save on computation time, we precompute and store a non-truncated Bonnor-Ebert profile with a central density of 1, and rescale the density and corresponding radii to conform to the condition $\rho(0) = \rho_c$. The scaling relations for ρ', r', and r are:

$$\rho' = \rho_c \rho^{*\prime} \tag{4.7a}$$

$$r' = \rho_c^{-1/2} r^{*\prime} \tag{4.7b}$$

$$r = {\rho_c}^{-1/6} r^*. \tag{4.7c}$$

where we have denoted the reference quantities with the superscript $*$. The $\rho_c^{-1/2}$ dependence in equation (4.7b) falls naturally from equations (4.4a) and (4.4b). This is also the origin of the ρ_0 dependence in equation (4.3) above. The factor of $\rho_c^{-1/6}$ in equation (4.7c) originates

from integrating equation (4.5) and solving for r:

$$r = \left(\frac{1}{3}\int \rho' r'^2 dr'\right)^{1/3} = \rho_c^{1/3}\rho_c^{-1/2}\left(\frac{1}{3}\int \rho^{*\prime} r^{*\prime 2} dr^{*\prime}\right)^{1/3} = \rho_c^{-1/6} r^*. \tag{4.8}$$

4.2.3 The Squeeze Transformation

This is a new PolCat transformation that transforms a sphere into a triaxial ellipsoid with principal axes a, b, c *without* conserving volume. This is distinct from PolCat's original, volume-conserving Scale transformation (see FF1 [§3.5.4]). The transformation equations are

$$x' = ax = \zeta cx \tag{4.9a}$$

$$y' = by = \xi cy \text{ and} \tag{4.9b}$$

$$z' = cz, \tag{4.9c}$$

where we have introduced normalized axis ratios $\zeta = a/c$, and $\xi = b/c$. Characterizing the ellipsoid by (ζ, ξ) has the advantage that cores with the same ζ and ξ are the exact same shape, but either larger ($c > 1$) or smaller ($c < 1$). That is, while (a, b, c) characterizes the amount of stretch on each axis, (ζ, ξ) characterize the overall shape and redefines c as the overall amount of compression. The effect of varying (ζ, ξ, c) is illustrated in Figure 4.2. Here c was chosen as the normalizing axis ratio because the the magnetic field is parallel to the z-axis at the centre of the core. Using ζ and ξ, we can easily characterize the core shapes:

- spherical: $\zeta = \xi = 1$;
- oblate spheroid: $\zeta = \xi > 1$;
- prolate spheroid: $\zeta = \xi < 1$;
- oblate triaxial: $\zeta > 1, \xi > 1$;
- prolate triaxial: $\zeta < 1, \xi < 1$;
- neither: all other cases.

We note that the "neither" category encompasses cores where the principal axis in the z-direction falls between the principal axes in the x- and y-directions.

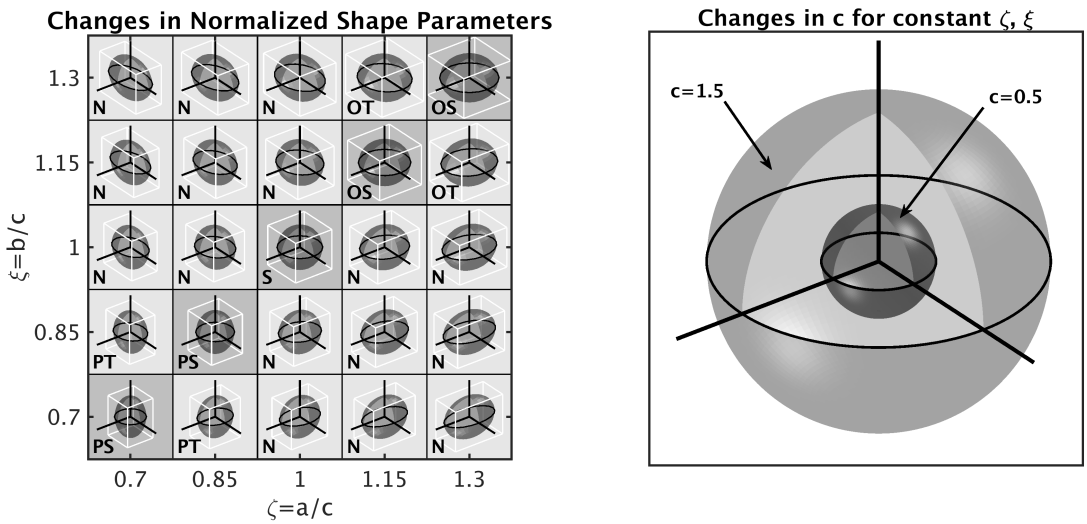


Figure 4.2: Left: Core shapes as a function of ζ and ξ. Cores are labelled to classify their shape: S (sphere), OS (oblate spheroid), PS (prolate spheroid), OT (oblate triaxial), PT (prolate triaxial), and N (neither). Right: Two cores with fixed ζ and ξ with different values of c.

The end result is a transformation that produces ellipsoidal density isosurfaces given by

$$r^2 = \frac{1}{c^2}\left(\frac{x'^2}{\zeta^2} + \frac{y'^2}{\xi^2} + z'^2\right), \tag{4.10}$$

where r is the spherical radius in the less-primed (x, y, z) system. Because this transformation does not conserve volume, the determinant of the Jacobian is not equal to unity and so the density is modified:

$$\rho' = \frac{\rho}{abc} = \frac{1}{c^3}\frac{\rho}{\zeta\xi}. \tag{4.11}$$

The earlier version of the Scale transformation from FF1 (§3.5.4) was found to not suitable for the present work due to the volume-conserving constraint on the stretch in the z-direction ($c = 1/(ab)$). This constraint resulted in a reduction of the magnitude of the gravitational energy for every value of a and b not equal to 1 (sphere), meaning gravitational energy (always negative) never becomes strong enough to counteract the positive terms in the virial balance. The new transformation adds flexibility to PolCat by changing the volume of the core (and thus scaling the density), so that there is potential for the gravitational energy to increase in magnitude to balance the contributions from the kinetic energy and magnetic field.

4.2.4 The Linear Twist Transformations

To produce magnetic fields twisted around the z-axis, we have defined two transformations, LinearTwistA and LinearTwistS defined (in cylindrical coordinates) by

$$r' = r \tag{4.12a}$$

$$\phi' = \phi + C_t f_t(z) \tag{4.12b}$$

$$z' = z, \tag{4.12c}$$

where C_t is a constant ≥ 0, and the function $f_t(z) = z$ for LinearTwistA, and $f_t(z) = |z|$ for LinearTwistS. This transformation is performed prior to the Bonnor-Ebert sphere transformation when used.

4.3 Tensor Virial Theorem

In Cartesian coordinates, the gravitational tensor is expressed as

$$W_{jk} = -\frac{1}{2} G \int_{V'} \int_{V} \rho(\boldsymbol{r}) \rho(\boldsymbol{r'}) \frac{(x_j - x'_j)(x_k - x'_k)}{|\boldsymbol{r} - \boldsymbol{r'}|^3} dV dV'. \tag{4.13}$$

However, this form is impractical to use for numerical evaluation due to the double integration over volume. A single integral may be simply computed by taking a sum of the integrand, but a double integral must first be evaluated for every voxel in the three-dimensional coordinate grid before the final sum. For a coordinate grid with 512^3 voxels, direct numerical evaluation of equation (4.13) requires $\sim 1.3 \times 10^8$ calculations to complete. But if we take advantage of the symmetry of our density isosurfaces, there is a much more efficient method to obtain all of the non-magnetic virial terms.

Chandrasekhar and Lebovitz (1962a,b,c) derived a method to compute the gravitational potential and gravitational potential energy tensors for density distributions constant on concentric similar ellipsoids, which were further refined by Roberts (1962). These results have been summarized and tabulated in Binney and Tremaine (1987). Defining

$$m^2 = a_1^2 \sum \frac{x_i^2}{a_i^2} = a_1^2 r^2, \tag{4.14}$$

where r is the radius of the ellipsoidal isosurfaces defined by equation (4.10) and a_1 is the largest ellipsoidal axis ratio, the gravitational potential energy tensor in ellipsoidal coordi-

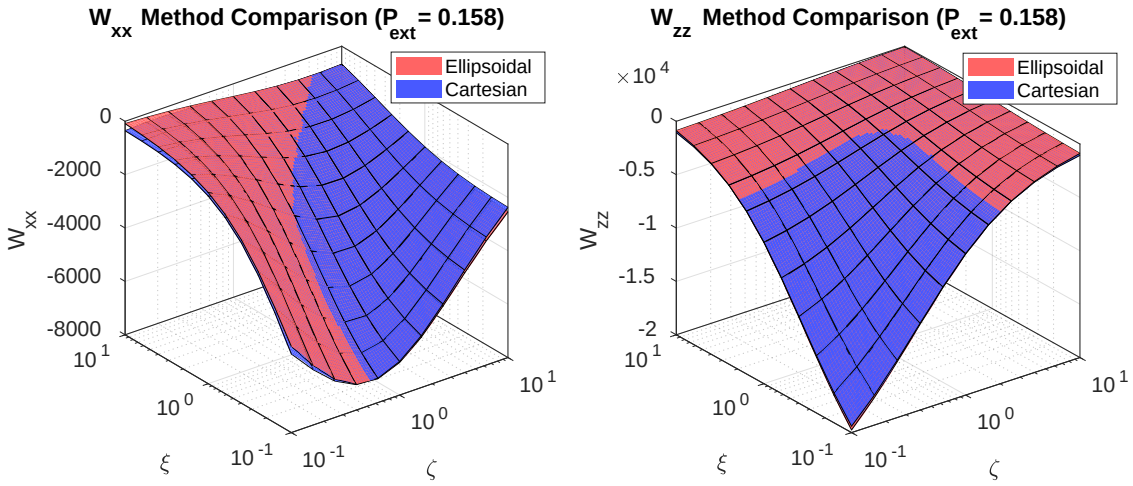


Figure 4.3: Comparison of W_{xx} (top) and W_{zz} (bottom) computed at constant pressure using the ellipsoidal formulation (equation (4.15), red), and cartesian formulation (equation (4.13), blue) calculated on a grid of 71^3 voxels.

nates is then

$$W_{jk} = -2\pi^2 G \frac{a_2 a_3}{a_1^2} \left(\frac{a_j}{a_1}\right)^2 A_j \delta_{jk} \int_0^{a_1^2 R^2} \rho(m^2) \left(\int_0^{m^2} \rho(m'^2) m' dm'^2 \right) dm^2 \tag{4.15}$$

(Binney and Tremaine, 1987, Table 2.2), assuming negligible contribution from material external to the core. Here $r = R$ is the radius of the core surface, A_j are geometry-dependent function coefficients, and quantities a_i represent any permutation of a, b or c following the rule $a_1 > a_2 > a_3$. The function coefficients A_j have different forms for the spheroidal and triaxial cases and are summarized in Binney and Tremaine (1987, Table 2.1).

This form allows us to convert the three-dimensional double-integration into a one-dimensional double-integration, which takes a fraction of the time to compute. We confirmed the implementation of equation (4.15) by direct numerical comparison of LUTs computed with equation (4.13) using a relatively coarse three-dimensional computation grid of 71 voxels per side. Figure 4.3 shows W_{xx} and W_{zz} computed for multiple shapes at constant pressure for both methods. There are small differences between the two methods at the extreme values of ζ and ξ, but the Cartesian lookup tables more closely approach those computed with equation (4.15) as the resolution of the computation grid increases.

Conversion of the volume kinetic term and surface kinetic terms to the same geometry gives

$$T_{jk} = \frac{1}{2} \left(\int_V \rho v_j v_k dV + \delta_{jk} \int_V P dV \right) \tag{4.16}$$

and

$$E_{jk} = \frac{1}{2}\int_S P_{ext} x_k dS_j, \tag{4.17}$$

where P is the pressure of the gas (from our Bonnor-Ebert profile in §4.2.2) with truncation pressure P_{ext} and v_i are the components of the velocity vector. We note that the pressure as defined in our computation of the Bonnor-Ebert profile described by §4.2.2 is not purely thermal, as the full one-dimensional velocity dispersion $\sigma_0^2 = \sigma_{th}^2 + \sigma_{nt}^2$ includes both thermal and turbulent motions. While we could include the turbulent support in the kinetic term, there is a long history of models where turbulent pressure is absorbed into an "effective pressure" (Myers and Fuller, 1992; Caselli and Myers, 1995; McKee and Holliman II, 1999; Fiege and Pudritz, 2000b). Therefore, we set $v_i = 0$ and define $P = \sigma_0^2 \rho$ as the effective pressure supporting the Bonnor-Ebert sphere, with matching truncation pressure P_{ext} at the boundary.

To take advantage of the ellipsoidal symmetry, we can also convert the expressions for T_{jk}, and E_{jk} into a more manageable form. The volume element becomes (in spherical coordinates)

$$dV = 4\pi abc r'^2 dr'. \tag{4.18}$$

Making equivalent changes to the form of T_{jk} we obtain

$$T_{jk} = \delta_{jk} 2\pi abc \int_0^r \sigma_0^2 \rho(r', a, b, c) r'^2 dr'. \tag{4.19}$$

For E_{jk}, the surface kinetic term, P_{ext} is constant over the surface and we obtain

$$E_{jk} = \frac{2\pi}{3} abc R^3 P_{ext} \delta_{jk}, \tag{4.20}$$

where R is the radius of the core surface determined by the truncation pressure P_{ext}.

The magnetic field does not share symmetry with the density. As a result, conversion to this coordinate system does not simplify the magnetic terms. Fortunately, the magnetic terms are comparatively rapid to compute in Cartesian form due to being single integrations over volume and surface, unlike the problematic six-dimensional integral of equation (4.13). The Cartesian forms of the magnetic tensor components are given by

$$M_{jk} = \frac{1}{8\pi}\int B_j B_k dV, \tag{4.21}$$

$$D_{jk} = \frac{1}{4\pi}\int x_k B_j (\boldsymbol{B} \cdot d\boldsymbol{S}) \tag{4.22}$$

and

$$Q_{jk} = \frac{1}{8\pi} \int x_k |\boldsymbol{B}|^2 dS_j. \tag{4.23}$$

The magnetic field structure can be obtained by computing three-dimensional models within PolCat's computational grid at the specified resolution. We note that due to the triaxial geometry of our models, only the tensor components along the diagonal are non-zero in all cases.

4.4 Implementation

Although the ellipsoid forms of equations (4.15) to (4.20) are now relatively quick to compute, we must also choose a high-resolution coordinate grid (typically on the order of several hundred voxels to a side) to compute the magnetic components as accurately as possible. To perform the surface and volume integration, we computed the fractional volume and surface area elements contained in the voxels that intersected with the core's surface, and approximated each surface area element as a plane. This represents the triaxial ellipsoid as a multifaceted polyhedron and allows for more accurate computation of the surface area elements and volume contained in the edge voxels.

The field is computed on a much finer grid than for a typical PolCat run, where the size in the x-z plane is defined by the size of the image data. Taking this into account, we instead pre-compute lookup tables (LUTs) for speed in computation.

At the moment, we only compute results for the Bonnor-Ebert case, leaving the general polytropic sphere case (POLY from (Franzmann and Fiege, 2017) [§3.5.1]) for a later date. We explore the following field geometries: hourglass field models generated with the transformations BES >Squeeze; helical hourglass field models generated with LinearTwistA >BES >Squeeze; and symmetrically twisted hourglass field models generated with LinearTwistS >BES >Squeeze. Each of these cases requires its own set of LUTs. We note that a typical PolCat model also includes transformations to rotate and reposition the core, but these have no effect on the tensor quantities.

To ensure the smallest number of dimensions in the LUTs, we must examine how each tensor component depends on the model parameters and factor out the parameters that have an analytic scaling effect on the results.

The hourglass field models are defined by eight parameters: $\rho_0, \sigma_0, \rho_c, P_{ext}, \rho_{ext}, a, b$, and c. The twist cases require an additional parameter C_t. The parameter ρ_{ext}, which defines the density of the medium outside the core surface, has no effect on the tensor calculation. As is, this would leave us with 7- and 8-dimensional tables which would be computationally

Scale Factor	Expression	Rescales
T_0	$\frac{\sigma_0^5 \rho_0^{-1/2} \rho_c^{-1/2}}{8\pi^{3/2} G^{3/2}}$	${T_{jk}}^*$, ${E_{jk}}^*$
W_0	$\frac{\sigma_0^5 \rho_0^{-1/2} \rho_c^{-1/2}}{32\pi^{5/2} G^{3/2}}$	${W_{jk}}^*$
M_0	$B_0^2 \frac{\sigma_0^3 \rho_0^{-3/2} \rho_c^{-1/6}}{8\pi^{3/2} G^{3/2}}$	${M_{jk}}^*$, ${D_{jk}}^*$, ${Q_{jk}}^*$

Table 4.1: Virial table scaling constants

unwieldy. However, dimensional analysis allows us to factor out the dependence of many of these parameters from the virial equation, allowing us to omit them from the stored LUTs. When we compute VE_{ii} for a particular model, we can then rescale the tables appropriately.

To factor out the parameters, we can express each fully dimensional tensor component X_{ii} as a dimensionless quantity ${X_{ii}}^*$ multiplied by a constant, X_0. With this method we obtain the four constants summarized in Table 4.1, which allows us to to compute each ${X_{ii}}^*$ using the stored, unscaled Bonnor-Ebert profile (§4.2.2) with corresponding magnetic field.

The reduced tensors are only functions of the truncation pressure P_{ext} (which defines the surface radius) and the squeeze parameters (a, b, c) (a_i in general notation), with the addition of adjusted twist parameter ${C_t}^* = \rho_c^{-1/6} C_t$ for the twisted models. This adjustment to C_t originates from equation (4.7c). Further parameter reductions are possible on specific tensor components, and are discussed in the following sections.

4.4.1 Non-magnetic tensor tables

As a result of the coordinate transformation method, the Squeeze transformation modifies the density (and therefore pressure) by a factor of $1/(abc)$ (as per equation (4.11)). When we take this into account in equations (4.19) and (4.20), the axis ratio dependence cancels out, making ${T_{ii}}^*$ and ${E_{ii}}^*$ independent of the model shape. Therefore these LUTs are one-dimensional tables as a function of the truncation pressure P_{ext}.

While equation (4.15) for the gravitational tensor would allow us to make a similar one-dimensional LUT for the integral that could be rescaled to the triaxial form, the functions A_i require evaluation of elliptical integrals that would increase on-the-fly computational time. Therefore, we include the squeeze parameters in the LUT for computational efficiency. However, we can make a further generalization in the table by computing equation (4.15) using the normalized axis ratios $\zeta = a/c$ and $\xi = b/c$. The values read from this table can

be properly scaled to the correct compression via

$$W_{ii}{}^*(P_{ext}, a, b, c) = \frac{1}{c} W_{ii}{}^*(P_{ext}, \zeta, \xi, 1). \tag{4.24}$$

As a result, our initially 7- or 8-dimensional LUTs are reduced to three-dimensional $W_{ii}{}^*$ tables with lookup parameters P_{ext}, ζ, and ξ.

4.4.2 Magnetic Tensor Tables

PolCat's transformation approach to generating molecular cloud core models allows for a similar simplification in the tables for the magnetic tensor components. For the final dimensionless magnetic field component $B_i{}^* = \boldsymbol{B}^* \cdot \hat{\boldsymbol{x}}_{\boldsymbol{i}}$ with corresponding non-normalized squeeze parameter a_i,

$$B_i{}^* = \frac{a_i}{abc} B_i^{\mathrm{BE}^*}, \tag{4.25}$$

where $B_i^{\mathrm{BE}^*}$ is the magnetic field component in the ith direction for the core prior to the triaxial squeeze transformation for all three model cases (i.e. $\boldsymbol{B}^{(N-1)}$ in the transformation order). If we define V^{BE^*} and S^{BE^*} as the volume and surface of the Bonnor-Ebert sphere defined by the surface pressure, we can substitute these into equations (4.21) and (4.22) to obtain

$$M_{ii}{}^*(P_{ext}, a, b, c, C_t{}^*) = \frac{a_i^2}{abc}\left[\frac{1}{8\pi}\int B_i^{\mathrm{BE}^*2} dV^{\mathrm{BE}^*}\right] = \frac{a_i^2}{abc} M_{ii}^{\mathrm{BE}^*}(P_{ext}, C_t{}^*), \tag{4.26}$$

and

$$D_{ii}{}^*(P_{ext}, a, b, c, C_t{}^*) = \frac{a_i^2}{abc}\left[\frac{1}{4\pi}\int x_i^{\mathrm{BE}^*} B_i^{\mathrm{BE}^*}(\boldsymbol{B}^{\mathrm{BE}^*} \cdot d\boldsymbol{S}^{\mathrm{BE}^*})\right] = \frac{a_i^2}{abc} D_{ii}^{\mathrm{BE}^*}(P_{ext}, C_t{}^*) \tag{4.27}$$

(for the hourglass field case, $C_t{}^* = 0$), where the dependence on the axis ratios has been absorbed into a scaling factor.

Equation (4.23) does not factor the same way as the other two magnetic terms, but we can perform a similar simplification if each $Q_{ii}{}^*$ is split into a sum of three integral terms, indexed by j:

$$Q_{ii}{}^*(P_{ext}, a, b, c, C_t{}^*) = \sum_{j=1}^{3} \frac{a_j^2}{abc}\left[\frac{1}{8\pi}\int x_i^{\mathrm{BE}^*} B_j^{\mathrm{BE}^*2} dS_i^{\mathrm{BE}^*}\right] = \sum_{j=1}^{3} \frac{a_j^2}{abc} q^j{}_{ii}^{\mathrm{BE}^*}(P_{ext}, C_t{}^*). \tag{4.28}$$

Therefore, we can reduce each of the stored magnetic tensor LUTs to one-dimensional (non-twisted hourglass) or two-dimensional (hourglass twist) tables.

We note that the tensor LUTs for both the symmetric and asymmetric twists are the same, because the field strength and angle that the field makes with the surface normal is identical in both versions.

4.4.3 Virial Equilibrium Computation

PolCat does not determine a value for the magnetic field scale parameter B_0 because field intensity cannot be determined directly from the polarization angles that we model. However, we obtain an estimate by setting it to the value that results in scalar virial equilibrium

$$B_0^2 = -\frac{2T_0T^* + W_0W^* - T_0E^*}{(M_0/B_0^2)(M^* + D^* - Q^*)}, \tag{4.29}$$

which simplifies to

$$B_0^2 = \sigma_0^2\rho_0\rho_c^{-1/3}\left[\frac{E^* - 2T^* - \frac{1}{4\pi}W^*}{M^* + D^* - Q^*}\right] = b_0^2\,[b^{*2}]. \tag{4.30}$$

Here, we have collected the common factor $\sigma_0\rho_0^{1/2}\rho_c^{-1/6}$into a scaling constant b_0, and defined the expression in square brackets as the square of the dimensionless tensor-dependent field strength b^*.[1]

If the gravitational and kinetic surface terms dominate over the volume kinetic and thermal energy terms, then a non-zero magnetic field strength is required to keep the core in equilibrium. If the volume kinetic and thermal terms dominate, there is no value of the magnetic field strength that results in equilibrium conditions, and a non-zero magnetic field strength throws it further out of balance.

Substituting the result of equation (4.30) into (**??**) and simplifying constants, we obtain:

$$VE_{ii}{}^* \equiv \frac{VE_{ii}}{T_0} = 2T_{ii}{}^* + \frac{1}{4\pi}W_{ii}{}^* + b^{*2}M^* - 2b^{*2}M_{ii}{}^* + b^{*2}D_{ii}{}^* - b^{*2}Q_{ii}{}^* - E_{ii}{}^*. \tag{4.31}$$

Normalizing each $VE_{ii}{}^*$ by T_0 simplifies the scaling, reducing the parameter dependence to five parameters: P_{ext}, a, b, c, and $C_t{}^*$.

[1]The scaling factor as stated in Franzmann and Fiege (2020) was originally $b_0 = \sigma_0\rho_0\rho_c$. This was a typo originating from an earlier iteration of our virial method, but has no effect on the results of the paper.

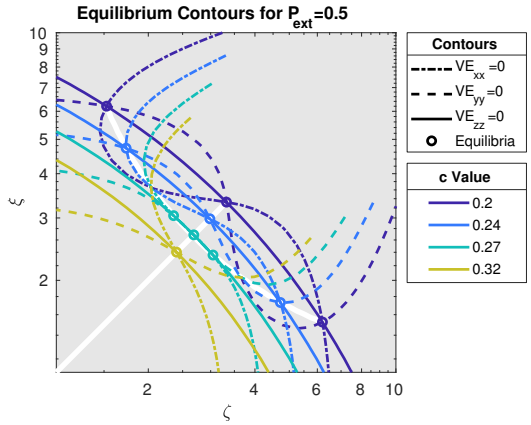


Figure 4.4: $VE_{ii} = 0$ contours for all three axes for four steps of c to demonstrate how equilibrium solutions were found. The curve in white represents the full set of intersection points.

4.5 Analysis of Solutions in Tensor Virial Equilibrium

Final LUTs were calculated using a model grid size of 513 voxels per side for 100 values of P_{ext} between 0.001–0.5, 100 values of ${C_t}^*$ between 0–2 for the twist tables, and 51 values of ζ and ξ spaced logarithmically between 0.1–10 for the ${W_{ii}}^*$ tables. The odd number in the coordinate grid ensures the inclusion of the core centre.

This section presents the results of analyzing the LUTs to find solutions in tensor virial equilibrium, which can be found by examining where all of the $VE_{ii} = 0$ contours intersect. We find that the contours allow for both spheroidal cores and, surprisingly, a selection of triaxial cores that are in virial equilibrium. These triaxial solutions appear as "wings" on either side of the spheroidal solutions when the normalized axis ratios are plotted, as demonstrated in Figure 4.4. This is possible due to the restriction that the cores be in both tensor *and* scalar virial equilibrium ($\sum_i VE_{ii} = 0$). Therefore, if the core is in virial equilibrium on two axes, then the third must be as well.

4.5.1 Hourglass Field Models

Examination of the intersection of the normalized $VE_{ii} = 0$ surfaces for the tensor components shows that all pure hourglass field cores in tensor virial equilibrium have their smallest dimension along the polar direction (e.g. oblate spheroids). Additionally, all equilibrium solutions have $c \leq 1$, indicating that all the equilibria are compressed.

Figure 4.5 (left) shows the distribution of equilibrium solutions for twelve pressure steps showing both spheroidal solutions (confined to the line $\zeta = \xi$ in log-log space) and triaxial wings, adjusted for 90° rotational core symmetry. For all pressure steps, as the cores become

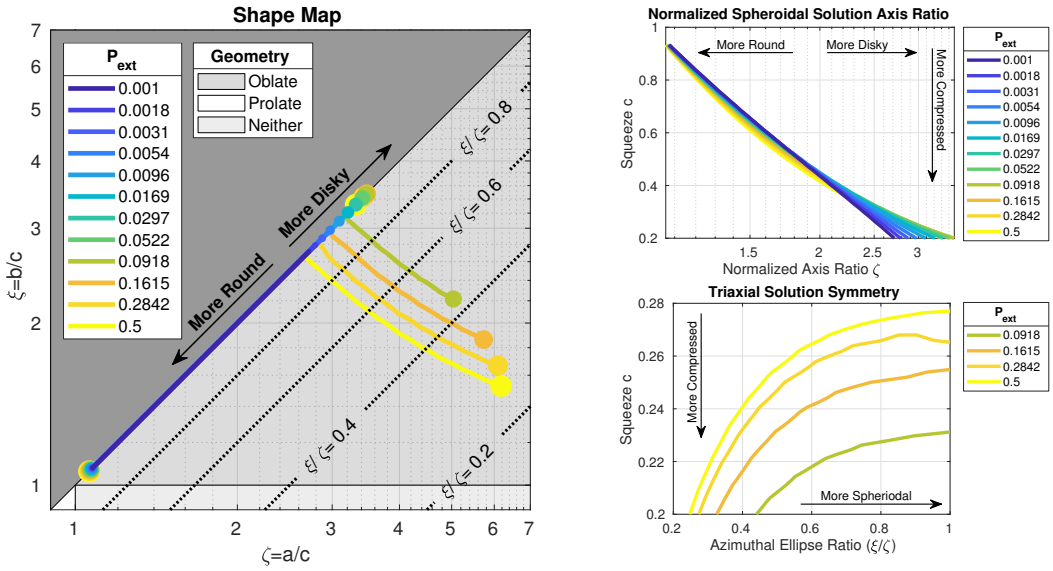


Figure 4.5: Plots mapping the tensor virial equilibrium shapes for multiple pressure steps at constant σ_0 for untwisted hourglass models. Left: Map of normalized triaxial axis ratios, adjusted such that $\zeta > \xi$ to account for 90° azimuthal degeneracy. The end points of each curve are indicated by dots of the corresponding colour due to spheroidal overlap. Top Right: The normalized axis ratios of the spheroidal solutions relative to the z-axis squeeze parameter, c. Bottom Right: The azimuthal (x-y plane) axis ratio ξ/ζ relative to c. Values of $c < 1$ indicate that the cores is compressed.

flatter (ζ, ξ increase), they also become more compressed (Figure 4.5, right top and bottom).

The triaxial wings first appear between $P_{ext} = 5.6 \times 10^{-2}$ and 5.9×10^{-2} (BE truncation radii between 6.97 and 7.11). These cores are highly compressed ($c < 0.3$), with their maximum c-value occurring at intersection with the spheroid line, and decreasing as the solutions become more azimuthally asymmetric (ξ/ζ decreasing). As the truncation pressure increases and the surface radius decreases, the solutions in the triaxial wings become less flat, with smaller values of ζ and ξ producing shapes with the same azimuthal axis ratio ξ/ζ.

The leftmost plots in Figure 4.5 show the effect of the c value on the shape of the solutions, with the spheroidal solutions on top, and the triaxial solutions on the bottom. For all pressures, as the ζ value increases for the spheroidal solutions (shapes become more disky), the equilibrium solutions also become more compressed, with the highest pressures resulting in the flattest equilibria. As the pressure increases for the triaxial solutions, the wings shift towards rounder shapes overall while simultaneously becoming less compressed. Therefore, cores with an identical azimuthal ratio of ξ/ζ are flatter and more compressed at lower truncation pressures. In general, as ζ increases, ξ decreases in the wings, resulting in cores that are flatter in the x-z plane and rounder in the y-z plane. The result is that the

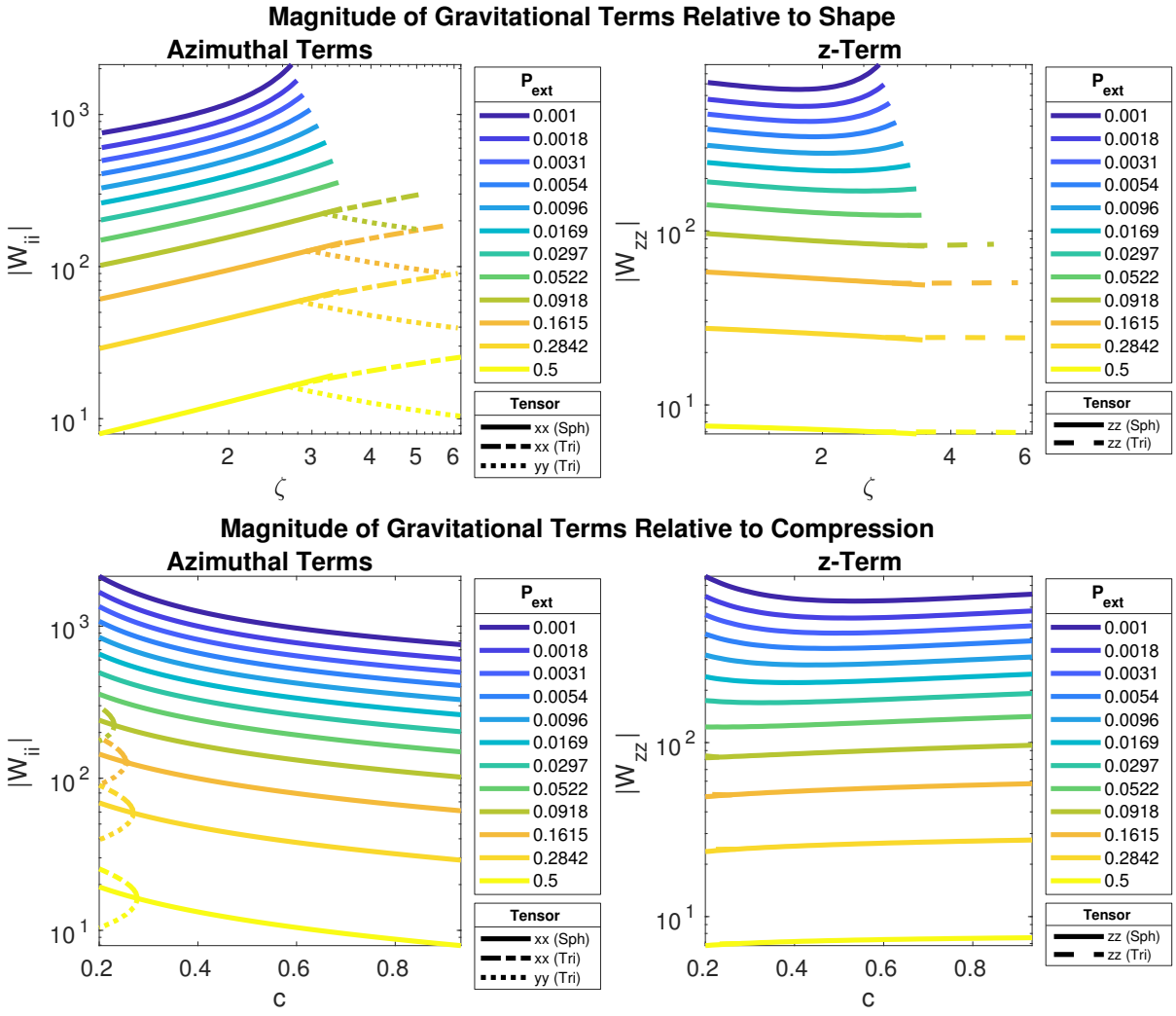


Figure 4.6: Magnitude of the gravitational tensors W_{xx} and W_{yy} (left) and W_{zz} (right) relative to the overall shape (top) and compression (bottom) for the equilibrium solutions shown in Figure 4.5. Triaxial solutions are plotted with dotted lines. The triaxial zz values are approximately the same as their spheroidal counterparts, and so are not visible on the bottom right plot.

triaxial cores become more elongated perpendicular to the magnetic field direction as they become more compressed.

Figures 4.6, 4.7, and 4.8 plot the magnitudes of the gravitational, total magnetic, and total kinetic terms of equation (4.31) for both the spheroidal and triaxial solutions. As expected, as the bounding pressure increases and the interior radius (and therefore enclosed mass) decreases, the magnitudes of all tensor components also decrease. The spheroidal solutions retain approximately the same curvature in the azimuthal tensors as the pressure increases, but the zz tensors flatten out with increasing pressure. In the z-direction, the

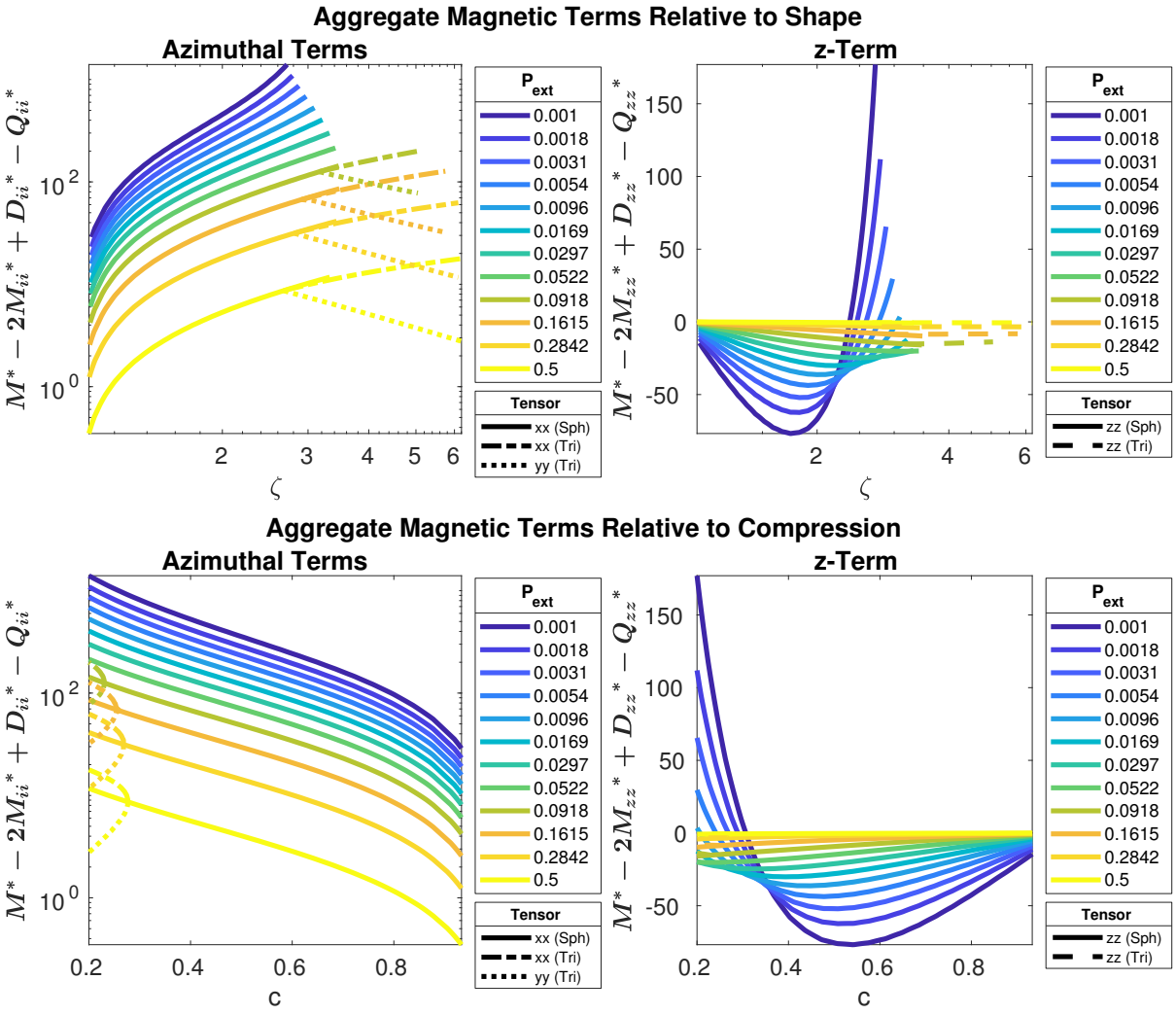


Figure 4.7: Plots of the aggregate magnetic field terms in Equation (4.31), arranged identically to the $|W_{ii}|$ plots in Figure 4.6.

net magnetic terms are mostly negative, with only truncation pressures $P_{ext} \approx 0.01$ and below having positive values at high compression. Therefore, the magnetic field is acting to confine the core in the z-direction for most of the solutions in tensor virial equilibrium. We note that the magnetic tensor in the z-direction is much smaller than the corresponding azimuthal components, so the magnetic contribution to the scalar virial theorem is still uniformly positive.

The triaxial solutions are shown in dotted lines in the same plots. The zz tensors are approximately the same as in the spheroidal case, whereas in each of the pressure steps the xx tensor is larger and the yy tensor is smaller than the spheroidal equivalent. While this result may seem counter-intuitive due to the core size in the x-direction being the largest and therefore most "spread out", this may be due to the $(a_i/a_1)^2 = (a_i/\zeta)^2$ dependence in the

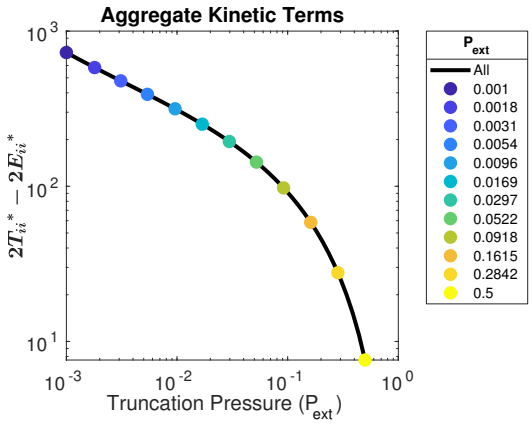


Figure 4.8: Kinetic pressure contribution to equation (4.31), with pressures shown in Figure 4.7 indicated in the same colours. The magnitude of T_{ii} and E_{ii} are independent of shape, and so depend only on the truncation pressure.

ellipsoidal definition of the gravitational tensor (equation 4.15). The shape map on the left side of Figure 4.5 shows that as ξ (and therefore the core size in the y-direction) decreases in the wings, the ratio ξ/ζ also decreases, causing W_{yy} to be smaller in magnitude than W_{xx}.

4.5.2 Twisted Hourglass Field Models

Examination of the normalized $VE_{ii} = 0$ intersection surfaces show that the presence of a twisted magnetic field has a strong effect on the equilibrium shapes. Figure 4.9 (see insets) shows that triaxial wings do occur at the same range of pressures as in the hourglass case. However, varying the twist parameter while holding P_{ext} constant shows that as the twist increases, the ζ and ξ values decrease. This moves the triaxial wings closer to the origin and causes the spheroidal equilibrium shapes to become more spherical. Once the twist increases above a certain amount, the triaxial solutions vanish, leaving only spheroids. As the twist increases further, the solutions transition from oblate into prolate spheroids (Figure 4.10). The exact C_t^* value where this occurs is dependent on the truncation pressure.

Figure 4.9 shows how the shape in the x-y plane relates to core compression, similar to the bottom right panel of Figure 4.5. For truncation pressures less than 0.2, where the Bonnor-Ebert density profile begins to transition from its core region into the r^{-2} asymptotic tail, increasing the twist parameter causes the cores to become more compressed and moves the azimuthal ratio ξ/ζ towards more symmetric values (see Figure 4.9, top). For truncation pressures above 0.2, increasing the twist initially causes the opposite to happen until C_t^* reaches a pressure-dependent value between 0.1-0.3. Once this value is reached, c begins to rapidly decrease until the triaxial solutions vanish. That is, at constant ξ/ζ, equilibrium shapes are less compressed with increasing C_t^* until the turnover value is reached, and at

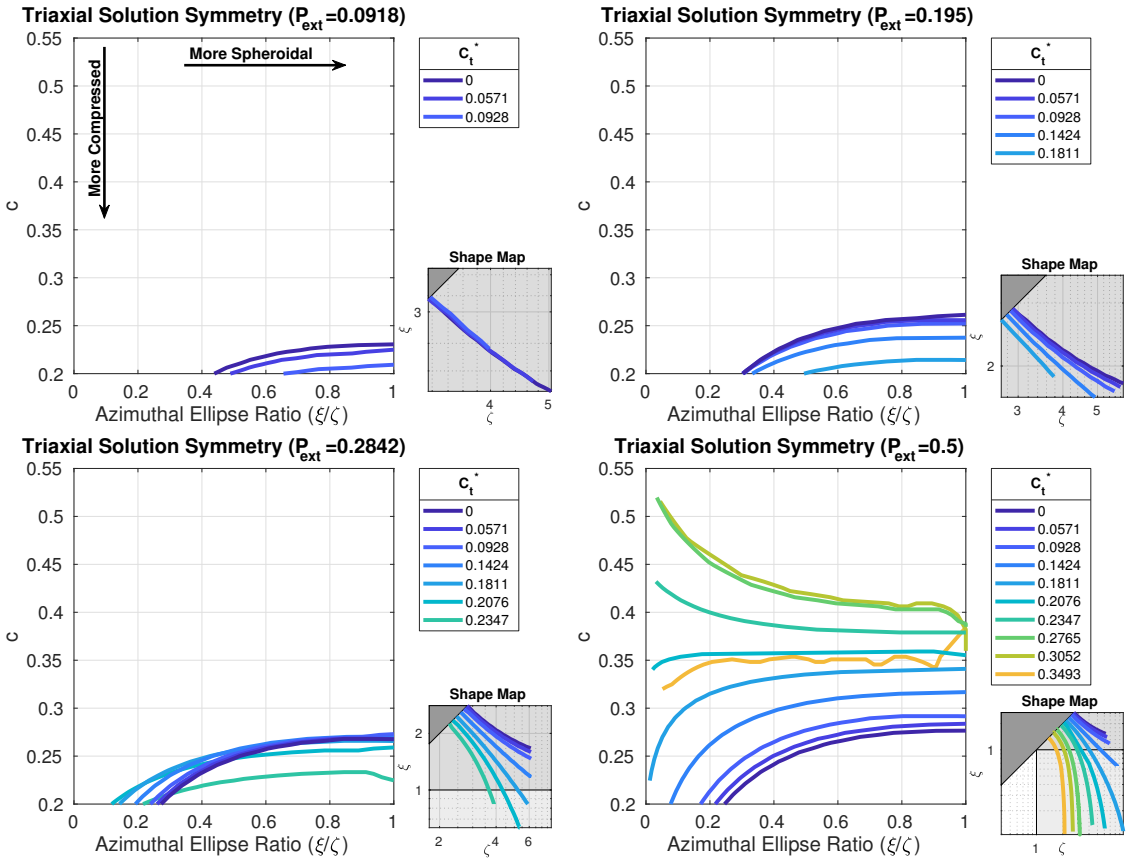


Figure 4.9: Plots of azimuthal eccentricity for triaxial equilibrium solutions against c for truncation pressures of 0.0918, 0.195, 0.3431, and 0.5 at multiple twist steps, scaled with identical axis limits to facilitate direct comparison between pressure steps. The small inset on the bottom right of each plot shows the corresponding shape maps (as in Figure 4.5, left). Pressure values were chosen to highlight how the twist affects the triaxial equilibrium geometry.

constant c, equilibrium shapes become more asymmetric as the turnover value is reached.

For the spheroidal solutions, as with the untwisted hourglass case, all ζ vs c curves (Figure 4.10) approach $\zeta = \xi = c = 1$ (spherical). This common intersection arises because the magnetic field computed from the virial balance approaches 0 (i.e. non-magnetized) for spherical solutions (Figure 4.11).

As $C_t{}^*$ increases while holding P_{ext} constant, the curves in Figure 4.10 begin to become more vertical, transitioning from purely oblate to purely spherical shapes ($\zeta = 1$). The value of $C_t{}^*$ for this change depends on the pressure, beginning at approximately $C_t{}^* = 0.46$ at the highest pressure. Increasing the twist above this point produces purely prolate spheroids. As $C_t{}^*$ increases further, the curves continue to pivot into the prolate region of the plot and become arched, with c initially increasing to a maximum value (expansion) with decreasing ζ before falling off sharply. Therefore, rounder prolate spheroids are closer to equilibrium

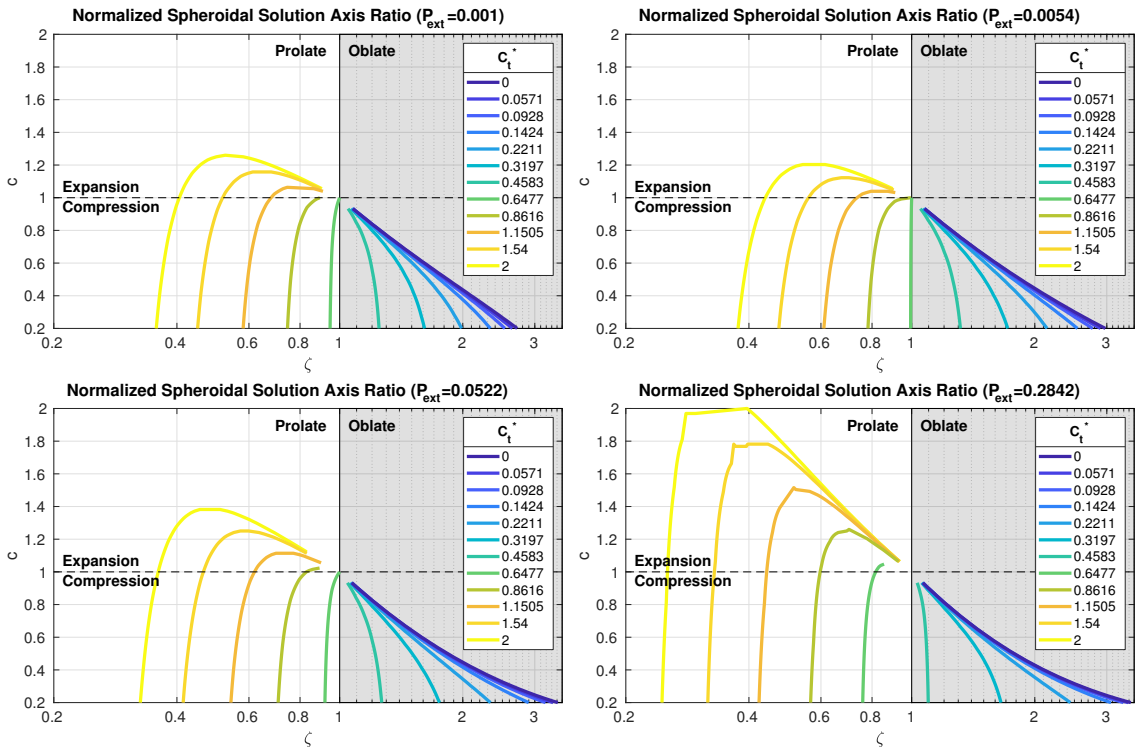


Figure 4.10: Plots of normalized axis ratio ζ of spheroidal solutions against c for truncation pressures of 0.001, 0.0054, 0.0522, and 0.2842 at multiple twist steps. Gaps in the curves are due to the intersection points proximity to where the trace of the aggregate magnetic terms $M^* + D^* - Q^*$ (the denominator in equation (4.30)) crosses zero.

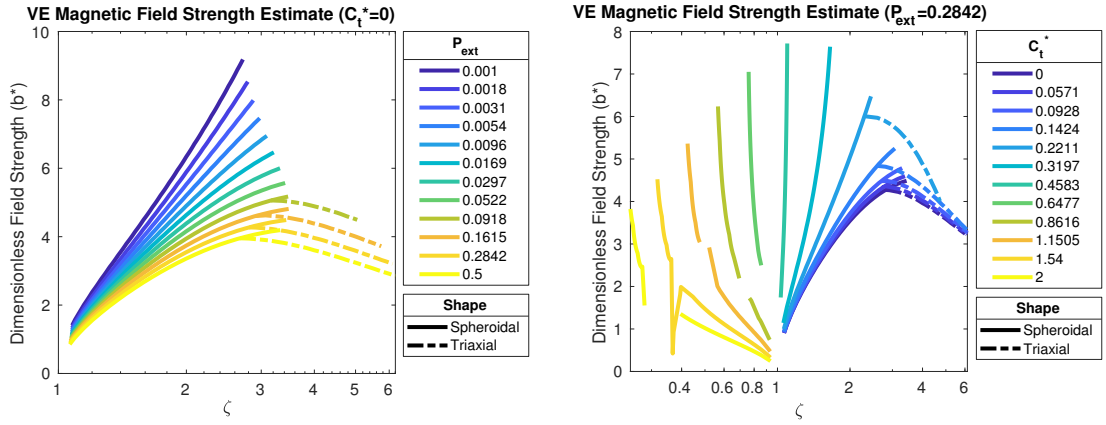


Figure 4.11: Plots of the dimensionless magnetic field strength as a function of ζ for both the non-twisted hourglass case for multiple pressure steps (top) and the twisted hourglass shapes for $P_{ext} = 0.2842$ at multiple twist steps (bottom). Gaps and sudden jumps in the prolate curves are due to numerical error where the trace of the aggregate magnetic terms $M^* + D^* - Q^*$ crosses 0.

when expanded along the z-axis, and narrower prolate spheroids are closer to equilibrium

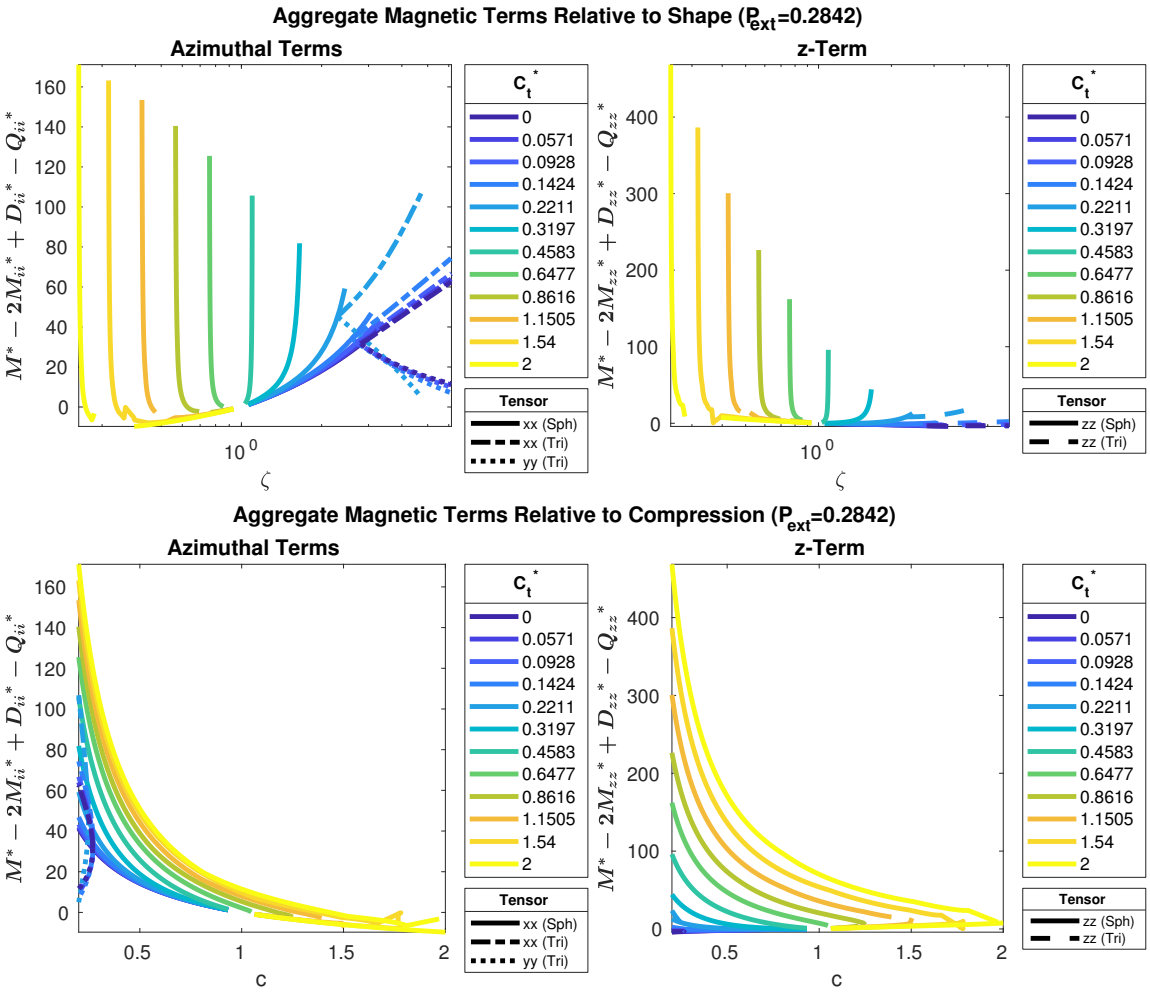


Figure 4.12: The aggregate magnetic terms at $P_{ext} = 0.2842$ as functions of ζ (top) and c (bottom). The gravitational terms have the same overall shape, but with larger minimum values.

when compressed.

The presence of a helical field has no effect on the kinetic terms in the virial equation, and so remain the same as in Figure 4.8. Figure 4.12 shows plots of the aggregate magnetic terms for twelve $C_t{}^*$ steps at a truncation pressure of $P_{ext} = 0.2842$. The overall shape of the curves is approximately the same between the aggregate magnetic tensors and the gravitational tensors with the latter having slightly higher magnitudes.

For hourglass field models with no field twists, the azimuthal terms dominate over the zz component in the trace of VE_{ii}. As the twist increases, the contribution from the azimuthal terms decreases and the zz term comes to dominate. This happens approximately where the equilibrium shapes switch from oblate to prolate.

Generally, the equilibrium shapes for cores with a twisted magnetic field causes the oblate

magnetic virial components to increase in magnitude, particularly for solutions with higher compression. Once the solutions turn prolate, equilibrium cores that are expanded ($c > 1$) have negative azimuthal magnetic tensor terms, meaning that the field is contributing to contraction in the x-y plane rather than supporting against it. The minimum value of the zz magnetic tensor increases with increasing twist, becoming purely positive.

As in the pure hourglass case, the triaxial azimuthal tensors (left half of Figure 4.12) diverge as the cores become more azimuthally asymmetric, and this divergence increases as the shapes become more compressed.

4.6 Monte Carlo Sampling

We performed a Monte Carlo sampling of the shapes belonging to the hourglass equilibrium samples at random orientations to explore the range of projected minor to major axis ratios B/A that could be observed from each population. Our Monte Carlo sampling was implemented by the following procedure:

1. Select a random orientation relative to the line of sight.

2. Select a random value of ζ and interpolate the corresponding ξ value from the original population of solutions (Figure 4.5).

3. Compute the projected axis ratio.

Once we have the projected axis ratios, we then bin the Monte Carlo sample in ζ and B/A, which gives a two-dimensional histogram of the relation between the projected ratio and the intrinsic ratios. We do not intend these histograms as any sort of general statement of an underlying physical distribution, as in Ryden (1996) for example. Rather, we intend them as a tool to find the most likely value of ζ (with corresponding ξ and c) from a projected axis ratio under the assumptions of 1) the observed core is in tensor virial equilibrium at a particular truncation pressure, and 2) whether the shape is triaxial or spheroidal.

4.6.1 Method

A general ellipsoid with intrinsic axis ratios $(\zeta, \xi, 1)$ projects to an ellipse with axis ratios (A, B) defined by the roots of

$$\Lambda^2 - [l^2(\xi^2 + 1) + m^2(\zeta^2 + 1) + n^2(\zeta^2 + \xi^2)]\Lambda + (l^2\xi^2 + m^2\zeta^2 + n^2\zeta^2\xi^2) = 0, \qquad (4.32)$$

where (l, m, n) is a unit vector in the line of sight direction as defined in the coordinate system of the core's principal axes (Vickers, 1996). If we orient our observational frame of reference such that the line of sight is along the y-direction, we can redefine the vector components in terms of the orientation of the core relative to the line of sight. Defining the orientation as an azimuthal rotation by angle ϕ and inclination of angle i, we obtain $(l, m, n) = (\sin\phi\cos i, \cos\phi\cos i, \sin i)$.

Our Monte Carlo sample consisted of 1×10^6 random values of $\sin i$ between -1 to 1, ϕ between 0 to 2π, and ζ values within the selected equilibrium population, treating the spheroidal and triaxial solutions as separate populations of cores. Since each c and ξ in the separate populations has a unique value of ζ, we can generate a random equilibrium solution using ζ alone. We chose to randomly sample $\sin i$ to evenly map the full range of polar orientations. Once we had defined our sample, we solved equation (4.32) to obtain the axis ratio B/A, where A is the major axis and B is the semi-major axis of the projected ellipse.

4.6.2 Results

The top row of Figure 4.13 shows two-dimensional histograms of the spheroidal and triaxial samples at $P_{ext} = 0.5$ binned logarithmically by ζ and linearly by B/A. We chose logarithmic binning for ζ to reflect the fact that the lookup tables are logarithmically spaced in the same variable. The middle rows show the histogram normalized by the total number of the sample contained in the B/A bins. This represents the discrete probability that a core with projected axis ratio B/A will have a particular ζ under the assumptions listed in the previous section. The bottom panel maps the minimum and maximum B/A for the range of ζ in the sample at specific inclinations between $\phi = 0 - \pi/2$. The hard boundary where $i = 0$ and $\phi = 0$ in the two-dimensional histograms and probability distributions reflects the minimum possible value of ζ that will project a particular B/A, and does not reflect any externally imposed limit on the parameters.

For any particular projected axis ratio, the peak of the histogram falls mostly along the line where $i = \pi/2$, with some minor enhancement along $i = 0, \phi = \pi/2$. However, this does not imply that all the cores in this region of the histogram are at this specific orientation. As the bottom panel of Figure 4.13 shows, there are multiple inclination angles that produce the same apparent axis ratio at various ϕ between 0 and $\pi/2$.

One interesting result of this analysis is that there are some preferred ζ modes for B/A values in each tensor virial equilibrium population. This is emphasized in Figure 4.14, which plots two slices from each of the two-dimensional discrete probability distributions shown in the middle row of Figure 4.13. The distributions are sharply peaked despite having broad

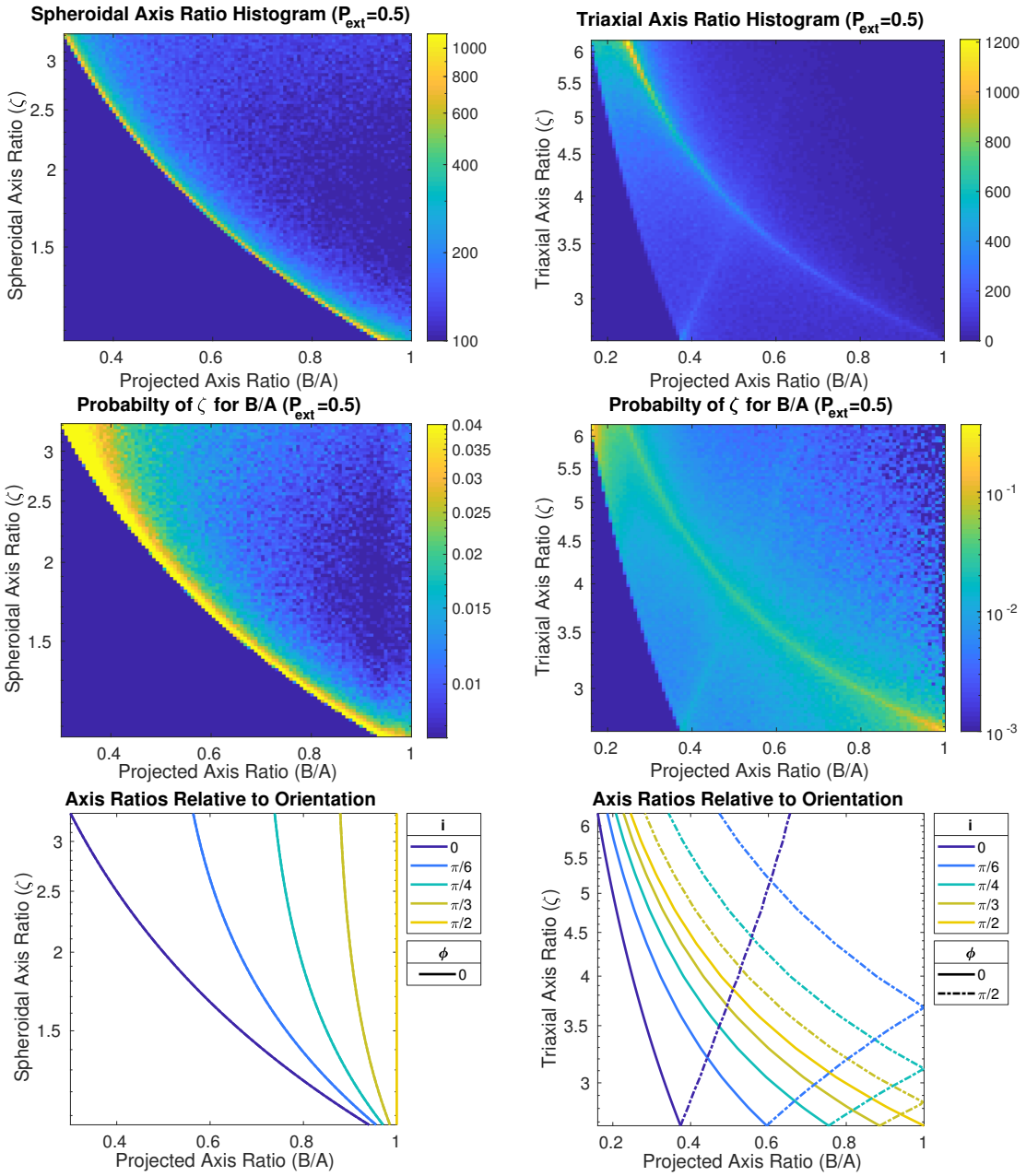


Figure 4.13: A sample of the Monte Carlo algorithm run for the triaxial sample of $P_{ext} = 0.5$. Top Row: The two-dimensional histograms for the spheroidal (left) and triaxial samples (right), binned to 100x100 with the ζ bins logarithmically spaced. Middle Row: Discrete probability of a particular B/A value having intrinsic ratio ζ. Bottom Row: Maps of the projected axis ratios as a function of triaxial ζ for specific orientation angles. The angle mapping for the spheroids is uniform across pressure steps.

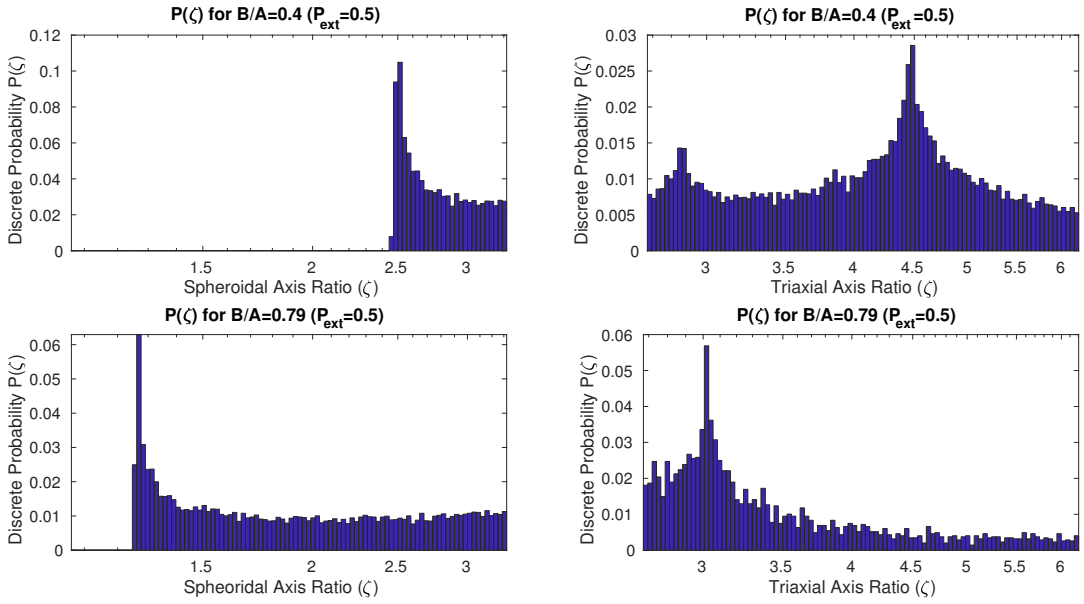


Figure 4.14: Vertical slices from the discrete probability distributions presented in Figure 4.13 for both the spheroidal (left) and triaxial samples (right).

bases.

Figure 4.15 plots the most probable (i.e. modal) ζ values for each projected axis ratio in addition to the mean value for both the spheroidal (top) and triaxial populations (middle). All spheroidal populations at all pressure steps had their most probable values along their shared minimum bound ($\phi = 0, i = 0$), while the mean values increased with the increase in truncation pressure. However, this latter result is most likely due to the different maximum ζ values at each pressure step, rather than any underlying structure in the histogram.

Likewise, the flat regions at low B/A in the most probable value curves in the triaxial sample (Figure 4.15, middle) are an artifact of the maximum ζ value in the parent population. Following the $\phi = \pi/2$ curve to the minimum plotted B/A value would imply that the peak in the distribution lies outside of the range of population ζ values. Correspondingly, the sharp dip in the most probable values of the triaxial $P_{ext} = 0.0918$ curve results from the minimum B/A at the $i = \pi/2, \phi = 0$ orientation occurring at a larger value of B/A than for the other triaxial samples. This causes the secondary peak at $i = 0$ at the lower ζ limit to dominate the distribution (Figure 4.15, bottom).

4.7 Discussion and Conclusions

We have presented the results of tensor virial equilibrium computation for pressure truncated magnetized Bonnor-Ebert spheres. Results from both non-twisted and twisted hourglass field

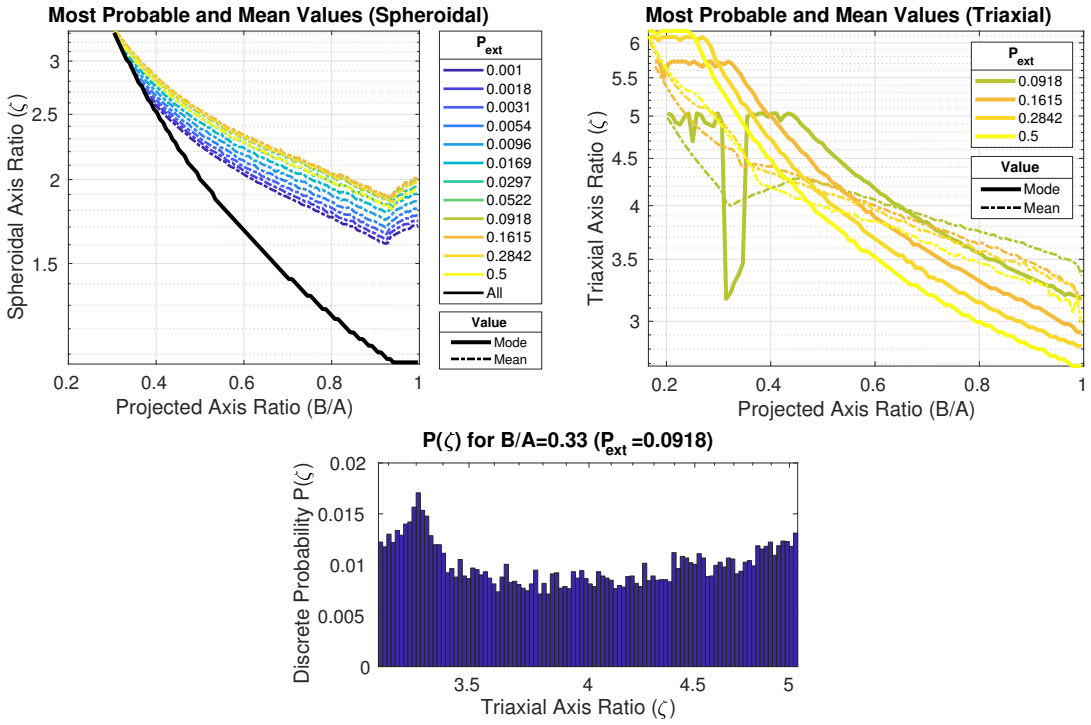


Figure 4.15: Most probable (modal) and mean values of ζ as a function of projected axis ratio B/A from the two-dimensional histograms for the spheroidal (top) and triaxial samples (middle) at multiple steps in truncation pressure P_{ext}. The bottom plot shows the discrete probability slice at $B/A = 0.33$ for $P_{ext} = 0.0918$ to illustrate the origin of the sudden dip in the modal curve between $B/A \approx 0.3$-0.35.

models show that tensor viral equilibria only exist in a specific subset of model geometries. Therefore, we can use this virial equilibrium criterion to successfully reduce the degeneracy in models produced by PolCat. However, we do not necessarily expect cores to be in perfect equilibrium. If we relax the $VE_{ii} = 0$ constraint to

$$\frac{|VE_{ii}|}{|W_{ii}|} \leq \alpha \tag{4.33}$$

where α is a threshold value of order unity, then our virial constraint becomes a physicality constraint requiring that cores are not "too far" from equilibrium. Such cores may be preferred by an Occam's razor argument, since magnetostatic cores are necessarily simpler objects than dynamic cores resulting from turbulent fluctuations.

While spheroidal equilibria dominate our solution space, it is particularly interesting that we have found a set of triaxial cores that are in tensor virial equilibrium on all three axes. It is unknown whether these equilibria are stable or unstable, but they warrant further investigation. Such equilibria have not been previously found in studies of exact magneto-

static equilibria (e.g. Mouschovias, 1976b; Tomisaka et al., 1988a; Fiege and Pudritz, 2000b) because the self-consistent field methods employed by these works assumed azimuthal symmetry. One additional potential complication with our calculation is that magnetic fields in low-density gas should quickly relax to force-free configurations, which cannot be guaranteed in PolCat's modelling framework. The magnetic surface terms in the tables are calculated using the field structure just interior to the truncation radius. As a result, the fields external to the core may physically be out of balance with the internal fields, which would affect the estimate of the magnetic energy. We have plans to investigate our new triaxial equilibria with a three-dimensional magnetohydrodynamic code in order to determine their stability.

Work is currently underway to apply the virial criterion to fits of actual data. An earlier version of PolCat was applied to data without our new tensor virial physicality criterion, and without the extensions to the code presented in this work, which allowed for very flattened or elongated geometries that were far from equilibrium. Preliminary testing with the virial criterion in place shows that it eliminates these unphysical extreme geometries while the fit is still running. The next stage of this research will involve applying the current version PolCat to a variety of cores from the SCUPOL legacy catalogue (Matthews et al., 2009) as well as new data from the JCMT BISTRO Collaboration (Ward-Thompson et al., 2017).

Chapter 5

Exploration of Non-Equilibrium Molecular Cloud Cores Under Tensor Virial Constraint

For application to PolCat runs, we desired a simplified parameter that we can use to assess how far each solution is from tensor virial balance. To that end, we opted to express the virial balance of each axis VE_{ii} as a fraction of its corresponding gravitational energy term W_{ii}. Due to cancellation of constants, this simplifies to

$$\frac{VE_{ii}}{W_{ii}} = \frac{{VE_{ii}}^*}{\frac{1}{4\pi}{W_{ii}}^*} = R_{ii} \tag{5.1}$$

where ${VE_{ii}}^*$ is as defined in equation (4.31). This allows us to compute a simple "upper virial limit" that can be used to restrict solutions.

For actual PolCat fits, we selected a hard upper bound for the normalized tensor virial components of 0.2. As this places a restriction on the models, we also wanted to explore the potential range of geometries that this criterion allows.

To map the parameter space, we used the ζ, ξ grids from the lookup tables (513x513), and generated a grid of 256 c values between 0.2 and 2 (the default PolCat limits). We then used them to calculate the virial balance at the same 12 pressure steps (and corresponding main ${C_t}^*$ steps for the twist tables) used in the previous chapter, and rejected all results where the magnitude of any of the R_{ii} values were greater than 0.2, or the square of the dimensionless magnetic field scale b^* was negative. This latter condition omits all geometries where there exists no solution that is in scalar virial equilibrium.

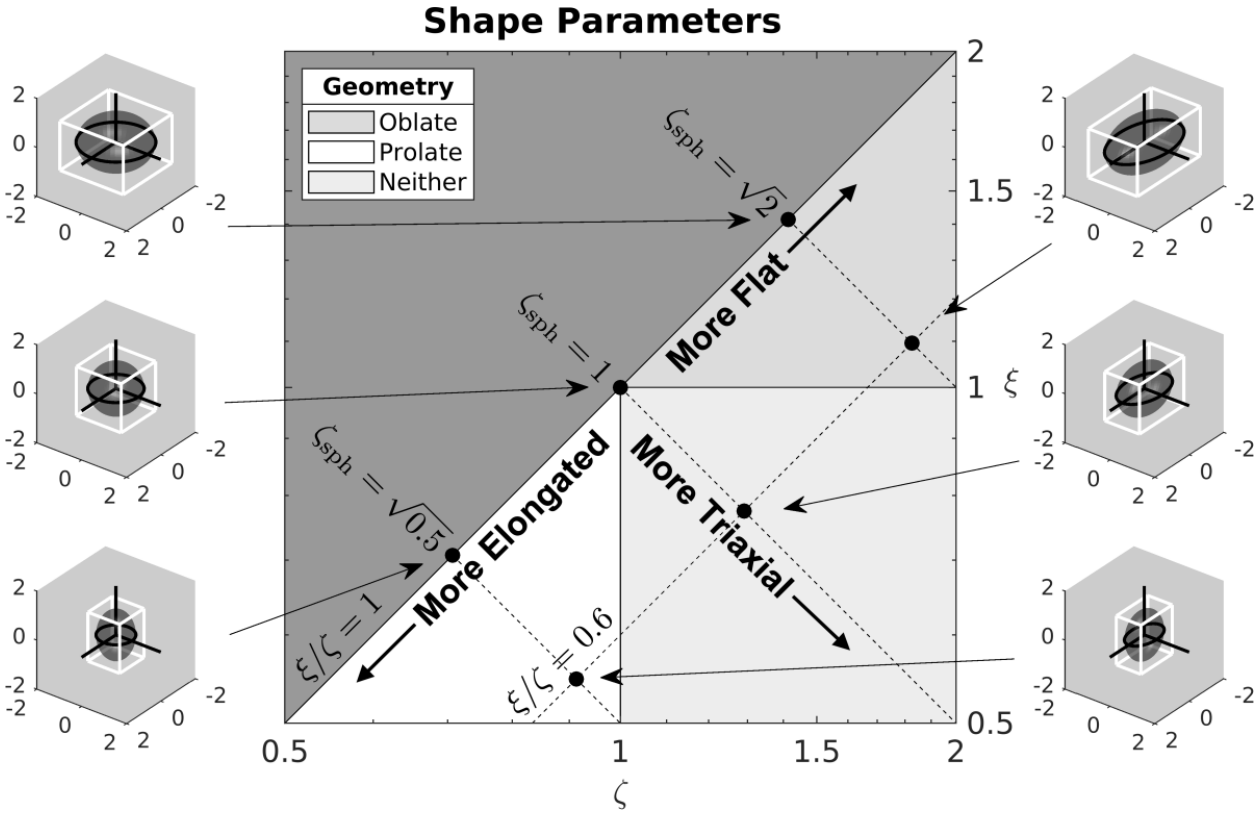


Figure 5.1: How location on the shape map relates to ellipsoidal geometry. The plot shows ellipsoids with azimuthal ratios of 0.6 (right) and 1 (spheroids, left), and $\zeta_{\rm sph}$ values of $\sqrt{0.5}$, 1, and $\sqrt{2}$ (bottom to top).

5.1 Some Notes on Core Shape

The utility of describing the our model shapes in terms of normalized ellipsoidal axis ratios $(\zeta, \xi, 1)$ is that we can easily classify the shapes by plotting ζ relative to ξ logarithmically (see Section 4.2.3, Figure 4.5). The resulting "shape maps" are symmetric across the line $\xi = \zeta$, which represents the subset of spheroidal solutions (henceforth we refer to this as the "spheroid line"). Due to this symmetry, we can simplify the shapes by adjusting the ratios such that $\zeta > \xi$ for our analysis. Figure 5.1 shows the effect that these ratios have on the overall shape, as well as additional relevant quantities that we describe below.

To thoroughly explore the effect that the shape has on the virial balance, we can quantify how triaxial the model is by calculating the azimuthal axis ratio ξ/ζ. For $\zeta > \xi$, the smaller the ratio, the more triaxial the core, with ratios of $\xi/\zeta = 1$ representing the spheroidal solutions. Two models sharing the same ξ/ζ value have the same projected shape in the x-y plane, and plotting curves of constant ξ/ζ on the shape map results in lines with a slope of -1, parallel to the spheroid line (Figure 5.1). We have previously used ξ/ζ to plot the

triaxial equilibrium solutions of the previous chapter (Figures 4.5 and 4.9) as it effectively provides a view of the solutions looking along the direction of the spheroid line.

While we know that two cores on the same ξ/ζ line have x-y plane cross-sections the same overall shape, the actual size of the cross section and how it relates to the z-axis is dependent on its position along that line. The normalized axis ratios ζ and ξ describe a general ellipsoid with a z-axis ratio of 1, and so solutions with larger values of ζ and ξ are proportionately flatter than those with smaller values. A useful way to quantify this is with the area of the x-y plane cross-section:

$$\frac{A}{\pi} = \zeta\xi = \zeta_{\rm sph}^2, \tag{5.2}$$

where $\zeta_{\rm sph}$ is the axis ratio of the spheroid with the equivalent cross-sectional area. The larger the value of $\zeta_{\rm sph}$, the flatter the model is relative to the z-axis and vice versa. Curves of constant $\zeta_{\rm sph}$ appear as lines with a slope of 1 on the shape maps, meaning they meet the ξ/ζ lines at right angles (shown in Figure 5.1). These two quantities effectively rotate the shape map 45°.

An additional benefit of quantifying the cross-sectional area in terms of $\zeta_{\rm sph}$ is that it allows for direct comparison with the plots of spheroidal equilibria in the previous chapter (Figures 4.5 and 4.10). We note, however, that two cores with the same $\zeta_{\rm sph}$ can look very different depending on their ξ/ζ values. For example, cores with large $\zeta_{\rm sph}$ appear like disks on the spheroid line, but become cigar-like (simultaneously flat and narrow) the smaller their ξ/ζ is. Additionally, when we refer to core "flatness" we are referring specifically to the core's geometry relative to its z-axis (and correspondingly its initial magnetic field direction).

5.2 Hourglass Models

The left plot of Figure 5.2 shows the range of ζ and ξ values permitted by the virial restriction. As before, we have adjusted the parameters such that $\zeta > \xi$. The rightmost plots in Figure 5.2 plot the squeeze parameter c against the area-equivalent axis ratio $\zeta_{\rm sph}$ (top) and azimuthal axis ratio ξ/ζ, producing plots analogous to the corresponding plots in Figure 4.5.

While the $R_{ii} \approx 0$ results (see Figure 4.5) were entirely contained in the oblate region of the plot, the looser restriction on R_{ii} values has allowed for cores with triaxial oblate, triaxial prolate, and "in-between" geometries ("neither" category in the shape map of Figure 5.2), with the outer boundary in these regions being identical at all pressure steps. The tip of the furthest extent of the common boundary into the prolate region occurs at $\zeta_{\rm sph} \approx 0.65$. This $\zeta_{\rm sph}$ value appears to indicate a minimum out to $\xi/\zeta = 0.89$, but this may be an artifact

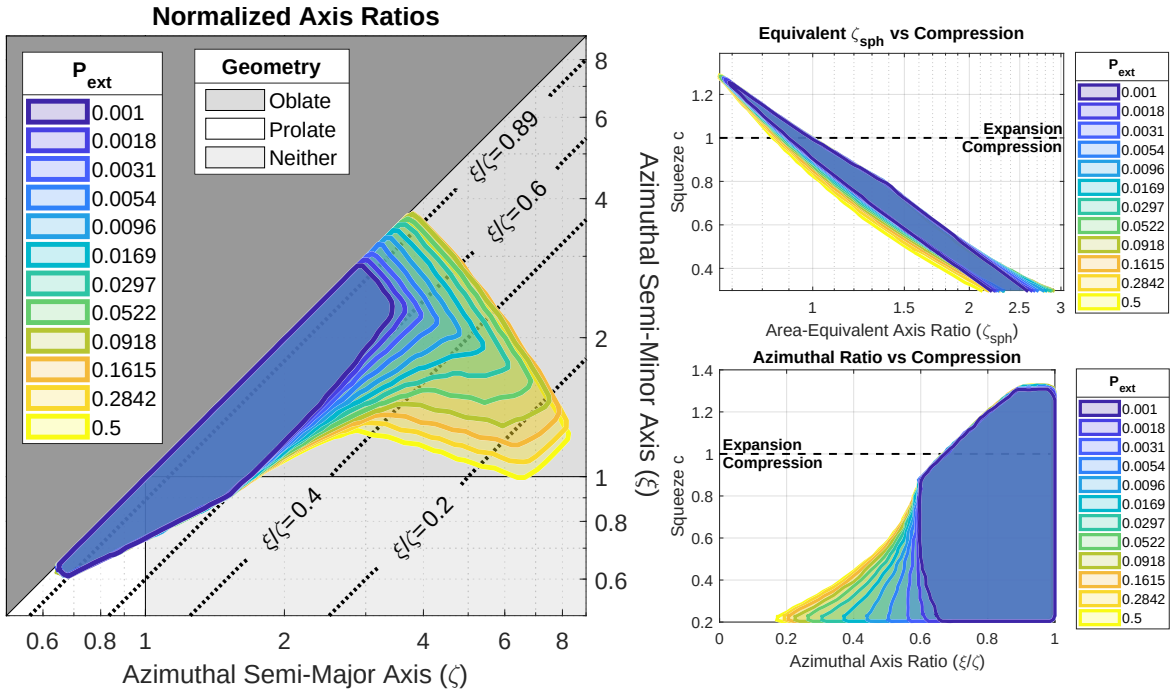


Figure 5.2: Plots mapping the allowed range of shapes for $R_{ii} \leq 0.2$. Regions are plotted with transparency due to overlap, with solid lines representing the outer bounds. Left: Map of normalized triaxial axis ratios, adjusted for azimuthal degeneracy. Top Right: Squeeze c plotted against $\zeta_{\rm sph}$, which expresses each set of (ζ, ξ) as the axis ratio of a spheroid with an equivalent x-y cross-sectional area and describes the degree of flatness relative to the z-axis. Lines of constant $\zeta_{\rm sph}$ are perpendicular to the spheroid line $\zeta = \xi$. Bottom Right: The azimuthal axis ratio ξ/ζ relative to c.

of our table resolution. Effectively, this means that there are no spheroidal or triaxial cores more elongated than this for this range of R_{ii} values. From the tip, the solutions remain prolate-like, until the ξ/ζ reaches 0.6 at the boundary between the in-between and oblate regions of the plot. As the cores get flatter from this point, the borders diverge, with the solutions belonging to higher pressure steps expanding out into smaller values of ξ/ζ.

At large values of $\zeta_{\rm sph}$, the maximum ζ value along the spheroid line has expanded only slightly from its equilibrium value into more flattened shapes. From this new end point, the border solutions expand out approximately perpendicular to the spheroid line, reducing slightly in $\zeta_{\rm sph}$ as they reach their minimum ξ/ζ. As the pressure increases (truncation radius decreases) the top edges of the regions widen out into thicker versions of the triaxial "wings" present in the high-pressure steps of the balanced case (Figure 4.5).

Both of the plots on the right side of Figure 5.2 show a range where all pressures share a common upper boundary. For the top plot, this is defined between $\zeta_{\rm sph}$ values of 0.63 and 1.4 where $c \geq 0.8$. In the bottom plot, the shared outer edge above $c = 0.87$ ranges between

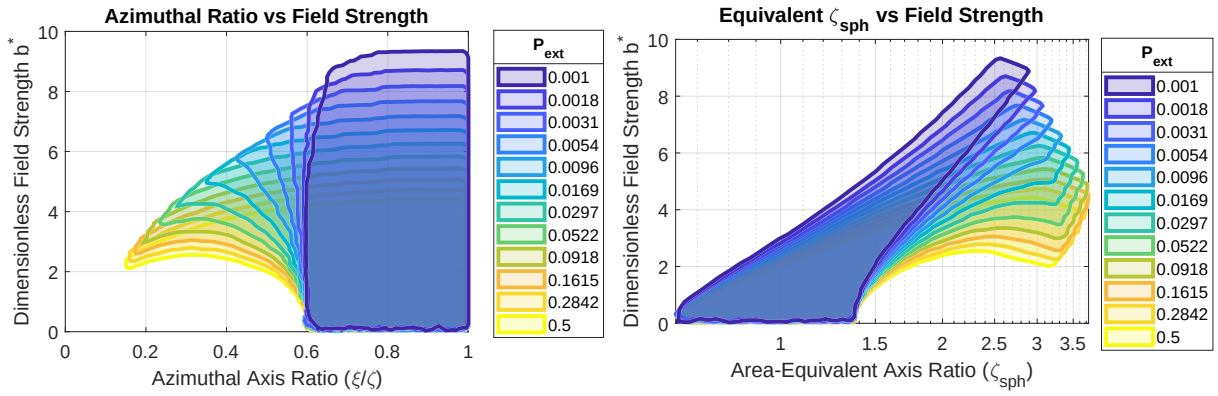


Figure 5.3: Borders of the dimensionless magnetic field strength b^* as a function of azimuthal axis ratio (left) and adjusted ζ (right).

azimuthal ratios of $0.6-1$. The range of $\zeta_{\rm sph}$ and ξ/ζ values in these two plots maps directly to same common border in the prolate/neither region of the shape map.

The top-right plot of Figure 5.2 shows that the range of c values widened only slightly from the balanced case, despite the large variance in azimuthal axis symmetry. The regions as a whole resemble a needle, tapering toward a "tip" at higher c values and lower $\zeta_{\rm sph}$ values. The solutions follow the same trend as the equilibrium case, where the diskier the solution, the more compressed it must be to stay within the acceptable range of R_{ii}.

Figure 5.3 shows two views of how b^* varies with shape. The plots show a common range at $b^* = 0$ of $0.6-1$ in the ξ/ζ plot (left), and $0.63-1.4$ in the $\zeta_{\rm sph}$ (right). This is the origin of the common boundaries exhibited in all three plots in Figure 5.2. To have $b^* = 0$, the scalar gravitational potential energy must exactly balance the two kinetic terms. The two kinetic terms are only dependent on pressure, and the gravitational term is dependent on both pressure and shape. The fact that the same boundary in ζ, ξ, and c appears at every pressure step indicates that these geometries always balance the kinetic energy regardless of truncation pressure (surface radius). Outside of this boundary, solutions in scalar virial equilibrium no longer exist because there is no positive value of b^{*2} that balances the equation. This would seem to indicate that highly filamentary structures with their field structures oriented parallel to their long axis are not near virial equilibrium, which is not generally true. However, we note that this analysis only encompasses cores with a Bonnor-Ebert density profile and a non-twisted hourglass field, and we expect filaments to have different density profiles to cores.

At all pressure steps, the model geometries with the largest magnetic field strengths required to balance the virial equation were spheroids with the maximum amount of compression (minimum c). The peak values occur for the model in this range with the smallest

value of $\zeta = \xi$, and the field strength drops as the spheroids become flatter. The field strength also decreases as the cores become more azimuthally eccentric (ξ/ζ decreases), and the range of b^* values becomes quite thin. This masks that the range thins with diskier shapes at the highest pressure steps in the b^* vs $\zeta_{\rm sph}$ plot.

5.3 Twisted Hourglass Models

Figure 5.4 shows plots similar to those in Figures 5.2 and 5.3 stepping through ${C_t}^*$ for maximum, minimum, and two in-between pressure steps. The turnover point where "holes" in the high-twist steps at $P_{ext} = 0.1615$ are appearing in the b^* vs $\zeta_{\rm sph}$ plots is where the solutions are thinned out by the scalar aggregate of the magnetic terms in the virial equation (§4.5.2) crossing the origin, which causes a numerical discontinuity. The much larger gaps in the corresponding $P_{ext} = 0.5$ regions in the corresponding plot are due to where the peak of the c curve lies outside the parameter range. From the shape maps (Figure 5.4, top row) as the twist increases from 0 to around 0.65, the top left boundaries (highest $\zeta_{\rm sph}$, diskiest solutions) move towards more spherical geometries, while the range of solutions protruding into the prolate and in-between regions stays fixed. Once the twist increases past this point, the solutions protrude further into the prolate region while the top border stays more-or-less fixed just inside the oblate region. This top border represents the maximum border of the region where ${b^*}^2 = 0$.

The wide triaxial "wings" behave the same way as their corresponding equilibrium cases, sweeping forward and vanishing as the twist increases. At the highest pressure step, where the wings survive for the largest range of ${C_t}^*$ values, the width of the wings becomes narrower in ζ as ${C_t}^*$ increases, but wider in c until the wings vanish. In the equilibrium case, for pressures less than 0.2, cores in the triaxial wings become more compressed as ${C_t}^*$ increases (Figure 4.9), which is also seen here. For pressures greater than 0.2, the equilibria became more azimuthally eccentric while the c value increased (less compressed) before the wings vanished. The same behaviour is exhibited here, except it has also resulted in a widening of the range of c values in the wings as the twist increases. Once the c values start to dip down (as seen in the bottom right panel of Figure 4.9), the lower c boundary of the wing appears to dip out of range until the wings disappear.

When b^* is plotted against $\zeta_{\rm sph}$ and c in three dimensions, it can be seen that when the curves turn into the prolate region of the plot, the appearance of the regions in the $\zeta_{\rm sph}$ vs c plots are due to the solutions in this projection forming a "ribbon" that twists over on itself as $\zeta_{\rm sph}$ decreases and b^* increases. The hard boundary at the top of the "needle" caused by ${b^*}^2$ crossing the origin remains fixed at the same coordinates in $\zeta_{\rm sph}$ and c. This result

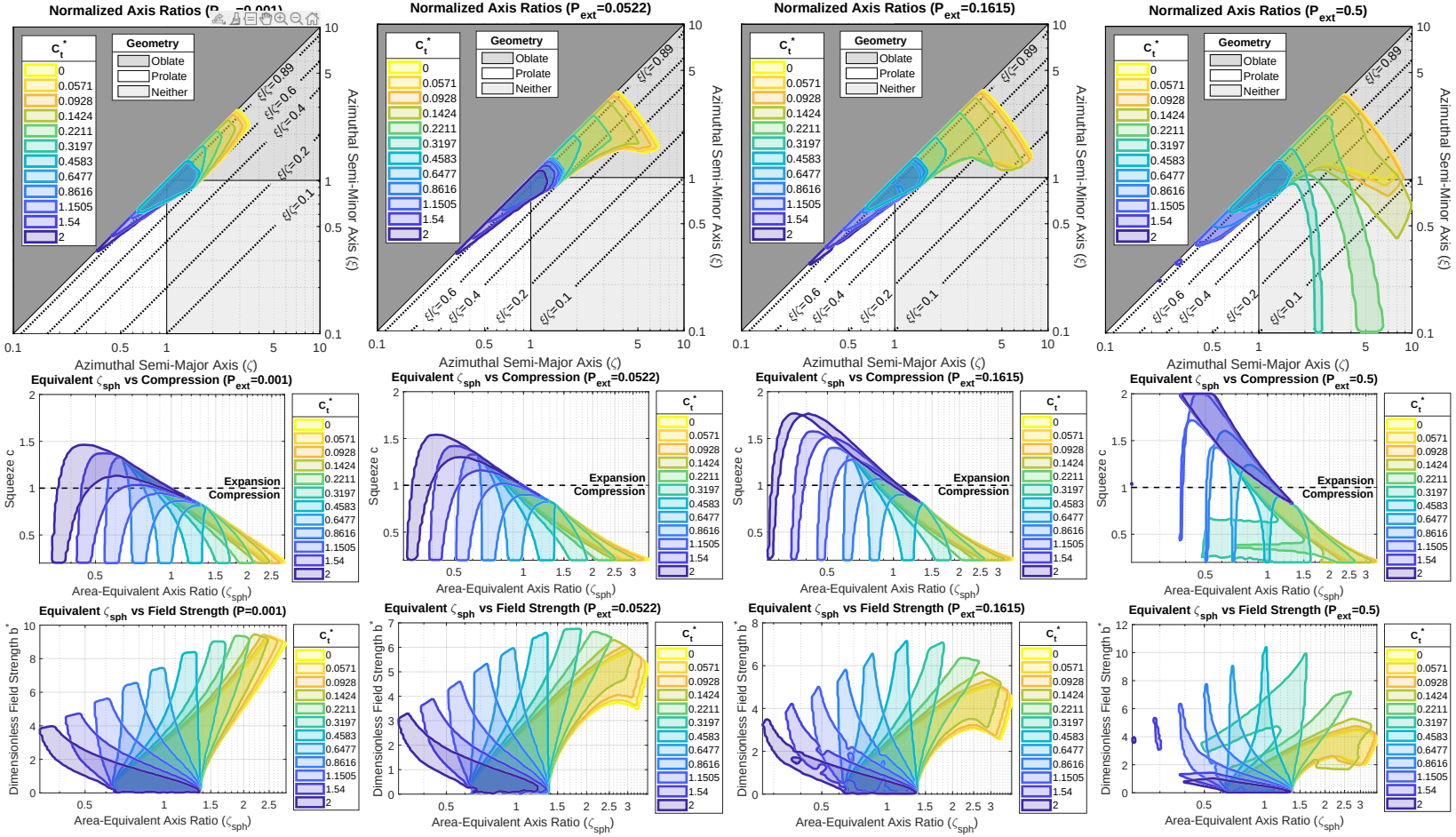


Figure 5.4: Approximate outer bounds of the normalized x-y plane axis ratios for four pressure steps at multiple values of C_t^*. The colourmap is inverted with respect to Chapter 4 as the layering with the original colourmap made the regions more difficult to distinguish. "Holes" in the high-twist steps at $P_{ext} = 0.1615$ are appearing in the b^* vs ζ_{sph} plots is where the solutions are thinned out by the scalar aggregate magnetic tensor crossing the origin, which causes a numerical discontinuity.

is expected, since this condition is caused by the trace of the gravitational potential energy balancing out the kinetic terms independent of the magnetic field geometry.

At all pressure steps, as the twist increases the magnetic field strength also initially increases. Once the twist increases past a certain point, the maximum b^* progressively decreases (Figure 5.4, bottom row). The precise twist step where this occurs changes with truncation pressure, with the critical ${C_t}^*$ increasing with increasing pressure. Between pressures of 0.001 and 0.1, the maximum value of b^* for each pressure step decreases from a value of ≈ 9.5 to ≈ 7. At higher pressures it gradually increases to a maximum value of ≈ 10 at $P_{ext} = 0.5$

For each individual pressure step at low ${C_t}^*$ values, the model geometry with the largest dimensionless field strength is the roundest spheroid with the minimum c value as in the hourglass case. Once the twist hits approximately ${C_t}^* = 0.3$, the peak model switches to the flattest spheroid with the minimum c value.

5.4 Discussion

We originally developed this virial constraint as a way to exclude unphysical geometries from PolCat fits. Previously, the only method we had of assessing whether a core was "unphysical" was to accept or reject models by visual inspection of the geometry. Thorough examination of the geometries within the virial criterion limit have revealed that some very eccentric models that would have been rejected through visual inspection are theoretically physically possible. However, these only appear at high pressures, we have only examined pressures up to 50% of the peak of the profile. Interestingly, the population of solutions in the triaxial wings for the hourglass models (Figure 5.2) shows similar cross-sectional structure to the self-consistent filament models with perpendicular field direction of Tomisaka (2014). We note however, that in Tomisaka (2014) the equilibria were computed in cross-section for infinite cylinders rather than the finite filamentary cores we are seeing in the triaxial wings.

Overall, the compression parameter c appeared to have the largest effect on b^* at any pressure step (and twist), with the solution with the highest b^* also having the minimum value of c in all cases. This is due to the trace of the unscaled magnetic field tensors being orders of magnitude smaller than the trace of the gravitational tensor, which also grows much faster in magnitude as c decreases than the aggregate magnetic terms. As a result, b^* needs to increase in magnitude to balance the virial equation.

The result of the magnitude of b^* being larger for rounder cores in the hourglass case is perhaps counterintuitive. For this field geometry, oblate shapes are expected due to preferential contraction at the poles (absence of Lorenz force), and a corresponding resistance

to contraction at the equator. It would therefore be expected that *flatter* geometries would indicate a stronger magnetic field at equivalent compression and truncation pressure, but that is not the case here. However, since the models are computed by mechanically contracting a uniform density and magnetic field into the final configuration, the flatter models are actually *less* contracted about the equator relative to the rounder model, leading to a smaller magnetic field strength.

As the magnetic field twist increases, the dot-product between the field direction and the normal to the flux tube cross-section ($\mathbf{B} \cdot \mathbf{A}_{\rm flux}$) decreases. While the flatter core has a more-expanded equator compared to the rounder model, the expansion at the equator increases the angle the twisted field makes with the flux tube cross section. Once $C_t{}^*$ is greater than ≈ 0.3, this effect dominates over that of the equatorial contraction, and the peak geometry switches.

However, we do note that this method assumes that cores are in *scalar* virial equilibrium to derive the magnetic field strengths, and this is not likely to be the case for general molecular cloud cores. As such, the geometries determined by our method represent a "best case" scenario. Future expansion into this area of the analysis could explore changes to the model families when the magnetic tensor components are scaled by independent estimates of magnetic field strength using Zeeman measurements or the Chandrasekhar-Fermi method. However, this is beyond the scope of this work.

Chapter 6

Virial Balance as a PolCat Fitness Penalty

The simplest method to restrict the Ferret solutions to the desired tensor virial factor is with a penalty function, such as those we already apply for centering, surface intersection, and fitness threshold as described in Section 3.2.4. For solutions that fail the penalty check, we add an arbitrarily large value scaled by $(1 + f)$ to all the fitness values, where f is a factor that scales with discrepancy from the desired quality.

The virial penalty function follows this basic procedure:

- Use the Ferret parameters to interpolate the relevant tensor quantities and traces,
- Solve equation (4.30) to compute ${b^*}^2$ (and use model parameters to compute b_0),
- Compute equation (4.31),
- Compute R_{ii} (equation (5.1)) by normalizing each ${VE_{ii}}^*$ by the corresponding $\frac{1}{4\pi}{W_{ii}}^*$.

Then we calculate a conditional "distance" from our desired threshold (in this case, 0.2) for all three axes,

$$d_{ii} = \begin{cases} 0 & \text{if } R_{ii} \leq 0.2, \\ |R_{ii}| - 0.2 & \text{if } R_{ii} > 0.2. \end{cases} \tag{6.1}$$

We then add the three "distances" together. Occasionally, solutions require an unphysical, negative ${b^*}^2$ (as defined in (4.30)) in order to be in scalar virial balance. This happens when the total magnetic terms have opposite sign to the sum of the kinetic and gravitational terms. Because there does not exist a solution that is in scalar viral balance in these cases, we penalize this condition as well. Instead of using the negative value to compute the tensor components, we set ${b^*}^2$ to its absolute value. This causes the trace to be non-zero, and we

add a fourth quantity to the penalty, d_{tr}, equivalent to the absolute value of the trace of equation (4.31) normalized by the corresponding factor of $\frac{1}{4\pi}\sum {W_{ii}}^*$. The virial penalty function is therefore

$$P_{vir} = P_{min}\left(d_{xx} + d_{yy} + d_{zz} + d_{tr} + 1\right). \tag{6.2}$$

The value P_{min} is the minimum scale of the penalty, which we determine by calculating the mean of the square of each stokes vector dataset map to its corresponding variance map, and taking the maximum of the three. Since this factor is much larger than the factors we were previously using for the other penalty functions described in Section 3.2.4.1, we adjusted those to the same scale (with the exception of the fitness penalty, which we did not apply in this case). The following sections present the results of fits both with and without this new penalty, for both test data (§6.1), and two polarization datasets of the region OMC-1 BN/KL (§6.2).

6.1 Fits To Test data

To test the efficacy of applying the virial restriction as a penalty, we first ran fits to test data, similar to the analysis of Chapter 3. However, we decided to update the density model to provide a more natural external envelope profile, rather than the flat envelope profiles we have used previously (§3.5.1 and §4.2.2).

6.1.1 Composite Bonnor-Ebert Sphere Transformation (CBES)

The BES model produces a core with a Bonnor-Ebert density profile embedded in a constant-density envelope. While this is an acceptable model, we felt the flat envelope was unrealistic. In order to produce more realistic envelope models, we switched to the composite polytropes of Curry and McKee (2000), and used their construction of an isothermal core embedded in a warmer isothermal envelope. This model's envelope attenuates naturally while allowing the core region to remain distinct. However, we note that Curry and McKee (2000) develop their composite core-envelope models as further bounded by a tenuous external medium and specifically search for critically stable solutions under these conditions. We are instead simplifying the model by treating the core-envelope interface as the "surface" with the envelope taking the role of the "flat" external density in the BES model, and not searching for specific critically stable solutions.

The central core ($r' < r'_s$) uses the same stored Bonnor-Ebert solution as the BES transformation and the virial tables, and the envelope is computed separately using the same unscaled dimensionless coordinates defined in Section 4.2.2, computed outward from the

truncation radius defined by P_{ext}. The radial transformation outside the truncation radius is computed via equation 3.6.

At the surface interface, the boundary conditions are

$$g'_{\rm env}(r^*{}_s) = g'_{\rm core}(r^{*\prime}{}_s)/\tau \tag{6.3}$$

$$\Phi'_{\rm env}(r^*{}_s) = \Phi'_{\rm core}(r^{*\prime}{}_s) + 2\ln\tau \tag{6.4}$$

$$\rho^{*\prime}{}_{\rm e} = \tau \tag{6.5}$$

where $\tau = T_{\rm env}/T_{\rm core} > 1$ (Curry and McKee, 2000). The density profile of the envelope is $\rho^{*\prime}{}_{\rm env} = \rho^{*\prime}{}_{\rm e} = \tau\exp(-\Phi')$. This expression originates from the well-known analytic solution of equation (4.4b). We then rescale the resulting core-envelope system in the same fashion as Section 4.2.2. With the above parameterization, we are left with a three-parameter model in the central density scale ρ_c, the truncation pressure as a fraction of the central pressure P_{out}, and the jump parameter τ.

6.1.2 Test Data Generation

As in Chapter 3, we performed a series of fits to test data generated from a series of "seed models." We selected four triaxial geometries from the population of VEFit solutions where the diagonal elements of the virial balance tensor VE_{ii} were within 0.2 of the gravitational value. Using these as a base, we generated models with the Bonnor-Ebert core profile, but changed the envelope from a flat profile to a naturally attenuating one, based on the composite polytrope model of Curry and McKee (2000) (see Section 6.1.1). This resulted in four "seed models" which we refer to as individual "cases" as in §3.6:

Case 1: an oblate triaxial core with an hourglass magnetic field,

Case 2: an approximately spherical core with an hourglass magnetic field

Case 3: a triaxial core with $\zeta > 1$ and $\xi < 1$ with a helical hourglass magnetic field

Case 4: an approximately prolate spheroid core with a helical hourglass magnetic field.

Cases 2 and 3 fall into the "neither" geometry class defined in §4.2.3. Figure 6.1 shows the three-dimensional structure of each test model geometry.

Each of the virial-criterion seed models shared common ρ_c and τ CBES-component parameters, with ρ_0 and σ_0 parameters selected to scale the core properly in the model grid. We generated two test datasets for each of these seed geometries, one where all orientation angles were set to zero, which we hereafter refer to as "VO", and one where the azimuthal

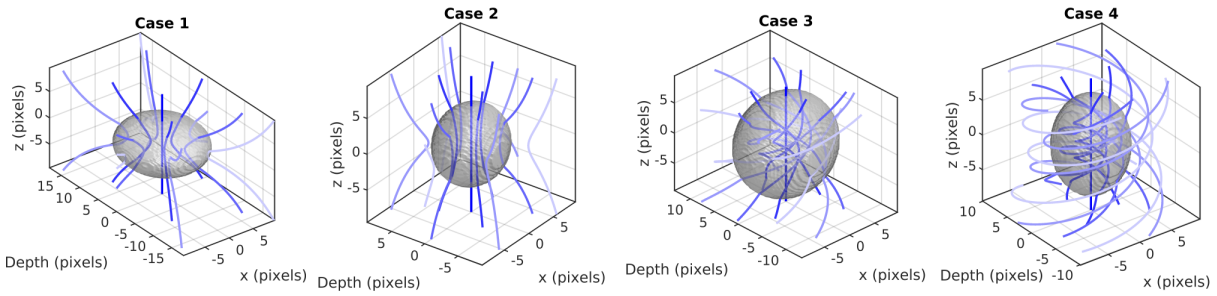


Figure 6.1: Three-dimensional representations of the four seed model geometries (specifically the VO models). Despite changes in parameters between the VO and NC/NE models, the overall core and field geometry of both are identical due to careful parameter scaling.

and inclination angle were set to unique values, which we hereafter refer to as "VA". The parameters for these four test data cases are summarized in Table 6.2.

However, since all of these sets are in virial equilibrium to begin with, we also wanted test datasets from cores that did not meet the virial criterion for comparison. Exploration of the parameter space showed that the parameter that had the strongest effect on the balance was the z-compression parameter c. Depending on the starting geometry, changing the c value significantly could result in an unphysical negative value of b^{*2} (due to the requirement that the core be in scalar equilibrium). These solutions would automatically fall into the penalized region of the fit.

To contrast with the virial-balanced sets, we took each of the four virial cases and changed c to make the core fail the virial check (i.e. at least one axis with $|R_{ii}| > 0.2$). We generated two non-virial seed models where c was either smaller ("NC," more compressed), or larger ("NE," expanded) than the original, with at least one of those selected to give a negative b^{*2} value. Under the virial criterion, such models would be penalized. Changing the z-axis stretch c necessitates adjusting the central density scale ρ_c by multiplying by a factor of c_{new}/c_{old} to keep the core the same size as the original virial dataset in the model grid. For simplicity, these test datasets were generated only at the same unique orientation angles as their corresponding VA set. Therefore, each of the four geometric cases has four corresponding test datasets: VO and VA – the two within the virial limit – and NC and NE – the two not within the limit.

For each of the resulting geometries, we generated artificial polarization data using the method we outlined in Section 3.6.2. These maps have added noise, and so we can calculate fitness values between each map and its generating seed model for comparison with the FERRET results.

For each test dataset, we ran four tests: 1) fit to hourglass field with virial mode turned

on and 2) off, and 3) fit to twisted hourglass field with virial mode turned on and 4) off. Each of these tests were run a minimum of three times and combined into a single solution set. All runs penalized fitness values above 25 for the reduced χ^2 for intensity, and 10 for the reduced χ^2 of the polarization position angle.

For these fits, we enabled simultaneous X- and F-niching. The niching settings in FERRET help fill out the fitness curve by calculating the number of nearest neighbours for each solution, and favouring the solution with the smaller number when in competition with other equivalently Pareto-optimal solutions (§3.3). With X-niching, this nearest neighbour calculation occurs in the parameter space, and with F-niching it occurs in the objective space.

6.1.3 Tweaks to PolCat

After some preliminary tests, we made some modifications to the TA_CBE_Sq_Sh template (twisted hourglass). In general, we do not favour highly twisted models (i.e. models where the field direction makes ten or more complete revolutions before hitting the core surface), so we changed the fit of the twist parameter from linear to logarithmic to encourage FERRET to more thoroughly map smaller values.

Another consideration was that the virial tables were dependent on the normalized twist parameter $C_t^* = C_t \rho_c^{-1/6}$, which is more representative of the number of twists in the field than C_t is, due to how it is affected by the central density scale. Additionally, since the virial tables specify limits on C_t^*, it is less efficient to fit in terms of C_t as it is impossible to restrict the fitness range to the table values for the same reason. In order to fit C_t^* rather than C_t, we needed to make a change to POLCAT's parameter assignment framework, to allow parameters to be expressed as functions of the values from FERRET, without hardcoding it directly into the transformation functions. Once we made this change, we were able to fit C_t^* directly.

6.1.4 Results

6.1.4.1 Fitness curves

Because we are running FERRET with multiple objectives, the solutions in the final set populate a "trade-off curve" – a surface where an attempt to further improve any one of the fitness values produces a corresponding degradation in the others. Typically, this surface has a sharp turning point, commonly called a "knee," where the solutions have achieved a decent balance between the fitness objectives.

Dataset		Parameter Values										Fitness	
Case	Type	ρ_0 (g cm^{-3})	σ_0 (km s^{-1})	$C_t{}^*$ (rad/$z^{(0)}$)	ρ_c	τ	P_{out}	ζ	ξ	c	ϕ (°)	i (°)	F_I	$F_{\chi_{pol}}$
1	VO	5.00E-20	1.339	–	150	5	0.0169	1.792	2.0146	0.4441	0	0	1.2166	0.9458
	VA	5.00E-20	1.339	–		5	0.0169	1.792	2.0146	0.4441	65	12	0.9652	1.1869
	NC	5.00E-20	1.339	–	93.1616	5	0.0169	1.792	2.0146	0.35	65	12	1.031	1.1333
	NE	5.00E-20	1.339	–	372.6463	5	0.0169	1.792	2.0146	0.7	65	12	1.297	1.0679
2	VO	2.00E-20	2.3304	–	150	5	0.1615	0.9999	0.8812	0.9967	0	0	0.9625	1.1087
	VA	2.00E-20	2.3304	–		5	0.1615	0.9999	0.8812	0.9967	80	24	1.1178	0.9717
	NC	2.00E-20	2.3304	–	96.6453	5	0.1615	0.9999	0.8812	0.8	80	24	1.091	1.0389
	NE	2.00E-20	2.3304	–	217.4518	5	0.1615	0.9999	0.8812	1.2	80	24	0.9905	1.1323
3	VO	2.00E-20	1.0008	0.6477	150	5	0.0169	1.0493	0.8818	0.6866	0	0	1.0235	1.1874
	VA	2.00E-20	1.0008	0.6477		5	0.0169	1.0493	0.8818	0.6866	50	33	0.9939	1.1784
	NC	2.00E-20	1.0008	0.6477	50.9104	5	0.0169	1.0493	0.8818	0.4	50	33	1.2231	1.0299
	NE	2.00E-20	1.0008	0.6477	385.0099	5	0.0169	1.0493	0.8818	1.1	50	33	1.022	1.2486
4	VO	5.00E-21	0.5977	1.54	150	5	0.1615	0.7367	0.7404	1.2685	0	0	1.0188	1.1772
	VA	5.00E-21	0.5977	1.54		5	0.1615	0.7367	0.7404	1.2685	21	58	0.9108	1.5601
	NC	5.00E-21	0.5977	1.54	93.2231	5	0.1615	0.7367	0.7404	1	21	58	1.1544	1.2604
	NE	5.00E-21	0.5977	1.54	182.7173	5	0.1615	0.7367	0.7404	1.4	21	58	0.9526	1.4684

Table 6.1: Parameters and templates used to generate the seed models for the test data. RotateA position angle PA is set to zero in all cases.

Overall, the minimum fitness values for intensity corresponded closely with those of their corresponding seed models, while the knees favoured slightly larger values of F_I. Some model geometries actually had smaller values of $F_{\chi_{pol}}$ than the seed model, which was common from other tests we have previously run (§3.6). However, the knee solutions had RMS error values between 1-2 times those between the seed model and the test dataset, but this was typically within 10^{-2} of the scale of the average map intensity. The RMS error for χ_{pol} values was almost exactly in line with the seed model, except in the case of hourglass (ie. non-generating template) fits to Cases 3 and 4. These showed RMS error angles of between approximately 35-55°, whereas the seed model had values of around 15°.

Tests run using the virial criterion typically had little influence on the fitness curves for Cases 1 and 2 (hourglass). The merged solution fitness curves overlaid the corresponding non-penalized fit with the same template. When applied to the hourglass template, there was typically no overall improvement over the non-penalized run. The exceptions were fits to Case 2 (approximately spherical) with the twisted template. For the VA and NC datasets the non-penalized twist model had a much worse fitness value, whereas the penalized run overlaid the two hourglass fits. The penalized fit to the NE dataset had improved $F_{\chi_{pol}}$.

Fits of the hourglass model template to test data for Cases 3 and 4 were universally poor. The face-on test data typically produced results that were within the fitness threshold, but the rotated sets never reached the fitness threshold for position angle. This indicates that regardless of virial fit, a dataset with an underlying field twist cannot adequately be fit to models that do not include one, repeating the results of Chapter 3.

Fits to the zero-rotation (VO) datasets of Cases 3 and 4 with the twisted hourglass model actually showed the best fits without the virial penalty. The virial-penalized run occupied the same area of the fitness space as the hourglass models. Otherwise, both solution sets with the twisted hourglass model were almost identical.

6.1.4.2 Azimuthal Geometry

For Cases 1 and 2, all solutions near the knee were able to find accurate ζ and ξ values while fitting with the seed model geometry (sans twist). Shape maps for these runs are the first two plots of the top row of Figure 6.2 (This includes the NC and NE datasets). The distribution of shapes overall for the Case 1 geometry were tightly clustered around the seed model parameters, whereas there was more spread in the Case 2 results. However, while the knees of the non-virial fits to the VO and NC datasets did not find the seed model shape, the knees of the penalized fits did.

Fitting these datasets with the twisted template (two leftmost plots in the bottom row of Figure 6.2) resulted in more variation in the selected shapes, and less accuracy in general

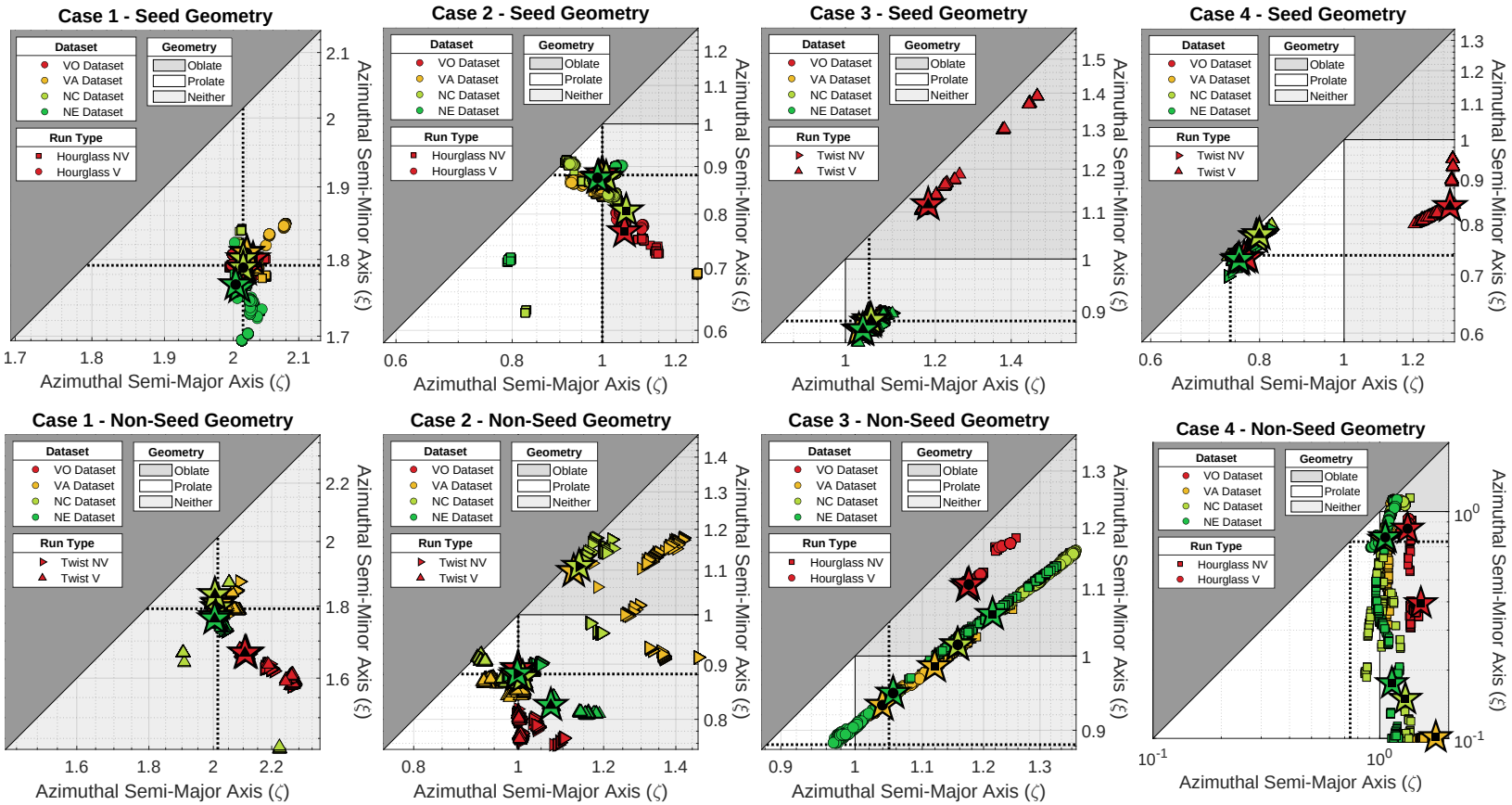


Figure 6.2: Shape maps for all test data geometries, adjusted for rotational symmetry. Fits to all four types of test data are shown. Fits to the seed models are in the top row, with fits to the corresponding non-seed models on the bottom. The dotted lines represent the seed values of (ζ, ξ). Note: the non-seed models for Cases 1 and 2 are able to reproduce seed model results with certain parameters, whereas this is not the case for Cases 3 and 4.

for the knee solutions for the non-penalized runs. In these cases, enabling the virial penalty led to better shape fidelity between the seed model and the knee regions of the solution sets.

The Case 3 and 4 fits with the twisted hourglass geometry also produced results clustered around the seed model shape, with the exception of the penalized VO datasets, which were both poor. However, poor shape matching to zero-inclination datasets was not an unexpected result, based on previous fits to test data (see §3.6.3.4). Additionally, inspection of the twist parameters for those two solution sets shows that they had twist parameters so small as to be practically non-existent, which likely influenced the direction of the virial parameters.

As expected, fits with the hourglass model did not produce core shapes in any way close to the seed values. This reinforces the results of Chapter 3, which found that a twisted field geometry cannot adequately be fit without a twist. However, the knee solutions for the penalized runs did appear to have more "reasonable" shapes. Interestingly, while all the Case 4 solutions ran more-or less along the line $\zeta = 1$, producing shapes that are very cigar-like, the Case 3 solutions mostly fell on a line of constant azimuthal symmetry ratio ξ/ζ. However, this line did not have the same ratio as the seed model.

6.1.4.3 Compression

Figure 6.3 plots the compression parameter c for all datasets relative to the area-equivalent spheroidal axis ratio $\zeta_{\rm sph}$ (§5.1), arranged transposed to Figure 6.2. Each plot also has the virial region from Figures 5.2 and 5.4 corresponding to their seed model P_{out} and $C_t{}^*$ values superimposed on the background.

For the Case 1 and 2 VO and VA datasets, the virial penalty tightly constrained the compression parameter to their seed values. The penalized NC solution set showed some slight expansion, and the NE set compression. This is consistent with what we would expect from the adjustment made to make the base models fail the virial check. The only non-penalized solution set that showed a knee solution with the same amount of compression was the fit to the NC dataset. The others were not constrained at all. The fits of these datasets with the twisted model showed similar results.

The seed geometry fits to Cases 3 and 4 were overall more tightly constrained in the azimuthal ratio, with the exception of the previously mentioned penalized fits to VO. The hourglass fits to these cases were wildly unconstrained, with very few of the knee solutions finding the seed model values. In Case 3, the penalized values for the VO and VA datasets skewed high, whereas the Case 4 results skewed low. Overall, the virial penalty did show slight improvement on the knee results.

While removing the virial constraint would have allowed fits to the NC and NE datasets to select their corresponding seed values of c, we find that in practice they did not. Even

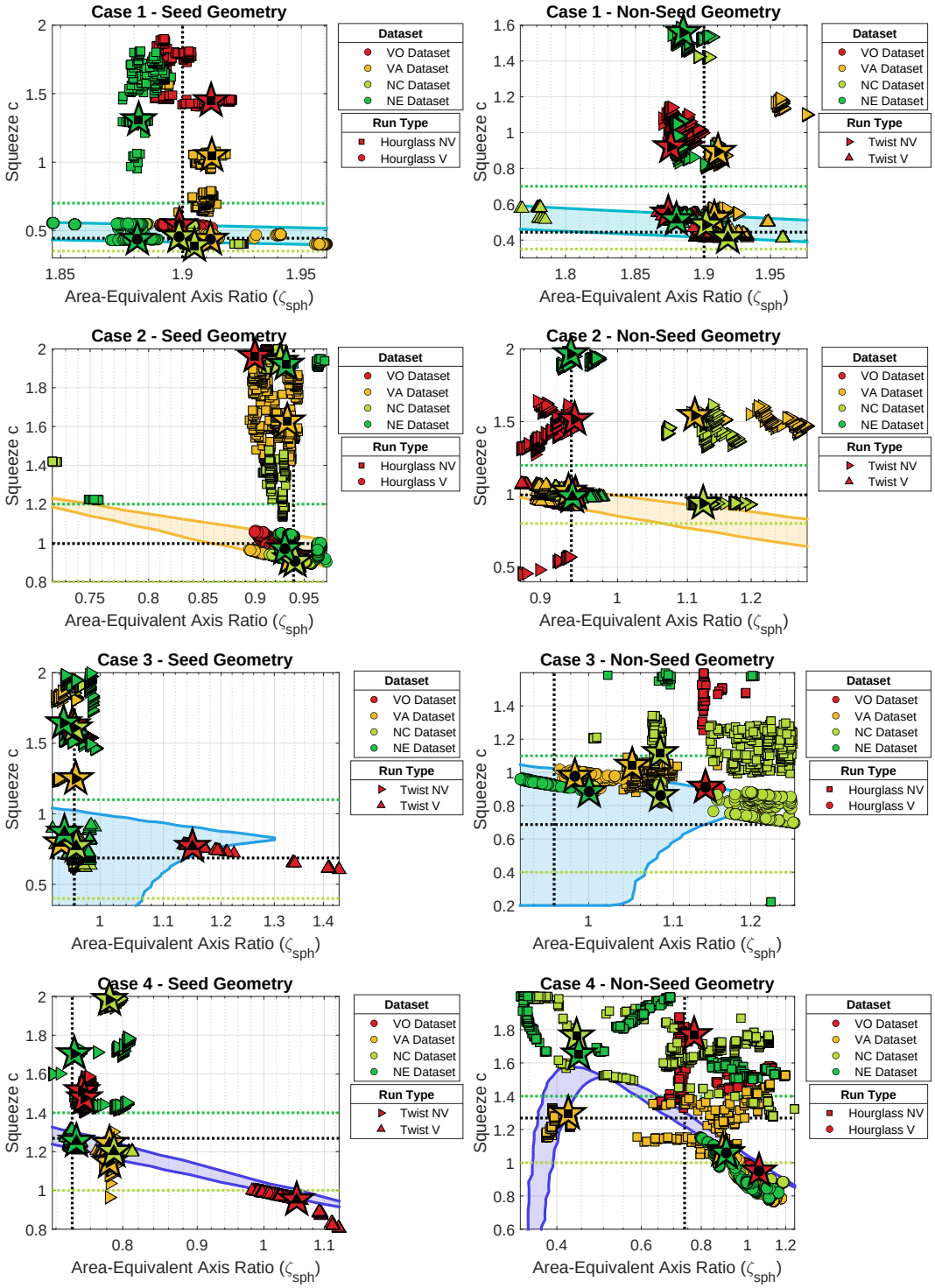


Figure 6.3: Plots of compression for all runs, c value versus area-equivalent axis ratio ζ_{sph} (§5.1). Each row represents a Case, with fits to the seed in the left column, and fits to the non-seed model geometry on the right. The shaded areas are the $|R_{ii}| \leq 0.2$ regions from Figures 5.2 and 5.4, corresponding to each Case's seed P_{out} and C_t^* values. Dotted lines indicate the seed model parameter values, with black indicating shared values.

when fit with the seed model geometry, none of the fits to the NC and NE datasets had c values that were close. Overall, the non-virial fits favoured larger values of c that indicated expanded geometries. Despite the virial constraint not allowing the seed values for the NE and NC datasets, the range of values allowed by the virial constraint provided a better estimate than the unconstrained fits.

The compression parameter affects the size of the core in dimensionless coordinates. Therefore, models with different compression compensate for the difference by adjusting the density and velocity dispersion scales to keep the core the same pixel size.

6.1.4.4 Density Profiles

To determine how well the solutions replicate the density structure of the seed models, several factors need to be taken into account. Firstly, the peak density of the final model not only depends on ρ_c, but also the overall density scale ρ_0. Additionally, because the squeeze transformation does not preserve volume, this results in the final peak density of the core being scaled by $1/\det(\boldsymbol{\mathcal{J}}_{squeeze})$:

$$\rho_{peak} = \frac{\rho_0 \rho_c}{\zeta \xi c^3}. \tag{6.6}$$

Consequently, this scaling also folds into the pressure (and the velocity dispersion σ_0 through the radial scaling) as well. Secondly, since the cores are all potentially different shapes with different compression values, the truncation radii of the core profiles do not necessarily line up.

In the analysis of Section 3.6.3.5, we defined a quantity α, which represented the amount of stretch the core experienced along the line of sight (hereafter LOS) from the transformations performed after the Bonnor-Ebert core density transformation. This quantity was obtained by applying the inverse RotateA and Squeeze coordinate transformations to a unit vector centred on the core parallel to the LOS. We then used the length ε of the resulting transformed vector to calculate $\alpha = 1/\varepsilon$. This factor affects the scaling of the intensity map, because the map involves integrating the three-dimensional core model along the LOS direction. The final fully scaled LOS surface radius is therefore $r_0 \alpha r_s$.

The results of Section 3.6.3.5 showed power law relationships between the LOS contraction α and respective peak density and pressure when they were normalized by their seed model values. While those runs showed identical power law relationships present in all runs to all test cores, this was not the case here. This is in part likely due to the substitution of the squeeze transformation for the scale transformation, since the squeeze transformation causes density enhancement. While some evidence of a power-law relationship exists from run-to-run for individual test datasets with a larger spread in normalized LOS r_s values, it

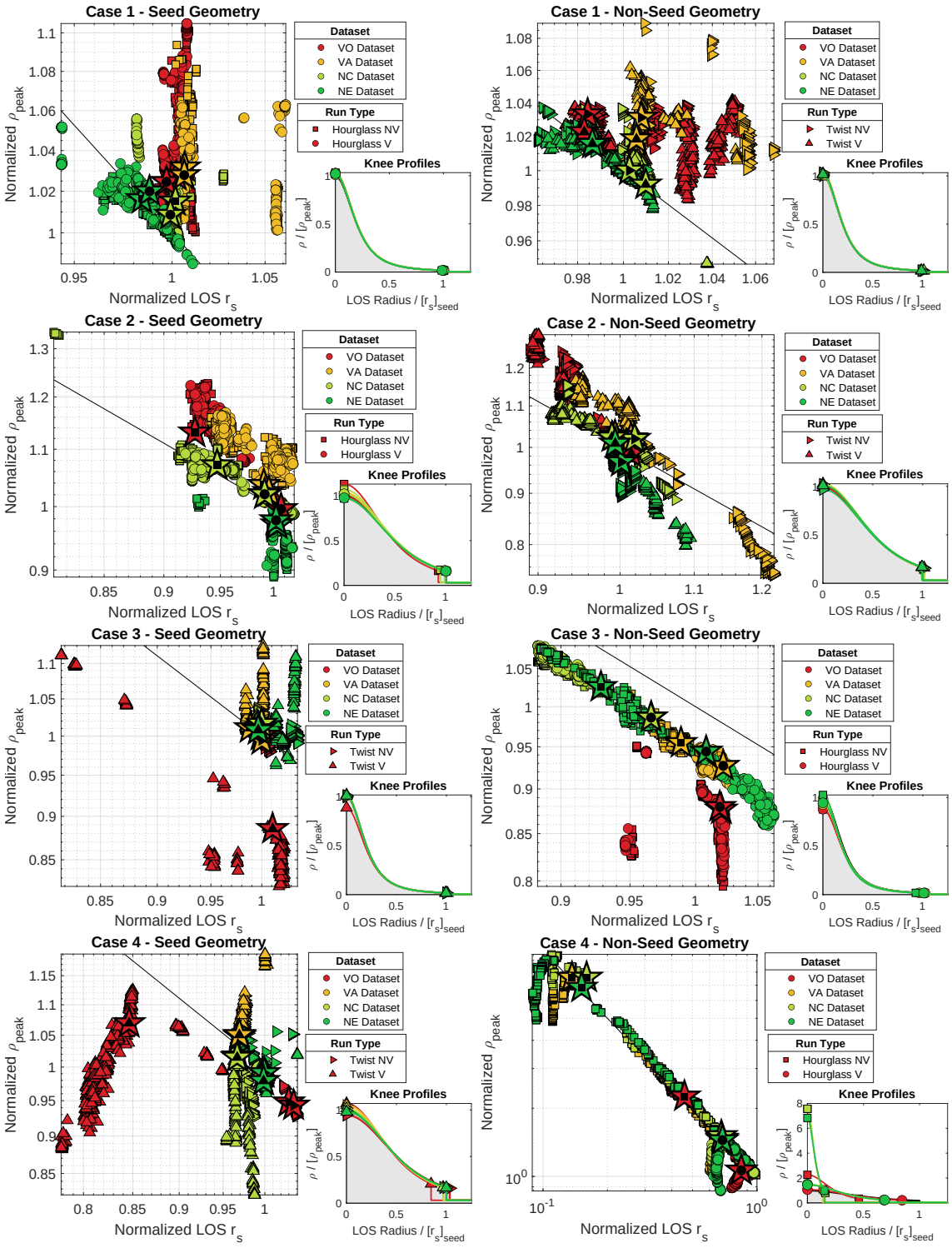


Figure 6.4: Plots of density and LOS truncation radius $\alpha r_0 r_s$ and knee solution LOS density profiles, normalized by respective seed model values. The solid black line in the plots represents the curve $\rho_{peak}/[\rho_{peak}]_{seed} = (R_s/[R_s]_{seed})^{-1}$. Radial values for density profiles are $\alpha r0r(\rho)/[\alpha r_0 r_s]_{seed}$. The shaded area in the density profile plots represents the seed model profile.

is not consistent between runs.

However, when we look at the density profile and scale the radius with α to represent the density profile along the LOS to the centre of the core, the radii line up. When the LOS compression is taken into account, the radius from the core's centre along the line of sight becomes $R = \alpha r_0 r$ where r in this case represents the profile used to calculate the three-dimensional transformation of CBES. The core's truncation radius becomes $R_s = \alpha r_0 r_s$. When we plot ρ_{peak} and R_s is normalized against the dataset's seed model values, all solutions approximately fall along the power law $\rho_{peak}/[\rho_{peak}]_{seed} \propto (R_s/[R_s]_{seed})^{-1}$, the LOS surface radius, except in the area approximately ± 0.2 around the seed model values. All solutions outside this area adhered to the power-law relation closely. Figure 6.4 plots the peak density versus LOS surface radius, normalized with respect to their respective seed model values, as well as density profiles of the knee solutions, normalized the same way.

For Case 1, all models fell within the ± 0.1 range of the seed values, meaning their core density profiles closely matched those of the seed model along the LOS direction. Case 2 was similar, but had a slightly wider overall range on the fits with the twisted hourglass model, but the knee solutions were tightly clustered around $(1, 1)$. Both sets of knee solutions produced good reproductions of the seed model density profile along the LOS.

Twisted hourglass fits to Cases 3 and 4 fit entirely between normalized ρ_{peak} ranges between ± 0.2 and normalized LOS r_s values of $0.79 - 1.04$. With the exception for the penalized VO outliers, the knee solutions were also very tightly clustered around $(1, 1)$. The hourglass fits were more disparate. For Case 3, with the exception of the penalized VO set, all of the solutions fell along a straight line on the log-log plot, with normalized ρ_{peak} approximately 0.05 lower than the $(r_s/[r_s]_{seed})^{-1}$ line, which appears to be a good approximation for all of the other fits. Nevertheless, the range of values is still within ± 0.2 and all the knee solutions produced good fits to the LOS density profile. The Case 4 fits fit more-or-less directly on the $y = x^{-1}$ line with normalized r_s values that ranged between approximately $0.1 - 1$. However, the penalized fits had the best results in the knee solutions, which also reasonably reproduced the LOS seed profile. Enabling the virial constraint here had a better effect on constraining the LOS density characteristics, despite field geometry permitted by the model.

6.1.4.5 Field Geometry

Overall, fits with the twisted model template were able to replicate the $C_t{}^*$ of the datasets. The exceptions were the non-virial fits to the Case 2 VA and NC datasets which had $C_t{}^* > 1$, with some models having $C_t{}^*$ as high as 5. The first result is consistent with previous findings from Chapter 3, where models with high field twists were able to replicate the polarization

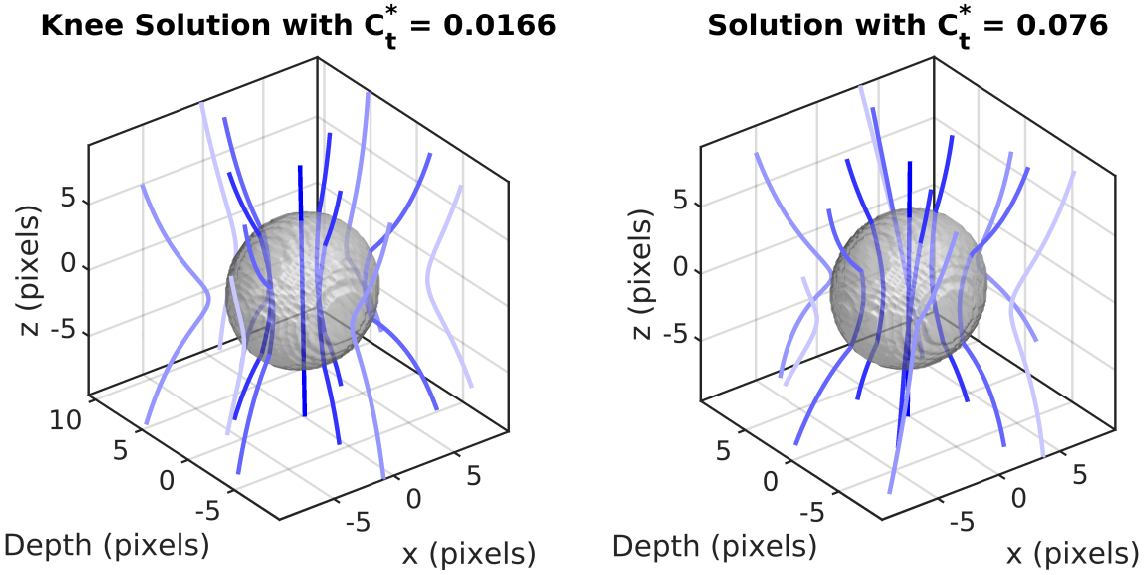


Figure 6.5: Two solutions from the non-virial Case 2 twist solution set. The knee solution is on the left and the solution with the largest C_t^* is on the right, to show the "drift" effect.

maps quite well. The other exceptions were the outlier virial fits to the Case 3 and 4 VO datasets, which selected C_t^* on the order of 10^{-2}.

Apart from the two sets in Case 2, the rest of the Case 1 and 2 fits produced results with C_t^* values of less than 0.1. Twists on this scale are barely detectable when viewed in three-dimensions. This presents like a slight "drift" in the field lines rather than a spiral (see Figure 6.5).

6.1.5 Discussion

While applying the virial penalty often did not have an effect on the fitness curves, there was some improvement in parameter constraint. Virial fits with the seed model geometry produced cores that were tightly clustered around the ζ and ξ values for the correct shape, and had generally better fits for compression. While almost all of the knee solutions were able to reproduce the line-of-sight density profile of the seed model, the virial fits did perform slightly better. The virial criterion typically had little effect on the twist parameter, but did select the correct twist when non-virial fits to the Case 2 VA and NC datasets produced high twist models. The only exception to this was the virial fits to the Case 3 and 4 zero-angle (VO) datasets, which selected C_t^* that were abnormally low.

While fits to the test datasets generated from the twisted hourglass model could not be adequately fit without the twisted field component (except in the zero-angle cases), enabling

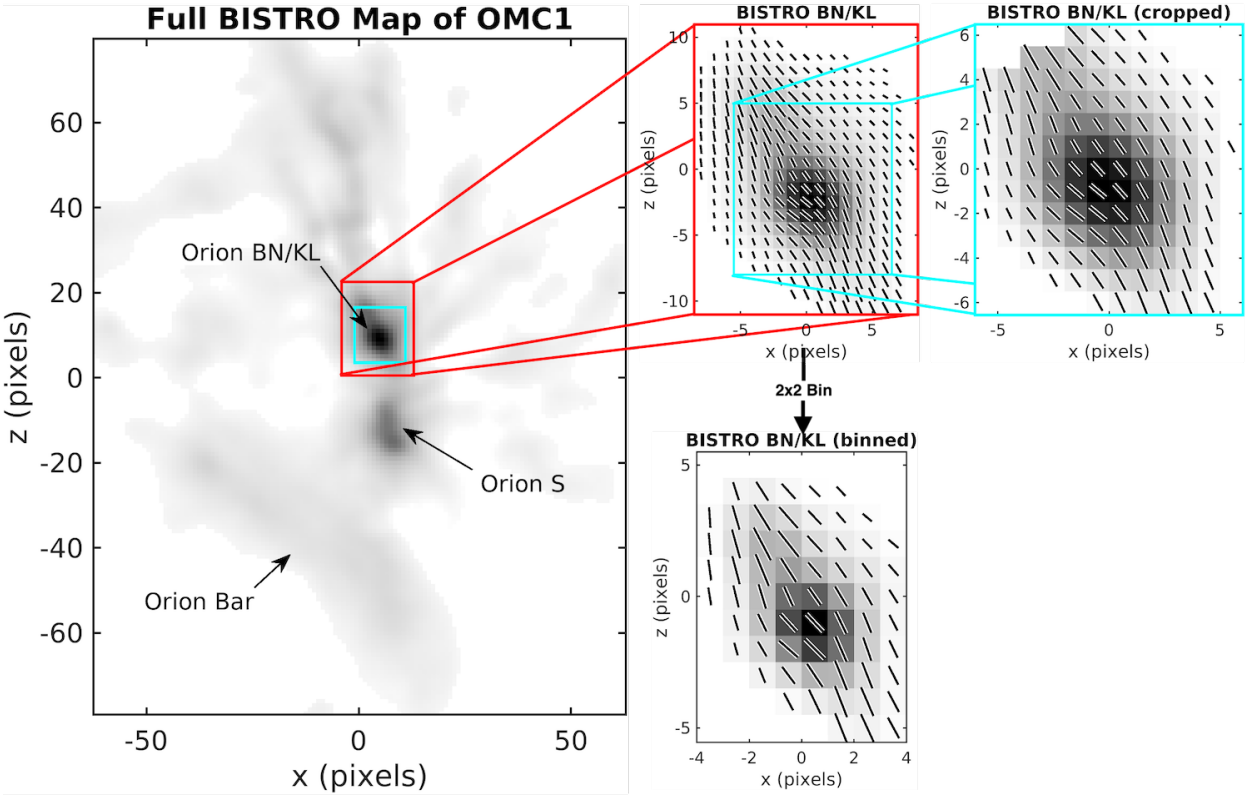


Figure 6.6: The full BISTRO OMC-1 intensity map with main objects labelled (left half) and datasets used for fitting (right half). The squares on the map of OMC-1 indicate the region boundaries of the full resolution dataset (red) and the cropped dataset (cyan). Vectors on the polarization maps are polarization **E**.

the virial penalty typically produced better fits to the azimuthal shape and compression in the knee regions. Additionally, it improved the fit to the line-of-sight density profile.

Fitting the NE and NC datasets with the virial penalty enabled generally produced good results fitting to the azimuthal geometry, and resulted both larger (NC) and smaller (NE) values of c, which was expected due to how those particular seed models were perturbed away from the $|R_{ii}| \leq 0.2$ criterion. The virial fits also reproduced the seed model's line-of-sight density profile better, though again with the exception of the zero-angle datasets. Overall, the application of the tensor virial penalty was successful at constraining parameters, and provides another tool to help assess the core characteristics.

6.2 Fits to Data: OMC-1 BN/KL

Previously, we have applied PolCat to data from the SCUPOL Legacy Catalogue (SLC) (Matthews et al., 2009), with the results presented in Franzmann (2014). This is a large

catalogue of uniformly reprocessed data from the entire operational lifetime of SCUPOL (1997-2005), the polarimeter on the SCUBA camera at the James Clerk Maxwell Telescope (JCMT). Currently, SCUBA has been replaced by the updated SCUBA2 instrument and its recently commissioned polarimeter POL-2. One large survey with this instrument is the B-fields In STar-forming Region Observations survey (BISTRO), which is aiming to produce a large high-resolution catalogue of the magnetic fields in the Gould Belt (Ward-Thompson et al., 2017). While the survey is still ongoing, multiple papers on objects using BISTRO data have already been published. Regions include OMC-1 (Ward-Thompson et al., 2017; Pattle et al., 2017; Hwang et al., 2021) and the Pillars of Creation in Orion (Pattle et al., 2018), Barnard 1 (Coudé et al., 2019), and ρ Ophiuchus C (Liu et al., 2019), among others. For this analysis, we are focusing on the OMC-1 dataset, specifically on the Brecklin-Neugebauer/Kleinmann-Low region (BN/KL). We present PolCat results of multiple fits to both SLC and BISTRO datasets of OMC-1 BN/KL, with and without the virial criterion $|R_{ii}| \leq 0.2$.

The Orion Nebula is a massive cloud complex that contains the closest region of high-mass star formation to us, the Kleinmann-Low nebula (Kleinmann and Low, 1967), at a distance of $\approx 388 \pm 5$ pc (Kounkel et al., 2017). The two brightest features in the OMC-1 region at submillimetre wavelengths are two large clumps, the Orion BN/KL region to the north, and the Orion S core to the south (Figure 6.6).

Density estimates of the BN/KL region by Pattle et al. (2017) (which uses the BISTRO dataset) range between approximately 8.1×10^{-19} to 7.1×10^{-18} g cm^{-3}. The polarization angles of the region are consistent with an hourglass morphology (Schleuning, 1998; Houde et al., 2004; Ward-Thompson et al., 2017; Pattle et al., 2017). Multiple magnetic field strength estimates have been made through a variety of techniques. Zeeman measurements have suggested values ranging from $0.1-0.44$ mG in the LOS direction in CN (Crutcher et al., 1996; Crutcher, 1999, though this was from a region 3' away), to approximately 1-16 mG from OH masers in the BN/KL region itself. Modified Chandrasekhar-Fermi methods have yielded values ranging between approximately 0.76 up to 3.8 mG in the plane-of-sky direction (Hildebrand et al., 2009; Houde et al., 2009). Additionally Pattle et al. (2017) have estimated the plane-of-sky field strength range between $1.9 - 11.3$ mG from the Chandrasekhar-Fermi analysis BISTRO data.

SCUPOL Legacy data has an effective beam width of 20" and a flux conversion factor of 227 Jy beam^{-1} Volt^{-1}. The BISTRO POL-2 data has an effective beam width of 14.1", with a flux conversion factor of 725 Jy beam^{-1} pW^{-1} (Ward-Thompson et al., 2017). This factor is scaled by a factor of 1.35 times the typical SCUBA2 value of 537 Jy beam^{-1} pW^{-1}, due to the presence of the polarimeter blocking some of the incoming light (Friberg et al.,

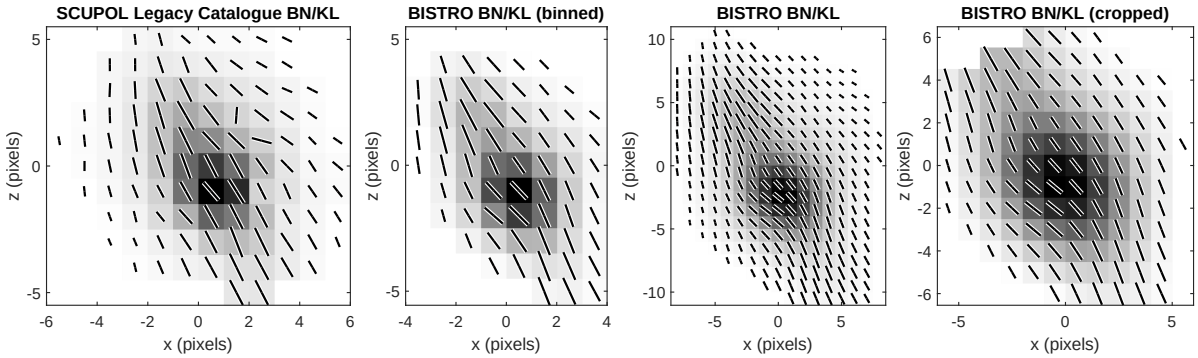


Figure 6.7: Full intensity map of the BISTRO OMC-1 dataset (Ward-Thompson et al., 2017), with polarization maps of the extracted BN/KL datasets.

2016).

6.2.1 Model Approach

For each final solution set, we combined solutions sets from six separate runs: three with Ferret's X-niching set to 0.25 (and F-niching set to 0), and three with F-niching set to 0.25 (and X-niching set to 0) (see Section 6.1.2). We took this approach due to the increased complexity of actual datasets over our test data. Because the BISTRO dataset has a higher resolution than the SLC data, we first binned the BISTRO dataset by 2x2 pixels, which produces a similar resolution to the SLC data, in order to fine-tune our initial fits. We then followed these with fits to the dataset at full resolution. The preliminary results of these fits were underestimating the intensity of the bright core region of the data while producing good fits to the diffuse envelope outside the core. As a result, we cropped the BISTRO data further to try and isolate the central bright region. To aid in differentiating this dataset from the others, we refer to the SLC and other two BISTRO datasets as the "larger regions" versus the "cropped region."

For each of the datasets we applied virial and non-virial penalized fits with the same hourglass and twist models that we applied to the test data. However, as the template we used for that analysis had $C_t{}^*$ fit logarithmically, and we had previously applied models with both logarithmic *and* linear fits to this parameter in the analysis of Franzmann (2014), we decided to do so here as well. Therefore, we effectively applied three models to the data.

One subtle distinction with $C_t{}^*$ is its comparative relevance in comparison to P_{ext}. We have defined $C_t{}^*$ for the purposes of the virial table lookup to be independent of the central density scale ρ_c, such that two otherwise identical cores with the same $C_t{}^*$ but different ρ_c have the same number of twists along the core z-axis from equation (4.12b) at the surface.

However, two otherwise identical cores with the same ${C_t}^*$ but one having a larger P_{ext} has a smaller number of twists before reaching the core's surface, as larger P_{ext} truncate the core at smaller surface radii. Therefore, models with high P_{ext} are usually less twisted than lower pressure models at high ${C_t}^*$ values. With this in mind, we computed alternate virial tables, increasing the upper ${C_t}^*$ limit from 2 ("low twist" tables) to 5 ("high twist" tables), and performed fits using both.

In total, for each of the datasets we applied 48 separate fits: 3 model templates $\times$ 2 virial modes (enabled and disabled) + 2 extra sets run with the ${{C_t}^*}_{\max} = 5$ virial tables, with each of those run 6 times.

6.2.2 Fitness And Residuals

The reduced χ^2 values for intensity were very large compared to the test data. This was expected due to the underlying dataset likely not being perfectly ellipsoidal, and the scale of the uncertainty relative to both datasets. Typical reduced χ^2 values at the knee for most of the runs were on the order of approximately 300-1000 for intensity, and on the order of about 100 for the polarization angle, with select runs on specific datasets having larger values. While the large reduced χ^2 values are not ideal, in this case the pixel-to-pixel fluctuations in the fitting error are much larger than the formal uncertainty of the observations. However, the mean absolute error (MAE) of the intensity ($\frac{1}{N}\sum|I - I_{data}|$) indicates that the high reduced χ^2 values were not necessarily indicative of the overall quality of fit, being typically on the order of 20% of the mean data value. This was consistent with previous fits to the SLC dataset from Franzmann (2014). However, this was not the case for the virial fits to the cropped dataset, which had MAE on the order of 120% of the mean data value for the virial fits. Regardless of whether the virial penalty was enabled, this dataset's knee solutions were typically selecting the fitting limits of the σ_0, P_{ext}, and c parameters (Table 6.2, which indicate some changes to the model need to be made. Switching on the virial penalty often resulted in larger fitness values for fits to the larger regions as well, though not to the same extent as for the cropped dataset. However, despite the fitness values increasing for virial runs, the knee model geometries from the non-virial runs were typically very unphysical, which we discuss more in the following section.

Overall, the intensity residuals of fits to the larger regions (SLC and both the binned and full resolution BISTRO data) tended to underestimate the intensity at the brightest part of the core by about 1-2x the mean data value, while fitting the surroundings much better (Figure 6.8). This was the case even for solutions with the smallest F_I and average RMS error values. This was the motivation behind cropping the full-resolution BISTRO dataset

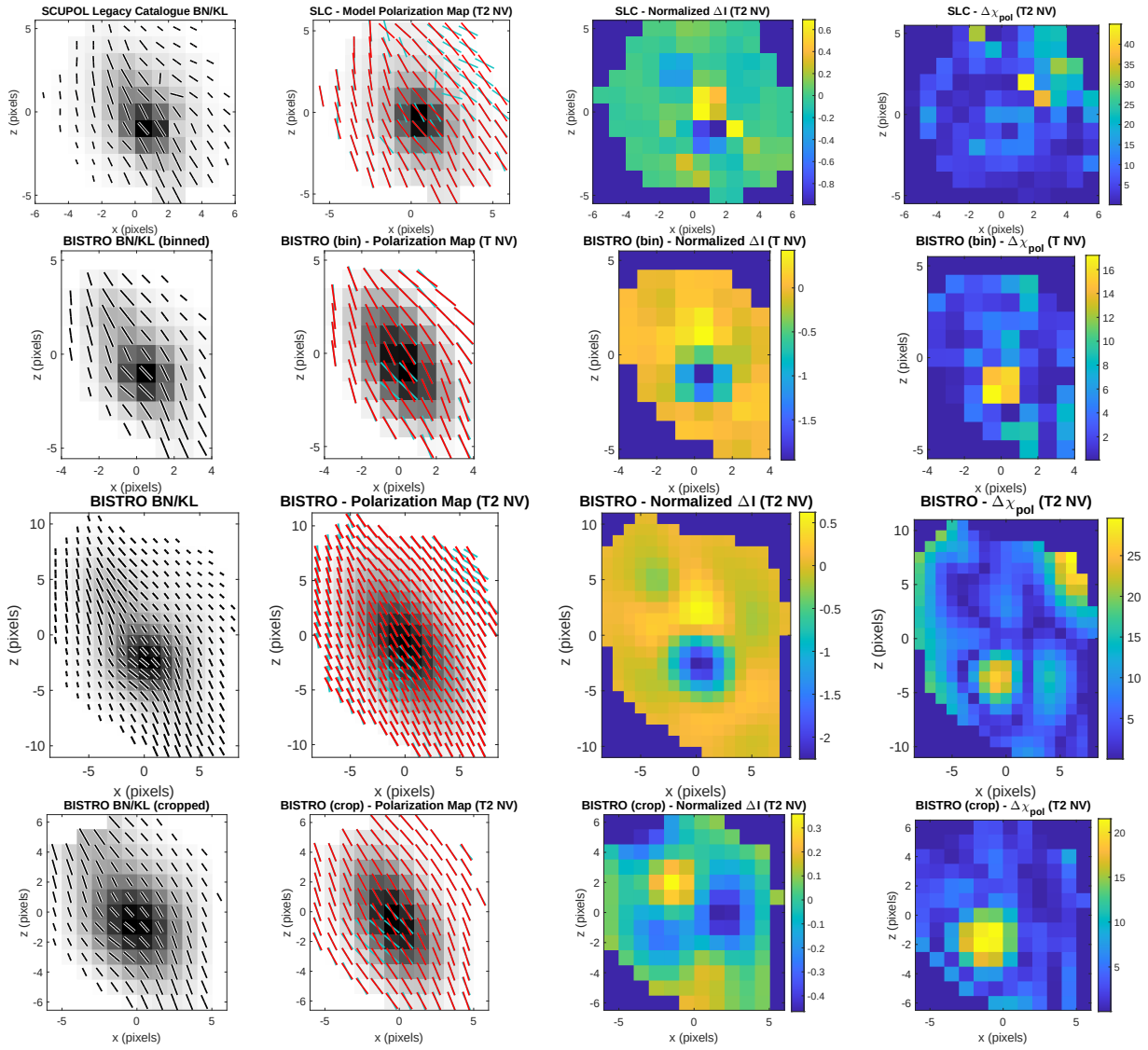


Figure 6.8: Select solutions for each dataset. From top to bottom: SLC dataset, binned BISTRO dataset, full-resolution BISTRO dataset, and cropped BISTRO dataset. From left to right: Data polarization map, model polarization map with model vectors in red and data vectors in blue, normalized intensity residuals, and χ_{pol} residuals in degrees. Intensity residuals are normalized by the mean dataset intensity value $\bar{I}_{data}$.

Info		Model Parameters								
Dataset	Run Type	ρ_0 (g cm^{-3})	σ_0 (km s^{-1})	Ct^* (rad/$z^{(0)}$)	ρ_c	τ	P_{out}	$\zeta_{squeeze}$	$\xi_{squeeze}$	$c_{squeeze}$
SLC	HG NV	3.14E-20	3.27	–	474.12	80.59	0.36	1.89	0.34	0.54
SLC	HG V	1.04E-19	1.56	–	72.94	1.45	0.17	7.89	1.42	0.20
SLC	T NV	1.08E-18	2.68	2.58	296.95	99.06	0.00	0.14	0.59	1.29
SLC	T V (2)	7.92E-20	3.43	0.14	242.26	16.49	0.38	1.05	1.80	0.73
SLC	T V (5)	4.03E-19	2.67	0.021	388.07	4.06	0.01	1.91	1.13	0.68
SLC	T2 NV	3.98E-18	2.80	2.79	112.26	97.46	0.00	0.10	0.67	1.38
SLC	T2 V (2)	2.46E-18	2.81	1.99	489.32	3.33	0.00	0.58	0.49	1.26
SLC	T2 V (5)	3.93E-19	2.64	2.85	452.84	100.00	0.00	0.68	0.54	1.25
BISTRO (bin)	HG NV	3.51E-19	3.09	–	350.75	91.69	0.16	2.05	0.10	0.84
BISTRO (bin)	HG V	5.82E-20	3.79	–	460.37	20.38	0.48	2.15	1.13	0.62
BISTRO (bin)	T NV	2.68E-19	2.85	0.038	70.94	98.74	0.34	1.69	0.10	0.61
BISTRO (bin)	T V (2)	2.86E-19	3.61	0.072	94.33	17.75	0.44	2.19	1.15	0.60
BISTRO (bin)	T V (5)	2.19E-18	3.00	3.49	62.73	8.35	0.13	0.54	0.43	1.67
BISTRO (bin)	T2 NV	3.73E-20	2.55	0.036	379.49	87.30	0.29	1.64	0.11	0.54
BISTRO (bin)	T2 V (2)	1.91E-19	2.67	0	368.89	7.06	0.11	1.17	2.14	0.63
BISTRO (bin)	T2 V (5)	3.80E-19	2.94	3.85	371.55	8.53	0.10	0.50	0.41	1.68
BISTRO	HG NV	5.90E-19	3.39	–	324.81	96.53	0.18	0.12	2.27	0.98
BISTRO	HG V	1.28E-19	3.89	–	218.33	20.14	0.50	1.95	1.06	0.70
BISTRO	T NV	6.64E-19	2.53	4.06	94.33	27.39	0.09	0.20	0.48	1.24
BISTRO	T V (2)	1.87E-19	3.71	0.090	149.95	19.92	0.46	1.08	1.98	0.68
BISTRO	T V (5)	4.21E-19	3.53	4.68	279.24	16.44	0.24	0.41	0.53	1.86
BISTRO	T2 NV	1.56E-19	2.39	3.99	238.42	14.95	0.10	0.52	0.33	1.08
BISTRO	T2 V (2)	2.00E-19	3.43	0.048	191.09	18.83	0.36	1.12	2.12	0.64
BISTRO	T2 V (5)	4.73E-19	3.13	3.98	312.42	14.97	0.13	0.46	0.39	1.80
BISTRO (crop)	HG NV	1.57E-19	0.40	–	429.65	74.39	0.46	0.78	9.78	1.97
BISTRO (crop)	HG V	1.45E-20	0.40	–	271.19	100.00	0.50	1.00	1.03	0.99
BISTRO (crop)	T NV	1.79E-19	0.42	0.015	158.04	29.00	0.50	4.30	6.97	1.97
BISTRO (crop)	T V (2)	1.03E-22	0.40	0.19	5.09	84.10	0.50	9.40	0.10	0.25
BISTRO (crop)	T V (5)	1.55E-20	0.4	4.41	414.03	100.00	0.50	0.56	0.56	2.00
BISTRO (crop)	T2 NV	2.50E-19	0.40	3.94E-04	328.58	95.43	0.43	0.76	8.74	1.99
BISTRO (crop)	T2 V (2)	3.65E-20	0.40	2.00	217.97	99.98	0.50	0.67	0.79	1.56
BISTRO (crop)	T2 V (5)	3.51E-20	0.4	3.36	205.72	100.00	0.50	0.55	0.57	2.00

Table 6.2: Results from fits to the SLC and BISTRO data. Run Type: "HG:" non-twisted hourglass, "T:" Twisted hourglass (log fit), "T2:" Twisted Hourglass (linear fit), "NV:" no virial penalty, and "V (N):" Virial penalty applied (${C_t^*}_{\max}$).

Info		Model Parameters (contd)					Fitness		Residuals		
Dataset	Run Type	ϕ (°)	i (°)	PA (°)	Δx (pix)	Δz (pix)	F_I	$F_{\chi_{pol}}$	$\overline{\Delta I}$ ($\bar{I}_{data}$%)	$[\Delta I]_{RMS}$ ($\bar{I}_{data}$%)	$[\Delta\chi_{pol}]_{RMS}$ (°)
SLC	HG NV	173.66	174.50	64.10	0.63	-0.46	9959.44	33.33	18.44	63.79	25.81
SLC	HG V	103.00	181.71	67.25	0.58	-0.40	5410.46	99.62	12.95	65.39	28.44
SLC	T NV	65.37	0.22	153.01	0.57	-0.39	5451.37	18.32	12.88	36.39	46.18
SLC	T V (2)	93.93	330.97	63.22	0.58	-0.38	11655.33	19.38	22.84	48.77	44.80
SLC	T V (5)	11.39	166.32	66.05	0.57	-0.38	4891.29	131.69	12.62	33.92	51.42
SLC	T2 NV	55.42	358.40	154.55	0.58	-0.42	5375.84	15.63	12.64	39.32	50.67
SLC	T2 V (2)	125.40	2.47	154.68	0.61	-0.51	5525.52	32.51	13.26	32.37	62.48
SLC	T2 V (5)	129.12	170.30	332.27	0.63	-0.56	7821.84	19.45	13.80	23.65	35.91
BISTRO (bin)	HG NV	168.52	23.67	62.19	-0.09	-0.61	3258.38	584.66	24.55	111.66	64.77
BISTRO (bin)	HG V	174.18	161.13	60.72	0.33	-0.48	2680.87	1120.14	24.90	54.00	27.89
BISTRO (bin)	T NV	179.39	319.11	62.37	0.13	-0.38	1727.23	376.34	19.90	83.36	45.13
BISTRO (bin)	T V (2)	172.54	21.71	240.27	0.33	-0.49	2544.93	930.56	24.50	48.15	27.76
BISTRO (bin)	T V (5)	44.33	178.45	152.57	0.24	-0.52	1855.14	791.75	19.87	43.17	46.02
BISTRO (bin)	T2 NV	179.55	322.09	62.11	0.20	-0.52	1655.53	435.68	18.95	73.49	37.34
BISTRO (bin)	T2 V (2)	98.74	187.38	60.59	0.28	-0.48	1709.72	4333.22	20.10	38.97	34.35
BISTRO (bin)	T2 V (5)	136.64	179.67	331.35	0.26	-0.50	1655.66	944.52	19.54	50.98	45.52
BISTRO	HG NV	62.10	177.49	62.21	-0.50	-0.83	710.19	217.34	24.38	82.89	51.20
BISTRO	HG V	7.08	165.53	62.18	0.24	-1.00	737.36	324.91	28.39	57.94	64.01
BISTRO	T NV	106.46	182.04	151.29	-0.01	-0.97	388.25	240.11	19.77	66.09	52.49
BISTRO	T V (2)	83.92	18.09	241.29	0.12	-0.89	705.27	261.39	27.80	64.47	63.40
BISTRO	T V (5)	148.65	180.24	151.83	-0.05	-0.82	481.90	212.27	22.75	47.31	49.05
BISTRO	T2 NV	34.41	1.62	331.33	-0.02	-0.91	440.43	227.75	21.21	52.34	49.07
BISTRO	T2 V (2)	85.09	14.42	241.20	0.00	-0.91	508.82	483.79	23.64	50.12	54.50
BISTRO	T2 V (5)	144.72	0.64	151.33	-0.03	-0.85	443.74	261.15	21.53	53.85	48.79
BISTRO (crop)	HG NV	30.81	179.08	61.35	-0.35	-0.36	409.10	76.74	12.49	32.74	33.42
BISTRO (crop)	HG V	18.76	182.95	62.35	-0.47	-0.99	41109.55	173.17	187.68	261.23	66.19
BISTRO (crop)	T NV	177.82	20.56	241.29	-0.31	-0.02	394.79	103.68	17.58	57.85	46.56
BISTRO (crop)	T V (2)	9.56	346.87	146.60	-5.50	3.68	3644.60	192.98	50.06	90.34	39.36
BISTRO (crop)	T V (5)	88.64	0.00	338.12	-0.48	-0.99	15230.42	265.22	110.74	157.26	34.64
BISTRO (crop)	T2 NV	36.76	178.70	241.38	-0.37	-0.44	452.92	64.17	12.70	46.51	69.04
BISTRO (crop)	T2 V (2)	103.11	174.51	152.33	-0.32	-0.91	26886.45	67.32	145.92	208.27	39.93
BISTRO (crop)	T2 V (5)	179.96	0.00	150.05	-0.40	-0.70	15433.65	99.26	112.23	167.98	13.15

Table 6.2 continued

closer to the central core. Doing so improved the intensity residuals for the non-virial runs. For the virial runs, the models switched from underestimating the bright area by 1-2 times to overestimating by approximately 6-10 times, except for the non-virial cases, and where the twist was fit logarithmically with the ${C_t^*}_{max} = 2$ virial tables. Despite the improvement in intensity fit on the non-virial models, the knee solutions were still unphysical because they were unrealistically flat.

Fits to the SLC dataset had an almost universal difficulty fitting the field at the top right edge of the map, except for the hourglass virial fit, which had more difficulty with the entire right edge of the dataset. The binned BISTRO data was slightly better, but we note that the problematic area in the SLC dataset appears to have been cropped from the map when we extracted the BN/KL region from the dataset of the whole OMC-1 complex. This dataset, and its corresponding full-resolution and cropped datasets, had more difficulty accommodating the region to the bottom left of the bright region where there is a slight change in direction to the polarization vectors (see Figure 6.7).

6.2.3 Virial Quantities

Knee solutions from fits to the SLC and binned BISTRO datasets without the virial criterion produced models in scalar virial balance despite not using the virial penalty technique, which produced a physical magnetic field scale $b^{*2} \geq 0$ (§4.4.3). The knee solutions from the full resolution BISTRO data (full and cropped) were not physical, meaning these models were not in scalar virial equilibrium, and *could not* be in scalar virial equilibrium with the selected parameters. In principle we could check for physicality of the magnetic field independently of the virial criterion, but as this was developed for the purposes calculating the virial constraint we do not currently have this functionality. We intend to incorporate separate unphysical field strength rejection into the next update of PolCat. However, this estimate of the field strength is dependent on the object of study being near scalar virial equilibrium, and this may not be the case.

The magnetic field strength scales B_0 derived from the scalar virial balance (equation (4.30)) varied. The cropped BISTRO dataset had the smallest values, ranging from 0.115 μG for the virial hourglass knee model to 2.4 μG for one of the virial linear twist models. The other datasets were closer in value to each other, and ranged between 30.6 μG and 0.273 mG. There seemed to be some general trend of the magnetic field scale decreasing as the central density scale increased (see Figure 6.9).

The magnetic field scale describes the unit conversion of the computed magnetic field to Gauss. For comparison purposes, we also took the mean amplitudes of the knee solution

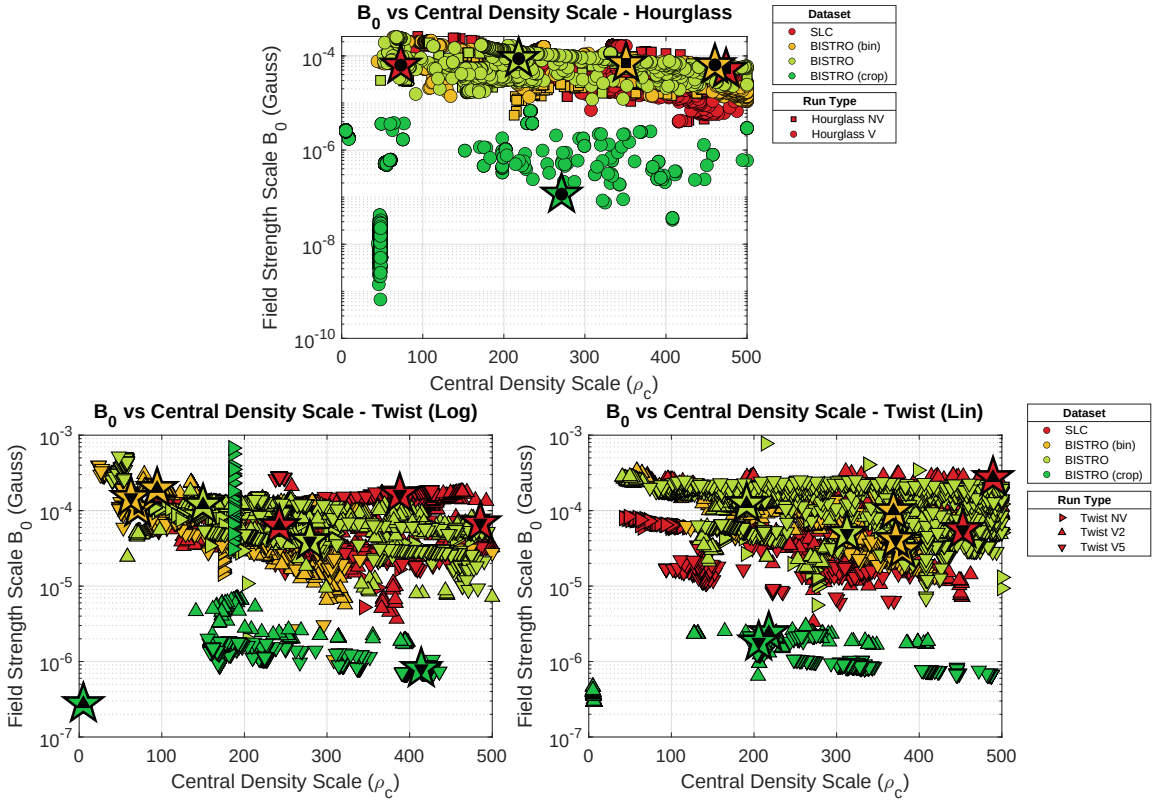


Figure 6.9: Field strength scale B_0 (where exists) in relation to the central density scale ρ_c. Each symbol on the plots represents a result from the whole solutions set of a PolCat run.

magnetic fields and used B_0 to convert to Gauss. The cropped BISTRO data still had the smallest values, now varying between 0.28 to 8.3 μG, while the rest of the datasets varied between $0.2-1.3$ mG. These latter values were more consistent with previous measurements (e.g. Pattle et al. (2017), Hildebrand et al. (2009), Houde et al. (2009)), which would seem to indicate that the assumption that the region is in approximate scalar virial equilibrium is valid. The reason for why the fits to the cropped dataset are so low compared to the others is not clear.

6.2.4 Model Geometries

Figure 6.10 shows the shape maps (see Section 5.1), and the bottom row shows plot of compression c relative to their area-equivalent spheroidal axis ratio $\zeta_{\rm sph}$ (see Figure 5.1 for the geometrical meaning of this quantity). Plots are separated by model type, with the linear and logarithmic fitting on ${C_t}^*$ shown separately. The overall appearance of the shape map of the hourglass model resembles the results of fitting the Case 4 test data (twisted geometry) with the hourglass model (Figure 6.2). These solutions were still found when we

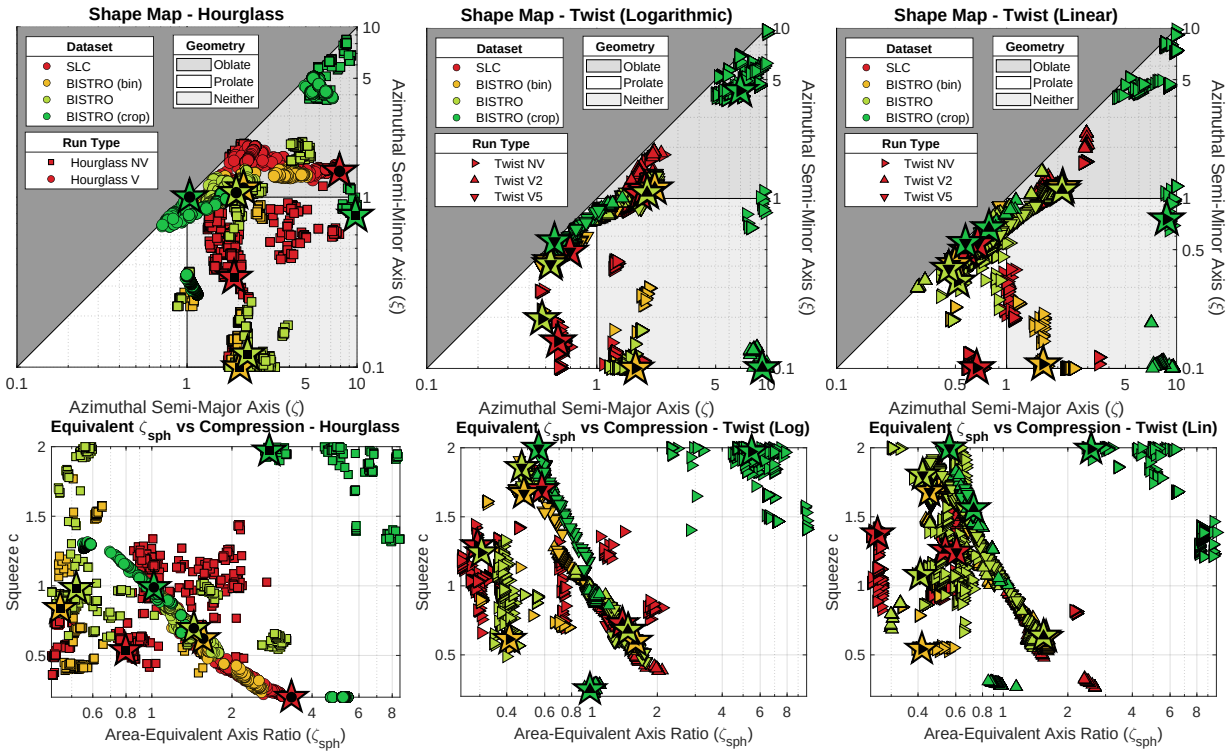


Figure 6.10: Shape maps and area-equivalent axis ratio relative to compression for all four datasets, separated by hourglass (left), logarithmic twist fit (centre) and linear twist fit (right). Stars indicate knee solutions.

fit with the twisted field geometry, but were much more concentrated in clusters. Models that were highly azimuthally eccentric were mostly confined to the non-virial fits, with the exception of some virial fits to the cropped BISTRO data. Figures 6.11 and 6.12 show what this means in terms of three-dimensional field and density structure for the knee solutions.

While both of the low-resolution datasets contained solutions that were more reasonable shapes, all of the non-virial fits to the SLC and binned BISTRO data selected models that were very azimuthally eccentric around the knee of the fitness curves. This produced ellipsoids with one axis very flattened perpendicular to the field, with the core closely resembling a pancake with the field lines travelling across the disk rather than perpendicular to it (see the top two rows of Figure 6.11), though fits to the SLC dataset with the twisted model produced twisted fields while still being flattened perpendicular to the core's z-axis. For the full-resolution BISTRO dataset, these solutions only appeared at the knee in the hourglass and logarithmically fit twist cases, with the latter also having a significantly twisted field (Figure 6.11). The knee solutions for the cropped dataset produced "pancake" models for both the hourglass and linear C_t^* fit models, and a very flattened oblate triaxial core in the case of the logarithmic fit (Figure 6.11, bottom row). Applying the virial constraint largely

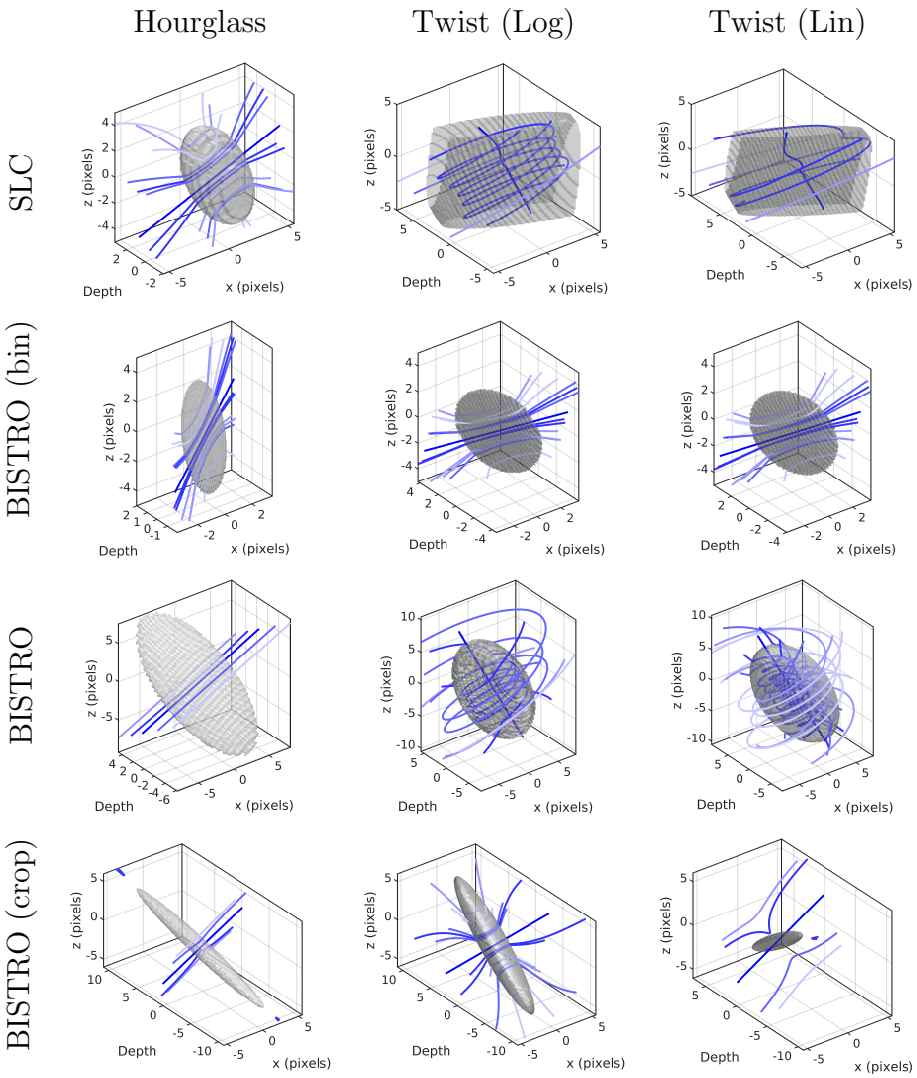


Figure 6.11: Knee solutions from non-virial fits to each dataset. Rows indicate the dataset, columns indicate the model applied.

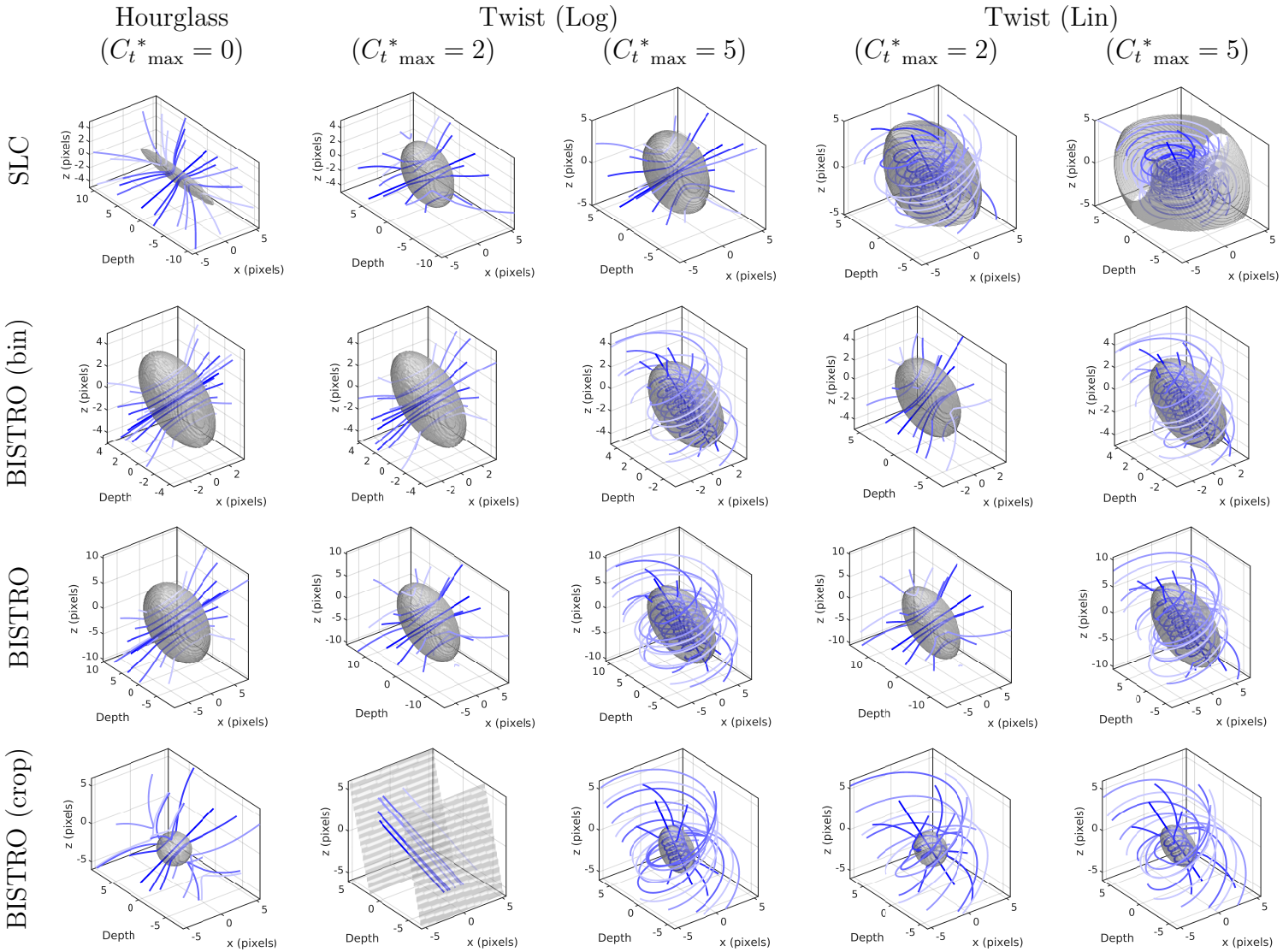


Figure 6.12: Knee solutions from virial fits, arranged as in Figure 6.11, with the two twisted hourglass models split between the $C_t^*{}_{\max} = 2$ (low twist) and $C_t^*{}_{\max} = 5$ (high twist) lookup tables.

eliminated these types of models from the fit (Figure 6.12). The main exception is from one of the twisted fits to the cropped dataset, where the model is so enlarged that it is present only as a segment of a sheet extending past the limits of the model cube (Figure 6.12).

As was the case for the twisted test models, the compression parameter c was largely unconstrained (Figure 6.10 bottom row). The fits with the hourglass model mostly appeared to prefer compressed models ($c \leq 1$), except for the cropped dataset. In that case, the non-virial fits were selecting models with c at or equal to 2 (expanded to the maximum extent of the parameter limit), and the non-virial fits had mostly $c \leq 1$ with a few exceptions. For the twisted fits, the solutions were mostly expanded ($c > 1$). However, solutions that were compressed in these cases appear to have selected low values of ${C_t}^*$, making them effectively hourglass models.

Comparing Figure6.11 to Figure 6.12 it is clear that enabling the virial penalty caused the model axis ratios to become more realistic, and provided much tighter constraints on the compression parameter. The only exceptions were twisted model fits to the cropped BISTRO dataset, which appear to have selected solutions at the tip of the highly compressed triaxial "wings" that exist for the twisted virial lookup tables at high truncation pressures (§5.3).

6.2.5 Density Profiles

Figure 6.13 plots the peak core density ρ_{peak} in relation to the line of sight truncation radius, and the corresponding density profiles of the knee solutions (§6.1.4.4). Core radius is presented in physical units (pc in this case), as polarization map computation is performed in physical units in the LOS direction (§3.2.3) and is most likely to cause better agreement between the truncation radii as was seen in Section 6.1.4.4.

Once again there was a split between the cropped BISTRO dataset and the other three. The majority of fits to the cropped dataset showed a range of peak densities between approximately 1×10^{-19} to 1×10^{-17} g cm^{-3}, and average voxel densities (i.e. cube average) between 8.9×10^{-21}–4.9×10^{-20} g cm^{-3} (excluding voxels with (x, z) coordinates in the masked region of the polarization map). This range of averages is several orders of magnitude smaller than the density estimates of Pattle et al. (2017), although the peak densities are in the right range. The average densities for the other datasets ranged between 1.4–2.05 $\times 10^{-18}$ g cm^{-3} for the SLC dataset, and 4.05–5.6 $\times 10^{-18}$ g cm^{-3} for the BISTRO datasets, which is consistent with Pattle et al. (2017). The binned BISTRO dataset had mean densities that were approximately 25-30% higher than the full-resolution dataset, but this was also consistent with the difference between their respective average peak densities.

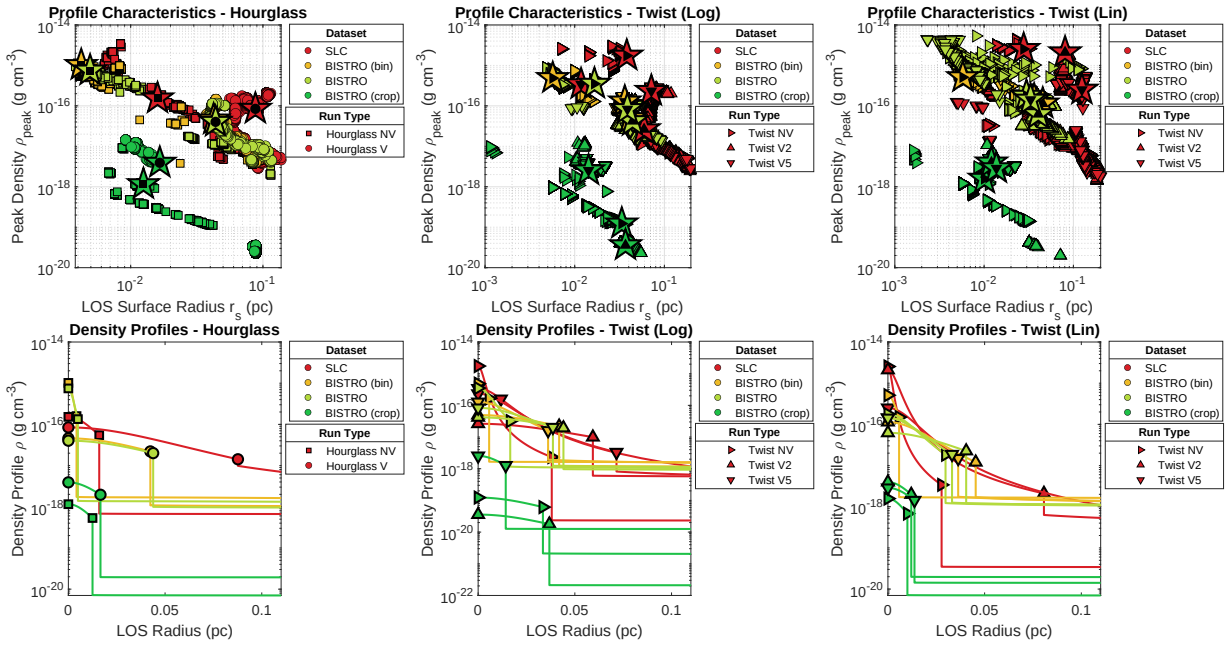


Figure 6.13: Peak density values ρ_{peak} (g cm^{-3}) relative to the truncation radius in the LOS direction (top row) and density profiles of the knee solutions (bottom row), separated by hourglass (left), logarithmic twist fit (centre) and linear twist fit (right). Stars indicate knee solutions.

6.2.6 Discussion

Overall the virial criterion had the desired effect of restricting the model solutions to more realistic geometries, despite the apparent degradation of reduced χ^2 values. This degradation in values was due to the limits on the parameter space imposed by the virial criterion. We remind the reader that we are fitting with highly idealized models, and that we are not trying to model every subtle variation in the data. Rather, we are trying to capture an overall large-scale field geometry and density structure, and such large values of reduced χ^2 are expected as a result. Reduced χ^2 on the order of 1 in this case would need to be from a model with a truly excessive number of parameters.

Virial fits to the large regions (SLC, binned and full resolution BISTRO) generally favoured hourglass fields without a twist even when a twist was allowed, except in cases where we fit with the ${C_t^*}_{\max} = 5$ tables. The cropped BISTRO data selected twisted datasets almost every time, but we are not confident in those fits for the reasons mentioned previously. Therefore, we do not see any strong evidence for the twisted fields from these results.

The fully-scaled central profile density was several orders of magnitude larger than previous estimates (except for the cropped BISTRO dataset), even at the knee of the fitness

curves. However, the density of the envelope external to the core surface was in very close agreement with the density estimates of Pattle et al. (2017) from the BISTRO dataset.

One potential consideration is that the external densities from the model cubes also contribute to the polarization maps, and this includes material along the line-of-sight. PolCat's model cube does not include potential contributions from all material between the object of interest and our location. Theoretically, if we assume any intervening material has a constant density, we could estimate its contribution to the intensity map using a constant offset. However, we have previously experimented with adding a constant intensity offset to PolCat fits, and found that the contribution of such a term was negligible to the final result and increased the degree of degeneracy in the solutions (Franzmann, 2014). However, the overall effect of this neglected material on the polarization position angle towards the core should be negligible, because the calculation of the simulated Stokes vector components is weighted by density (as seen in equations (3.8) to (3.11)). This is further aided by the density models we have used for this analysis having a naturally-attenuating external density much smaller than that at the core surface.

The fully-scaled average magnetic field amplitude for the knee solutions was on the order of $0.2 - 1.3$ mG for the large regions, and $0.28 - 8.3$ μG for the cropped dataset. The former range of values is in good agreement with the Chandrasekhar-Fermi measurements from Pattle et al. (2017) while the latter were at least two orders of magnitude smaller than those computed from the Zeeman measurements of Crutcher (1999). Since we computed our magnetic field strength scale B_0 based on scalar virial balance, the agreement between the Pattle et al. (2017) measurements and the average field strengths of the knee models for the larger regions lends credence to the assumption that the core is in scalar virial equilibrium. The discrepancy in the cropped region would seem to indicate the opposite for the central region, but we do not have confidence in those fits.

The difference between the fits to the cropped OMC-1 BISTRO dataset and the other three needs more examination beyond the scope of this work. This dataset was consistently selecting values for velocity dispersion σ_0, truncation pressure P_{out}, and z-axis squeeze c that were at the edges of the specified parameter limits. Yet it was also selecting ρ_0 such that the coordinate conversion factor between physical and dimensionless coordinates r_0 (§3.4,§4.2.1) remained consistent with fits to the other datasets. More experimentation with the dataset is needed here.

Future expansion of this approach may include estimating the value of virial parameters based on plausible magnetic field estimates, rather than relying on scalar virial balance. Additionally, using the method to approximate the "standard" virial quantities outlined in Section 2.1 to provide analogues to the observationally-computed properties could provide

additional observational insight when comparing the models to data.

Chapter 7

Alfvén Wave Propagation

7.1 Alfvén Wave Propagation in Uniform Media

The linearized ideal MHD equations for a magnetic field in a perfectly conducting thin fluid with an isothermal equation of state are represented by the Navier-Stokes and Euler equations. Neglecting gravity, the relevant differential equations are:

$$\frac{\partial \rho}{\partial t} + \boldsymbol{\nabla} \cdot (\rho \boldsymbol{\mathcal{V}}) = 0 \tag{7.1}$$

$$\rho \frac{\partial \boldsymbol{\mathcal{V}}}{\partial t} + \rho(\boldsymbol{\mathcal{V}} \cdot \boldsymbol{\nabla})\boldsymbol{\mathcal{V}} = -\sigma^2 \boldsymbol{\nabla}\rho - \frac{1}{4\pi}\mathbf{B} \times (\boldsymbol{\nabla} \times \mathbf{B}) \tag{7.2}$$

$$\frac{\partial \mathbf{B}}{\partial t} = \boldsymbol{\nabla} \times (\boldsymbol{\mathcal{V}} \times \mathbf{B}) \tag{7.3}$$

(Jackson, 1975) assuming an isothermal equation of state $P = \sigma^2 \rho$. Under static conditions, $\boldsymbol{\mathcal{V}} = 0$, leading to the a zero left hand side for equation (7.2). For small time-dependent perturbations ρ_1, $\mathbf{b}$, and $\mathbf{V}$ we express the total magnetic field, density, and velocity field as

$$\mathbf{B}_t = \mathbf{B} + \mathbf{b}(\mathbf{x}, t) \tag{7.4}$$

$$\rho_t = \rho + \rho_1(\mathbf{x}, t) \tag{7.5}$$

$$\boldsymbol{\mathcal{V}}_t = \mathbf{V}(\mathbf{x}, t) \tag{7.6}$$

where $\mathbf{B}$ and ρ represent the unperturbed magnetic field and density structures. While this notation varies from the standard perturbation notation which uses B_0 and ρ_0 to indicate unperturbed quantities, we have chosen this notation in order to avoid confusion with PolCat's constant magnetic field and density scales, which feature heavily in the following sections.

Substituting the above expressions into equations (7.1) to (7.3) and neglecting second-

order perturbation terms results in

$$\frac{\partial \rho_1}{\partial t} = -\rho \boldsymbol{\nabla} \cdot \mathbf{V} \tag{7.7}$$

$$\frac{\partial \mathbf{V}}{\partial t} = -\frac{\sigma^2}{\rho}\boldsymbol{\nabla}(\rho + \rho_1) - \frac{1}{4\pi\rho}\left[\mathbf{B} \times (\boldsymbol{\nabla} \times \mathbf{B}) + \mathbf{B} \times (\boldsymbol{\nabla} \times \mathbf{b}) + \mathbf{b} \times (\boldsymbol{\nabla} \times \mathbf{B})\right] \tag{7.8}$$

$$\frac{\partial \mathbf{b}}{\partial t} = \boldsymbol{\nabla} \times (\mathbf{V} \times \mathbf{B}). \tag{7.9}$$

The above takes into account $1/\rho_t \approx 1/\rho$. The static terms in equation (7.8) vanish as previously established, leaving

$$\frac{\partial \mathbf{V}}{\partial t} = -\frac{\sigma^2}{\rho}\boldsymbol{\nabla}\rho_1 - \frac{1}{4\pi\rho}\left[\mathbf{B} \times (\boldsymbol{\nabla} \times \mathbf{b}) + \mathbf{b} \times (\boldsymbol{\nabla} \times \mathbf{B})\right]. \tag{7.10}$$

Assuming a uniform medium and magnetic field, equation (7.10) further reduces to

$$\frac{\partial \mathbf{V}}{\partial t} = -\sigma^2\boldsymbol{\nabla}\rho_1 - \frac{1}{4\pi\rho}\left[\mathbf{B} \times (\boldsymbol{\nabla} \times \mathbf{b})\right]. \tag{7.11}$$

To derive the wave equation for $\mathbf{v}$, we define the Alfvén velocity

$$\mathbf{c}_{A0} = \frac{\mathbf{B}}{\sqrt{4\pi\rho}} \tag{7.12}$$

And take the partial derivative of equation (7.11) with respect to time, substituting in equations (7.7) and (7.9) to obtain

$$\frac{\partial^2 \mathbf{V}}{\partial t^2} - \sigma^2\boldsymbol{\nabla}(\boldsymbol{\nabla} \cdot \mathbf{V}) + \mathbf{c}_{A0} \times \boldsymbol{\nabla} \times [\boldsymbol{\nabla} \times (\mathbf{V} \times \mathbf{c}_{A0})]. \tag{7.13}$$

Assuming a plane wave perturbation with constant amplitude $\mathbf{V}(\mathbf{x}, t) = \mathbf{v}e^{i\psi}$, with $\psi = \mathbf{k} \cdot \mathbf{x} - i\omega t$ representing the phase of the wave, and substituting vector identities for the curl expressions the resulting expression for equation (7.13) is equivalent to

$$-\omega^2\mathbf{V} + (\sigma_0^2 + c_{A0}^2)(\mathbf{k} \cdot \mathbf{V})\mathbf{k} + \mathbf{c}_{A0} \cdot \mathbf{k}[(\mathbf{c}_{A0} \cdot \mathbf{k})\mathbf{V} - (\mathbf{c}_{A0} \cdot \mathbf{V})\mathbf{k} - (\mathbf{k} \cdot \mathbf{V})\mathbf{c}_{A0}] = 0. \tag{7.14}$$

For a pure Alfvén wave, $\mathbf{V}$ is perpendicular to both $\mathbf{B}_0$ and $\mathbf{k}$, causing multiple terms to vanish, producing

$$\omega^2 = k^2 c_{A0}^2. \tag{7.15}$$

Applying this condition to equation (7.9) yields the equation for the perturbed field

$$\mathbf{b} = -\frac{|\mathbf{B}|}{c_{A0}}\mathbf{V}. \tag{7.16}$$

We note that this standard derivation does not include the effect of self-gravity, which would add a $-\boldsymbol{\nabla}\Phi$ term to equation (7.2) and is relevant for gravitationally-bound objects such as molecular cloud cores. However, this derivation for the standard case assumes general compressible flow. We are only interested in the Alfvén modes, which are incompressible. We can demonstrate that it is acceptable to ignore the self-gravity term as follows. From Poisson's equation of gravitation assuming the gravitational perturbation Φ_1 and the density perturbation ρ_1 follow the same form as the velocity with constant amplitude, we can write

$$\boldsymbol{\nabla}^2\Phi_t = 4\pi G\rho_t \tag{7.17}$$

$$\Rightarrow \boldsymbol{\nabla}^2\Phi_1 = -k^2\Phi_1 = 4\pi G\rho_1. \tag{7.18}$$

For incompressible flow, $\boldsymbol{\nabla}\cdot\mathbf{V} = 0$, and therefore equation (7.7) gives $\rho_1 = 0$. However, even if we do not directly assume that the velocity is divergence-free, evaluating (7.7) gives

$$-i\omega\rho_1 + i\rho\mathbf{V}\cdot\mathbf{k} = 0. \tag{7.19}$$

For the Alfvén wave condition, $\mathbf{V}$ and $\mathbf{k}$ are perpendicular, and therefore $\rho_1 = 0$ independently and gravitational perturbations can safely be neglected. While the next section discusses perturbations with non-uniform fields and densities which would couple the shear Alfvén wave to the compressive modes (Cramer, 2001; Goedbloed et al., 2019), in Section 7.2.4.1 we show that we achieve the same result in the 0th order eikonal approximation (small wavelength), which is our domain of interest.

7.2 Alfvén Wave Propagation in Non-Isotropic Media

While the uniform wave equations are useful to aid understanding, it is more complete in our case to generalize to non-uniform media. In order to compute the necessary field perturbations, we need to know: 1) basis vectors perpendicular to the field lines at all points, 2) how the phase of the perturbation changes as the wave propagates through the non-uniform region, and 3) how the amplitude of the wave changes as it propagates down the curved field lines through areas of varying density.

Scheurwater (1990) developed a formalism for the propagation of magnetic waves along curved field lines by operating in a curvilinear coordinate frame where the magnetic field lines lie along one of the principal axes. This is directly analogous to the coordinate-transformation technique we use to generate our models. In Scheurwater (1990), the curvilinear orthogonal coordinate frame has coordinates (u^1, u^2, u^3) where u^m are continuously differentiable, invertible functions of (x, y, z) (Cartesian coordinates) that incorporate the scaling of the magnetic field. This new system is defined by setting the ordered magnetic field parallel to u^3, and defining u^1 and u^2 according to the Clebsch representation

$$\mathbf{B} = \boldsymbol{\nabla} u^1 \times \boldsymbol{\nabla} u^2 = \boldsymbol{\nabla} \times \left(\frac{u^1}{2} \boldsymbol{\nabla} u^2 - \frac{u^2}{2} \boldsymbol{\nabla} u^1 \right) \tag{7.20}$$

This leads to a vector potential of

$$\mathbf{A} = \frac{u^1}{2} \boldsymbol{\nabla} u^2 - \frac{u^2}{2} \boldsymbol{\nabla} u^1 + \boldsymbol{\nabla} u^3. \tag{7.21}$$

In this coordinate frame, magnetic field lines lie on the intersections of the surfaces $u^1 =$ constant and $u^2 =$ constant. Scheurwater (1990) defines their method in terms of the Jacobian matrix for the transformation from Cartesian to the curvilinear system $J = (\boldsymbol{\nabla} u^1 \times \boldsymbol{\nabla} u^2) \cdot \boldsymbol{\nabla} u^3$. Drawing a direct connection to PolCat, this Jacobian is the inverse of the PolCat definition for model generation. To avoid confusion with the notation, we choose to keep our notation consistent with PolCat's definition, and define the curvilinear basis in terms of the forward transformation $\mathcal{J}$ rather than the inverse used by Scheurwater (1990). Therefore in this convention $J = \mathcal{J}^{-1}$. Because PolCat generates models by computing an initial coordinate frame where the magnetic fields are uniform along a principal axis and using Jacobian matrices to transform the field and density into their final configurations in a Cartesian system, we already have the necessary tools to apply this method.

The main benefit of the Scheurwater (1990) method is that it allows for the simple computation of the velocity amplitudes and wavevectors as they propagate down the curved field lines using a ray-tracing formalism. However, in order to use these results we must first prove that we can apply our more complex magnetic fields to the Scheurwater (1990) method. In addition, Scheurwater (1990) makes some assumptions that we do not, namely assuming force-free or potential magnetic fields such that $\boldsymbol{\nabla} \times \mathbf{B} = \alpha \mathbf{B}$. This simplifies equation (7.8) and has the result that the metric tensor for the curvilinear system is block-diagonal, which is not the case for a general PolCat model.

In this section, we first connect PolCat's model-building process to the Scheurwater (1990) formalism, defining the necessary unit vectors. Then, we solve equations (7.1) to (7.3)

in the curvilinear system to prove that we can apply the wavevector propagation equations to our more complex case. We also discuss the application of the method to determine the velocity amplitudes, but in this latter case the differential equations involved are much too complex to apply directly. Therefore, we also derive an equivalent formalism using geometrical arguments to compute the velocity amplitudes in order to obtain the perturbed fields.

7.2.1 PolCat Jacobians

In the Scheurwater (1990) method, the coordinate transformation is encoded in a single Jacobian matrix. However, PolCat uses multiple coordinate transformations applied in sequence to transform from the Cartesian system to the curvilinear system where the magnetic field is uniform. Nevertheless, we can treat the multiple Jacobians as a single Jacobian to apply this method, which we show below.

We define a simple Cartesian grid $(x^{(N)}, y^{(N)}, z^{(N)}) = x^m$ that we back-transform to a curvilinear system $(x^{(0)}, y^{(0)}, z^{(0)}) = u^m$ where the density and magnetic field are uniform. The magnetic field $\mathbf{B}^{(N)}$ and density $\rho^{(N)}$ in the Cartesian system are computed using the uniform magnetic field $\mathbf{B}^{(0)}$ and density $\rho^{(0)}$ in the curvilinear system by:

$$\rho^{(N)} = \frac{\rho^{(0)}}{\mathcal{J}^{(N)}\mathcal{J}^{(N-1)}...\mathcal{J}^{(1)}} \tag{7.22}$$

$$\mathbf{B}^{(N)} = \frac{\boldsymbol{\mathcal{J}}^{(N)}\boldsymbol{\mathcal{J}}^{(N-1)}...\boldsymbol{\mathcal{J}}^{(1)}\mathbf{B}^{(0)}}{\mathcal{J}^{(N)}\mathcal{J}^{(N-1)}...\mathcal{J}^{(1)}}. \tag{7.23}$$

Because determinants are distributive, if we define $\boldsymbol{\mathcal{J}} = \boldsymbol{\mathcal{J}}^{(N)}\boldsymbol{\mathcal{J}}^{(N-1)}...\boldsymbol{\mathcal{J}}^{(1)}$, then the corresponding determinant is $\mathcal{J} = \det(\boldsymbol{\mathcal{J}}) = \mathcal{J}^{(N)}\mathcal{J}^{(N-1)}...\mathcal{J}^{(1)}$, and we can write

$$\rho^{(N)} = \frac{\rho^{(0)}}{\mathcal{J}} \tag{7.24}$$

$$\mathbf{B}^{(N)} = \frac{\boldsymbol{\mathcal{J}}\mathbf{B}^{(0)}}{\mathcal{J}}. \tag{7.25}$$

It follows then that $\boldsymbol{\mathcal{J}}$ is the aggregate Jacobian of the direct transformation between the uniform field space u^m, and Cartesian space x^m. This aggregate Jacobian therefore has elements

$$\mathcal{J}_{nm} = \mathcal{J}^{(N)}_{np}\mathcal{J}^{(N-1)}_{pq}...\mathcal{J}^{(1)}_{rm} = \frac{\partial x^n}{\partial u^m} \tag{7.26}$$

with non-zero determinant. Because we have defined the process this way, we have, in effect, a single matrix that defines the transformation from a uniform, flat medium to our more

complex model, as in Scheurwater (1990).

7.2.2 Curvilinear Basis and Metric Tensor Definitions

In this section, we walk through the required bases and vector identities to apply the Scheurwater (1990) method, adapted for PolCat's notation and density formalism.

The general expression of a vector field $\mathbf{F}$ in the curvilinear space is

$$\mathbf{F} = F^m \boldsymbol{f}_m = F_m \boldsymbol{f}^m \tag{7.27}$$

where $\boldsymbol{f}_m$ and $\boldsymbol{f}^m$ are the covariant and contravariant basis vectors, and coefficients F^m and F_m are the contravariant and covariant vector components. The basis vectors have the form

$$\boldsymbol{f}_m = \frac{\partial \mathbf{r}}{\partial u^m} = \frac{\partial x^n}{\partial u^m} \boldsymbol{e}_n \tag{7.28}$$

$$\boldsymbol{f}^m = \boldsymbol{\nabla} u^m = \frac{\partial u^m}{\partial x^n} \boldsymbol{e}_n. \tag{7.29}$$

We can replace the vector coefficients on the right side of Equation (7.28) with the elements of the aggregate Jacobian transformation matrix as defined by equation (7.26) to obtain

$$\boldsymbol{f}_m = \mathcal{J}_{nm} \boldsymbol{e}_n. \tag{7.30}$$

Correspondingly, the vector coefficients in equation (7.29) represent the elements of the Jacobian of the inverse transformation (i.e. $\boldsymbol{\mathcal{J}}^{(-1)}$), and the following identities hold:

$$\boldsymbol{f}^m \cdot \boldsymbol{f}_m = \delta^m_n \qquad\qquad \boldsymbol{f}^k \boldsymbol{f}_k = \boldsymbol{f}_k \boldsymbol{f}^k = \mathbb{I} \tag{7.31}$$

Where δ^m_n is the Kronecker delta, and $\mathbb{I}$ is the identity matrix. Therefore, we can also express each basis of vectors in terms of the others:

$$\begin{aligned} \boldsymbol{f}^1 &= \mathcal{J}^{-1} \boldsymbol{f}_2 \times \boldsymbol{f}_3 & \boldsymbol{f}_1 &= \mathcal{J} \boldsymbol{f}^2 \times \boldsymbol{f}^3 \\ \boldsymbol{f}^2 &= \mathcal{J}^{-1} \boldsymbol{f}_3 \times \boldsymbol{f}_1 & \boldsymbol{f}_2 &= \mathcal{J} \boldsymbol{f}^3 \times \boldsymbol{f}^1. \\ \boldsymbol{f}^3 &= \mathcal{J}^{-1} \boldsymbol{f}_1 \times \boldsymbol{f}_2 & \boldsymbol{f}_3 &= \mathcal{J} \boldsymbol{f}^1 \times \boldsymbol{f}^2 \end{aligned} \tag{7.32}$$

The factor of $\mathcal{J}$ enters the equation due to conditions (7.31) needing to hold. It then follows that taking the cross product of two general vectors $\mathbf{a} \times \mathbf{b}$ in the contravariant basis can be written

$$\mathbf{c} \times \mathbf{d} = c^m d^n \boldsymbol{f}_m \times \boldsymbol{f}_n = c^m b^n \mathcal{J}\, \varepsilon_{kmn} \boldsymbol{f}^k. \tag{7.33}$$

Once we have the new basis, we compute the components of the metric tensor $\mathbf{g}$

$$g_{mn} = (\boldsymbol{f}_m \cdot \boldsymbol{f}_n) = \mathcal{J}_{qm}\mathcal{J}_{qn} \qquad g^{mn} = (\boldsymbol{f}^m \cdot \boldsymbol{f}^n) \tag{7.34}$$

with determinant

$$g \equiv [(\boldsymbol{f}_1 \times \boldsymbol{f}_2) \cdot \boldsymbol{f}_3]^2 = \mathcal{J}^2. \tag{7.35}$$

The metric relates the covariant and contravariant vector forms via

$$F^m = g^{mn}F_n \qquad F_m = g_{mn}F^n \tag{7.36}$$

Because equation (7.26) defines an "aggregate Jacobian" representing the transformation from the initial curvilinear coordinate system to the cartesian coordinate system, we can use it to obtain the basis vectors $\boldsymbol{f}^m$ of the curvilinear coordinate system u^m. As such, not only can we use the results of §7.2.1, but we can also make the further statement

$$\tilde{\rho} = \frac{1}{\mathcal{J}} = \frac{1}{\sqrt{g}} \tag{7.37}$$

due to our transformation technique. That is, the square root of the determinant of the metric tensor is equal to the unscaled density structure $\tilde{\rho} = \rho/\rho_0$, where ρ_0 is the density scaling constant as fit by PolCat.

In this new basis, the unperturbed, ordered magnetic field vector is expressed with initial constant magnetic field strength scale B_0 as

$$\mathbf{B} = B_0\frac{\mathcal{J}_{n3}\boldsymbol{e}^n}{\mathcal{J}} = B_0\frac{\boldsymbol{f}_3}{\sqrt{g}} = \tilde{\rho}B_0\boldsymbol{f}_3 = B^3\boldsymbol{f}_3, \tag{7.38}$$

where we define the term $B^3 = \tilde{\rho}B_0$ to express $\mathbf{B}$ in the general vector form of equation (7.27). Therefore, curvilinear basis vector $\boldsymbol{f}_3$ describes the direction of the magnetic field at all points, and correspondingly $\boldsymbol{f}^1$ and $\boldsymbol{f}^2$ are perpendicular to the field at all points by equations (7.31). The corresponding vector magnitude is

$$|\mathbf{B}| = \sqrt{\mathbf{B}\cdot\mathbf{B}} = \tilde{\rho}B_0\sqrt{\boldsymbol{f}_3 \cdot \boldsymbol{f}_3} = \tilde{\rho}B_0\sqrt{g_{33}}. \tag{7.39}$$

The constant factor B_0 originates from a main difference between our formulation and that of Scheurwater (1990). Scheurwater (1990) incorporates the magnetic field strength into the coordinate transformations, whereas PolCat does not due to the model-building convention outlined in equations (7.24) and (7.25). We also note that the factor of B_0 used here is the same B_0 used in the implementation of the virial analysis (§4.4), and represents the scaling

Identity	Curvelinear Definition	
Magnetic Flux Density	$\mathbf{B} \cdot d\mathbf{S} = B_0 du^1 du^2$	(7.41)
Line Element	$ds^2 = g_{mn}\, du^m du^n$	(7.42)
Surface Element	$d\mathbf{S} = \frac{1}{2}\,\tilde{\rho}^{-1}\,\varepsilon_{mnk}\, du^m du^n \boldsymbol{f}^k$	(7.43)
Volume Element	$dV = \tilde{\rho}^{-1}\, du^1 du^2 du^3$	(7.44)
Cross Product (contravariant vectors)	$\mathbf{c} \times \mathbf{d} = \tilde{\rho}^{-1}\,\varepsilon_{kmn} c^m d^n \boldsymbol{f}^k$	(7.45)
Divergence	$\boldsymbol{\nabla} \cdot \mathbf{F} = \tilde{\rho} \frac{\partial}{\partial u^m}\left(\tilde{\rho}^{-1}\, F^m\right)$	(7.46)
Curl	$\boldsymbol{\nabla} \times \mathbf{F} = \tilde{\rho}\,\varepsilon^{mnk} \frac{\partial F_n}{\partial u^m} \boldsymbol{f}_k$	(7.47)
Gradient	$\boldsymbol{\nabla}\mathbf{F} = \boldsymbol{f}^m \frac{\partial \mathbf{F}}{\partial u^m}$	(7.48)

Table 7.1: Curvilinear vector identities, substituting $\tilde{\rho} = 1/\sqrt{g}$ into the corresponding identities listed in Scheurwater (1990)

required to convert the computed model magnetic field from dimensionless to dimensional coordinates (Gauss). Correspondingly, the Alfvén velocity expressed in terms of the new basis is

$$\mathbf{c}_{A0} = \frac{\mathbf{B}}{\sqrt{4\pi\rho}} = \frac{B^3}{\sqrt{4\pi\rho_0\tilde{\rho}}}\boldsymbol{f}_3 = \frac{\tilde{\rho}^{1/2} B_0}{\sqrt{4\pi\rho_0}}\boldsymbol{f}_3 = c_{A0}^3 \boldsymbol{f}_3, \tag{7.40}$$

with a magnitude of $c_{A0} = \sqrt{g_{33}} c_{A0}^3$. Further identities in the new basis are summarized in Table 7.1 as quoted in Scheurwater (1990) modified using equation (7.37).

7.2.3 MHD Equations in Curvilinear Coordinates

To derive the proper curvilinear equations, we once again operate on equations (7.1) to (7.3) in the same manner as in Section 7.1. This time, our goal is to reduce the equations to a form where perturbation methods may be applied to the velocity amplitudes. To draw direct comparison to the proof of Section 7.1 and to extend to other ISM systems where

self-gravity is not important, we keep density perturbation while omitting the gravitational perturbation. Our motivation for omitting the gravitational term in this case is an extension of the proof in Section 7.1, and is outlined in Section 7.2.4.1. The full derivations of the curvilinear MHD equations are outlined in Appendix D, and we summarize the results below.

Differentiating equation (7.8) by time, we obtain

$$\frac{\partial^2 \mathbf{V}}{\partial t^2} = -\frac{\sigma_0^2}{\rho_0 \tilde{\rho}} \boldsymbol{\nabla} \frac{\partial \rho_1}{\partial t} - \frac{1}{4\pi \rho_0 \tilde{\rho}} \left[\mathbf{B} \times \left(\boldsymbol{\nabla} \times \frac{\partial \mathbf{b}}{\partial t} \right) + \frac{\partial \mathbf{b}}{\partial t} \times (\boldsymbol{\nabla} \times \mathbf{B}) \right]. \tag{7.49}$$

Expanding this out into our curvilinear coordinate representation yields

$$\begin{aligned} \frac{\partial^2 V^k}{\partial t^2} = = g^{kp} \frac{\sigma^2}{\tilde{\rho}} \left[\frac{\partial V^q}{\partial u^q} \frac{\partial \tilde{\rho}}{\partial u^p} + \tilde{\rho} \frac{\partial^2 V^q}{\partial u^p \partial u^q} \right] - g^{kp} \frac{B^3}{4\pi \rho_0 \tilde{\rho}} \frac{\partial b^q}{\partial t} \left(\frac{\partial g_{3q}}{\partial u^p} - \frac{\partial g_{pq}}{\partial u^3} \right) \\ - g^{kp} \frac{B^3}{4\pi \rho_0 \tilde{\rho}} \left[g_{3q} \frac{\partial}{\partial u^p} \left(\frac{\partial b^q}{\partial t} \right) - g_{pq} \frac{\partial}{\partial u^3} \left(\frac{\partial b^q}{\partial t} \right) \right] \\ - g^{kp} \frac{1}{4\pi \rho_0 \tilde{\rho}} \frac{\partial b^q}{\partial t} \left[B^3 \left(\frac{\partial g_{q3}}{\partial u^p} - \frac{\partial g_{p3}}{\partial u^q} \right) + \left(g_{q3} \frac{\partial B^3}{\partial u^p} - g_{p3} \frac{\partial B^3}{\partial u^q} \right) \right] \end{aligned} \tag{7.50}$$

where the time-derivative of the magnetic field (7.3)) has the form

$$\frac{\partial b^q}{\partial t} = B^3 \left(\frac{\partial V^q}{\partial u^3} - \frac{\partial V^m}{\partial u^m} \delta_3^q \right). \tag{7.51}$$

While this equation is too complex to be useful in its current form, we can simplify it somewhat by applying the eikonal approximation. This assumes that the local wavelength of the perturbations is much smaller than the scale on which the magnetic field and density spatially changes.

7.2.4 The Eikonal Approximation

The Scheurwater (1990) method for propagating waves down field lines originates from applying the eikonal approximation and using perturbation methods to expand the velocity amplitudes of equation (7.52) into an asymptotic series. The solutions for the velocity and wavevector fall out from the 0^{th} and 1^{st} order terms. While our more complicated wave equation is too complex to obtain the differential equations for the velocity amplitudes without significant struggle, we *can* obtain the differential equations for the wavevector in the same fashion of Scheurwater (1990). We have provided mathematical proof in Appendix E, and summarize the logic an main findings here for brevity.

Assuming a plane-wave form for $\mathbf{V}$ with a spatially dependent amplitude, we can repre-

sent the contravariant components of the velocity vector as

$$V^k(\mathbf{x},t) = v^k(\mathbf{x})e^{i\psi(\mathbf{x},t)} \tag{7.52}$$

where v^k are the contravariant velocity amplitudes and ψ is the phase, such that

$$\mathbf{k} = \boldsymbol{\nabla}\psi = f^m\frac{\partial\psi}{\partial u^m}, \qquad \omega = -\frac{\partial\psi}{\partial t}. \tag{7.53}$$

The eikonal approximation assumes the local wavelength $\lambda = 2\pi/k$ is small compared to the scale of the spatial changes in the magnetic field and density $(\lambda_\rho, \lambda_B)$. When $\mathbf{k}$ and v^k are on the order of $\varepsilon = (k\lambda)^{-1} \ll 1$, where λ represents the minimum between λ_ρ and λ_B, we can apply perturbation methods to expand the velocity amplitudes in an asymptotic series:

$$v^k = \sum_n^\infty \varepsilon^n v^k_{(n)} \tag{7.54}$$

and scaling the physical scales by ε to enforce operations on small scales, we define

$$\overline{u^m} = \varepsilon u^m \tag{7.55}$$

$$\overline{\psi} = \varepsilon\psi \tag{7.56}$$

with velocity amplitudes

$$\overline{v^m_n} = v^m_n. \tag{7.57}$$

These definitions keep $\boldsymbol{\nabla}\psi = \overline{\boldsymbol{\nabla}}\,\overline{\psi} = \mathbf{k}$. Making the further transformation

$$\bar{t} = \varepsilon t \tag{7.58}$$

keeps consistency for the angular velocity $\frac{\partial\psi}{\partial t} = \frac{\partial\overline{\psi}}{\partial\bar{t}} = -\omega$.This change of variable is useful, because of the effect it has on the velocity series. Single derivatives result in

$$\frac{\partial V^k}{\partial u^p} = \varepsilon\sum_n^\infty \varepsilon^n \frac{\partial}{\partial\overline{u^q}}(v^k_{(n)}e^{i\overline{\psi}\varepsilon^{-1}}) \tag{7.59}$$

$$= \sum_n^\infty \varepsilon^n \left[\varepsilon\frac{\partial v^k_{(n)}}{\partial\overline{u^p}} + ik_p v^k_{(n)}\right] e^{i\overline{\psi}\varepsilon^{-1}} \tag{7.60}$$

where we have substituted $\frac{\partial\overline{\psi}}{\partial\overline{u^p}} = k_p$. This results in only the second term contributing to the 0^{th} order velocity component. Higher order derivatives produce similar results, with the

end effect being that the 0^{th} order expansion of equation (7.49) has the much simpler form

$$0 = \omega^2 v^k_{(0)} - (\sigma_0^2 + c^2_{A0})k^k k_m v^m_{(0)} - (c^3_{A0}k_3)\left[c^3_{A0}k_3 v^k_{(0)} - c^3_{A0}v_{(0)3}k^k - c^3_{A0}k_m v^m_{(0)}\delta^k_3\right], \quad (7.61)$$

which is just the version of equation (7.14) for the uniform field and density case written in tensor notation (see Appendix E for full proof).

We can also write this equation in operator form as $\Lambda^k_{(0)_m} v^m_{(0)} = 0$, where

$$\Lambda^k_{(0)_m} = \omega^2\delta^k_m - (\sigma_0^2 + c^2_{A0})k_m k^k - (c^3_{A0}k_3)^2\delta^k_m + {c^3_{A0}}^2 k_3 k^k g_{3m} + k_m k_3 {c^3_{A0}}^2\delta^k_3. \quad (7.62)$$

In Scheurwater (1990), this sets up an eigenvalue problem where the roots are the Alfvén and fast modes. While our full expression is more complex than the block-diagonal form of (Scheurwater, 1990), the Alfvén condition $\omega^2 - (\mathbf{c}_{A0}\cdot\mathbf{k}) = 0$ nevertheless falls out naturally as the first root. In order for equation (7.61) to meet the condition $\omega^2 - (\mathbf{c}_{A0}\cdot\mathbf{k}) = 0$, both $\mathbf{k}$ and $\mathbf{c}_{A0}$ must be perpendicular to $\mathbf{v}_{(\mathbf{0})}$. The two other roots represent the fast and slow modes, but we are only concerned with the propagation of the Alfvén mode for this work. Additionally, it is worth noting that realistic MHD turbulence spectra such as the Kolmogorov spectrum ($E(k) \propto k^{-5/3}$) contain most of their power in the long-wavelength modes (Elmegreen and Scalo, 2004). As a result, while the derivations of this section apply on the small scales, we need to investigate further before we are confident that Scheurwater's result of $\omega = \mathbf{c}_{A0}\cdot\mathbf{k}$ being conserved along field lines holds at larger scales. Nevertheless, this approach allows for preliminary exploration of the effects of magnetic field perturbations on their resultant polarization maps.

7.2.4.1 On The Neglect of Gravitational Perturbations

We have previously claimed that the gravitational term in equation (7.49) can be safely neglected under the eikonal approximation, and we outline our argument here. Returning to the continuity equation

$$\frac{\partial\rho_1}{\partial t} = -\boldsymbol{\nabla}\cdot(\rho\mathbf{V}) \quad (7.63)$$

and applying the vector identity for divergence from Table 7.1, we obtain

$$\frac{\partial\rho_1}{\partial t} = \rho_0\tilde{\rho}\frac{\partial V^m}{\partial u^m} \quad (7.64)$$

for the curvilinear coordinate frame. For the derivation of this expression, see Appendix D. Assuming that the density perturbation ρ_1 (and gravitational perturbation Φ_1) have spatially dependent amplitudes with a similar series expansions to the velocity amplitude $\mathbf{v}$ (equation

(7.54)), we obtain

$$\varepsilon \sum_n^\infty \varepsilon^n i\omega\varepsilon^{-1}\rho_{1_{(n)}} e^{i\overline{\psi}\varepsilon^{-1}} = -\rho_0\tilde{\rho}\ \varepsilon \sum_n^\infty \varepsilon^n \left[\frac{\partial v^m_{(n)}}{\partial u^m} + i\varepsilon^{-1}k_m v^m_{(n)}\right] e^{i\overline{\psi}\varepsilon^{-1}} \tag{7.65}$$

where $\rho_{1_{(n)}}$ are the n^{th} order asymptotic series coefficients of ρ_1(as in equation (7.54)). Therefore, the 0^{th} order (ε^0) equation is

$$\omega\rho_{1_{(0)}} = \mathbf{k}\cdot\mathbf{v}_{(0)}. \tag{7.66}$$

As before, the pure Alfvén mode requires $\mathbf{k}\perp\mathbf{v}_{(0)}$, and so the 0^{th} order density perturbation is equal to zero. From the above manipulations, in can easily be proven that the corresponding 0^{th} order term in Poisson's equation is therefore

$$-k^2\Phi_{1_{(0)}} = -4\pi G\rho_{1_{(0)}} = 0 \tag{7.67}$$

and gravity perturbations can be neglected in the eikonal approximation.

7.2.4.2 Magnetic Field Vector

From equation (7.51),

$$\frac{\partial b^k}{\partial t} = B^3\left(\frac{\partial V^k}{\partial u^3} - \frac{\partial V^m}{\partial u^m}\delta^k_3\right). \tag{7.68}$$

Keeping with the eikonal approximation, we convert to $\overline{u^m}$ and $\bar{t}$, and expand into the series representation used before

$$\varepsilon\frac{\partial b^k}{\partial\bar{t}} = \sum_n^\infty B^3\left[\varepsilon^{n+1}\frac{\partial[v^k_{(n)}e^{i\overline{\psi}\varepsilon^{-1}}]}{\partial\overline{u^3}} - \varepsilon^{n+1}\frac{\partial[v^m_{(n)}e^{i\overline{\psi}\varepsilon^{-1}}]}{\partial\overline{u^m}}\delta^k_3\right] \tag{7.69}$$

$$= \sum_n^\infty B^3\left[\varepsilon^{n+1}\left(\frac{\partial v^k_{(n)}}{\partial\overline{u^3}} - \frac{\partial v^m_{(n)}}{\partial\overline{u^m}}\delta^k_3\right)\right. \tag{7.70}$$

$$\left. + i\varepsilon^n\left(k_3 v^k_{(n)} - k_m v^m_{(n)}\delta^k_3\right)\right] e^{i\overline{\psi}\varepsilon^{-1}}.$$

The only time-dependent term in this expression is $e^{i\overline{\psi}\varepsilon^{-1}}$, which has $\int e^{i\overline{\psi}\varepsilon^{-1}}d\bar{t} = -i\varepsilon e^{i\overline{\psi}\varepsilon^{-1}}/\omega$. Integrating both sides of the above equation by $\bar{t}$ yields

$$b^k = -\frac{iB^3}{\omega}\sum_n^\infty\left[\varepsilon^{n+1}\left(\frac{\partial v^k_{(n)}}{\partial\overline{u^3}} - \frac{\partial v^m_{(n)}}{\partial\overline{u^m}}\delta^k_3\right) + i\varepsilon^n\left(k_3 v^k_{(n)} - k_m v^m_{(n)}\delta^k_3\right)\right] e^{i\overline{\psi}\varepsilon^{-1}}. \tag{7.71}$$

Taking the 0th order coefficients from above, we then have

$$b^k \approx -\frac{B^3}{\omega}\left(k_3 v^k_{(0)} - k_m v^m_{(0)} \delta^k_3\right) e^{i\psi} \tag{7.72}$$

where we have substituted $\overline{\psi}/\varepsilon = \psi$. According to the Alfvén condition of the wave equation, the velocity vector $\mathbf{v}_{(0)}$ must be perpendicular to $\mathbf{k}$ and $\mathbf{B}$. Therefore $k_m v^m_{(0)} = \mathbf{k} \cdot \mathbf{v}_{(0)} = 0$, leaving

$$b^k = -\frac{k_3}{\omega} B^3 v^k_{(0)} e^{i\psi}. \tag{7.73}$$

The quantity k_3/ω is $(c^3_{A0})^{-1}$, applying this to equation (7.73), and expressing in vector form produces

$$\mathbf{b} = -\frac{1}{c^3_{A0}} B^3 \, \mathbf{v}_{(0)} e^{i\psi}. \tag{7.74}$$

We note that the ratio $B^3/c^3_{A0} = B/c_{A0}$ since both vectors lie along $\boldsymbol{f}_3$.

With $\mathbf{v}_{(0)}$ perpendicular to both $\mathbf{k}$ and $\mathbf{B}$, and under the assumption that $\mathbf{k} \parallel \mathbf{B}$, the perturbation must lie in the plane normal to $\boldsymbol{f}_3$. Using this to define a set of orthonormal unit vectors perpendicular to the field lines $\mathbf{p_n}$, we choose the first vector to be parallel to the x-axis projected onto the propagation plane, and the second to be perpendicular to both:

$$\hat{\mathbf{p}}_1 = \frac{\hat{\mathbf{x}} - (\hat{\mathbf{x}} \cdot \boldsymbol{f}_3)\boldsymbol{f}_3}{g_{33}} \tag{7.75}$$

$$\hat{\mathbf{p}}_2 = \frac{\boldsymbol{f}_3 \times \mathbf{p}_1}{|\boldsymbol{f}_3 \times \hat{\mathbf{p}}_1|}. \tag{7.76}$$

With these definitions, we can express a unit vector pointing in the direction of the velocity vector as

$$\hat{\mathbf{v}} = \cos(\phi)\mathbf{p}_1 + \sin(\phi)\mathbf{p}_2, \tag{7.77}$$

with ϕ the orientation angle relative to $\mathbf{p}_1$.

7.2.4.3 Propagating the Velocity Vector

In order to propagate the velocity vector down the field line, we must obtain both the change in phase and the change in velocity amplitude. The former can be computed by using the Scheurwater (1990) methods, but the latter involves the first-order component of equation (7.50), which is much more complex in our case than in Scheurwater (1990). Instead, we opt to do a geometrical analysis to obtain the propagation of the amplitudes, under the assumption of constant energy density as the vector propagates down the magnetic flux tubes.

Obtaining the Alfvén Ray equations For Alfvén waves, the propagation is all along the magnetic field direction and bends with it, maintaining

$$\omega = (\mathbf{c}_{A0} \cdot \mathbf{k}). \tag{7.78}$$

A similar analogy can be made with how light bends travelling through a non-isotropic medium, and so we can take a similar approach by using ray-tracing. Scheurwater (1990) derived the necessary Alfvén ray equations, which I present here. For the complete proof, see Appendix F.

The total derivative along the field line is

$$\frac{d\mathbf{r}}{dt} = \mathbf{c}_{A0} \tag{7.79}$$

$$\frac{d\mathbf{k}}{dt} = -\boldsymbol{\nabla}\mathbf{c}_{A0} \cdot \mathbf{k}. \tag{7.80}$$

Because the field is aligned with the u^3 coordinate, the arc length element is $ds = \sqrt{g_{33}}du^3$ (Table 7.1) which gives

$$\frac{d\mathbf{k}}{ds} = -\frac{\boldsymbol{\nabla}\mathbf{c}_{A0}}{c_{A0}} \cdot \mathbf{k} \tag{7.81}$$

$$\frac{d\mathbf{r}}{ds} = \boldsymbol{f}_3 \frac{1}{\sqrt{g_{33}}}. \tag{7.82}$$

These equations can be written in vector component form as

$$\frac{dk_m}{ds} = -\frac{k_3}{\sqrt{g_{33}}} \frac{\partial \ln(c_{A0}^3)}{\partial u^m}, \text{ and} \tag{7.83}$$

$$\frac{du^m}{ds} = \frac{1}{\sqrt{g_{33}}} \delta_3^m. \tag{7.84}$$

Equations (7.84) and (7.83) can now be used to propagate the Alfvén waves down the field lines.

Solving the Alfvén Ray Equations Starting with $p = 3$ we see that we can write (7.83) in separable form. Separating the variables and integrating both sides produces

$$\int_0^s \frac{1}{k_3(s')} \frac{dk_3(s')}{ds'} ds' = -\int_0^s \frac{\partial \ln(c_{A0}^3(s'))}{\partial u^3} \frac{ds'}{\sqrt{g_{33}}}. \tag{7.85}$$

We have $ds = \sqrt{g_{33}}\, du^3$, therefore

$$\ln(k_3(s)) - \ln(k_3(0)) = -\ln(c_{A0}^3(s)) + \ln(c_{A0}^3(0)), \tag{7.86}$$

$$\implies k_3(s) = k_3(0)\frac{c_{A0}^3(0)}{c_{A0}^3(s)} = k_3(0)\frac{\tilde{\rho}(0)^{1/2}}{\tilde{\rho}(s)^{1/2}}. \tag{7.87}$$

While we can use (7.83) to also obtain k_1 and k_2 as functions of propagation distance s, k_3 is important for determining the change in phase of the velocity propagation down the field line. Calling back to equations (7.53) the phase change along the u^3 direction can be determined by

$$\psi - \psi(0) = \int k_3 du^3 = k_3(0)\tilde{\rho}(0)^{1/2} \int \tilde{\rho}(u^3)^{-1/2} du^3. \tag{7.88}$$

Since we're only looking at the Alfvén mode with propagation down the field line, u^1 and u^2 are constant. If we assume each component of the turbulent perturbation at $s = 0$ enters the system with an initial phase ψ_0 independent of its (u^1, u^2) position, we can use (7.88) to propagate the wave down the field lines via

$$\mathbf{V_{(0)}} = \mathbf{v_{(0)}} e^{i\psi}. \tag{7.89}$$

Amplitude Propagation While equation (7.88) gives us the phase propagation, we have yet to obtain an equivalent relation for velocity. In order to obtain such an equation, let us consider that the wave energy propagating through the flux tube must be conserved as it travels from one end to the other.

While Scheurwater (1990) does outline a method for obtaining the velocity amplitudes from the first-order differential equations in the eikonal approximation, applying this method to our case results in a complicated differential equation that is difficult to solve in the same way. Instead, we compute the velocity amplitudes during propagation down field lines assuming conservation of energy flux density and the geometrical formulations of the previous section. This assumption is consistent with the findings of Zweibel and McKee (1995) and McKee and Zweibel (1995), where the wave energy is constant along field lines under similar assumptions.

We assume that the total energy flux within the tube is conserved at both ends, which allows us to define this last quantity by geometry. We already know magnetic flux density is conserved at both ends of the flux tube defined by a cross sectional area. In the curvilinear system the magnetic flux density (Φ_M) is

$$d\Phi_M = \mathbf{B} \cdot d\mathbf{S} = B_0 du^1 du^2 = B_0 dA. \tag{7.90}$$

Coordinates u^1 and u^2 are constant along field lines (which also have cylindrical symmetry in the curvilinear system), meaning we can write du^1du^2 as a pseudo-area element $dA = du^1du^2 = 2\pi\alpha d\alpha$ where $\alpha = \sqrt{(u^1)^2 + (u^2)^2}$ is the cylindrical radius in the curvilinear system.[1]

For the energy flux, we can write power transfer across a cross-sectional area from Alfvén waves as

$$d\mathcal{P} = \epsilon\, \mathbf{c}_{A0} \cdot d\mathbf{S} = \frac{\epsilon\, B_0\tilde{\rho}}{\sqrt{4\pi\rho_0\tilde{\rho}}}\tilde{\rho}^{-1}du^1du^2 = \frac{\epsilon}{\sqrt{4\pi\rho_0\tilde{\rho}}}d\Phi_M. \tag{7.91}$$

This quantity is also conserved as the wave propagates down the flux tubes. Therefore, we can state

$$\frac{\partial\mathcal{P}}{\partial\Phi_M} = \frac{\epsilon}{\sqrt{4\pi\rho_0\tilde{\rho}}} = constant \tag{7.92}$$

and so

$$\mathcal{P} = \frac{\epsilon\Phi_M}{\sqrt{4\pi\rho_0\tilde{\rho}}} = \frac{\pi\epsilon B_0\alpha^2}{\sqrt{4\pi\rho_0\tilde{\rho}}} \tag{7.93}$$

where α is characteristic of the flux tube. As the waves propagate down the field flux tube (constant α), $\mathcal{P}_{\rm in} = \mathcal{P}_{\rm out}$. Therefore

$$\epsilon_{\rm in}\tilde{\rho}_{\rm in}^{-1/2} = \epsilon_{\rm out}\tilde{\rho}_{\rm out}^{-1/2}. \tag{7.94}$$

Assuming equipartion, the kinetic energy density of the wave is $\epsilon = 1/2\rho_0\tilde{\rho}v^2$, so it follows

$$\tilde{\rho}_{\rm in}^{1/2}v_{\rm in}^2 = \tilde{\rho}_{\rm out}^{1/2}v_{\rm out}^2, \tag{7.95}$$

which gives

$$\frac{v_{\rm out}}{v_{\rm in}} = \left(\frac{\tilde{\rho}_{\rm out}}{\tilde{\rho}_{\rm in}}\right)^{-1/4}. \tag{7.96}$$

Therefore, if we perturb the field with a turbulent spectrum of waves we can obtain the velocity amplitude at every u^3 position on the flux tube.

[1]Note that A is not a "true" area or circular cylindrical cross-section in the Cartesian system. However, it is a conserved quantity of the flux tube with changes in u^3.

Chapter 8

Propagation Code

In this chapter, we describe the methods applied towards computing the perturbed field lines. We make the notation change for the 0^{th} order velocity of the previous chapter from $v_{(0)}$ to simply v, with the understanding that we are still referring to the 0^{th} order velocity vector and amplitudes.

8.1 Computation Setup

The eikonal approximation applies in cases where the local wavelength λ is small compared to the distance scale over which density and field structure change significantly. In our case, we define the maximum wavelength λ_{max} to be the smallest dimension of a voxel on the coordinate grid in dimensionless units. This defines a minimum initial wavevector amplitude of $k_{\text{min}} = 2\pi/\lambda_{\text{max}}$.

Our computation grid is quite coarse, to match the resolution of the input dataset in the x-z plane. However, the wavelengths in the eikonal approximation are smaller than our grid resolution. In order to calculate the perturbation, we subdivide the three-dimensional model grid further, such that each individual voxel contains N^3 sub-voxels where N is 5. The perturbation is computed on this much finer grid, then the polarization map of the perturbed model is computed and binned back to the initial resolution. This method compensates for the small wavelengths of the perturbations, and approximates the nature of a physical observation of the system, where the results are typically binned to lower resolutions to enhance the signal-to-noise ratio of the data. As we are mainly concerned with the overall statistical effects of the perturbations on the polarization angles of the data, this approach allows us to obtain a reasonable estimate of the polarization angle deflections despite the small size of the perturbations relative to the final grid size.

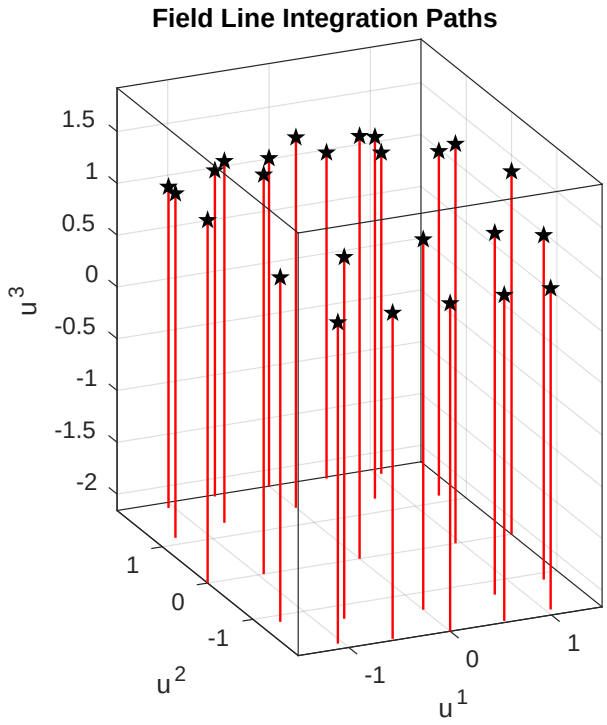


Figure 8.1: Field lines of integration to compute ψ and k_3 propagation. The black stars represent individual (u^1, u^2, u^3) coordinates in the grid. The bottom plane is the entry point for the wave. Because the propagation is computed in the curvilinear coordinates, the field lines appear straight.

8.2 Propagating the Perturbation

To calculate the propagation, we first operate on the coordinate grid to transform it back to the initial (u^1, u^2, u^3) system. The field line that corresponds to any individual coordinate in the grid has constant u^1 and u^2 coordinates down its entire length, as shown in Figure 8.1. For simplicity, we set the start point for the wave propagation at the overall minimum value of u^3 in the grid, and use these start and end points to compute an individual integration grid for each coordinate to calculate the phase propagation. An example is illustrated in Figure 8.1. Referring to equation (7.87), the phase is then calculated on these field line grids via

$$\psi = \psi(0) + k_3(0)\,\tilde{\rho}(0)^{1/2} \int_{u^3(0)}^{u^3(s)} \tilde{\rho}(s)^{-1/2} du^3. \tag{8.1}$$

For the transformations we currently use, the only transformation with a Jacobian determinant that depends on coordinates (i.e. not constant) is the density transformation (§6.1.1). Therefore, the dimensionless density structure is just $\tilde{\rho}^{\mathrm{BE}} = \tilde{\rho}/C_{\mathcal{J}}$, where $C_{\mathcal{J}}$ absorbs the constant Jacobian determinant components. As the wave propagates, k_3 (and therefore ψ)

remains proportional to the ratio of $\tilde{\rho}^{1/2}$ at the start and end points, $C_{\mathcal{J}}$ cancels, leaving

$$\psi = \psi_0 + k_3(0)[\tilde{\rho}^{\mathrm{BE}}(0)]^{1/2} \int_{u^3(0)}^{u^3(s)} [\tilde{\rho}^{\mathrm{BE}}(s)]^{-1/2} du^3. \tag{8.2}$$

When PolCat computes the reverse coordinate transformation for the density transformation, the high-resolution radial density profile is stored for use with the forward field transformation. We can therefore interpolate this radial profile onto the field line grids directly rather than using our coarser model grid, which improves the accuracy of the calculation. This method has the benefit that this calculation only needs to be performed once for a particular base model and used to compute every following field perturbation.

8.3 Characterizing the magnetic field perturbation

The Chandrasekhar-Fermi method demonstrates that deflections from the mean magnetic field direction are inversely proportional to the magnetic field strength. PolCat provides a model that includes scaling for the density and velocity dispersion, but not magnetic field strength. In the analysis of Chapter 7 we defined a constant scale B_0 that contains the physical scaling of the magnetic field. However, what is actually stored when PolCat generates a model is $\mathbf{B}/B_0 = \tilde{\rho}\boldsymbol{f}_3$, meaning our perturbed field $\mathbf{b}$ needs to be divided by B_0 as well to put it on the same scaling. From equations (7.74), (7.40), and (7.89) we find that

$$\frac{\mathbf{b}}{B_0} = -\frac{\sqrt{4\pi\rho_0}}{B_0}\, \tilde{\rho}^{1/2}\, v\, e^{i\psi}\hat{\mathbf{v}}, \tag{8.3}$$

where v is the velocity amplitude, and $\hat{\mathbf{v}}$ is the unit vector in the direction of the velocity perturbation. The constant $v_A = B_0/\sqrt{4\pi\rho_0}$ is just the physical scale of the Alfvén speed: $c^3_{A0} = v_A\tilde{\rho}^{1/2}$, where c^3_{A0} is the Alfvén speed coefficient of the $\boldsymbol{f}_3$ vector (§7.2.2). Substituting equation (7.96), the expression for the velocity propagation, the field perturbation vector becomes

$$\frac{\mathbf{b}}{B_0} = -\frac{v_0}{v_A}\, \tilde{\rho}(0)^{1/4}\, \tilde{\rho}^{1/4}\, e^{i\psi}\hat{\mathbf{v}} = \frac{v_0}{v_A}\, \tilde{b}\, e^{i\psi}\hat{\mathbf{v}} \tag{8.4}$$

where v_0 is the amplitude of the incoming velocity vector at $s = 0$ on the ray path, and $\tilde{b}$ is dependent only on the model structure. The strength of the magnetic field perturbation can therefore be dialled up or down via the ratio of the amplitude of the incoming velocity v_0 to the Alfvén speed scale v_A. To set reasonable values for this parameter, we can use the ratio of the energy of the Alfvén waves to the potential energy of the unperturbed magnetic field $\mathbf{B}$ contained in the model cube.

The magnetic energy of the unperturbed field $U_{\mathbf{B}}$ integrated over the cube is

$$U_{\mathbf{B}} = {B_0}^2 r_0^3 \int_{\tilde{V}_{cube}} \frac{(B/B_0)^2}{8\pi} d\tilde{V} \tag{8.5}$$

$$= {B_0}^2 r_0^3 \tilde{U}_{\mathbf{B}} \tag{8.6}$$

where $\tilde{U}_{\mathbf{B}}$ is the magnetic energy computed in PolCat's dimensionless coordinates (§3.4).[1] Since we are calculating the energy in the whole cube, we approximate the integral in equation (8.5) by

$$\tilde{U}_{\mathbf{B}} \approx \frac{1}{8\pi} \sum_i \tilde{B}_i^2 \Delta\tilde{V}_i, \tag{8.7}$$

where $\tilde{B}_i = B_i/B_0$ is the normalized value of the magnetic field strength at the i$^{\text{th}}$ voxel, and $\Delta\tilde{V}_i$ is the dimensionless volume that voxel. This is a coarser calculation than the more refined method we employed in Chapter 4, but it is sufficient as we are concerned with the whole-cube value instead of the interior-to-surface core value.

Alfvén waves are by nature electromagnetic, and therefore an individual wave has energy density

$$u_{\mathbf{b}} = \frac{E^2}{8\pi} + \frac{b^2}{8\pi} \tag{8.8}$$

In the MHD approximation the electric field component of the wave is $\mathbf{E} = -\frac{1}{c}\mathbf{v} \times \mathbf{B}$[2]. As we have previously defined, $\mathbf{v} \perp \mathbf{B}$, and so $E^2 = \frac{1}{c^2} v^2 B^2$. We are not concerned with relativistic velocities, so we may neglect this term. Therefore the total wave energy in the cube is

$$U_{\mathbf{b}} = \int_{V_{cube}} \frac{b^2}{8\pi} dV \approx {B_0}^2 r_0^3 \frac{v_0^2}{v_A^2} \sum_i \frac{\tilde{b_i}^2}{8\pi} \Delta\tilde{V}_i \tag{8.9}$$

$$= {B_0}^2 \frac{v_0^2}{v_A^2} \tilde{U}_{\mathbf{b}}. \tag{8.10}$$

The ratio of the two energies is therefore

$$\frac{U_{\mathbf{b}}}{U_{\mathbf{B}}} = \frac{v_0^2}{v_A^2} \frac{\tilde{U}_{\mathbf{b}}}{\tilde{U}_{\mathbf{B}}}. \tag{8.11}$$

The quantities $\tilde{U}_{\mathbf{b}}$ and $\tilde{U}_{\mathbf{B}}$ are inherent to the base model, and we can set the velocity scale

[1] $U_{\mathbf{B}}$ here is the same as the scalar magnetic potential energy in Chapter 4, we have just switched the notation to avoid confusion with mass in an upcoming section.

[2] See equation (7.9), combined with the Maxwell-Faraday equation

by choosing a value for $R_U = U_{\mathbf{b}}/U_{\mathbf{B}}$ and rearranging

$$\frac{v_0}{v_A} = \sqrt{R_U \frac{\tilde{U}_{\mathbf{B}}}{\tilde{U}_{\mathbf{b}}}}. \tag{8.12}$$

For the purposes of this analysis, we have chosen steps of R_U between 5-50%.

8.4 Single-Mode Alfvén Perturbations

Now that we have a method for perturbing the field with Alfvén waves, we want to know how the perturbations affect the polarization maps. For this portion of the analysis, we focused on perturbing the base magnetic fields with Alfvén waves of a single k magnitude. For the first part of this analysis we calculate the effect of a single wave polarized in the plane of the sky to maximize its effect on the polarization map. For the second part, we perturb the field multiple times with the same k amplitude, varying the phase and polarization of the wave, as a proof of concept for future work using a proper turbulent spectrum.

We applied these methods to the same four test geometries that we used in our virial analysis (Chapter 6). For simplicity, we constrained our analysis to the virial (VO, VA) base models (which share all parameters except orientation), rather than including the NC and NE datasets. In addition to the VO and VA orientations, we also generated ten random orientations for each of the cases studied, to help quantify the effect that the orientation has on the resulting perturbation of the polarization vectors.

8.4.1 Single wave perturbations

For this portion of the analysis, we perturbed each base model with an Alfvén wave of constant k and v amplitudes with random initial phase ψ_0, keeping the velocity vector along $\hat{\mathbf{p}}_1$ (equation 7.75). This maximizes the effect that the magnetic field perturbations have on the polarization vectors, regardless of the orientation of the base model.

For every test, we perturbed the model 50 times with random values of ψ_0 between $[-\pi, \pi]$ to produce 50 individual polarization position angle (χ_{pol}) maps. This method is equivalent to taking snapshots at different times as the wave travelled through the model. We then calculated a "deflection map" ($\Delta\chi_{pol}$) for each perturbation via

$$[\Delta\chi_{pol}(i,j)]_n = |\,[\chi_{pol}(i,j)]_n - [\chi_{pol}(i,j)]_{model}\,|\,, \tag{8.13}$$

where (i, j) represent pixel coordinates of the map, and n represents the n^{th} perturbation.

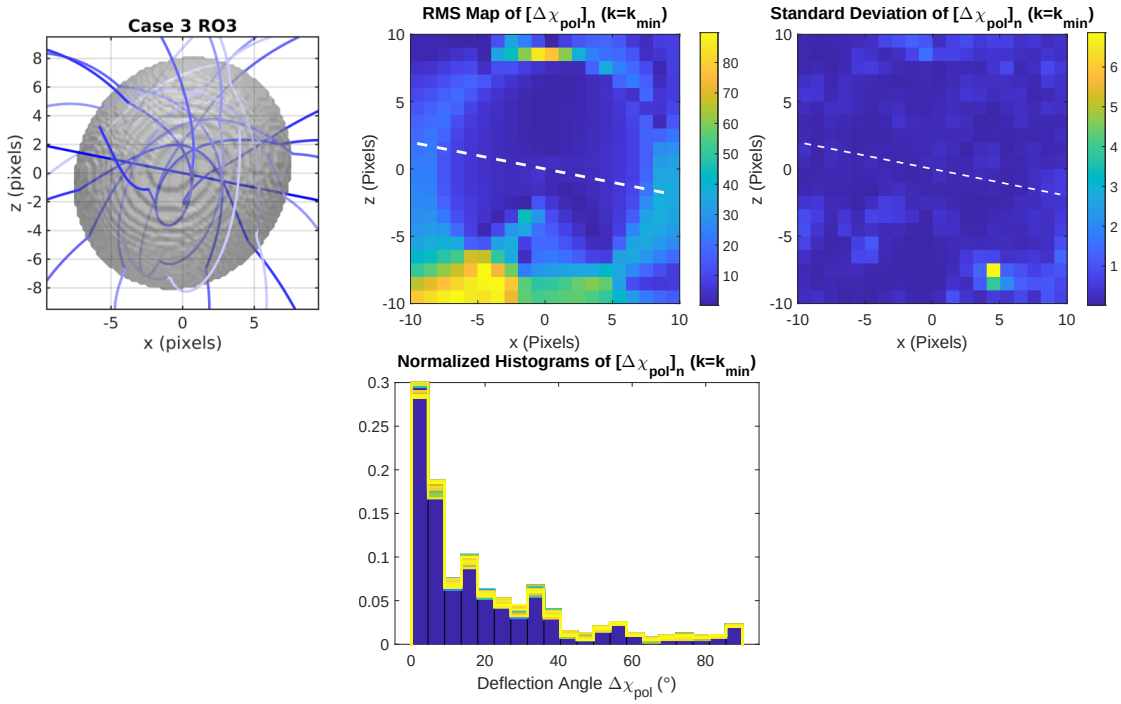


Figure 8.2: From left to right: the three-dimensional structure of the Case 3 RO3 orientation, with corresponding RMS deflection ($[\Delta\chi_{pol}]_{RMS}$) and standard deviation ($\sigma_{\Delta\chi_{pol}}$) maps, and histogram of each of the individual $[\Delta\chi_{pol}]_n$ (lines) overlaid onto that of the $[\Delta\chi_{pol}]_{RMS}$ Map (bars).

We then combined the 50 deflection maps by calculating the RMS value of each pixel

$$[\Delta\chi_{pol}(i,j)]_{RMS} = \sqrt{\frac{1}{N}\sum_{n}[\Delta\chi_{pol}(i,j)]_n^2}. \tag{8.14}$$

This combined map represents the RMS error of the perturbations with respect to the unperturbed model. For analysis purposes, we also calculated the standard deviation map $\sigma_{\Delta\chi_{pol}}$ of the individual $\Delta\chi_{pol}$ maps:

$$\sigma_{\Delta\chi_{pol}}(i,j) = \sqrt{\frac{1}{N-1}\sum_{n=1}^{N}([\Delta\chi_{pol}(i,j)]_n - \overline{\Delta\chi_{pol}}(i,j))^2}. \tag{8.15}$$

In all cases, all 50 individual perturbation maps (with random initial phase ψ_0) with the same v, k and R_U were similar to each other, but different from the unperturbed base model, regardless of the distribution of initial phases. The average of the standard deviation deflection maps were typically on the order of approximately 1° or less, but individual pixels could have maximum standard deviations of up to 10° for the hourglass models, and 20-30°

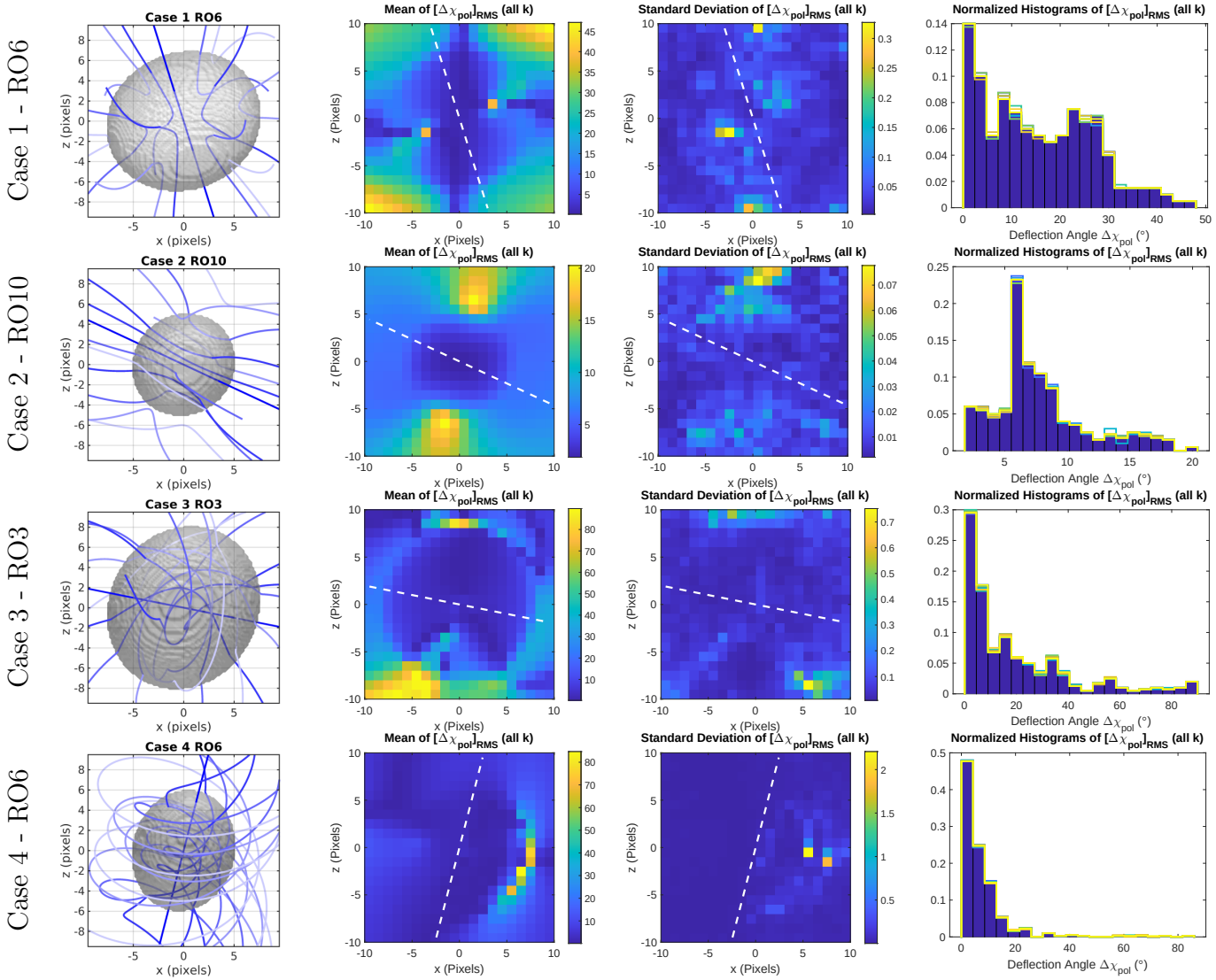


Figure 8.3: Examples of average and standard deviation maps of $[\Delta\chi_{pol}]_{RMS}$ for all k steps for select orientations of all four test cases with Case 1 in the top row, and Case 4 at the bottom. From left to right: the three-dimensional model of each base model, the average of the $[\Delta\chi_{pol}]_{RMS}$ for all k steps, the corresponding standard deviation, and the normalized histograms of each of the individual $[\Delta\chi_{pol}]_{RMS}$ maps plotted over the histogram of the mean map in the second column.

for the twisted field models. However, these represented extreme cases and were only one or two pixels out of the whole map. Because the wave is propagated on a grid smaller than the binned pixel sizes, the binning step averages out the effect of the varying initial phase, and we find that most pixels for most maps are visually similar.

8.4.1.1 Effect of Varying the Perturbation Wavelength

We produced maps for different steps of k between k_{min} and $100k_{min}$ at $R_U = 25\%$ to examine the effect that changing the wavelength of the perturbation would have on the polarization angle deflections. Additionally, at the maximum and minimum values of k, we also computed perturbations stepping R_U in increments of 0.05 between 0.05 and 0.5.

Overall, varying $k \geq k_{min}$ (subvoxel wavelength) at constant R_U had negligible effect on the resulting deflection map. For any given model orientation, the RMS deflection maps between k steps were visually similar, with standard deviations on the order of approximately 0.5° or less, with the occasional pixel having a standard deviation of up to 5°. This is likely also due to the size of the perturbation being smaller than the grid, which averaged out the overall effect. The main effect that varying k appeared to have was producing noisier standard deviation maps as each step increased without increasing the maximum standard deviation. The resulting RMS deflection maps at each k step were still visually similar. Figure 8.3 shows the average and standard deviation of the $[\Delta\chi_{pol}]_{RMS}$ maps for each k, along with the combined histograms of each $[\Delta\chi_{pol}]_{RMS}$ map for each k step for a sample of test data.

Figure 8.3 shows that the areas of enhancement in the deflection maps are slightly askew relative to the z-axis line. This is likely due to the combined effect of the model's azimuthal and inclination rotation angles, as the k-averaged deflection maps for the VO (zero orientation) datasets are all symmetric across the z-axis line.

8.4.1.2 Effect of Varying R_U

Following from the previous results, we generated maps at different energy ratios (and therefore velocity scales) using k amplitudes of 1 and 100 k_{min}, rather than the full spread we used previously (examples from the 0.05, 0.25, and 0.5 shown in Figure 8.4). As before, deflection maps with the same incoming velocity amplitudes at both 1 and $100k_{min}$ were consistent with each other. However, stepping R_U produced significant variation in the structure of the deflection map, beyond simply increasing the scale of the deflections. The precise effect depended on the core's orientation, but the pattern of enhancement shifted towards different pixels as the energy increased. This seems to indicate that as the energy scale increases,

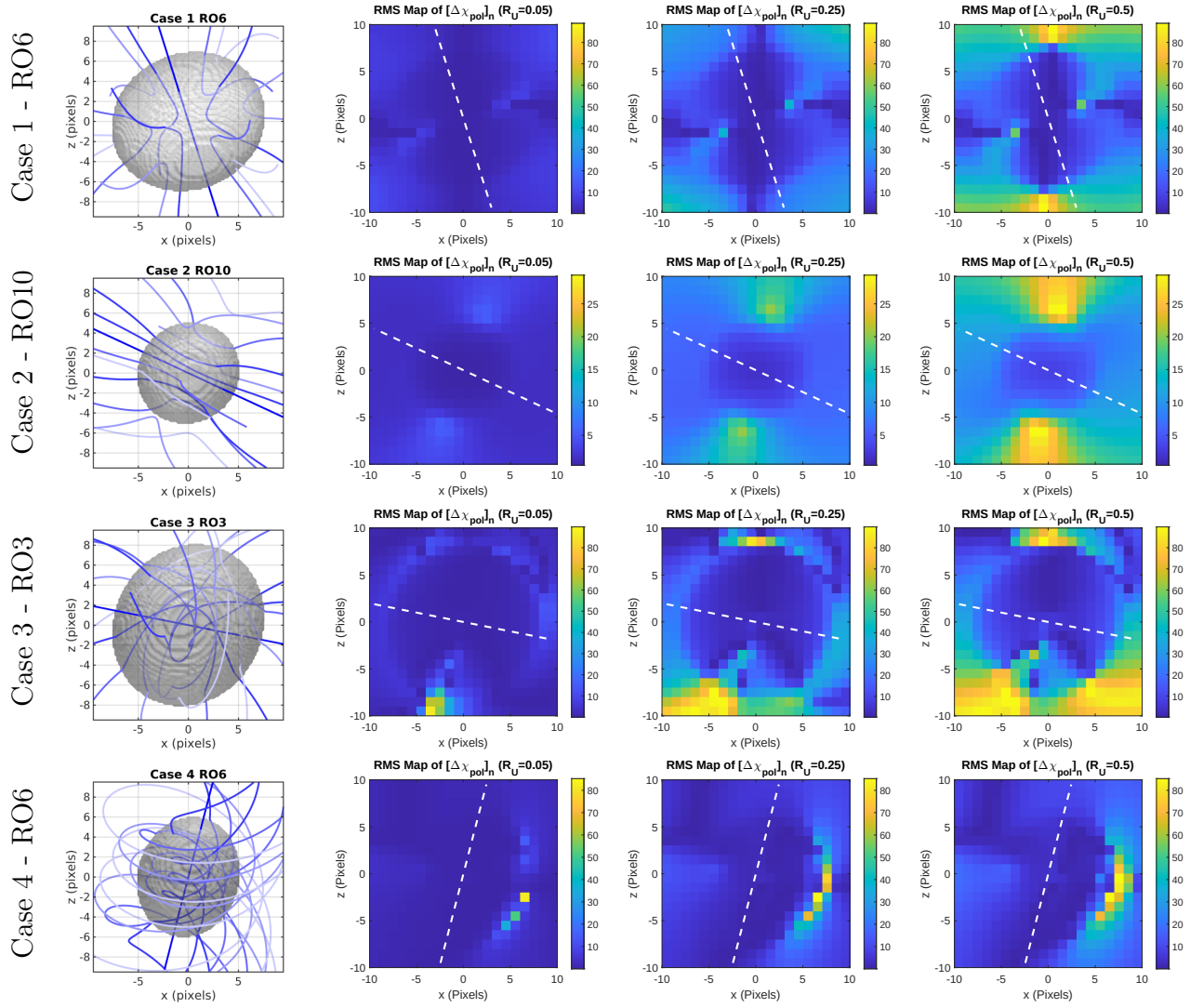


Figure 8.4: RMS Deflection maps for the models shown shown in Figure 8.3, for R_U values of 0.05 (left), 0.25 (centre), and 0.5 (right) shown on the same colour scale. As before, the dotted lines indicate the orientation of the core's z-axis. The three-dimensional field structures are shown here again for convenience.

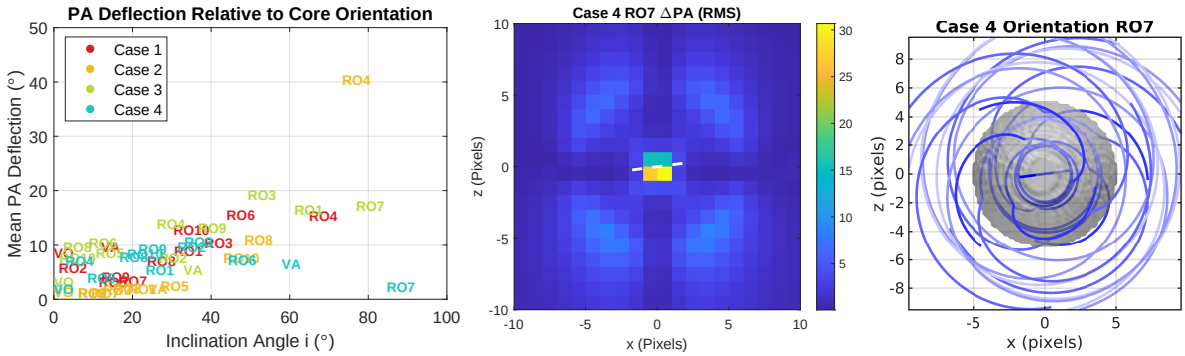


Figure 8.5: Mean polarization angle deflection as a function of orientation angle relative to the LOS (left), deflection map for the Case 4 RO7 orientation (centre) and corresponding field geometry as projected (right). The dotted line in the deflection map represents the orientation of the core's z-axis, terminated at the surface of the cube.

different areas of the field accumulate larger polarization angle deflections than they do at lower energies.

8.4.1.3 Model Orientation

Different orientations of a base model perturbed with the same wave parameters produced different deflection maps. The left plot of Figure 8.5 shows the mean value of each combined RMS deflection map plotted against the angle the base model's core z-axis makes with the LOS.

In general, maps for the VO orientation typically had the smallest average χ_{pol} deflections, while cores oriented with their z-axis close to the LOS typically had the largest. However, the Case 4 models had two exceptions, VA and RO7, where the average deflection decreased. The RMS map for the Case 4 RO7 model is shown in the centre of Figure 8.5. The reason for this discrepancy is not clear, but as these orientations are quite close to having the core z-axis pointing along the line of sight (as shown in the left panel of Figure 8.5), the wrapping of the field lines is likely strongly reinforcing the polarization position angles in the periphery, while cancelling out deflections caused by the perturbations when the field is integrated (Fiege and Pudritz, 2000a). While the Case 3 models show a trend more similar to the hourglass models, the two sets with similar orientations (RO1 and RO7) do also show a slight decrease in average deflection angle, but not to the extent that the Case 4 models do. With the deflection maps being so consistent, each orientation for a single base model produced a unique pattern that was often drastically different from the others.

8.4.2 Additive Perturbations

For perturbing the model with a series of Alfvén waves, we needed to make a slight change to the amplitude scaling. Instead of the incoming velocity amplitude for each wave being equal to v_0/v_A, which would add an overly large amount of energy to the system, we make the adjustment that the sum of the kinetic energy per unit mass of the incoming velocity amplitudes be equal to the magnetic energy of the wave per unit mass. This is not the precise wave energy of the total superimposed wave, but it is a reasonable approximation for our purposes. In this approximation, the mean kinetic energy per unit mass for N waves is therefore

$$\left\langle \frac{T}{M} \right\rangle = \frac{1}{2}\langle v_i^2 \rangle = \frac{B_0^2}{\rho_0}\frac{R_U \tilde{U}_{\mathbf{B}}}{N\tilde{M}_\rho} \tag{8.16}$$

$$\Rightarrow \frac{\langle v_i^2 \rangle}{v_A^2} = 8\pi \frac{R_U \tilde{U}_{\mathbf{B}}}{N\tilde{M}_\rho} \tag{8.17}$$

where ρ_0 is the PolCat density scale (§3.4), and $M_\rho = \rho_0 r_0^3 \tilde{M}_\rho$ represents the mass of the model, computed in the same fashion as the magnetic energies (§8.3). Our choice to scale the amplitudes with the average kinetic energy is motivated by our desire to extend this technique to actual turbulent k spectra, which define velocity as a function of wavenumber (Elmegreen and Scalo, 2004; Hennebelle and Falgarone, 2012).

We then generated $N = 50$ random values between $[-\pi, \pi]$ for the initial phase ψ_0, and orientation angle ϕ (§7.2.4.2). Due to results of the previous section showing that varying the perturbation wavelength had a negligible effect on the resulting deflection maps, we chose $k = k_{min}$ for all amplitudes. The starting model was then perturbed with each randomized wave in succession before the polarization map was computed and binned back to the original resolution.

We performed this computation for the same R_U steps as the previous section (0.05-5), repeating each computation 10 times for each step. While this is a small sample, this portion of the analysis functions something of a pilot study for future application to turbulent spectra.

Each repetition of the calculation at constant R_U produced a large variation in $\Delta\chi_{pol}$, such that the standard deviation of the 10 maps was only slightly lower than the level of the combined RMS map. While the areas of $\Delta\chi_{pol}$ enhancement were in similar locations to the single-wave perturbations, the RMS deflection maps of the additive perturbations were more symmetric about the midline perpendicular to the projected z-axis. Due to the randomized ϕ angle, the overall $\Delta\chi_{pol}$ level was smaller than that of their corresponding

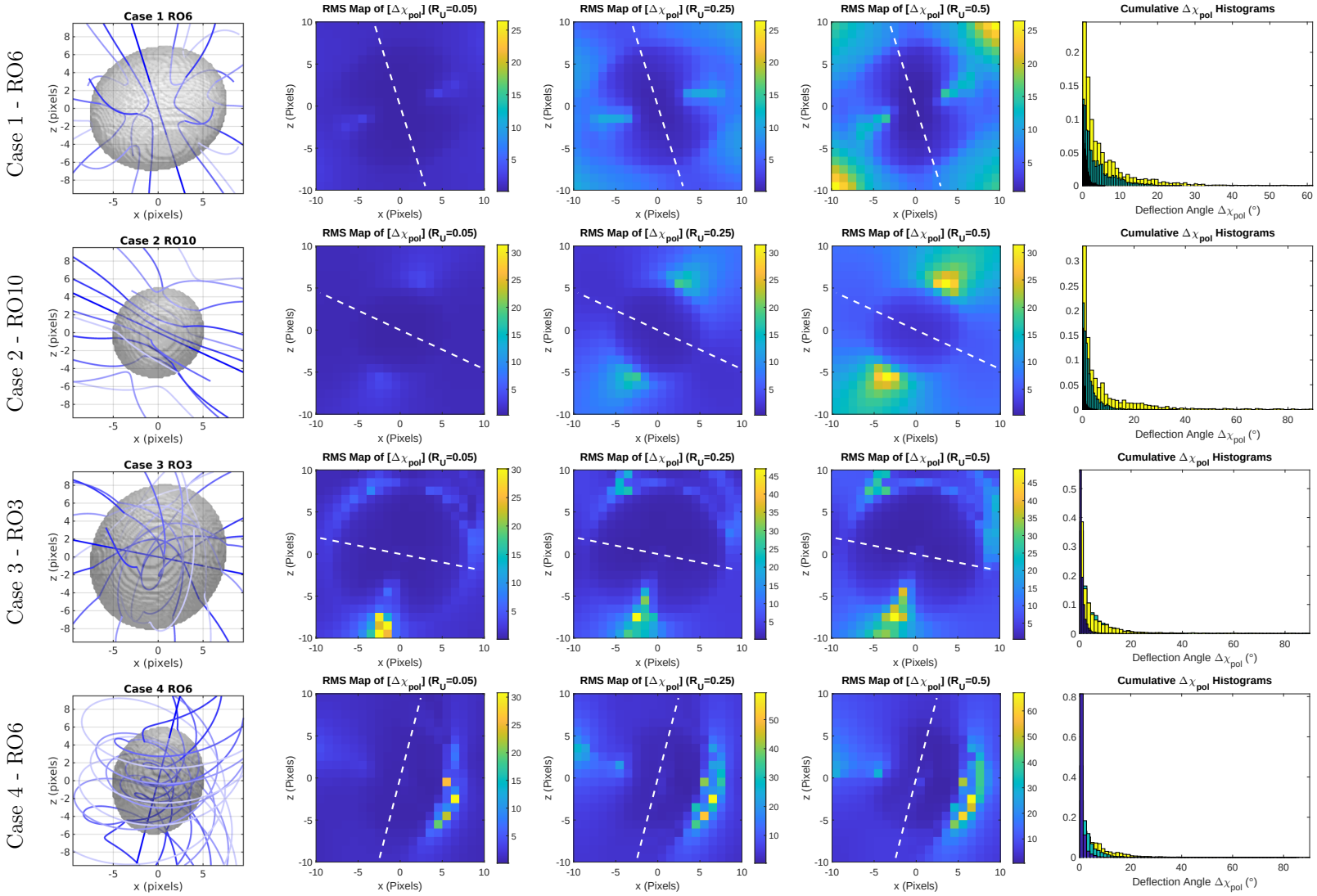


Figure 8.6: Combined RMS deflection maps and histograms for the same models and energy steps as Figures 8.3 and 8.4, for the additive perturbations. The three-dimensional core structures are shown here again for convenience. The histograms count total values of $\Delta\chi_{pol}$ for all 10 maps at a particular R_U, with blue representing $R_U = 0.05$, green representing 0.25, and yellow representing 0.5.

single-perturbation map (Figure 8.4). Interestingly, the $R_U = 0.25$ map (and corresponding histogram) actually had a more high values of $\Delta\chi_{pol}$ than the $R_U = 0.5$ map. A larger sample of runs would be required to test this.

8.5 Discussion and Conclusions

In the hourglass cases, the largest deflections in the polarization vectors typically occurred at or near the edges of the cores, where the field undergoes a sudden change of direction due to the jump conditions at the core's surface. This effect can be seen most easily in the three-dimensional representation of the Case 2 RO10 dataset in Figure 8.3. While this is also the case for the twisted hourglass cores, the twisted field also added additional areas of enhancement. When the field is inclined (unless the inclination is near 90°), the plane-of-sky projection of the field on one side of the core crosses and tangles, while the other forms arcs and loops. The looped side creates a "wedge-like" area of deflection, and the tangled side creates an "arc-like" area with sharp edges. These regions were consistent in all cases (Case 3 and 4 examples, Figures 8.3, 8.4, and 8.6), except those with inclinations that aligned them very closely to the line-of-sight or plane-of-sky.

The structure of the deflection maps being so strongly tied to the orientation of the field has interesting implications for the eventual application to PolCat fits. In effect, each individual model orientation and field structure created a different pattern of polarization angle deflection, which could act as a fingerprint of sorts.

Our tests with the additive perturbations functioned as a proof-of-concept for future use with realistic turbulence spectra. While, in this case, we only perturbed the field with one wave mode multiple times, the change in the structure of the combined deflection maps relative to the single-wave perturbation at the same energy was still noticeable.

One consideration with this approach is that short wavelength modes could be expected to experience significant damping before they could travel all the way through the core (McKee and Zweibel, 1995). Additionally, the expectation for realistic turbulent spectra is that most of the power lies in the long-wavelength modes, which does not fall under the eikonal approximation. Applying such a criterion to large wavelengths would imply that the angular frequency $\mathbf{c}_{A0} \cdot \mathbf{k}$ is conserved along the field lines at all wavelengths. We are not confident of this assertion outside of the limits of the eikonal approximation at this juncture, but we do have future plans to apply a three-dimensional MHD-code to the models to perform a similar analysis. Comparing the results between MHD simulations and the method outlined in this analysis under the general assumption of conserved angular frequency for all wavelengths could potentially verify or refute the validity of this approach.

Chapter 9

Summary of Conclusions

This thesis explored the use of tensor virial theorem and Alfvén wave perturbations as a new tool for understanding magnetic fields in molecular cloud cores. Over the course of this work, we have

- investigated tensor virial theorem in triaxial cores as a method to impose a physicality constraint onto models of magnetized molecular cloud cores,
- developed methodology to understand the shapes of triaxial cores in light of tensor virial theorem,
- explored both equilibrium and non-equilibrium models of triaxial cores,
- explored virialized models of the OMC-1 BN/KL region and made field strength predictions based on the assumption of scalar virial balance
- used theoretical results to numerically propagate waves along field lines to shed light on the Chandrasekhar-Fermi effect due to curved magnetic field geometries.

This chapter touches on the highlights of the thesis from each of the preceding results chapters in order.

9.1 Tensor Virial Theorem

The first development was to implement a tensor virial "stability check" such that unrealistically unstable models could be eliminated from PolCat fits on the fly, and would also allow us to provide an independent estimate of the magnetic field strength for our models based on the assumption that the core is in scalar virial equilibrium (§4.4.3). Our intent was to calculate each solution's three-axis virial tensor and reject solutions with at least one axis

outside our specified limit. This involved pre-computing high-resolution lookup tables for a minimal set of model parameters, such that calculating tensor virial balance for each model was computationally inexpensive. These tables, therefore, provided a store of information on the virial balance for ellipsoidal cores with a Bonnor-Ebert radial density profile.

In Chapter 4, our exploration of the virial tables has yielded not only the expected spheroidal equilbria that have been observed in simulation (e.g. Mouschovias, 1976b; Tomisaka et al., 1988a; Fiege and Pudritz, 2000b), but also unexpected populations of triaxial cores. These cores have similar cross-section and field-configuration to the infinite cylinder filament models of Tomisaka (2014), but are finite in their long axes. The stability of these triaxial equilibria has yet to be determined, and they may be easily perturbed out of equilibrium. These cores appear at high truncation pressures (smaller core surface radii) and exist for both hourglass and twisted hourglass magnetic field geometries. To see how the equilibria would most likely appear when observed, we performed Monte Carlo sampling from the population of equilibrium solutions, oriented at random angles, and calculated the axis ratios of the projected ellipses. The resulting two-dimensional histograms represented the most probable value of ζ (S4.2.3) for the observed two-dimensional ellipse axes, assuming either spheroidal or triaxial virial equilibrium.

In addition to exploring equilibria, we have also mapped the range of solutions defined by our desired virial criterion of 20% of the gravitational term (i.e. $R_{ii} = |VE_{ii}/W_{ii}| \leq 0.2$) in order to thoroughly explore how the model parameters affect the tensor virial balance (Chapter 5). Additionally, we wanted to explore the available families of models that this criterion allows.

We found that the virial constraint maps out a minimum range of ellipsoids where the magnitude of the dimensionless magnetic field scale b^{*2} (equation (4.30)) can only cause scalar virial balance if the field strength is 0 (i.e. the gravitational binding energy exactly balances the volume and surface kinetic terms). This range is common for all models, and essentially serves as a "pivot" point as the permitted range of b^* varies with shape. These geometries have a limited range in the prolate region of the plot with a maximum $\zeta_{\rm sph}$ of approximately 0.65, and a maximum of approximately 1.4, and have a maximum azimuthal axis ratio of $\xi/\zeta = 0.6$. These solutions also exist at a common upper limit of the compression parameter c. In contrast to the range of ζ and ξ values the virial criterion allows, the range of compression values is quite narrow. Additionally, the triaxial equilibria of Chapter 4 are also present, and therefore there are some very azimuthally eccentric cores that can pass the virial criterion. One implication of the existence of these equilibria is that more eccentric core geometries could theoretically be possible in nature if they are found to be stable.

9.2 Application of the Virial Criterion to PolCat Fits

To test PolCat fits with the virial criterion, we generated test data based on four geometries located within the regions mapped in Chapter 5. For comparison, we also perturbed those geometries in such a way that they would fail the virial criterion either by having R_{ii} values outside of the specified range, or by having a negative value of b^{*2}. The most effective method for this was changing the compression parameter, c, to a value outside the allowed range for the particular (ζ, ξ) values at the original model's pressure (and twist) step. For each the test datasets, we fit with an hourglass model and a twisted field model, both with and without the virial criterion.

Overall, regardless of whether the seed model itself passed the virial check, enabling the virial penalty usually did not affect the fitness curves for the test data. However, runs with the virial criterion enabled typically selected compression values closer to the seed model, even in the cases where the input parameters for the seed models had compression values out of range. As had been previously established in the results of Chapter 3, fitting a dataset generated from a twisted field model with an hourglass model typically failed to replicate the seed dataset, in addition to having poor fitness values. However, enabling the virial criterion in these cases improved the fit geometries in the solution set.

Once we had the test model baseline established, we moved on to fitting data of the OMC-1 BN/KL region (Section 6.2). We used two data sources: The SCUPOL Legacy Catalogue (Matthews et al., 2009), which is a uniformly-processed catalogue of data from the operational lifetime of the SCUBA polarimeter, SCUPOL; and the BISTRO survey (Ward-Thompson et al., 2017), which uses SCUBA2 and its polarimeter POL-2.

Fits to this region without the virial criterion typically chose geometries that were unrealistically flattened perpendicular to the field direction. Enabling the virial criterion produced models that were more realistic. One result of note is that the fits did not seem to prefer twisted field geometries, even when the model allowed for one, unless the virial tables were swapped for ones with a higher maximum twist. Therefore, we do not see strong evidence for twisted fields from these results.

Previous estimates of the magnetic field strength from this region have determined an overall range of between 0.1 to 16 mG, with a range of $1.9 - 11.3$ mG from Chandrasekhar-Fermi analysis on the BISTRO dataset specifically (Pattle et al., 2017). We find that the average magnetic field strength from our models was in a range of $0.2 - 1.3$ mG for our fits to the larger regions, which is in good agreement. This appears to reinforce that our requirement for scalar virial balance is valid in this case.

9.3 Alfvén Wave Propagation

We have extended the wave-propagation formalism of Scheurwater (1990) from those of force-free fields to more general field conditions, proving that the same propagation characteristics apply (Chapter 7, see Appendices D, E, and F).

Our goal when developing this method was to develop code that would allow Alfvén waves to propagate through PolCat models, with the end goal of using it to develop a three-dimensional Chandrasekhar-Fermi analogue that we could use to provide an independent estimate of magnetic field strengths. While we have not managed to accomplish this latter goal over the course of this thesis, we *have* successfully developed code that propagates Alfvén waves down the curved field lines of our models via the method of Scheurwater (1990).

Results of perturbing test models with both single and successive Alfvén waves (Chapter 7) show that the pattern of polarization vector deflections for a particular core model is highly dependent on the inclination angle of the magnetic field to the line-of-sight, i. The orientations with inclination close to the line-of-sight tended to produce more extreme variations in the polarization angle deflections $\Delta\chi_{pol}$ for the hourglass models. For the twisted models, the enhancement only occurred at the centre at the z-symmetry axis of the cores the cores, as the wrapping of the field lines appeared to reinforce the position angle direction.

While applying a perturbation always produced a tangible deflection in the polarization vectors, we found that varying the wavelength had no noticeable effect on the pattern produced at constant energy ratio R_U. This is likely due to our operating on the small-wavelength limit, which means that our perturbations are always sub-grid. Varying R_U, produced deflection patterns that, while similar in the areas that showed enhancement, nevertheless had distinct differences beyond simply increasing the scale of the deflection.

We also observed that the cores exhibit shape changes in polarization deflections near the surface boundary. This is likely due to the magnetic field undergoing a sharp change in direction at the core-envelope interface as a result of the jump conditions at the surface. The twisted fields in particular had a very unique deflection pattern, due to how the field projects when inclined. These cores showed enhanced position angle deflections in an arc along the surface boundary where the field appears to cross and tangle in projection, and a "wedge" directly opposite where the field projects in loops. This characteristic deflection pattern may be useful in identifying whether a particular object truly has a twisted field or not.

Experiments with additive perturbations have yielded a useful modification to the velocity scaling for the individual wave modes that we hope to apply to realistic turbulent velocity spectra in future. Successive perturbations with the same wave mode at randomized phases

and orientation angles around the field line did show some minor differences in the deflection map structure versus the corresponding single-wave map at equivalent energy ratio. However, the patterns were not entirely dissimilar.

9.4 Future Work

In future, we plan to apply this tool to more observational datasets from both the SCUPOL Legacy Catalogue and the BISTRO survey to further test the magnetic field estimation, as well as revisit the OMC-1 dataset to refine our results and model some of the other objects. One interesting potential branch of the virial analysis would be to use independent magnetic field strength estimates with the virial criterion in order to use the field strength to constrain the geometries instead of the other way around. We are also preparing to collaborate with other members of the BISTRO survey to provide fits to other regions under study, in order to help provide insight on the underlying density and magnetic field structures of these objects.

While PolCat is currently set up to only model molecular cloud cores, we do have plans to expand into modelling filaments. Since both clusters of cores and individual isolated cores are often embedded in filaments (McKee and Ostriker, 2007), this will further extend PolCat's utility to observers. Another potential approach worth considering is comparing orientations of the model magnetic fields to the expected large-scale field of the galaxy, which could provide another constraint on the plausibility of models in the solution set.

One current limitation with PolCat is the requirement for cropping individual cores from larger datasets, as well as its inability to model several cores in the field of view at once. This limitation originates from the currently implemented set of density transformations, as the significant motion of material required to contract a uniform density into a centrally-condensed structure tends to obliterate any other nearby condensations. We are exploring multiple potential approaches to this problem, including alternative density transformations, and potentially "additive" models, where the individual three-dimensional cores are generated separately and then combined into a single model prior to polarization map generation. However, the latter approach loses some of the main benefits of the "history" provided by the individual transformations, and also some of the physical significance imparted by the current virial method. Both multi-core approaches would also necessitate resorting to numerical methods to calculate the virial parameters, rather than being able to rely on the semi-analytic formulas outlined in Chapter 4.

Additionally, we plan to further develop the Alfvén wave propagation method to incorporate realistic turbulent spectra. While the propagation method is too computationally intensive to calculate on-the-fly like the virial criterion is, we may apply this to the final

solution sets from PolCATfits to use this to characterize the turbulence in star-forming regions.

Bibliography

Alexakis, A. and L. Biferale (2018). Cascades and transitions in turbulent flows. *Physics Reports 767-769*, 1–101.

Alfvén, H. (1942). Existence of Electromagnetic-Hydrodynamic Waves. *Nature 150*(3805), 405–406.

Ballesteros-Paredes, J., E. Vázquez-Semadeni, A. Palau, and R. S. Klessen (2018). Gravity or turbulence? IV. collapsing cores in out-of-virial disguise. *Monthly Notices of the Royal Astronomical Society 479*(2), 2112–2125.

Bally, J. (1989). The structure and kinematics of star forming clouds. In B. Reipurth (Ed.), *European Southern Observatory Conference and Workshop Proceedings*, Volume 33, pp. 1–32.

Binney, J. and S. Tremaine (1987). *Galactic Dynamics*. Princeton, NJ: Princeton University Press.

Bonnor, W. B. (1956). Boyle's Law and gravitational instability. *Monthly Notices of the Royal Astronomical Society 116*, 351.

Brunt, C. M. and M. H. Heyer (2002a). Interstellar Turbulence. I. Retrieval of Velocity Field Statistics. *The Astrophysical Journal 566*(1), 276–288.

Brunt, C. M. and M. H. Heyer (2002b). Interstellar Turbulence. II. Energy Spectra of Molecular Regions in the Outer Galaxy. *The Astrophysical Journal 566*(1), 289–301.

Burkhart, B., D. C. Collins, and A. Lazarian (2015). Observational diagnostics of self-gravitating mhd turbulence in giant molecular clouds. *Astrophysical Journal 808*(1), 48.

Carraro, G. (2021). *Astrophysics of the Interstellar Medium* (1 ed.). UNITEXT for Physics. Cham: Springer International Publishing.

Caselli, P. and P. C. Myers (1995). The Line Width–Size Relation in Massive Cloud Cores. *ApJ 446*, 665.

Chandrasekhar, S. (1960). The virial theorem in hydromagnetics. *Journal of Mathematical Analysis and Applications 1*(2), 240–252.

Chandrasekhar, S. and E. Fermi (1953l). Magnetic Fields in Spiral Arms. *The Astrophysical Journal 118*, 113.

Chandrasekhar, S. and N. R. Lebovitz (1962a). On Super-Potentials in the Theory of Newtonian Gravitation. *The Astrophysical Journal 135*, 238.

Chandrasekhar, S. and N. R. Lebovitz (1962b). On Superpotentials in the Theory of Newtonian Gravitation. II. Tensors of Higher Rank. *The Astrophysical Journal 136*, 1032.

Chandrasekhar, S. and N. R. Lebovitz (1962c). The Potentials and the Superpotentials of Homogeneous Ellipsoids. *The Astrophysical Journal 136*, 1037.

Chen, C.-Y., Z.-Y. Li, R. R. Mazzei, J. Park, L. M. Fissel, M. C.-Y. Chen, R. I. Klein, and P. S. Li (2022). The DavisChandrasekharFermi method revisited. *Monthly Notices of the Royal Astronomical Society 514*(2), 1575–1594.

Coudé, S., P. Bastien, M. Houde, S. Sadavoy, R. Friesen, J. D. Francesco, D. Johnstone, S. Mairs, T. Hasegawa, W. Kwon, S.-P. Lai, K. Qiu, D. Ward-Thompson, D. Berry, M. C.-Y. Chen, J. Fiege, E. Franzmann, J. Hatchell, K. Lacaille, B. C. Matthews, G. H. Moriarty-Schieven, A. Pon, P. André, D. Arzoumanian, Y. Aso, D.-Y. Byun, C. Eswaraiah, H.-R. Chen, W. P. Chen, T.-C. Ching, J. Cho, M. Choi, A. Chrysostomou, E. J. Chung, Y. Doi, E. Drabek-Maunder, C. D. Dowell, S. P. S. Eyres, S. Falle, P. Friberg, G. Fuller, R. S. Furuya, T. Gledhill, S. F. Graves, J. S. Greaves, M. J. Griffin, Q. Gu, S. S. Hayashi, T. Hoang, W. Holland, T. Inoue, S.-i. Inutsuka, K. Iwasaki, I.-G. Jeong, Y. Kanamori, A. Kataoka, J.-h. Kang, M. Kang, S.-j. Kang, K. S. Kawabata, F. Kemper, G. Kim, J. Kim, K.-T. Kim, K. H. Kim, M.-R. Kim, S. Kim, J. M. Kirk, M. I. N. Kobayashi, P. M. Koch, J. Kwon, J.-E. Lee, C. W. Lee, S.-S. Lee, D. Li, D. Li, H.-b. Li, H.-L. Liu, J. Liu, S.-Y. Liu, T. Liu, S. van Loo, A.-R. Lyo, M. Matsumura, T. Nagata, F. Nakamura, H. Nakanishi, N. Ohashi, T. Onaka, H. Parsons, K. Pattle, N. Peretto, T.-S. Pyo, L. Qian, R. Rao, M. G. Rawlings, B. Retter, J. Richer, A. Rigby, J.-F. Robitaille, H. Saito, G. Savini, A. M. M. Scaife, M. Seta, H. Shinnaga, A. Soam, M. Tamura, Y.-W. Tang, K. Tomisaka, Y. Tsukamoto, H. Wang, J.-W. Wang, A. P. Whitworth, H.-W. Yen, H. Yoo, J. Yuan, T. Zenko, C.-P. Zhang, G. Zhang, J. Zhou, and L. Zhu (2019). The JCMT BISTRO

Survey: The Magnetic Field of the Barnard 1 Star-forming Region. *The Astrophysical Journal 877*(2), 88.

Cramer, N. F. (2001). *The Physics of Alfvén Waves*. Wiley.

Crutcher, R. (2004). Observations of Magnetic Fields in Molecular Clouds. In B. Uyaniker, W. Reich, and R. Wielebinski (Eds.), *The Magnetized Interstellar Medium*, pp. 123–132.

Crutcher, R., C. Heiles, and T. Troland (2003). Observations of Interstellar Magnetic Fields. In E. Falgarone and T. Passot (Eds.), *Turbulence and Magnetic Fields in Astrophysics*, Volume 614 of *Lecture Notes in Physics, Berlin Springer Verlag*, pp. 155–181. Springer Berlin Heidelberg.

Crutcher, R. M. (1999). Magnetic Fields in Molecular Clouds: Observations Confront Theory. *The Astrophysical Journal 520*(2), 706–713.

Crutcher, R. M. (2012). Magnetic Fields in Molecular Clouds. *Annual Review of Astronomy and Astrophysics 50*(1), 29–63.

Crutcher, R. M. and A. J. Kemball (2019). Review of Zeeman Effect Observations of Regions of Star Formation. *Frontiers in Astronomy and Space Sciences 6*(October).

Crutcher, R. M., T. H. Troland, B. Lazareff, and I. Kazes (1996). CN Zeeman Observations of Molecular Cloud Cores. *The Astrophysical Journal 456*, 217.

Curry, C. L. and C. F. McKee (2000). Composite Polytrope Models of Molecular Clouds. I. Theory. *The Astrophysical Journal 528*(2), 734–755.

Davis, L. (1951). The Strength of Interstellar Magnetic Fields. *Physical Review 81*(5), 890–891.

Dib, S., J. Kim, E. Vázquez-Semadeni, A. Burkert, and M. Shadmehri (2007, may). The Virial Balance of Clumps and Cores in Molecular Clouds. *The Astrophysical Journal 661*(1), 262–284.

Doi, Y., K. Tomisaka, T. Hasegawa, S. Coudé, D. Arzoumanian, P. Bastien, M. Matsumura, M. Tahani, S. Sadavoy, C. L. H. Hull, D. Johnstone, J. Di Francesco, Y. Shimajiri, R. S. Furuya, J. Kwon, M. Tamura, D. Ward-Thompson, V. J. M. Le Gouellec, T. Hoang, F. Kirchschlager, J. Hwang, C. Eswaraiah, P. M. Koch, A. P. Whitworth, K. Pattle, W. Kwon, J. Kang, S.-i. Inutsuka, T. L. Bourke, X. Tang, L. Fanciullo, C. W. Lee, H.-L. Liu, A.-R. Lyo, K. Qiu, and S.-P. Lai (2021). The JCMT BISTRO Survey: Evidence for

Pinched Magnetic Fields in Quiescent Filaments of NGC 1333. *The Astrophysical Journal Letters 923*(1), L9.

Draine, B. (2003). Interstellar Dust Grains. *Annual Review of Astronomy and Astrophysics 41*(1), 241–289.

Ebert, R. (1955). Über die Verdichtung von H I-Gebieten. Mit 5 Textabbildungen. *Zeitschrift für Astrophysik 37*, 217.

Elmegreen, B. G. and J. Scalo (2004). Interstellar Turbulence I: Observations and Processes. *Annual Review of Astronomy and Astrophysics 42*(1), 211–273.

English, J., J. D. Fiege, T. Wiegert, B. Koribalski, W. Kerzendorf, and K. C. Freeman (2010). The DiVA's Mask: Iconifying Galaxies and Revealing HII Anomalies. In D. L. Block, K. C. Freeman, and I. Puerari (Eds.), *Galaxies and their Masks*, pp. 105–112. New York, NY: Springer New York.

Esquivel, A., A. Lazarian, S. Horibe, J. Cho, V. Ossenkopf, and J. Stutzki (2007). Statistics of velocity centroids: Effects of density-velocity correlations and non-Gaussianity. *Monthly Notices of the Royal Astronomical Society 381*(4), 1733–1744.

Falceta-Gonçalves, D., A. Lazarian, and G. Kowal (2008). Studies of Regular and Random Magnetic Fields in the ISM: Statistics of Polarization Vectors and the Chandrasekhar-Fermi Technique. *The Astrophysical Journal 679*(1), 537–551.

Fiege, J. D. (2010). Qubist User's Guide: Optimization, Data-Modeling, and Visualization with the Qubist Global Optimization Toolbox for MATLAB.

Fiege, J. D., D. Johnstone, R. O. Redman, and P. A. Feldman (2004). A GENETIC ALGORITHMBASED EXPLORATION OF THREE FILAMENT MODELS : A CASE FOR THE MAGNETIC SUPPORT OF THE G11.11 - 0 . 12 INFRARED-DARK CLOUD. *The Astrophysical Journal 616*, 925–942.

Fiege, J. D., B. McCurdy, P. Potrebko, H. Champion, and A. Cull (2011). PARETO: A novel evolutionary optimization approach to multiobjective IMRT planning. *Medical physics 38*(9), 5217–29.

Fiege, J. D. and R. Pudritz (2000a). Polarized Submillimeter Emission from Filamentary Molecular Clouds. *The Astrophysical Journal 544*, 830.

Fiege, J. D. and R. E. Pudritz (2000b). Prolate Cores in Filamentary Molecular Clouds. *The Astrophysical Journal 534*(1), 291–308.

Fonseca, C. and P. Fleming (1993). Genetic algorithms for multiobjective optimization: formulation, discussion and generalization. In *Proceedings of the Fifth International Conference on Genetic Algorithms*, San Mateo, CA, USA, pp. 416 – 23.

Fonseca, C. and P. Fleming (1998a). Multiobjective optimization and multiple constraint handling with evolutionary algorithms. I. A unified formulation. *IEEE Transactions on Systems, Man, and Cybernetics - Part A: Systems and Humans 28*(1), 26–37.

Fonseca, C. and P. Fleming (1998b). Multiobjective optimization and multiple constraint handling with evolutionary algorithms. II. Application example. *IEEE Transactions on Systems, Man, and Cybernetics - Part A: Systems and Humans 28*(1), 38–47.

Franzmann, E. (2014). *Modeling Submillimetre Polarization of Molecular Cloud Cores Using Successive Parametrized Coordinate Transformations*. Master's thesis, University of Manitoba.

Franzmann, E. L. and J. D. Fiege (2017). PolCat: Modelling submillimetre polarization of molecular cloud cores using successive parametrized coordinate transformations. *Monthly Notices of the Royal Astronomical Society 466*, 4592–4613.

Franzmann, E. L. and J. D. Fiege (2020). An Exploration of Tensor Virial Equilibrium in Magnetized Molecular Cloud Cores. *The Astrophysical Journal 899*(2), 101.

Friberg, P., P. Bastien, D. Berry, G. Savini, S. F. Graves, and K. Pattle (2016). POL-2: a polarimeter for the James-Clerk-Maxwell telescope. *Millimeter, Submillimeter, and Far-Infrared Detectors and Instrumentation for Astronomy VIII 9914*(July 2016), 991403.

Girart, J. M., R. Rao, and D. P. Marrone (2006). Magnetic Fields in the Formation of Sun-Like Stars. *Science 313*(5788), 812–814.

Goedbloed, H., R. Keppens, and S. Poedts (2019). *Magnetohydrodynamics of Laboratory and Astrophysical Plasmas*. Cambridge University Press.

Goldberg, D. E. (2002). *The Design of Innovation*, Volume 7 of *Genetic Algorithms and Evolutionary Computation*. Boston, MA: Springer US.

Goldreich, P. and S. Sridhar (1995). Toward a theory of interstellar turbulence. 2: Strong alfvenic turbulence. *The Astrophysical Journal 438*, 763.

González-Casanova, D. F. and A. Lazarian (2017). Velocity Gradients As a Tracer for Magnetic Fields. *The Astrophysical Journal 835*(1), 41.

Goodman, A. A., T. J. Jones, E. A. Lada, and P. C. Myers (1995). Does Near-Infrared Polarimetry Reveal the Magnetic Field in Cold Dark Clouds? *ApJ 448*, 748.

Guo, J., F. Wei, X. Feng, H. Liu, W. Wan, Z. Yang, J. Xu, and C. Liu (2016). Alfvén waves as a solar-interplanetary driver of the thermospheric disturbances. *Scientific Reports 6*, 1–7.

Heiles, C. and R. Crutcher (2005). Magnetic Fields in Diffuse HI and Molecular Clouds. In R. Wielebinski and R. Beck (Eds.), *Cosmic Magnetic Fields*, Volume 664 of *Lecture Notes in Physics, Berlin Springer Verlag*, pp. 137.

Heiles, C., A. Goodman, C. McKee, and E. Zweibel (1993). Magnetic fields in star-forming regions - Observations. In E. Levy and J. Lunine (Eds.), *Protostars and Planets III*, pp. 279–326. University of Arizona Press.

Heitsch, F., E. G. Zweibel, M.-M. Mac Low, P. Li, and M. L. Norman (2001, nov). Magnetic Field Diagnostics Based on FarInfrared Polarimetry: Tests Using Numerical Simulations. *The Astrophysical Journal 561*(2), 800–814.

Hennebelle, P. and E. Falgarone (2012). Turbulent molecular clouds. *The Astronomy and Astrophysics Review 20*(1), 55.

Hildebrand, R. H., L. Kirby, J. L. Dotson, M. Houde, and J. E. Vaillancourt (2009). Dispersion of Magnetic Fields in Molecular Clouds. I. *The Astrophysical Journal 696*(1), 567–573.

Hoang, T. and A. Lazarian (2016). A unified model of grain alignment: radiative alignment of interstellar grains with magnetic inclusions. *The Astrophysical Journal 831*(2), 1–20.

Houde, M., C. D. Dowell, R. H. Hildebrand, J. L. Dotson, J. E. Vaillancourt, T. G. Phillips, R. Peng, and P. Bastien (2004). Tracing the Magnetic Field in Orion A. *The Astrophysical Journal 604*(2), 717–740.

Houde, M., J. E. Vaillancourt, R. H. Hildebrand, S. Chitsazzadeh, and L. Kirby (2009). Dispersion of Magnetic Fields in Molecular Clouds. Ii. *The Astrophysical Journal 706*(2), 1504–1516.

Hwang, J., J. Kim, K. Pattle, W. Kwon, S. Sadavoy, P. M. Koch, C. L. H. Hull, D. Johnstone, R. S. Furuya, C. Won Lee, D. Arzoumanian, M. Tahani, C. Eswaraiah, T. Liu, F. Kirchschlager, K.-T. Kim, M. Tamura, J. Kwon, A.-R. Lyo, A. Soam, J.-h. Kang, T. L. Bourke, M. Matsumura, S. Mairs, G. Kim, G. Park, F. Nakamura, T. Onaka, X. Tang,

H.-L. Liu, D. Ward-Thompson, D. Li, T. Hoang, T. Hasegawa, K. Qiu, S.-P. Lai, and P. Bastien (2021). The JCMT BISTRO Survey: The Distribution of Magnetic Field Strengths toward the OMC-1 Region. *The Astrophysical Journal 913*(2), 85.

Jackson, J. D. (1975). *Classical electrodynamics* (2nd ed.). Wiley.

Johnstone, D., J. D. Fiege, and R. Redman (2003). The G11.11-0.12 Infrared-Dark Cloud: Anomalous Dust and a Nonmagnetic Isothermal Model. *The Astrophysical Journal 588*, L37–L40.

Kleinmann, D. E. and F. J. Low (1967). Discovery of an Infrared Nebula in Orion. *The Astrophysical Journal 149*(July 1967), L1.

Kounkel, M., L. Hartmann, L. Loinard, G. N. Ortiz-León, A. J. Mioduszewski, L. F. Rodríguez, S. A. Dzib, R. M. Torres, G. Pech, P. A. B. Galli, J. L. Rivera, A. F. Boden, N. J. Evans II, C. Briceño, and J. J. Tobin (2017). the Gould'S Belt Distances Survey (Gobelins). Ii. Distances and Structure Toward the Orion Molecular Clouds. *The Astrophysical Journal 834*(2), 142.

Kudoh, T. and S. Basu (2008). Three-dimensional Simulation of Magnetized Cloud Fragmentation Induced by Nonlinear Flows and Ambipolar Diffusion. *The Astrophysical Journal 679*(2), L97–L100.

Lai, S., R. M. Crutcher, J. M. Girart, and R. Rao (2002). Interferometric Mapping of Magnetic Fields in Starforming Regions. II. NGC 2024 FIR 5. *The Astrophysical Journal 566*(2), 925–930.

Larson, R. (1981). Turbulence and star formation in molecular clouds. *Monthly Notices of the Royal Astronomical Society 194*, 809–826.

Lazarian, A. (2004). Turbulence Statistics From Spectral Line Observations. *Journal of The Korean Astronomical Society 37*(5), 563–570.

Lazarian, A. (2007). Tracing magnetic fields with aligned grains. *Journal of Quantitative Spectroscopy and Radiative Transfer 106*(1-3), 225–256.

Lazarian, A. (2009). Obtaining spectra of turbulent velocity from observations. *Space Science Reviews 143*(1-4), 357–385.

Lazarian, A., A. A. Goodman, and P. C. Myers (1997). On the Efficiency of Grain Alignment in Dark Clouds. *The Astrophysical Journal 490*(1), 273–280.

Lee, H. and B. Draine (1985). Infrared Extinction and Polarization Due to Partially Aligned Spheroidal Grains: Models for the Dust Toward the BN Object. *The Astrophysical Journal 290*, 211–228.

Liu, J., K. Qiu, D. Berry, J. Di Francesco, P. Bastien, P. Koch, R. Furuya, K.-T. Kim, S. Coudé, C. Lee, A. Soam, C. Eswaraiah, D. Li, J. Hwang, A.-R. Lyo, K. Pattle, T. Hasegawa, W. Kwon, S.-P. Lai, D. Ward-Thompson, T.-C. Ching, Z. Chen, Q. Gu, D. Li, H.-B. Li, H.-L. Liu, L. Qian, H. Wang, J. Yuan, C.-P. Zhang, G. Zhang, Y.-P. Zhang, J. Zhou, L. Zhu, P. André, D. Arzoumanian, Y. Aso, D.-Y. Byun, M.-Y. Chen, H.-R. Chen, W. Chen, J. Cho, M. Choi, A. Chrysostomou, E. Chung, Y. Doi, E. Drabek-Maunder, C. Dowell, S. Eyres, S. Falle, L. Fanciullo, J. Fiege, E. Franzmann, P. Friberg, R. Friesen, G. Fuller, T. Gledhill, S. Graves, J. Greaves, M. Griffin, I. Han, J. Hatchell, S. Hayashi, T. Hoang, W. Holland, M. Houde, T. Inoue, S.-I. Inutsuka, K. Iwasaki, I.-G. Jeong, D. Johnstone, Y. Kanamori, J.-H. Kang, M. Kang, S.-J. Kang, A. Kataoka, K. Kawabata, F. Kemper, G. Kim, J. Kim, K. Kim, M.-R. Kim, S. Kim, J. Kirk, M. Kobayashi, T. Kusune, J. Kwon, K. Lacaille, C.-F. Lee, J.-E. Lee, H. Lee, S.-S. Lee, S.-Y. Liu, T. Liu, S. Van Loo, S. Mairs, M. Matsumura, B. Matthews, G. Moriarty-Schieven, T. Nagata, F. Nakamura, H. Nakanishi, N. Ohashi, T. Onaka, J. Parker, H. Parsons, E. Pascale, N. Peretto, A. Pon, T.-S. Pyo, R. Rao, M. Rawlings, B. Retter, J. Richer, A. Rigby, J.-F. Robitaille, S. Sadavoy, H. Saito, G. Savini, A. Scaife, M. Seta, H. Shinnaga, M. Tamura, Y.-W. Tang, K. Tomisaka, Y. Tsukamoto, J.-W. Wang, A. Whitworth, H.-W. Yen, H. Yoo, and T. Zenko (2019). The JCMT BISTRO Survey: The Magnetic Field in the Starless Core ρ Ophiuchus C. *Astrophysical Journal 877*(1).

Matthews, B. C., C. A. McPhee, L. M. Fissel, and R. L. Curran (2009). THE LEGACY OF SCUPOL: 850 μm IMAGING POLARIMETRY FROM 1997 TO 2005. *The Astrophysical Journal Supplement Series 182*(1), 143–204.

McKee, C. F. and J. H. Holliman II (1999). Multipressure Polytropes as Models for the Structure and Stability of Molecular Clouds. I. Theory. *The Astrophysical Journal 522*(1), 313–337.

McKee, C. F. and E. C. Ostriker (2007). Theory of Star Formation. *Annual Review of Astronomy and Astrophysics 45*(1), 565–687.

McKee, C. F. and E. G. Zweibel (1995). Alfven Waves in Interstellar Gasdynamics. *The Astrophysical Journal 440*(1), 686.

Mouschovias, T. C. (1974). Static Equilibria of the Interstellar Gas in the Presence of Magnetic and Gravitational Fields: Large-Scale Condensations. *The Astrophysical Journal 192*, 37.

Mouschovias, T. C. (1976a). Nonhomologous contraction and equilibria of self-gravitating, magnetic interstellar clouds embedded in an intercloud medium: Star formation. I Formulation of the problem and method of solution. *ApJ 206*, 753.

Mouschovias, T. C. (1976b). Nonhomologous contraction and equilibria of self-gravitating, magnetic interstellar clouds embedded in an intercloud medium: Star formation. II - Results. *The Astrophysical Journal 207*, 141–158.

Myers, P. C. and G. A. Fuller (1992). Density structure and star formation in dense cores with thermal and nonthermal motions. *The Astrophysical Journal 396*(9), 631.

Ostriker, E. C., J. M. Stone, and C. F. Gammie (2001). Density, Velocity, and Magnetic Field Structure in Turbulent Molecular Cloud Models. *The Astrophysical Journal 546*(2), 980–1005.

Pattle, K., D. Ward-Thompson, D. Berry, J. Hatchell, H.-R. Chen, A. Pon, P. M. Koch, W. Kwon, J. Kim, P. Bastien, J. Cho, S. Coudé, J. Di Francesco, G. Fuller, R. S. Furuya, S. F. Graves, D. Johnstone, J. Kirk, J. Kwon, C. W. Lee, B. C. Matthews, J. C. Mottram, H. Parsons, S. Sadavoy, H. Shinnaga, A. Soam, T. Hasegawa, S.-P. Lai, K. Qiu, and P. Friberg (2017). The JCMT BISTRO Survey: The Magnetic Field Strength in the Orion A Filament. *The Astrophysical Journal 846*(2), 122.

Pattle, K., D. Ward-Thompson, T. Hasegawa, P. Bastien, W. Kwon, S.-P. Lai, K. Qiu, R. Furuya, and D. Berry (2018). First Observations of the Magnetic Field inside the Pillars of Creation: Results from the BISTRO Survey. *The Astrophysical Journal 860*(1), L6.

Roberts, P. H. (1962). On the Superpotential and Supermatrix of a Heterogeneous Ellipsoid. *The Astrophysical Journal 136*, 1108.

Rogers, A. and D. Fiege (2012). GLOBAL OPTIMIZATION METHODS FOR GRAVITATIONAL LENS SYSTEMS WITH REGULARIZED SOURCES. *The Astrophysical Journal 759*(1), 27.

Rogers, A. and J. D. Fiege (2011a). ERRATUM: GRAVITATIONAL LENS MODELING WITH GENETIC ALGORITHMS AND PARTICLE SWARM OPTIMIZERS (2011, ApJ, 727, 80). *The Astrophysical Journal 733*(1), 73.

Rogers, A. and J. D. Fiege (2011b). Gravitational Lens Modeling With Genetic Algorithms and Particle Swarm Optimizers. *The Astrophysical Journal 727*(2), 80.

Ryden, B. (1996). The shapes of dense cores and bok globules. *The Astrophysical Journal 471*, 822.

Scheurwater, R. (1990). Geometrical mode coupling and wave propagation in cold non-uniform magnetoplasmas. *Astronomy & Astrophysics 237*, 545–552.

Schleuning, D. a. (1998). Far-infrared and submillimeter polarization of omc-1 : evidence for magnetically regulated star formation. *The Astrophysical Journal 493*(2), 811–825.

Solomon, P. M., A. R. Rivolo, J. Barrett, and A. Yahil (1987). Mass, luminosity, and line width relations of Galactic molecular clouds. *The Astrophysical Journal 319*, 730.

Stevens, A. L., J. D. Fiege, D. A. Leahy, and S. M. Morsink (2016). Neutron Star MassRadius Constraints Using Evolutionary Optimization. *The Astrophysical Journal 833*(2), 244.

Swift, J. J. and W. J. Welch (2008). A Case Study of LowMass Star Formation. *The Astrophysical Journal Supplement Series 174*(1), 202–222.

Tilley, D. A. and R. E. Pudritz (2007). The formation of star clusters - II. 3D simulations of magnetohydrodynamic turbulence in molecular clouds. *Monthly Notices of the Royal Astronomical Society 382*(1), 73–94.

Tomisaka, K. (1991). The equilibria and evolutions of magnetized, rotating, isothermal clouds. V - The effect of the toroidal field. *The Astrophysical Journal 376*, 190.

Tomisaka, K. (2014). Magnetohydrostatic equilibrium structure and mass of filamentary isothermal cloud threaded by lateral magnetic field. *Astrophysical Journal 785*(1).

Tomisaka, K., S. Ikeuchi, and T. Nakamura (1988a). The equilibria and evolutions of magnetized, rotating, isothermal clouds. I - Basic equations and numerical methods. *The Astrophysical Journal 326*, 208.

Tomisaka, K., S. Ikeuchi, and T. Nakamura (1988b). The Equilibria and evolutions of magnetized, rotating, isothermal clouds. II - The extreme case: Nonrotating clouds. *The Astrophysical Journal 335*, 239.

Tomisaka, K., S. Ikeuchi, and T. Nakamura (1989). The equilibria and evolutions of magnetized, rotating, isothermal clouds. III - Critical mass. *The Astrophysical Journal 341*, 220.

Tomisaka, K., S. Ikeuchi, and T. Nakamura (1990). The equilibria and evolutions of magnetized, rotating, isothermal clouds. IV - Quasi-static evolution. *The Astrophysical Journal 362*, 202.

Vázquez-Semadeni, E., J. Kim, M. Shadmehri, and J. Ballesteros-Paredes (2005). The Lifetimes and Evolution of Molecular Cloud Cores. *The Astrophysical Journal 618*(1), 344–359.

Vickers, G. T. (1996). The projected areas of ellipsoids and cylinders. *Powder Technology 86*(2), 195–200.

Ward-Thompson, D., K. Pattle, P. Bastien, R. Furuya, W. Kwon, S.-P. Lai, K. Qiu, D. Berry, M. Choi, S. Coudé, J. Francesco, T. Hoang, E. Franzmann, P. Friberg, S. Graves, J. Greaves, M. Houde, D. Johnstone, J. Kirk, P. Koch, J. Kwon, C. Lee, D. Li, B. Matthews, J. Mottram, H. Parsons, A. Pon, R. Rao, M. Rawlings, H. Shinnaga, S. Sadavoy, S. Loo, Y. Aso, D.-Y. Byun, C. Eswaraiah, H.-R. Chen, M.-Y. Chen, W. Chen, T.-C. Ching, J. Cho, A. Chrysostomou, E. Chung, Y. Doi, E. Drabek-Maunder, S. Eyres, J. Fiege, R. Friesen, G. Fuller, T. Gledhill, M. Griffin, Q. Gu, T. Hasegawa, J. Hatchell, S. Hayashi, W. Holland, T. Inoue, S.-I. Inutsuka, K. Iwasaki, I.-G. Jeong, J.-H. Kang, M. Kang, S.-J. Kang, K. Kawabata, F. Kemper, G. Kim, J. Kim, K.-T. Kim, K. Kim, M.-R. Kim, S. Kim, K. Lacaille, J.-E. Lee, S.-S. Lee, D. Li, H.-B. Li, H.-L. Liu, J. Liu, S.-Y. Liu, T. Liu, A.-R. Lyo, S. Mairs, M. Matsumura, G. Moriarty-Schieven, F. Nakamura, H. Nakanishi, N. Ohashi, T. Onaka, N. Peretto, T.-S. Pyo, L. Qian, B. Retter, J. Richer, A. Rigby, J.-F. Robitaille, G. Savini, A. Scaife, A. Soam, M. Tamura, Y.-W. Tang, K. Tomisaka, H. Wang, J.-W. Wang, A. Whitworth, H.-W. Yen, H. Yoo, J. Yuan, C.-P. Zhang, G. Zhang, J. Zhou, L. Zhu, P. André, C. Dowell, S. Falle, and Y. Tsukamoto (2017). First Results from BISTRO: A SCUBA-2 Polarimeter Survey of the Gould Belt. *Astrophysical Journal 842*(1).

Wardle, M. and A. Konigl (1990). A Model for the Magnetic Field in the Molecular Disk at the Galactic Center. *The Astrophysical Journal 362*, 120–134.

Weintraub, D., A. Goodman, and R. Akeson (2000). Polarized Light from Star-Forming Regions. In V. Mannings, A. Boss, and S. S. Russell (Eds.), *Protostars and Planets IV*, Chapter 9, pp. 247. Tucson: University of Arizona Press.

Zweibel, E. G. (1990). Virial theorem analysis of the structure and stability of magnetized clouds. *The Astrophysical Journal 348*, 186.

Zweibel, E. G. and C. F. McKee (1995). Equiparatition of energy for turbulent astrophysical fluids: Accounting for the unseen energy in molecular clouds. *The Astrophysical Journal 439*(1), 779.

Appendix A

Acronyms

A short glossary of some abbreviations used in the text:

BES Bonnor-Ebert sphere, usually refers to PolCat models containing the transformation described in Section 4.2.2

BISTRO B-fields In STar-forming Region Observations survey (Ward-Thompson et al., 2017)

BN/KL Brecklin- Neugebauer/Kleinmann-Low region, an area of interest in the Orion Molecular Cloud complex

CBES The composite Bonnor-Ebert sphere transformation described in Section 6.1.1

CF Chandrasekhar-Fermi (of or referring to the Chandrasekhar-Fermi (or Chandrasekhar-Fermi-Davis) method of plane-of-sky magnetic field strength estimation (Chandrasekhar and Fermi, 1953)

LOS Line-of-sight, the direction along our sightline to an object

LUT Look-Up Table, a stored table of values that can be used for interpolation

MAE Mean Absolute Error, the average of the absolute differences between the data and the model for the pixels in each polarization map

MHD Magnetohydrodynamic, of or referring to the dynamics of conducting fluids under the influence of magnetic fields

ODE Ordinary differential equations

OMC Orion Molecular Cloud

POS plane-of-sky, in the plane perpendicular to our sightline

RMS Root-mean-square, the square root of the mean of the differences between the data and the model for the pixels in each polarization map

SLC SCUPOL Legacy Catalogue (Matthews et al., 2009)

VE Virial equation, mostly used as a variable representing the value of the virial equation

Virial test model categories (Chapter 6):

VO Test dataset generated from a virial-criterion-compliant core model with orientation angles set to 0. Also referred to as "zero-rotation" or "zero-inclination" datasets.

VA Test dataset generated from a core model with the same parameters as the corresponding VO dataset but generated at a specific orientation.

NC Test dataset generated from a non-virial-criterion-compliant core with the same overall geometry as the corresponding VO and VA datasets, but with a smaller squeeze c parameter (more compressed). The model's central density has also been adjusted to keep the core the same approximate size as the VO and VA datasets in the model cube.

NE Test dataset generated using a similar method to the NC dataset, but with squeeze c adjusted to be larger than the corresponding VO and VA datasets (more expanded). The model core's central density has also been adjusted for the same reasons as the NC dataset.

Appendix B

Test Data Figures from Chapter 3

This section contains the simulated test data maps used as input for the tests discussed in Section 3.6.2. These figures show the three-dimensional seed model structure and simulated polarization maps for Cases 2-5, similar to the Case 1 example shown in Figure 3.4.

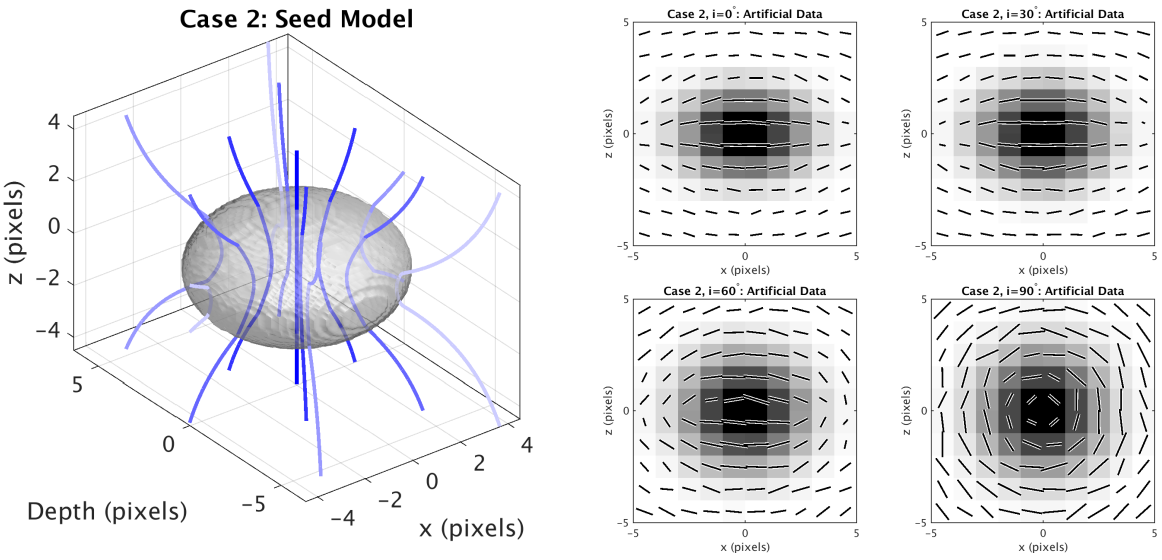


Figure B.1: Seed model for the Case 2 dataset at 0° inclination (left), with all four of the Case 2 artificial datasets (0°, 30°, 60°, and 90°, right)

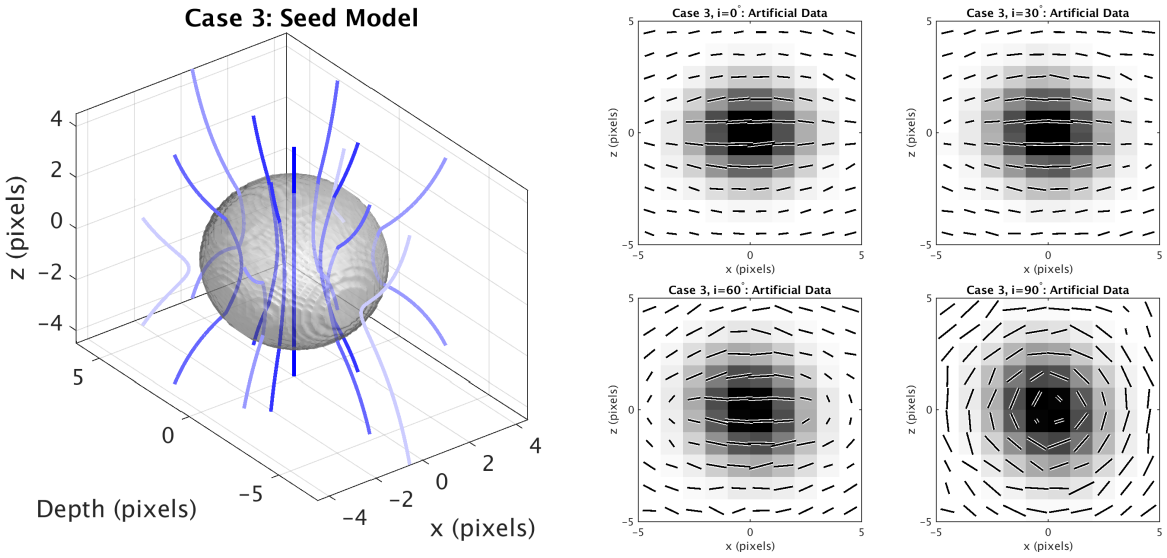


Figure B.2: Seed model for the Case 3 dataset at 0° inclination (left), with all four of the Case 3 artificial datasets (0°, 30°, 60°, and 90°, right)

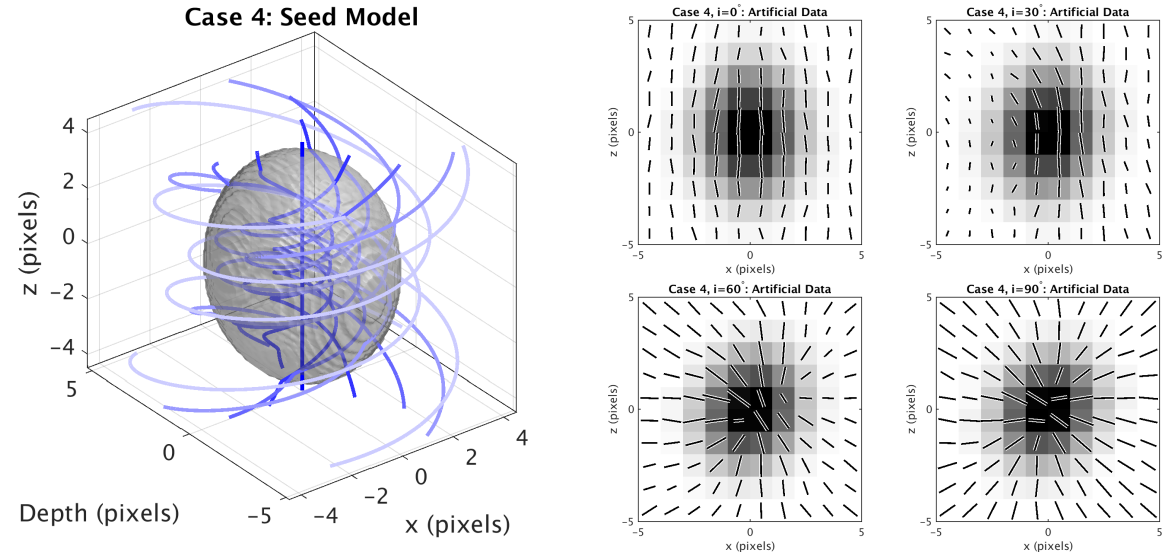


Figure B.3: Seed model for the Case 4 dataset at 0° inclination (left), with all four of the Case 4 artificial datasets (0°, 30°, 60°, and 90°, right)

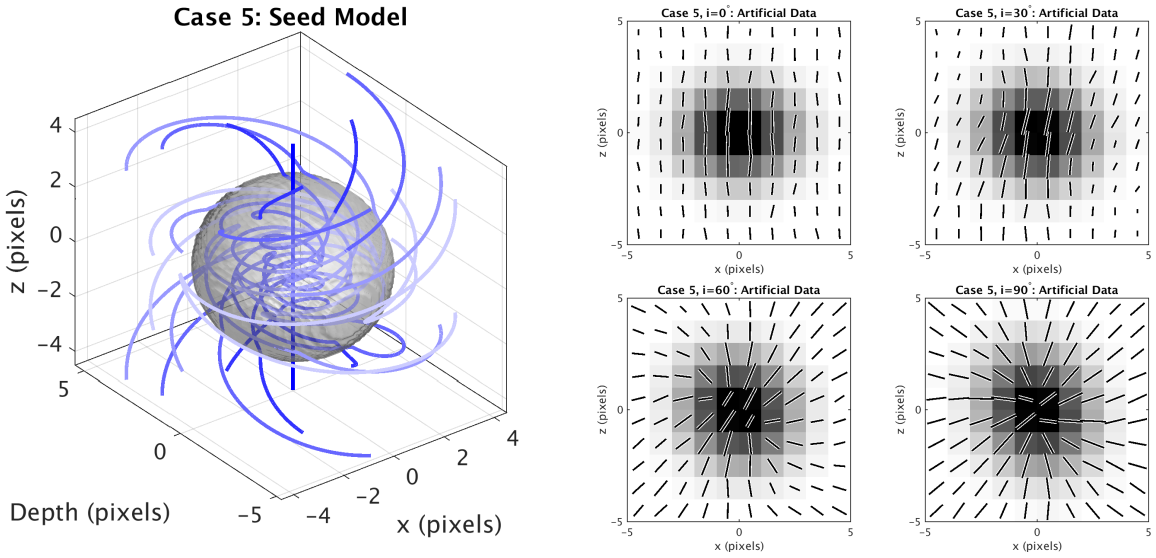


Figure B.4: Seed model for the Case 5 dataset at 0° inclination (left), with all four of the Case 5 artificial datasets (0°, 30°, 60°, and 90°, right)

Appendix C

Volume and Surface Area Estimation

The computation of the magnetic field volume and surface terms for the virial lookup table calculation is performed on a three-dimensional numerical model. Typical practice is to perform volume integrals numerically is to use a high-resolution grid and treat each interior voxel as a discrete volume element:

$$\int_V f(\mathbf{r})dV = \sum_i f_i dV_i. \tag{C.1}$$

However, this is an inaccurate approximation in our case, as our grid is rectangular but our cores are ellipsoidal. This causes the cores to only partially intersect with the voxels at the surface. Therefore, if we include the full volume of all voxels that intersect the surface in our sum, some of the edge values are weighted more than others. A corresponding technique for surface area would be to obtain surface area elements relative to the voxel faces. While this would provide a reasonable estimate of the surface area elements, this technique is problematic as it would draw connections between the voxel centres rather than the actual points of intersection, which would also over or under estimate the surface area depending on the amount of volume contained in the voxels. We would also need to interpolate the magnitude and direction of the model magnetic field on each facet because they would be offset from our grid.

To get around the volume integration problem, we treat the voxels that intersect with the core's surface ("edge" voxels) as containing only a fraction of the core's surface. To compute this fractional volume, we approximate the surface segment as a plane defined by where the surface intersects the edges of the voxel (Figure C.1). Computing the volume contained between a the plane and the interior surfaces of the voxel is relatively simple. Approximating the surface in this way has the additional benefit of defining a surface area segment $d\mathbf{S}$ complete with vector normal.

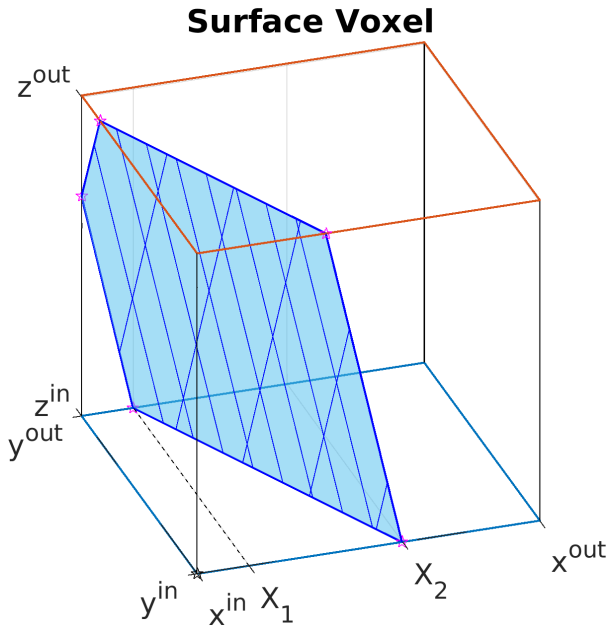


Figure C.1: An example of an edge voxel, with surface segment and intersection points marked. The number of intersection points varies between 3-6 depending on the orientation of the surface segment in the voxel.

The coordinates (x_i, y_i, z_i) describe the centres of the voxels. First, we find all the voxels that intersect the surface defined by $r = r_s$ in equation (4.10). These voxels fall into two categories: 1) those with $r_i < r_s$, but at least one voxel corner $(x_i^{out}, y_i^{out}, z_i^{out})$ having $r_i^{out} > r_s$, and 2) those with $r_i > r_s$ but at least one corner $(x_i^{in}, y_i^{in}, z_i^{in})$ having $r_i^{in} < r_s$. These corner coordinates are described relative to distance from the origin, e.g.

$$x_i^{in} = \begin{cases} x_i^{min}(x_i \geq 0) \\ x_i^{max}(x_i < 0). \end{cases} \tag{C.2}$$

Once we have determined these "surface voxels," we then find the points p_j, where the surface intersects with any of the twelve edges of the voxel, which can range from three to six points depending on the voxel's location on the surface. These points define a plane that approximates the chunk of surface contained within the voxel. The surface normal $\hat{\mathbf{n}} = (A, B, C)/(A^2 + B^2 + C^2)$ is determined by vectorizing the points (i.e. $\mathbf{v_j} = p_j - p_1$) and averaging their cross-products. Arranging the vectorized points in either clockwise or counter-clockwise order also allows computation of the plane segment surface area via

$$d\mathbf{S} = \hat{\mathbf{n}} \frac{1}{2} \sum_{j=2}^{N-1} |\mathbf{v_j} \times \mathbf{v_{j+1}}|. \tag{C.3}$$

Now that the surface normal has been obtained, the plane of intersection with the voxel is then

$$z = \frac{D - Ax - By}{C} \tag{C.4}$$

where D is obtained by plugging p_1 into the plane equation $Ax + By + Cz = D$. We can now approximate the volume element by integrating between $z = z^{in}$ and equation (C.4) analytically within the confines of the voxel. For convenience, the voxel, the intersection points, and the plane are shifted so that z^{in} lies on the x-y plane before integrating. Using the in-out coordinate definitions, we can split the enclosed volume into two sections. We have V_1 between (y^{in}, y^{out}) and (x^{in}, X_1):

$$V_1 = \frac{(y^{out} - y^{in})(X_1 - x^{in})}{C}\left(D - \frac{1}{2}A(X_1 + x^{in}) - \frac{1}{2}B(y^{out} + y^{in})\right) \tag{C.5}$$

where $X_1 = (By^{out} - D)/A$ is between x^{in} and x^{out}, and V_2:

$$\begin{aligned} V_2 = \frac{1}{6}\frac{A^2}{BC}(X_2^3 - X_1^3) \\ + \left(\frac{D}{B} - y^{in}\right)(X_2 - X_1)\left(\frac{D}{C} - \frac{1}{2}A\frac{(X_2 + X_1)}{C} - \frac{1}{2}B\frac{\left(\frac{D}{B} + y^{in}\right)}{C}\right) \end{aligned} \tag{C.6}$$

where $X_2 = (By^{in} - D)/A$ is within the same x-range as X_1. The total volume enclosed is therefore $V_{max} = |V_1 + V_2|$. However, this also includes volume above $z = z^{out}$. To remove this from the total, the voxel is shifted down again so that $z = z^{out}$ lies on the x-y plane, the enclosed volume V_{top} is computed via equations (C.5) and (C.6) and subtracted from V_{max} to obtain only the volume contained within the voxel of interest. For all voxels outside of these surface voxels with $r > r_s$, the voxel volumes are set to zero so as not to contribute to the integral.

Appendix D

Derivation of MHD Equations in Curvilinear Coordinates

Here we walk through the full derivation of equation (7.50) from Section 7.2.3 based on the curvilinear coordinate framework of Scheurwater (1990).

D.1 Mass Conservation Equation

Beginning with the mass conservation equation (7.1) and substituting the definition of the divergence from Table 7.1 we obtain

$$\frac{\partial \rho}{\partial t} = -\tilde{\rho}\frac{\partial}{\partial u^m}(\tilde{\rho}^{-1}\,[\rho \mathcal{V}^m]). \tag{D.1}$$

Substituting the perturbation approximations (7.5) and (7.6) the equation becomes

$$\frac{\partial(\rho_0\tilde{\rho} + \rho_1)}{\partial t} = -\tilde{\rho}\frac{\partial}{\partial u^m}(\tilde{\rho}^{-1}(\rho_0\tilde{\rho} + \rho_1)V^m), \tag{D.2}$$

and neglecting the second-order perturbation term $\rho_1 V^m$, we obtain for the final form

$$\frac{\partial \rho_1}{\partial t} = -\rho_0\tilde{\rho}\,\frac{\partial V^m}{\partial u^m}. \tag{D.3}$$

D.2 Lorenz Equation

The time derivative of the magnetic field in curvilinear tensor notation is the same as the uniform case (equation (7.9))

$$\frac{\partial \mathbf{b}}{\partial t} = \boldsymbol{\nabla} \times (\mathbf{V} \times \mathbf{B}) \tag{D.4}$$

To express this equation in tensor notation, first we turn our attention to the term $\mathbf{V} \times \mathbf{B}$

$$\mathbf{V} \times \mathbf{B} = (V^l \boldsymbol{f}_l) \times (B^3 \boldsymbol{f}_3) = V^l B^3 \boldsymbol{f}_l \times \boldsymbol{f}_3. \tag{D.5}$$

Applying the cross product identity (equation (7.45) in Table 7.1) and substituting $B^3 = \tilde{\rho} B_0$ we can represent the above equation as:

$$\mathbf{V} \times \mathbf{B} = V^l \tilde{\rho} B_0 \tilde{\rho}^{-1} \, \varepsilon_{nl3} \boldsymbol{f}^n \tag{D.6}$$

$$= V^l B_0 \, \varepsilon_{nl3} \boldsymbol{f}^n = F_n \boldsymbol{f}^n. \tag{D.7}$$

That is, this result describes the components of a covariant vector. From Table 7.1 the curl of a vector $\mathbf{F}$ is expressed

$$\boldsymbol{\nabla} \times \mathbf{F} = \tilde{\rho} \, \varepsilon^{mnk} \frac{\partial F_n}{\partial u^m} \boldsymbol{f}_k \tag{D.8}$$

which implies

$$\boldsymbol{\nabla} \times (\mathbf{V} \times \mathbf{B}) = \tilde{\rho} B_0 \, \varepsilon_{nl3} \, \varepsilon^{mnk} \frac{\partial V^l}{\partial u^m} \boldsymbol{f}_k. \tag{D.9}$$

Because two indices in the Levi-Civita tensors are shared, we can simplify the product $\varepsilon_{nl3} \, \varepsilon^{mnk} = -\varepsilon_{nl3} \, \varepsilon^{nmk} = \delta_l^k \delta_3^m - \delta_l^m \delta_3^k$, which allows us to write the vector components of equation (D.4) as

$$\frac{\partial b^k}{\partial t} = B^3 \left(\frac{\partial V^k}{\partial u^3} - \frac{\partial V^m}{\partial u^m} \delta_3^k \right). \tag{D.10}$$

D.3 Momentum Equation

Once the forms of the previous (much simpler) equations have been determined, we can apply the results to the momentum equation (7.8). We begin with equation (7.49)

$$\frac{\partial^2 \mathbf{V}}{\partial t^2} = -\frac{\sigma_0^2}{\rho_0 \tilde{\rho}} \boldsymbol{\nabla} \frac{\partial \rho_1}{\partial t} - \frac{1}{4\pi \rho_0 \tilde{\rho}} \left[\mathbf{B} \times \left(\boldsymbol{\nabla} \times \frac{\partial \mathbf{b}}{\partial t} \right) + \frac{\partial \mathbf{b}}{\partial t} \times (\boldsymbol{\nabla} \times \mathbf{B}) \right]. \tag{D.11}$$

To help break down the derivation into manageable chunks, we define

$$\boldsymbol{\mathcal{A}} = -\frac{\sigma_0^2}{\rho_0 \tilde{\rho}} \boldsymbol{\nabla} \frac{\partial \rho_1}{\partial t}, \tag{D.12}$$

$$\boldsymbol{\mathcal{B}} = -\frac{1}{4\pi \rho_0 \tilde{\rho}} \mathbf{B} \times \left(\boldsymbol{\nabla} \times \frac{\partial \mathbf{b}}{\partial t} \right) \tag{D.13}$$

$$\boldsymbol{\mathcal{C}} = -\frac{1}{4\pi \rho_0 \tilde{\rho}} \frac{\partial \mathbf{b}}{\partial t} \times (\boldsymbol{\nabla} \times \mathbf{B}) \tag{D.14}$$

so that we can write

$$\frac{\partial^2 \mathbf{V}}{\partial t^2} = \boldsymbol{\mathcal{A}} + \boldsymbol{\mathcal{B}} + \boldsymbol{\mathcal{C}} \tag{D.15}$$

and address each term separately.

D.3.1 Term $\boldsymbol{\mathcal{A}}$

$$\boldsymbol{\mathcal{A}} = -\frac{\sigma_0^2}{\rho_0 \tilde{\rho}} \boldsymbol{\nabla} \frac{\partial \rho_1}{\partial t} \tag{D.16}$$

Substituting in equation (D.3) and using the gradient operator definition in Table 7.1 we obtain

$$\boldsymbol{\mathcal{A}} = -\frac{\sigma_0^2}{\rho_0 \tilde{\rho}} \boldsymbol{f}^p \frac{\partial}{\partial u^p} \left(-\rho_0 \tilde{\rho} \frac{\partial V^q}{\partial u^q} \right) \tag{D.17}$$

$$= \frac{\sigma_0^2}{\tilde{\rho}} \left[\frac{\partial V^q}{\partial u^q} \frac{\partial \tilde{\rho}}{\partial u^p} + \tilde{\rho} \frac{\partial^2 V^q}{\partial u^p \partial u^q} \right] \boldsymbol{f}^p \tag{D.18}$$

$$= \mathcal{A}_p \boldsymbol{f}^p. \tag{D.19}$$

That is, we obtain an expression for the covariant coefficients of $\boldsymbol{\mathcal{A}}$ in terms of the contravariant components of $\mathbf{V}$.

D.3.2 Term $\boldsymbol{\mathcal{B}}$

$$\boldsymbol{\mathcal{B}} = -\frac{1}{4\pi \rho_0 \tilde{\rho}} \mathbf{B} \times \left(\boldsymbol{\nabla} \times \frac{\partial \mathbf{b}}{\partial t} \right) \tag{D.20}$$

Beginning with the term in brackets:

$$\boldsymbol{\nabla} \times \frac{\partial \mathbf{b}}{\partial t} = \tilde{\rho}\, \varepsilon^{mnk} \frac{\partial}{\partial u^m} \left(\frac{\partial b_n}{\partial t} \right) \boldsymbol{f}_k. \tag{D.21}$$

Therefore

$$\boldsymbol{\mathcal{B}} = -\frac{B^3}{4\pi \rho_0 \tilde{\rho}}\, \varepsilon^{mnk} \frac{\partial}{\partial u^m} \left(\frac{\partial b_n}{\partial t} \right) \tilde{\rho} \boldsymbol{f}_3 \times \boldsymbol{f}_k \tag{D.22}$$

$$= -\frac{B^3}{4\pi \rho_0 \tilde{\rho}}\, \varepsilon_{p3k}\, \varepsilon^{mnk} \frac{\partial}{\partial u^m} \left(\frac{\partial b_n}{\partial t} \right) \boldsymbol{f}^p \tag{D.23}$$

$$= \mathcal{B}_p \boldsymbol{f}^p \tag{D.24}$$

once again substituting the cross-product identity (7.45). This yields the components of the covariant form of $\boldsymbol{\mathcal{B}}$. Expanding the product of the two Levi-Civita tensors in the vector

components and substituting $b_n = g_{nq}b^q$ as per equation (7.36) yields:

$$\mathcal{B}_p = -\frac{1}{4\pi\rho_0\tilde{\rho}}(\delta_p^m\delta_3^n - \delta_3^m\delta_p^n)B^3\frac{\partial}{\partial u^m}\left(\frac{\partial b_n}{\partial t}\right) \tag{D.25}$$

$$= -\frac{1}{4\pi\rho_0\tilde{\rho}}\left[B^3\frac{\partial}{\partial u^p}\left(\frac{\partial b_3}{\partial t}\right) - B^3\frac{\partial}{\partial u^3}\left(\frac{\partial b_p}{\partial t}\right)\right] \tag{D.26}$$

$$= -\frac{1}{4\pi\rho_0\tilde{\rho}}\left[B^3\frac{\partial}{\partial u^p}\left(g_{3q}\frac{\partial b^q}{\partial t}\right) - B^3\frac{\partial}{\partial u^3}\left(g_{pq}\frac{\partial b^q}{\partial t}\right)\right]. \tag{D.27}$$

Expanding the resulting expression via product rule gives us

$$\mathcal{B}_p = -\frac{B^3}{4\pi\rho_0\tilde{\rho}}\frac{\partial b^q}{\partial t}\left(\frac{\partial g_{3q}}{\partial u^p} - \frac{\partial g_{pq}}{\partial u^3}\right) - \frac{B^3}{4\pi\rho_0\tilde{\rho}}\left[g_{3q}\frac{\partial}{\partial u^p}\left(\frac{\partial b^q}{\partial t}\right) - g_{pq}\frac{\partial}{\partial u^3}\left(\frac{\partial b^q}{\partial t}\right)\right]. \tag{D.28}$$

That is, the covariant components of $\boldsymbol{\mathcal{B}}$ are expressed in terms of equation (D.10), which depends on the contravariant components of $\mathbf{V}$.

D.3.3 Term $\mathcal{C}$

$$\boldsymbol{\mathcal{C}} = -\frac{1}{4\pi\rho_0\tilde{\rho}}\frac{\partial \mathbf{b}}{\partial t} \times (\boldsymbol{\nabla} \times \mathbf{B}) \tag{D.29}$$

Again, beginning with the term in brackets, the curl of the magnetic field is

$$\boldsymbol{\nabla} \times \mathbf{B} = \tilde{\rho}\,\varepsilon^{mnk}\frac{\partial B_n}{\partial u^m}\boldsymbol{f}_k, \tag{D.30}$$

therefore

$$\boldsymbol{\mathcal{C}} = -\frac{1}{4\pi\rho_0\tilde{\rho}}\frac{\partial b^q}{\partial t}\,\varepsilon^{mnk}\frac{\partial B_n}{\partial u^m}\tilde{\rho}\boldsymbol{f}_q \times \boldsymbol{f}_k \tag{D.31}$$

$$= -\frac{1}{4\pi\rho_0\tilde{\rho}}\,\varepsilon_{pqk}\,\varepsilon^{mnk}\frac{\partial b^q}{\partial t}\frac{\partial B_n}{\partial u^m}\boldsymbol{f}^p \tag{D.32}$$

$$= -\frac{1}{4\pi\rho_0\tilde{\rho}}(\delta_p^m\delta_q^n - \delta_q^m\delta_p^n)\frac{\partial b^q}{\partial t}\frac{\partial B_n}{\partial u^m}\boldsymbol{f}^p \tag{D.33}$$

$$= -\frac{1}{4\pi\rho_0\tilde{\rho}}\frac{\partial b^q}{\partial t}\left(\frac{\partial B_q}{\partial u^p} - \frac{\partial B_p}{\partial u^q}\right)\boldsymbol{f}^p \tag{D.34}$$

$$= \mathcal{C}_p\boldsymbol{f}^p \tag{D.35}$$

where we have expanded the product of the two Levi-Civita tensors as before. As in the previous two cases, the end result is the covariant vector components of $\boldsymbol{\mathcal{C}}$. Utilizing $B_q =$

$g_{q3}B^3$ and expanding using product rule, we obtain for the covariant coefficients

$$\mathcal{C}_p = -\frac{1}{4\pi\rho_0\tilde{\rho}}\frac{\partial b^q}{\partial t}\left[B^3\left(\frac{\partial g_{q3}}{\partial u^p} - \frac{\partial g_{p3}}{\partial u^q}\right) + \left(g_{q3}\frac{\partial B^3}{\partial u^p} - g_{p3}\frac{\partial B^3}{\partial u^q}\right)\right]. \tag{D.36}$$

D.3.4 Bringing It Back Together

All of the above results produce covariant vector components, i.e.

$$\frac{\partial^2 V_p}{\partial t^2} = \mathcal{A}_p + \mathcal{B}_p + \mathcal{C}_p \tag{D.37}$$

where each of the terms on the right hand side involves spatial derivatives of V^q. To make the equation self-consistent, we use $V^k = g^{kp}V_p$ to obtain the complete wave equation

$$\begin{aligned}\frac{\partial^2 V^k}{\partial t^2} = g^{kp}\frac{\partial^2 V_p}{\partial t^2} = g^{kp}\frac{\sigma^2}{\tilde{\rho}}\left[\frac{\partial V^q}{\partial u^q}\frac{\partial \tilde{\rho}}{\partial u^p} + \tilde{\rho}\frac{\partial^2 V^q}{\partial u^p \partial u^q}\right] - g^{kp}\frac{B^3}{4\pi\rho_0\tilde{\rho}}\frac{\partial b^q}{\partial t}\left(\frac{\partial g_{3q}}{\partial u^p} - \frac{\partial g_{pq}}{\partial u^3}\right) \\ - g^{kp}\frac{B^3}{4\pi\rho_0\tilde{\rho}}\left[g_{3q}\frac{\partial}{\partial u^p}\left(\frac{\partial b^q}{\partial t}\right) - g_{pq}\frac{\partial}{\partial u^3}\left(\frac{\partial b^q}{\partial t}\right)\right] \\ - g^{kp}\frac{1}{4\pi\rho_0\tilde{\rho}}\frac{\partial b^q}{\partial t}\left[B^3\left(\frac{\partial g_{q3}}{\partial u^p} - \frac{\partial g_{p3}}{\partial u^q}\right) + \left(g_{q3}\frac{\partial B^3}{\partial u^p} - g_{p3}\frac{\partial B^3}{\partial u^q}\right)\right]\end{aligned} \tag{D.38}$$

where

$$\frac{\partial b^q}{\partial t} = B^3\left(\frac{\partial V^q}{\partial u^3} - \frac{\partial V^m}{\partial u^m}\delta^q_3\right) \tag{D.39}$$

as per §D.2.

Appendix E

Derivation of the 0^{th} Order MHD Wave Equation Under the Eikonal Approximation

Here we summarize the manipulation required to use the rescaled variables defined in Section7.2.4 to obtain the 0^{th} order wave equation (7.61). As before, this is an expansion of the corresponding manipulations in Scheurwater (1990).

E.1 Change of Variable

We assume a plane wave form for the velocity with coordinate dependent amplitude:

$$V^k(\mathbf{x}, t) = v^k(\mathbf{x}) e^{i\psi(\mathbf{x},t)} \tag{E.1}$$

where v^k are the contravariant velocity amplitudes and ψ is the phase, such that

$$\mathbf{k} = \boldsymbol{\nabla}\psi = f^m \frac{\partial \psi}{\partial u^m}, \qquad \omega = -\frac{\partial \psi}{\partial t}. \tag{E.2}$$

The eikonal approximation assumes the local wavelength $\lambda = 2\pi/k$ is small compared to the scale of the spatial changes in the magnetic field and density $(\lambda_\rho, \lambda_B)$. When $\mathbf{k}$ and v^k are on the order of $\varepsilon = (k\lambda)^{-1} \ll 1$, where λ represents the minimum between λ_ρ and λ_B, we can apply perturbation methods to expand the velocity amplitudes in an asymptotic series:

$$v^k = \sum_n^\infty \varepsilon^n v^k_{(n)} \tag{E.3}$$

and scaling the physical scales by ε to enforce operations on small scales, we define

$$\overline{u^m} = \varepsilon u^m \tag{E.4}$$

$$\overline{\psi} = \varepsilon \psi \tag{E.5}$$

with velocity amplitudes

$$\overline{v_n^m} = v_n^m. \tag{E.6}$$

These definitions keep $\boldsymbol{\nabla}\psi = \overline{\boldsymbol{\nabla}}\,\overline{\psi} = \mathbf{k}$. Making the further transformation

$$\bar{t} = \varepsilon t \tag{E.7}$$

keeps consistency for the angular velocity $\frac{\partial \psi}{\partial t} = \frac{\partial \overline{\psi}}{\partial \bar{t}} = -\omega$.

To help break down the number of terms into manageable chunks, we once again split the right-hand side of equation (7.50) into the three sub functions $\boldsymbol{\mathcal{A}}$, $\boldsymbol{\mathcal{B}}$, and $\boldsymbol{\mathcal{C}}$ from the previous appendix and modify them individually.

E.1.1 Term $\boldsymbol{\mathcal{A}}$

We have

$$\mathcal{A}^k = g^{kp}\frac{\sigma_0^2}{\tilde{\rho}}\left[\frac{\partial \tilde{\rho}}{\partial u^p}\frac{\partial V^q}{\partial u^q} + \tilde{\rho}\frac{\partial^2 V^q}{\partial u^p \partial u^q}\right] \tag{E.8}$$

$$= \sum_n^\infty \varepsilon^n g^{kp}\frac{\sigma_0^2}{\tilde{\rho}}\left[\varepsilon^2\frac{\partial \tilde{\rho}}{\partial \overline{u^p}}\frac{\partial (v_{(n)}^q e^{i\overline{\psi}\varepsilon^{-1}})}{\partial \overline{u^q}} + \varepsilon^2\tilde{\rho}\frac{\partial^2 (v_{(n)}^q e^{i\overline{\psi}\varepsilon^{-1}})}{\partial \overline{u^p}\partial \overline{u^q}}\right] \tag{E.9}$$

which becomes:

$$\begin{aligned}\mathcal{A}^k = \sum_n^\infty \varepsilon^n g^{kp}\frac{\sigma_0^2}{\tilde{\rho}}\Bigg[\tilde{\rho}\Bigg(&\varepsilon^2\frac{\partial^2 v_{(n)}^q}{\partial \overline{u^p}\partial \overline{u^q}} + i\varepsilon\frac{\partial v_{(n)}^q}{\partial \overline{u^q}}\frac{\partial \overline{\psi}}{\partial \overline{u^p}} + i\varepsilon\frac{\partial v_{(n)}^q}{\partial \overline{u^p}}\frac{\partial \overline{\psi}}{\partial \overline{u^q}} + i\varepsilon\frac{\partial^2 \overline{\psi}}{\partial \overline{u^q}\partial \overline{u^p}}v_{(n)}^q \\ &- \frac{\partial \overline{\psi}}{\partial \overline{u^q}}\frac{\partial \overline{\psi}}{\partial \overline{u^p}}v_{(n)}^q\Bigg) + \varepsilon^2\frac{\partial v_{(n)}^q}{\partial \overline{u^q}}\frac{\partial \tilde{\rho}}{\partial \overline{u^p}} + i\varepsilon\frac{\partial \overline{\psi}}{\partial \overline{u^q}}v_{(n)}^q\frac{\partial \tilde{\rho}}{\partial \overline{u^p}}\Bigg] e^{i\overline{\psi}\varepsilon^{-1}}\end{aligned} \tag{E.10}$$

$$\begin{aligned}= \sum_n^\infty \varepsilon^n g^{kp}\frac{\sigma_0^2}{\tilde{\rho}}\Bigg[\tilde{\rho}\Bigg(&\varepsilon^2\frac{\partial^2 v_{(n)}^q}{\partial \overline{u^p}\partial \overline{u^q}} + i\varepsilon\frac{\partial v_{(n)}^q}{\partial \overline{u^q}}k_p + i\varepsilon\frac{\partial v_{(n)}^q}{\partial \overline{u^p}}k_q + i\varepsilon\frac{\partial k_q}{\partial \overline{u^p}}v_{(n)}^q - k_q k_p v_{(n)}^q\Bigg) \\ &+\varepsilon^2\frac{\partial \tilde{\rho}}{\partial \overline{u^p}}\frac{\partial v_{(n)}^q}{\partial \overline{u^q}} + i\varepsilon k_q v_{(n)}^q\frac{\partial \tilde{\rho}}{\partial \overline{u^p}}\Bigg] e^{i\overline{\psi}\varepsilon^{-1}}.\end{aligned} \tag{E.11}$$

where we have evaluated $\frac{\partial\overline{\psi}}{\partial\overline{u^n}}$ using equation (7.53). Only terms that are coefficients of ε^0 are relevant for our current analysis, so we can define the further sub-expression representing the ε^0 coefficients af $\mathcal{A}^k$:

$$\left[\mathcal{A}^k\right]_{\varepsilon^0} = -g^{kp}\sigma_0^2 k_p k_q v^q_{(0)} e^{i\overline{\psi}\varepsilon^{-1}} = -\sigma_0^2 k^k k_q v^q_{(0)} e^{i\overline{\psi}\varepsilon^{-1}} \tag{E.12}$$

$$= -\sigma_0^2(\mathbf{v}_{(0)}\cdot\mathbf{k})k^k e^{i\overline{\psi}\varepsilon^{-1}} \tag{E.13}$$

where we have made the substitution $k_q v^q_{(0)} = (\mathbf{v}_{(0)}\cdot\mathbf{k})$).

E.1.2 Term $\mathcal{B}$

For $\mathcal{B}^k$:

$$\mathcal{B}^k = -g^{kp}\frac{B^3}{4\pi\rho_0\tilde{\rho}}\frac{\partial b^q}{\partial t}\left(\frac{\partial g_{3q}}{\partial u^p} - \frac{\partial g_{pq}}{\partial u^3}\right) - g^{kp}\frac{B^3}{4\pi\rho_0\tilde{\rho}}\left[g_{3q}\frac{\partial}{\partial u^p}\left(\frac{\partial b^q}{\partial t}\right) - g_{pq}\frac{\partial}{\partial u^3}\left(\frac{\partial b^q}{\partial t}\right)\right] \tag{E.14}$$

$$= -\varepsilon^2 g^{kp}\frac{B^3}{4\pi\rho_0\tilde{\rho}}\frac{\partial b^q}{\partial\overline{t}}\left(\frac{\partial g_{3q}}{\partial\overline{u^p}} - \frac{\partial g_{pq}}{\partial\overline{u^3}}\right) - \varepsilon^2 g^{kp}\frac{B^3}{4\pi\rho_0\tilde{\rho}}\left[g_{3q}\frac{\partial}{\partial\overline{u^p}}\left(\frac{\partial b^q}{\partial\overline{t}}\right) - g_{pq}\frac{\partial}{\partial\overline{u^3}}\left(\frac{\partial b^q}{\partial\overline{t}}\right)\right] \tag{E.15}$$

To evaluate this equation, we need to first evaluate equation (D.10) in terms of $\overline{u^m}$, absorbing the factor of ε^2:

$$\varepsilon^2\frac{\partial b^q}{\partial\overline{t}} = B^3\left(\varepsilon^2\frac{\partial v^q}{\partial\overline{u^3}} - \varepsilon^2\frac{\partial v^m}{\partial\overline{u^m}}\delta^q_3\right) \tag{E.16}$$

$$= \sum_n^\infty \varepsilon^n B^3\left(\varepsilon^2\frac{\partial(v^q_{(n)}e^{i\overline{\psi}\varepsilon^{-1}})}{\partial\overline{u^3}} - \varepsilon^2\frac{\partial(v^m_{(n)}e^{i\overline{\psi}\varepsilon^{-1}})}{\partial\overline{u^m}}\delta^q_3\right) \tag{E.17}$$

$$= \sum_n^\infty \varepsilon^n B^3\left(\varepsilon^2\frac{\partial v^q_{(n)}}{\partial\overline{u^3}} + i\varepsilon k_3 v^q_{(n)} - \varepsilon^2\frac{\partial v^m_{(n)}}{\partial\overline{u^m}}\delta^q_3 - i\varepsilon k_m v^m_{(n)}\delta^q_3\right)e^{i\overline{\psi}\varepsilon^{-1}}. \tag{E.18}$$

once again using equation (7.53) as in the previous case. For the first term in equation (E.15), we want terms that are coefficients of ε^0:

$$\left[\varepsilon^2\frac{\partial b^q}{\partial\overline{t}}\right]_{\varepsilon^0} = 0. \tag{E.19}$$

Then, to evaluate the second term in equation (E.15), we evaluate the spatial derivative

of equation (E.18):

$$\varepsilon^2\frac{\partial^2 b^q}{\partial\overline{u^l}\partial\overline{t}} = \sum_n^\infty \varepsilon^n \frac{\partial}{\partial\overline{u^l}}\left[B^3\left(\varepsilon^2\frac{\partial v^q_{(n)}}{\partial\overline{u^3}} + i\varepsilon k_3 v^q_{(n)} - \varepsilon^2\frac{\partial v^m_{(n)}}{\partial\overline{u^m}}\delta^q_3 - i\varepsilon k_m v^m_{(n)}\delta^q_3\right)e^{i\overline{\psi}\varepsilon^{-1}}\right] \tag{E.20}$$

$$\begin{aligned}
&= \sum_n^\infty \varepsilon^n \frac{\partial B^3}{\partial\overline{u^l}}\left(\varepsilon^2\frac{\partial v^q_{(n)}}{\partial\overline{u^3}} + i\varepsilon k_3 v^q_{(n)} - \varepsilon^2\frac{\partial v^m_{(n)}}{\partial\overline{u^m}}\delta^q_3 - i\varepsilon k_m v^m_{(n)}\delta^q_3\right)e^{i\overline{\psi}\varepsilon^{-1}} \\
&\quad + \varepsilon^n B^3\left(\varepsilon^2\frac{\partial^2 v^q_{(n)}}{\partial\overline{u^l}\partial\overline{u^3}} + i\varepsilon\frac{\partial k_3}{\partial\overline{u^l}}v^q_{(n)} + i\varepsilon k_3\frac{\partial v^q_{(n)}}{\partial\overline{u^l}} - \varepsilon^2\frac{\partial^2 v^m_{(n)}}{\partial\overline{u^l}\partial\overline{u^m}}\delta^q_3\right. \\
&\qquad \left. - i\varepsilon\frac{\partial k_m}{\partial\overline{u^l}}v^m_{(n)}\delta^q_3 - i\varepsilon k_m\frac{\partial v^m_{(n)}}{\partial\overline{u^l}}\delta^q_3\right)e^{i\overline{\psi}\varepsilon^{-1}} \\
&\quad + \varepsilon^n B^3\left(i\varepsilon k_l\frac{\partial v^q_{(n)}}{\partial\overline{u^3}} - k_l k_3 v^q_{(n)} - i\varepsilon k_l\frac{\partial v^m_{(n)}}{\partial\overline{u^m}}\delta^q_3\right. \\
&\qquad \left. + k_l k_m v^m_{(n)}\delta^q_3\right)e^{i\overline{\psi}\varepsilon^{-1}}.
\end{aligned} \tag{E.21}$$

Once again, we want terms with ε^0 from the above expression:

$$\left[\varepsilon^2\frac{\partial^2 b^q}{\partial\overline{u^l}\partial\overline{t}}\right]_{\varepsilon^0} = B^3\left[-k_l k_3 v^q_{(0)} + k_l k_m v^m_{(0)}\delta^q_3\right]e^{i\overline{\psi}\varepsilon^{-1}}. \tag{E.22}$$

Substituting these expressions back into equation (E.15) we obtain

$$\begin{aligned}
\left[\mathcal{B}^k\right]_{\varepsilon^0} &= -g^{kp}\frac{B^3}{4\pi\rho_0\tilde{\rho}}\left[\varepsilon^2\frac{\partial b^q}{\partial\overline{t}}\right]_{\varepsilon^0}\left(\frac{\partial g_{3q}}{\partial\overline{u^p}} - \frac{\partial g_{pq}}{\partial\overline{u^3}}\right) \\
&\quad - g^{kp}\frac{B^3}{4\pi\rho_0\tilde{\rho}}\left[g_{3q}\left[\varepsilon^2\frac{\partial^2 b^q}{\partial\overline{u^p}\partial\overline{t}}\right]_{\varepsilon^0} - g_{pq}\left[\varepsilon^2\frac{\partial^2 b^q}{\partial\overline{u^3}\partial\overline{t}}\right]_{\varepsilon^0}\right]
\end{aligned} \tag{E.23}$$

$$\begin{aligned}
&= -g^{kp}\frac{B^{3^2}}{4\pi\rho_0\tilde{\rho}}\left[g_{3q}(-k_p k_3 v^q_{(0)} + k_p k_m v^m_{(0)}\delta^q_3)\right. \\
&\qquad \left. - g_{pq}(-k_3 k_3 v^q_{(0)} + k_3 k_m v^m_{(0)}\delta^q_3)\right]e^{i\overline{\psi}\varepsilon^{-1}}.
\end{aligned} \tag{E.24}$$

We can contract some of the indices in equation (E.24) and substitute in the Alfvén speed definition (7.40) to produce:

$$\begin{aligned}
\left[\mathcal{B}^k\right]_{\varepsilon^0} &= -g^{kp}{c^3_{A0}}^2\left[(-k_p k_3 v_{(0)3} + g_{33}k_p k_m v^m_{(0)})\right. \\
&\qquad \left. -(-k_3 k_3 v_{(0)p} + g_{p3}k_3 k_m v^m_{(0)})\right]e^{i\overline{\psi}\varepsilon^{-1}}
\end{aligned} \tag{E.25}$$

$$\begin{aligned}
&= \left[(k^k c^3_{A0}k_3 c^3_{A0}v_{(0)3} - g_{33}c^3_{A0}c^3_{A0}k^k k_m v^m_{(0)})\right. \\
&\qquad \left. +(-c^3_{A0}k_3 c^3_{A0}k_3 v^k_{(0)} + \delta^k_3 c^3_{A0}c^3_{A0}k_3 k_m v^m_{(0)})\right]e^{i\overline{\psi}\varepsilon^{-1}}.
\end{aligned} \tag{E.26}$$

Inspection of the terms in this expression yields several expressions for the dot products of the vectors $\mathbf{v}_{(0)}, \mathbf{k}$, and $\mathbf{c}_{A0}$, allowing us to express equation (E.26) as

$$\begin{aligned}\left[\mathcal{B}^k\right]_{\varepsilon^0} = \big[&(\mathbf{c}_{A0}\cdot\mathbf{k})(\mathbf{c}_{A0}\cdot\mathbf{v}_{(0)})k^k - c_{A0}^2(\mathbf{v}_{(0)}\cdot\mathbf{k})k^k - (\mathbf{c}_{A0}\cdot\mathbf{k})^2 v_{(0)}^k \\ &+(\mathbf{c}_{A0}\cdot\mathbf{k})(\mathbf{v}_{(0)}\cdot\mathbf{k})c_{A0}^3\delta_3^k)\big]\, e^{i\overline{\psi}\varepsilon^{-1}}.\end{aligned} \tag{E.27}$$

E.1.3 Term $\mathcal{C}$

For $\mathcal{C}^k$:

$$\mathcal{C}^k = -\frac{g^{kp}}{4\pi\rho_0\tilde{\rho}}\frac{\partial b^q}{\partial t}\left[B^3\left(\frac{\partial g_{q3}}{\partial u^p} - \frac{\partial g_{p3}}{\partial u^q}\right) + \left(g_{q3}\frac{\partial B^3}{\partial u^p} - g_{p3}\frac{\partial B^3}{\partial u^q}\right)\right] \tag{E.28}$$

$$= -\varepsilon^2\frac{g^{kp}}{4\pi\rho_0\tilde{\rho}}\frac{\partial b^q}{\partial \bar{t}}\left[B^3\left(\frac{\partial g_{q3}}{\partial \overline{u^p}} - \frac{\partial g_{p3}}{\partial \overline{u^q}}\right) + \left(g_{q3}\frac{\partial B^3}{\partial \overline{u^p}} - g_{p3}\frac{\partial B^3}{\partial \overline{u^q}}\right)\right]. \tag{E.29}$$

So $\left[\mathcal{C}^k\right]_{\varepsilon^0}$ is

$$\left[\mathcal{C}^k\right]_{\varepsilon^0} = -\frac{g^{kp}}{4\pi\rho_0\tilde{\rho}}\left[\varepsilon^2\frac{\partial b^q}{\partial \bar{t}}\right]_{\varepsilon^0}\left[B^3\left(\frac{\partial g_{q3}}{\partial \overline{u^p}} - \frac{\partial g_{p3}}{\partial \overline{u^q}}\right) + \left(g_{q3}\frac{\partial B^3}{\partial \overline{u^p}} - g_{p3}\frac{\partial B^3}{\partial \overline{u^q}}\right)\right] \tag{E.30}$$

$$= 0. \tag{E.31}$$

from equation (E.19).

E.1.4 Complete 0th order wave equation

Evaluating the left hand side of equation (7.50) we obtain

$$\frac{\partial^2 V^k}{\partial t^2} = \varepsilon^2\frac{\partial^2(\varepsilon^n v_{(n)}^k e^{i\overline{\psi}\varepsilon^{-1}})}{\partial \bar{t}^2} \tag{E.32}$$

$$= \sum_n^\infty \varepsilon^{n+2} v_{(n)}^k\left(i\varepsilon^{-1}\frac{\partial\overline{\psi}}{\partial\bar{t}}\right)^2 e^{i\overline{\psi}\varepsilon^{-1}} \tag{E.33}$$

$$= -\sum_n^\infty \varepsilon^n v_{(n)}^k\left(\frac{\partial\overline{\psi}}{\partial\bar{t}}\right)^2 e^{i\overline{\psi}\varepsilon^{-1}}. \tag{E.34}$$

From equation (7.53)

$$\frac{\partial\psi}{\partial t} = \frac{\partial\overline{\psi}}{\partial\bar{t}} = -\omega. \tag{E.35}$$

Combining this with the ε^0 coefficients of the previous subsections (equations (E.13), (E.27), and (E.31)), we obtain

$$0 = \left[\frac{\partial^2 V^k}{\partial t^2}\right]_{\varepsilon^0} + \left[\mathcal{A}^k\right]_{\varepsilon^0} + \left[\mathcal{B}^k\right]_{\varepsilon^0} + \left[\mathcal{C}^k\right]_{\varepsilon^0} \tag{E.36}$$

$$\begin{aligned} = \omega^2 v^k_{(0)} e^{i\overline{\psi}\varepsilon^{-1}} - \sigma_0^2(\mathbf{v}_{(0)}\cdot\mathbf{k})k^k e^{i\overline{\psi}\varepsilon^{-1}} + \big[&(\mathbf{c}_{A0}\cdot\mathbf{k})(\mathbf{c}_{A0}\cdot\mathbf{v}_{(0)})k^k - c_{A0}^2(\mathbf{v}_{(0)}\cdot\mathbf{k})k^k \\ &-(\mathbf{c}_{A0}\cdot\mathbf{k})^2 v^k_{(0)} + (\mathbf{c}_{A0}\cdot\mathbf{k})(\mathbf{v}_{(0)}\cdot\mathbf{k})c_{A0}^3\delta^k_3\big] e^{i\overline{\psi}\varepsilon^{-1}} \end{aligned} \tag{E.37}$$

Which we can write in general vector form as

$$\begin{aligned} 0 = \omega^2\mathbf{v}_{(\mathbf{0})} &- (\sigma_0^2 + c_{A0}^2)(\mathbf{v}_{(0)}\cdot\mathbf{k})\mathbf{k} \\ &- (\mathbf{c}_{A0}\cdot\mathbf{k})\left[(\mathbf{c}_{A0}\cdot\mathbf{k})\mathbf{v}_{(0)} - (\mathbf{c}_{A0}\cdot\mathbf{v}_{(0)})\mathbf{k} - (\mathbf{v}_{(0)}\cdot\mathbf{k})\mathbf{c}_{A0}\right]. \end{aligned} \tag{E.38}$$

$$\Rightarrow 0 = \omega^2 v^k_{(0)} - (\sigma_0^2 + c_{A0}^2)k^k k_m v^m_{(0)} - (c_{A0}^3 k_3)\left[c_{A0}^3 k_3 v^k_{(0)} - c_{A0}^3 v_{(0)3}k^k - c_{A0}^3 k_m v^m_{(0)}\delta^k_3\right] \tag{E.39}$$

This equation is identical to the wave equation in Jackson (1975) before vector orientations are applied. Continuing to follow the Scheurwater (1990) derivation, we define the tensor operator $\Lambda^k_{(0)_m}$ such that $\Lambda^k_{(0)_m} v^m_{(0)}$ reproduces equation (E.38):

$$\Lambda^k_{(0)_m} = \omega^2\delta^k_m - (\sigma_0^2 + c_{A0}^2)k_m k^k - (c_{A0}^3 k_3)^2\delta^k_m + {c_{A0}^3}^2 k_3 k^k g_{3m} + k_m k_3 {c_{A0}^3}^2\delta^k_3. \tag{E.40}$$

Because $\Lambda^k_{(0)_m} v^m_{(0)} = 0$ it follows that $\det\Lambda^k_{(0)_m} = 0$ also. Evaluating the determinant of $\Lambda^k_{(0)_m}$ yields

$$\begin{aligned} \det\Lambda^k_{(0)_m} &= \omega^6 - \left[(c_{A0}^3 k_3)^2 - (c_{A0}^2 + \sigma_0^2)k^2\right]\omega^4 \\ &\quad + (c_{A0}^3 k_3)^2(c_{A0}^2 + 2\sigma_0^2)k^2\omega^2 - (c_{A0}^3 k_3)^4 k^2\sigma_0^2 = 0 \end{aligned} \tag{E.41}$$

$$= \left(\omega^2 - (c_{A0}^3 k_3)^2\right)\left(\omega^4 - (\sigma_0^2 + c_{A0}^2)k^2\omega^2 + (c_{A0}^3 k_3)^2 k^2\sigma_0^2\right) = 0 \tag{E.42}$$

(here k^2 is the square of the magnitude of $\mathbf{k}$). The first root, $(\omega^2 - (c_{A0}^3 k_3)^2) = (\omega^2 - (\mathbf{c}_{A0}\cdot\mathbf{k})^2) = 0$ is the Alfvén condition, and the remaining roots describe the fast and slow compression wave modes respectively. Notably, these roots exist for both the 0^{th} and 1^{st} order solutions, as $\Lambda^k_{(0)_m} v^m_{(1)}$ is the real part of the ε^1 wave equation.

Now that the Alfvén mode has been verified as a solution, we may now use it to obtain $\mathbf{k}$.

Appendix F

Derivation of the Alfvén Ray equations

This proof is as presented in Scheurwater (1990). We include it here for quick reference. From equation (7.53)

$$\frac{\partial \psi}{\partial u^3} = k_3, \tag{F.1}$$

since the wave is travelling along the magnetic field direction. Therefore, the phase can be determined by integrating k_3 along the magnetic field line, and we must obtain the propagation characteristics for k_3, which is worked out in Scheurwater (1990). Returning to the definition of $\mathbf{k}$ and ω as functions of ψ, we obtain

$$\frac{\partial \mathbf{k}}{\partial t} = \frac{\partial(\boldsymbol{\nabla}\psi)}{\partial t} = \boldsymbol{\nabla}\frac{\partial \psi}{\partial t} = -\boldsymbol{\nabla}\omega. \tag{F.2}$$

The wave vector of the Alfvén wave must obey

$$\omega = (\mathbf{c}_{A0} \cdot \mathbf{k}) \tag{F.3}$$

at all points, therefore

$$\frac{\partial \mathbf{k}}{\partial t} + \boldsymbol{\nabla}(\mathbf{c}_{A0} \cdot \mathbf{k}) = 0. \tag{F.4}$$

Expanding the second term, we obtain

$$\frac{\partial \mathbf{k}}{\partial t} + \mathbf{c}_{A0} \cdot \boldsymbol{\nabla}\mathbf{k} + \boldsymbol{\nabla}\mathbf{c}_{A0} \cdot \mathbf{k} = 0. \tag{F.5}$$

Because the wave is propagating along the field line, we can express the first two terms in this expression as the total derivative along the "ray path" $\mathbf{r}$ the wave travels

$$\frac{d\mathbf{k}}{dt} = \frac{\partial \mathbf{k}}{\partial t} + \mathbf{c}_{A0} \cdot \boldsymbol{\nabla} \mathbf{k} \tag{F.6}$$

$$= \frac{\partial \mathbf{k}}{\partial t} + \frac{d\mathbf{r}}{dt} \cdot \boldsymbol{\nabla} \mathbf{k} \tag{F.7}$$

and so we can write

$$\frac{d\mathbf{k}}{dt} = -\boldsymbol{\nabla} \mathbf{c}_{A0} \cdot \mathbf{k} \tag{F.8}$$

and the group velocity along the ray path is

$$\frac{d\mathbf{r}}{dt} = \boldsymbol{f}_m \frac{du^m}{dt} = \mathbf{c}_{A0}. \tag{F.9}$$

These two equations are the ray equations for an Alfvén wave. Along the field line, the arc length element is $ds = \sqrt{g_{33}}\, du^3$ which implies

$$\frac{ds}{dt} = \sqrt{g_{33}} \frac{du^3}{dt} = \sqrt{g_{33}}\, c_{A0}^3 = c_{A0} \tag{F.10}$$

which we can use to modify the ray equations (F.8) and (F.9) to obtain

$$\frac{d\mathbf{k}}{ds} = -\frac{\boldsymbol{\nabla} \mathbf{c}_{A0}}{c_{A0}} \cdot \mathbf{k} \tag{F.11}$$

$$\frac{d\mathbf{r}}{ds} = \boldsymbol{f}_3 \frac{1}{\sqrt{g_{33}}}. \tag{F.12}$$

To get equation (F.11) into a more usable form, we expand out both sides. However, we also want to express the above equation in general vector notation, since evaluating equation (F.11) involves gradients of basis vectors which makes it difficult to properly associate a pointing direction. In order to match the pointing on both sides, we evaluate

$$\frac{d\mathbf{k}}{ds} = \left[\boldsymbol{f}_p \cdot \frac{d\mathbf{k}}{ds} \right] \boldsymbol{f}^p = -\left[\boldsymbol{f}_p \cdot \frac{\boldsymbol{\nabla} \mathbf{c}_{A0}}{c_{A0}} \cdot \mathbf{k} \right] \boldsymbol{f}^p. \tag{F.13}$$

Starting with the left hand side, we have

$$\frac{d\mathbf{k}}{ds} = \left[\boldsymbol{f}_p \cdot \frac{dk_m}{ds}\boldsymbol{f}^m + \boldsymbol{f}_p \cdot k_m \frac{d\boldsymbol{f}^m}{ds}\right]\boldsymbol{f}^p \tag{F.14}$$

$$= \left[\frac{dk_p}{ds} + \left(\boldsymbol{f}_p \cdot \frac{d\boldsymbol{f}^m}{ds}\right)k_m\right]\boldsymbol{f}^p \tag{F.15}$$

$$= \left[\frac{dk_p}{ds} + \left(\boldsymbol{f}_p \cdot \frac{d\boldsymbol{f}^m}{du^q}\right)\frac{du^q}{ds}k_m\right]\boldsymbol{f}^p \tag{F.16}$$

$$= \left[\frac{dk_p}{ds} + \left(\boldsymbol{f}_p \cdot \frac{d\boldsymbol{f}^m}{du^3}\right)\frac{k_m}{\sqrt{g_{33}}}\right]\boldsymbol{f}^p. \tag{F.17}$$

On the right hand side, we have

$$-\frac{\boldsymbol{\nabla}\mathbf{c}_{A0}}{c_{A0}} \cdot \mathbf{k} = -\left[\boldsymbol{f}_p \cdot \left(\frac{\boldsymbol{\nabla}c_{A0}^3}{\sqrt{g_{33}}\,c_{A0}^3}\boldsymbol{f}_3\right) \cdot \boldsymbol{f}^m k_m + \frac{\boldsymbol{f}_p}{\sqrt{g_{33}}} \cdot \boldsymbol{\nabla}\boldsymbol{f}_3 \cdot \boldsymbol{f}^m k_m\right]\boldsymbol{f}^p \tag{F.18}$$

$$= -\left[\frac{k_3}{\sqrt{g_{33}}}\frac{\partial \ln(c_{A0}^3)}{\partial u^p} + \frac{k_m}{\sqrt{g_{33}}}\frac{\partial \boldsymbol{f}_3}{\partial u^p} \cdot \boldsymbol{f}^m\right]\boldsymbol{f}^p. \tag{F.19}$$

Therefore, in terms of the covariant components

$$\frac{dk_p}{ds} + \left(\boldsymbol{f}_p \cdot \frac{d\boldsymbol{f}^m}{du^3}\right)\frac{k_m}{\sqrt{g_{33}}} = -\frac{k_3}{\sqrt{g_{33}}}\frac{\partial \ln(c_{A0}^3)}{\partial u^p} - \frac{k_m}{\sqrt{g_{33}}}\frac{\partial \boldsymbol{f}_3}{\partial u^p} \cdot \boldsymbol{f}^m. \tag{F.20}$$

While this expression does not seem particularly useful in its current form, we can make some further simplifications using the definitions of the basis vectors. Due to the definition of the contravariant basis (equation (7.28))

$$\frac{\partial \boldsymbol{f}_3}{\partial u^p} = \frac{\partial}{\partial u^p}\frac{\partial x^n}{\partial u^3}\boldsymbol{e}^n = \frac{\partial}{\partial u^3}\frac{\partial x^n}{\partial u^p}\boldsymbol{e}^n = \frac{\partial \boldsymbol{f}_p}{\partial u^3}. \tag{F.21}$$

In addition, we know $\boldsymbol{f}_p \cdot \boldsymbol{f}^m = \delta_p^m$ so

$$\frac{\partial(\boldsymbol{f}_p \cdot \boldsymbol{f}^m)}{\partial u^3} = \frac{\partial \boldsymbol{f}_p}{\partial u^3} \cdot \boldsymbol{f}^m + \boldsymbol{f}_p \cdot \frac{\partial \boldsymbol{f}^m}{\partial u^3} = 0, \tag{F.22}$$

meaning the second terms on either side of equation (F.20) cancel, leaving

$$\frac{dk_p}{ds} = -\frac{k_3}{\sqrt{g_{33}}}\frac{\partial \ln(c_{A0}^3)}{\partial u^p}. \tag{F.23}$$

Equations (F.9) and (F.23) can now be used to propagate the Alfvén waves down the field lines.